Determining Distributed Source Waveforms in Causal, Lossy, Dispersive, Plane-Wave (CLDP) Materials

by

R. Joseph Lyons
B.A. English, University Of Colorado (1986)
M.S. Electrical Engineering, Boston University (1991)

Submitted to the Department of Electrical Engineering and Computer Science
in Partial Fulfillment of the Requirements for the Degree of
Doctor of Philosophy in Electrical Engineering and Computer Science

at the

Massachusetts Institute of Technology
June 1998

Signature of Author .....
Department of Electrical Engineering and Computer Science
May 14, 1998

Certified by .....
Chathan M. Cooke
Principal Research Engineer
Thesis Supervisor

Accepted by .....
Arthur C. Smith
Chairman, Committee on Graduate Students
Department of Electrical Engineering and Computer Science

Luck is a mighty power.

Determining Distributed Source Waveforms in Causal, Lossy, Dispersive, Plane-Wave (CLDP) Materials

by

R. Joseph Lyons
B.A. English, University Of Colorado (1986)
M.S. Electrical Engineering, Boston University (1991)

Submitted to the Department of Electrical Engineering and Computer Science on May 14, 1998 in Partial Fulfillment of the Requirements for the Degree of Doctor of Philosophy in Electrical Engineering and Computer Science

ABSTRACT

This thesis presents and employs novel mathematics for the inversion of linear, first-kind Fredholm integral equations (IEs) which have a time t dependent response signal, a space z dependent source waveform, and a kernel with time dependence (at each z) corresponding to the impulse response of a thickness z slab of causal, lossy, dispersive, homogeneous material through which planar disturbances propagate according to the wave equation. These materials are called CLDP materials; these IEs are called CLDP IEs. These novel mathematics are applicable to the PESAW (*aka* PEA) charge recovery method.

The proposed inversion method recognizes that the (temporal) Fourier transform of a CLDP IE's response signal can be interpreted as the values of the (spatial) Laplace transform of that IE's source waveform along a Laplace plane path determined by the material's propagation wavenumber $\underline{k}(f)$. Executing the Laplace transform inversion integral along this CLDP path yields an inverse CLDP IE which recovers the true source waveform provided that source waveform is real, causal, Fourier-transformable, and also satisfies the proposed $\underline{k}(f)$-dependent 'CLDP criterion'. The forward and inverse CLDP IEs corresponding to a particular CLDP material model $\underline{k}(f)$ therefore comprise a particular integral transform relationship applicable to waveforms satisfying the CLDP criterion for that material. The CLDP transform relationship for a lossless/dispersionless material reduces to the (unilateral) Fourier transform.

Even without noise, the 'inverse CLDP'-recovered waveform gleaned from an abruptly bandlimited CLDP response signal requires regularization – a generalized Gibbs-Dirichlet kernel dubbed 'the Darrell' comes into effect. The measured (time sampled) PESAW signal is necessarily bandlimited; this thesis investigates regularization via lowpass filtering of the measured signal. Both synthetic and experimental examples are investigated. The focus is on MHz-range signals culled from mm-range polymeric PESAW experiments. A method for determining the requisite model $\underline{k}(f)$ from measured PESAW signals is also presented and employed.

Thesis Supervisor: Chathan M. Cooke
Title: Principal Research Engineer

Acknowledgements

• First of all I would like to thank my advisor, Dr. Chathan M. Cooke. You are the model for clear headed, practical scientific research. You asked the questions, questioned the answers, and kept me on the path. Truly, it would not have been possible nor nearly so memorable without you.

• I would also like to thank my mentors: Cooke (again), Hohlfeld, Horenstein, Morgenthaler, and Zahn – for, well, mentoring.

• Thanks also to Marilyn Pierce, Kathy McCue, and Maxine Milstean – for believing in me and encouraging me to go on when going on seemed pointless. And for making the way more passable.

• And of course I would like to thank everyone else who acted like a friend to me during my grad school years. And so I will, starting with my family, roughly in order of appearance: Pop & T; Guille, Vicky, Erik; Moon, The Commandress, Gwynn, Carmen, Carol; Couga', Zane, Teresa, Gracie & li'l Zane; Joe, Jane, Stewart, Ben, Lex; Alfred, Johnnie Mike. And Rose, rose, rose ...

• Also Jessica, Rob & Gail Mills. Sarah Trickett. Kaarina & Jon. Mary Nell, Zachary Knight, and Rebecca Morss. Bart, Jamie, Terry, Eric, Anna, Jim, Jeff. Ollie. James Goodberlet. Siegfried Fleischer. Eric Mauer. John Barr. Bill Bresee. Jay Wasserman & Oribe. Also Hiroki Shigetsugu and Pam Ikegami. Yanqing Du, Alexander Mamishev & Kristina. And Priscilla and Caia & Amy and Ronnie. No way will I forget to thank Judy Rudolph or Wayne Ryan. You know why. I thank Cecelia as well ...

• A big thanks to Sara Jamileh and Heather Heimarck, who were always there through thick and thin.

• Thanks to Melissa Collins, who saved me from going off the brink. More than once.

• Thanks to Darrell "The Darrell" Schlicker, Greg Derderian & Rhonda – for listening to me talk about this thesis *ad nauseam.* Aaron M^{c}Cabe and Mitch Meinhold did this too, *and* read and offered insightful comments upon early versions of the text. To Mr. Schlicker in particular: your comments and observations, and your finite width and asymmetry, were a boon and an inspiration, respectively.

• Thanks to the creators of the Macintosh, and also to the creators of Mathematica, LabVIEW, Igor, and Textures. You made my life easier.

• Last but far from least: consistent, steady support from the Tokyo Electric Power Company is acknowledged with deep gratitude. Especial thanks to Yoji (Naohisa Yoshifuji)!

Contents

Appendices

Chapter 1

Overview

1.1 Requisite Background Material

The reader will find this thesis easier to digest if he first familiarizes himself with the information in this short section and appendices E, F, and G.

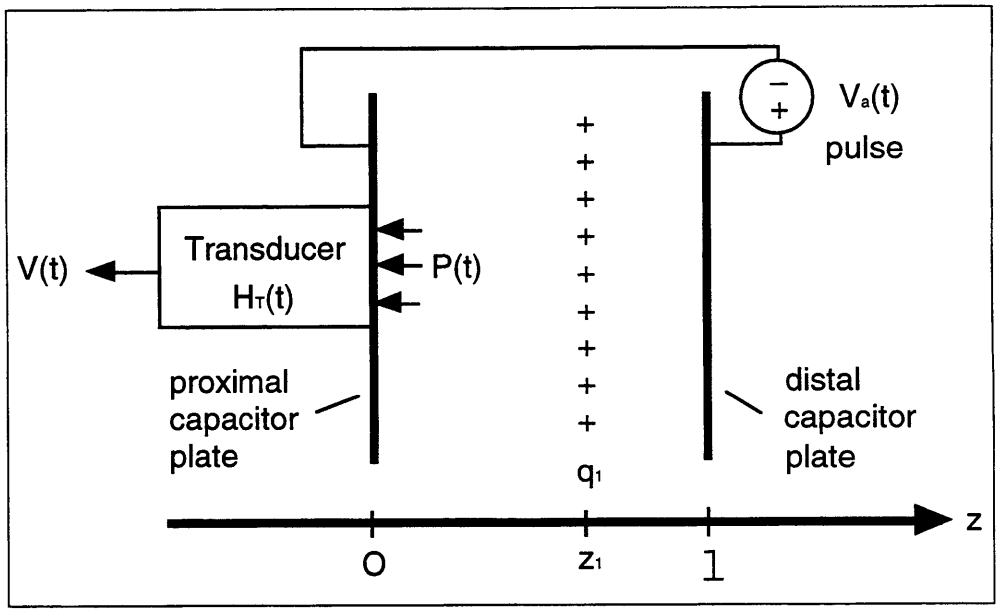

Figure 1.1: The PESAW data collection apparatus: a parallel-plate capacitor with a pressure-to-voltage transducer $H_T(t)$ attached to its proximal plate. Also shown: a column of plusses representing a hypothetical embedded surface charge layer q_1 at position $z = z_1$. Not shown: surface charges generated on the inside surface of each plate in response to both the bulk charge $Q(z) = q_1\delta(z - z_1)$ and the applied voltage $V_a(t)$.

Figure 1.1's charge waveform $Q(z) = q_1\delta(z - z_1)$, where $\delta(z)$ is the Dirac delta function and q_1 is measured in units of nC/cm^2. The position z (distance from the proximal plate) is measured in millimeters, so $Q(z)$ has units nC/(cm^2 mm). The applied, pulsive excitation voltage $V_a(t)$ is the impetus for the measured voltage $V(t)$. The Coulomb force $F(z,t) = Q(z)\ V_a(t)/l$ provides the coupling between them.

Note that there will also be surface charge on the capacitor plates. Some of this plate charge is constant over the acquisition time of the PESAW signal – the image charges corresponding to the embedded charge waveform $Q(z)$. Some of this capacitor plate charge is time varying – the surface charge C' $V_a(t)$ due to the time varying voltage $V_a(t)$ applied to the capacitor C' $= \epsilon/l$, where ϵ is the permittivity of the capacitor's dielectric and l is the distance between the plates. Bear in mind that the desired, experimental $Q(z)$ will generally be a continuous function of position z. Figure 1.1's spatially impulsive $Q(z)$ is introduced for didactic purposes only, to simplify the analysis.

1.2 Thesis Motivation – PESAW & CLDP

The motivation for the research that led to this thesis was the desire to improve the Pulsed Electrically Stimulated Acoustic Wave (PESAW, *aka* PEA; see section 1.18.2) charge recovery method. Figure 1.1 depicts the PESAW data collection apparatus. The applied excitation voltage pulse $V_a(t)$ is the impetus for the measured voltage $V(t)$. The Coulomb-force interaction F = Q E between the embedded charge waveform $Q(z)$ and the $V_a(t)$-generated excitation electric field $E(z,t)$ provides the coupling between $V_a(t)$ and $V(t)$.

In this thesis' one-dimensional planar geometry $E(z,t) = V_a(t)/l$ is independent of z. However, other geometries (*eg*: coaxial cable) yield $E(z,t)$'s that are not independent of z. In the interests of generality, this thesis' results are presented in terms of the general $E(z,t)$ instead of this thesis' particular form $E(z,t) = V_a(t)/l$.

Over the duration of the excitation pulse the excitation electric field generally causes bulk charges to move slightly from their pre-excitation positions, in accordance with Hooke's law F = - K X [83]. The electric field does (spatially distributed) work on the dielectric, which stores the energy in the form of distributed compression.

Just after the excitation pulse has been applied (time $t = 0^+$) the distributed compression starts to uncoil into kinetic energy, launching a compressional wave toward the proximal capacitor plate (and also toward the distal plate, although with opposite polarity. This thesis focusses upon the wave launched toward the proximal plate.).

In the PESAW context, CLDP theory applies to the mapping between this initial, distributed source (pressure) waveform and the response (pressure) signal $\mathcal{P}(t)$ it would cause to pass through $z = 0$ if the dielectric region continued for negative z.

1.3 The Quasi-Static Approximation (QSA)

If the duration of the pulsive $V_a(t)$ is much longer than the time required for an electromagnetic wave to traverse the capacitor then, according to the quasistatic approximation (QSA,[86]), $V_a(t)$ will generate a temporally pulsive, spatially distributed $E(z,t)$ proportional to the product of the signal (function of time alone) $V_a(t)$ and some waveform (function of space alone) $E_z(z)$ that depends only upon the capacitor's geometry (see section 2.2.3).

Under the QSA the force $F(z,t) = Q(z)\,E(z,t) \propto [Q(z)E_z(z)]V_a(t)$ must also have separable space and time dependencies, and the time dependence of $F(z,t)$ must also be given by $V_a(t)$. Therefore the actual signal $V(t)$ measured as a response to a finite duration $V_a(t)$ will be simply related to the hypothetical signal $V_\delta(t)$ that would be recorded if the time dependence of $F(z,t)$ were truly impulsive: $V(t) \propto V_\delta(t) * V_a(t)$, where the $*$ denotes convolution.

So although it is physically impossible (see section 4.6) to have a temporally impulsive $F(z,t)$, under the QSA it is as reasonable as it is simplifying *to think of* $F(z,t)$ as having the separable, temporally impulsive form $F(z,t) = \mathcal{Q}(z)\delta(t)$ where $\delta(t)$ is the Dirac delta function.

The proceeding discussion speaks of applying an impulsive excitation voltage $V_a(t) = \mathcal{V}\delta(t)$ to generate spatially distributed, temporally impulsive fields $E(z,t)$ and $F(z,t)$. According to the above discussion, this approach to analysis of the PESAW experiment makes sense provided the QSA holds. Throughout this thesis, it will be assumed that the QSA holds.

The following chapter's more rigorous analysis introduces a meaningful $\mathcal{Q}(z) = \mathcal{V}Q(z)/l$ which has units of pressure (Pascals, Pa) per velocity (millimeters per microsecond, mm/μs). Therefore, dividing $\mathcal{Q}(z)$ by [Pa μs] yields a normalized $\mathcal{Q}(z)$ with units mm^{-1}. Similarly, dividing $\mathcal{P}(t)$ by [Pa μs] yields a normalized $\mathcal{P}(t)$ with units μs^{-1}. The same notation ($\mathcal{Q}(z)$ and $\mathcal{P}(t)$) is used for both the normalized and the un-normalized (physical) quantities. It is in this manner that the physical, PESAW quantities are generalized into the larger CLDP context.

1.4 PESAW Essentials

With $P(z,t)$ representing a $-z$ directed, Coulomb-force-generated pressure wave travelling through the dielectric after the pulsive $V_a(t) = \mathcal{V}\delta(t)$ has been applied, the PESAW method seeks knowledge of $\mathcal{P}(t) = P(0,t)$, and the frequency dependent attenuation coefficient $\alpha(f)$ and phase velocity $c(f)$ of pressure waves inside the dielectric, as a means to determine first $\mathcal{Q}(z)$ ($\propto P(z,0^+)$), and then (using $E_z(z)$) the desired charge versus position waveform $Q(z)$.

Expanding on the preceeding discussion, this thesis' essential PESAW concepts are –

1. that a $-z$ directed travelling pressure wave $P(z,t)$ will be launched by the interaction (Coulomb force law, F = Q E) of the applied temporally pulsive, spa-

tially distributed PESAW excitation electric field $E(z,t)$ with the assumed-one-dimensional, spatially distributed charge waveform $Q(z)$ inside the dielectric.

2. that the temporally pulsive pressure signal $F(z_o,t) \propto \mathcal{Q}(z_o)V_a(t)$ injected into the dielectric by the charge layer at position z_o will be modified (via $\alpha(f)$ and $c(f)$) as a result of having propagated through the slab of dielectric between that charge layer and the proximal capacitor plate

3. that the modifications imposed upon each layer's injected pressure signal will depend upon that layer's position because the thickness of the intermediate slab depends upon that layer's position

4. that this travelling pressure wave will, after having been modified, eventually impinge upon the proximal capacitor plate

5. that some of this impingent pressure wave will be transmitted through the capacitor plate and into the transducer, where it is ultimately registered as $V(t) = H_T(t) * \mathcal{P}(t)$

6. that the measured $V(t)$ therefore contains 'tangled' information about the desired source charge waveform $Q(z)$

7. that information about $V_a(t)$, $H_T(t)$, $\alpha(f)$, and $c(f)$ is required to 'un-tangle' the information in the measured $V(t)$ and arrive at some estimate to the source pressure waveform $\tilde{\mathcal{Q}}(z) \equiv R(z)$ which can then be mapped, via $E_z(z)$, to an estimate for the desired charge waveform $Q(z)$

As a practical matter, the transducer depicted in figure 1.1 is often comprised of a delay line with a piezoelectric device attached to its left hand side. Some of the pressure waves $P(z,t)$ travelling through the dielectric are transmitted through the proximal plate and into the delay line. These pressure waves eventually arrive at the piezo device and cause it to emit a voltage signal which can be sampled and stored by a digitizing oscilloscope. The delay line is added so that the electrical transients generated by $V_a(t)$ will have mostly decayed away by the time the desired, slower-travelling, pressure-wave signal is recorded by the oscilloscope.

1.5 The PESAW-CLDP Integral Equation

Chapter 2 of this thesis derives a linear, first-kind Fredholm integral equation (IE) model of the forward problem which expresses the response signal $\mathcal{P}(t)$ as the integral over position z of the product of the source waveform $\mathcal{Q}(z)$ with a position-dependent impulse response function $H(z,t)$ that takes into account the propagation properties of the dielectric. That is,

$$\mathcal{P}(t) = \int_0^l \mathcal{Q}(z)\ \mathrm{H}(z,t)\ dz \tag{1.1}$$

Experimental factors such as the sample thickness l and the applied voltage have been normalized out so that $\mathcal{Q}(z)$ has dimensions of inverse length, and $\mathcal{P}(t)$ and $\mathrm{H}(z,t)$ have dimensions of inverse time. This normalization procedure is discussed in more detail in sections 2.2 and 2.3. A one-page overview of the CLDP-PESAW connection may be found in appendix G.

1.6 The Dominant Recovery

Setting aside, for now, a discussion of this normalization procedure and the methods used for reducing the influence of systematic errors and noise upon the measured signal, the dominant method for mapping temporal signals to spatial waveforms simply maps time to space via some constant velocity c_d. This dominant recovery $\mathrm{R}_d(z)$ corresponds to the assumption that acoustic waves inside the dielectric propagate without attenuation or dispersion (see sections 2.5.6 and 2.5.7). The result

$$\mathrm{R}_d(z) = \frac{1}{c_d}\mathcal{P}(\frac{z}{c_d}) = \frac{1}{c_d}\int_{-\infty}^{\infty} \underline{\mathcal{P}}(f)\ \exp(\mathrm{j}\ 2\pi f/c(f))\ df \tag{1.2}$$

yields a perfect recovery provided that pressure waves passing through the material are *only* delayed, not attenuated or dispersed, so that

$$\mathrm{H}(z,t) = \delta(t - \frac{z}{c_d}) \equiv \mathrm{H}_d(z,t)$$

where $\delta(t)$ is the Dirac delta function. Such a material is called a delay-only material.

When it was found that pressure signals measured by the PESAW apparatus could be interpreted to yield frequency f dependent estimates for the attenuation coefficient $\alpha(f)$ and phase velocity $c(f)$ of pressure waves travelling inside the dielectric (see sections 4.11 and 4.12), the following question naturally arose: how can this information be used to improve the time to space mapping algorithm?

1.7 CLDP Materials, Paths, and Transforms

The previous section ended by asking how information about $\alpha(f)$ and $c(f)$ could be used to improve the time to space mapping algorithm. This thesis' answer to that question was found to be, in some sense, larger than the question that prompted it. The result is that, if the dielectric is a CLDP material (Causal, Lossy, Dispersive, Plane-wave; see the abstract, or chapter 2) then there exists an inverse CLDP IE that exactly undoes the forward CLDP IE. The CLDP forward and inverse problem IEs

comprise an integral transform relation which relate spatial waveforms to temporal signals, and vice-versa. These transform relations are unilateral in the sense that all the spatial waveforms and the temporal signals treated must be causal, meaning each must vanish for negative values of its respective argument (z or t).

Bear in mind that, owing to the uniqueness of the Fourier transform, the information in each temporal signal could equally well be represented in the frequency domain. That is, the time domain signal $\mathcal{P}(t)$ possesses the same information as the frequency domain signal given by its Fourier transform $\underline{\mathcal{P}}(f)$. See appendix F for this thesis' definitions of the Fourier and Laplace transforms.

Although PESAW data is collected in time, and although these CLDP transform relations could be expressed as space-time transformations, the mathematical analysis and computer implementation are simpler if the CLDP transform relations are thought of as space-frequency transformations. From the CLDP transform point of view, functions of space alone (waveforms) are considered to be *direct-space* functions whereas functions of frequency alone or time alone (signals) are considered to be *inverse-space* functions.

Because each CLPD material corresponds to a unique integral transform relation, and because there are an infinite number of CLDP materials, this result amounts to the discovery of an infinite number of transform relations. This set of transform relations are called the CLDP transforms.

For example, the familiar Fourier transform relation is that member of the set of CLDP transform relations which corresponds to the delay-only material characterized by $\mathrm{H}_d(z,t)$. That is: letting $l \to \infty$, inserting the delay-only $\mathrm{H}(z,t)$ into the forward IE expression for $\mathcal{P}(t)$, and then Fourier transforming both sides of the IE yields a scaled, unilateral version of the Fourier transform. The dominant recovery $\mathrm{R}_d(z)$ yields a scaled version of the inverse Fourier transform. See sections 2.5.6 and 2.5.7.

This thesis' demonstration of the correspondence between a CLDP material and its associated transform relation utilizes the realization that the Fourier transform $\underline{\mathcal{P}}(f)$ of a CLDP IE's output signal $\mathcal{P}(t)$ can be interpreted as the values of the Laplace transform of the desired source waveform along the Laplace-plane CLDP path

$$\underline{\mathcal{K}}(f) = \alpha(f) + \mathrm{j}\,\underbrace{2\pi f/c(f)}_{\equiv\beta(f)}$$

where the familiar temporal Laplace transform variable $\underline{s}$ has been replaced by the spatial Laplace transform variable $\underline{\mathcal{K}}$ so that

$$\begin{array}{ccccccc} \underline{s} & = & \sigma & + & \mathrm{j} & \omega \\ & & \downarrow & & & \\ \underline{\mathcal{K}} & = & \alpha & + & \mathrm{j} & \beta \end{array}$$

This correspondence between $\underline{\mathcal{P}}(f)$ and the spatial Laplace transform $\underline{\tilde{\mathcal{Q}}}(\underline{\mathcal{K}})$ of $\mathcal{Q}(z)$ is detailed in chapter 7. The result is that, if $\underline{\tilde{\mathcal{Q}}}(\underline{\mathcal{K}})$ is the unilateral Laplace transform of a causal $\mathcal{Q}(z)$, then

$$\underline{\mathcal{P}}(f) = \underline{\tilde{\mathcal{Q}}}(\,\underline{\mathcal{K}}(f)\,)$$

$$= \underline{\tilde{\mathcal{Q}}}(\,\alpha(f) + \mathrm{j}\,\beta(f)\,)$$

$$= \underline{\tilde{\mathcal{Q}}}(\,\alpha(f) + \mathrm{j}\,2\pi f/c(f)\,)$$

For now, suffice to say that if the Fourier transform $\underline{\mathcal{Q}}(b)$ of the source pressure waveform $\mathcal{Q}(z)$ exists, application of the Cauchy-Goursat theorem to the analytic [56, 57] Laplace plane region between the j β axis and the CLDP path results in the realization that the CLDP transforms merely exploit the independence of path of Laplace transforms.

1.8 CLDP Inverse Transforms and the Darrell

The added import of CLDP materials, paths, and transforms follow from the requisite exponential form of the Fourier transform $\underline{H}(z, f)$ of a CLDP material's temporally causal impulse response function $\mathrm{H}(z, t)$. For these materials, the source waveform recovery $\mathrm{R}(f_m, z)$ given by inserting an abruptly bandlimited response signal $\underline{\mathcal{P}}(f_m, f)$ into the inverse IE can be shown to be the convolution of the true source waveform $\mathcal{Q}(z)$ with a waveform called the Darrell $\mathrm{D}(f_m, z)$ which is determined solely by the CLDP material's properties $\alpha(f)$ and $c(f)$ (or simply $\underline{\mathcal{K}}(f)$), and the bandlimiting frequency f_m. This relationship is called "the Darrell property," and it is expressed mathematically as

$$\mathrm{R}(f_m, z) = \mathcal{Q}(z) * \mathrm{D}(f_m, z)$$

where the $*$ denotes spatial convolution and "the Darrell" $\mathrm{D}(f_m, z)$ is given by

$$\mathrm{D}(f_m, z) = \frac{\Im_m\{\,\exp(z\,\underline{\mathcal{K}}(f_m))\}}{\pi z}$$

$$= \exp(z\,\alpha(f_m))\,\frac{\sin(2\pi f_m z/c(f_m))}{\pi z}$$

Note that the Darrell can be rewritten in terms of the two functions λ and Λ of f_m:

$$\mathrm{D}(f_m, z) = \exp(z/\Lambda)\,\frac{\sin(2\pi z/\lambda)}{\pi z}$$

where

$$\lambda = \lambda(f_m) \equiv \frac{c(f_m)}{f_m}$$

$$\Lambda = \Lambda(f_m) \equiv \frac{1}{\alpha(f_m)}$$

The function $\lambda(f_m)$ does not depend on the material's attenuation coefficient $\alpha(f)$; the function $\Lambda(f_m)$ does not depend on the material's phase velocity $c(f)$. And yet λ and Λ are not truly independent; the functions $\alpha(f)$ and $c(f)$ are linked because they must correspond to a causal material.

Raising the bandlimiting frequency to infinity results in the exact inverse transform. Therefore the $f_m \rightarrow \infty$ limit of any CLDP material's Darrell must converge to the Dirac delta function. That is, the Darrell is a delta convergent sequence in f_m provided $\alpha(f)$ and $c(f)$ describe a causal material.

The form of $\mathrm{D}(f_m, z)$ ensures this convergence provided that the quantities $[\alpha(f)]$ and $[f/c(f)]$ exhibit appropriate asymptotic behavior in the limit $f \rightarrow \infty$. (see the *Technical Introduction*'s section titled *The Darrell As Delta Convergent Sequence*). If some test function varies slowly over every region of width $\lambda \ll \Lambda$ then $\mathrm{D}(f_m, z)$ acts like a delta function for that test function, at least for $z \ll \Lambda$.

This result is consistent with the interpretation of the Darrell as a generalized Gibbs-Dirichlet kernel: just as the usual Gibbs-Dirichlet kernel (a sinc function [53, 77]) converges to a Dirac delta function as the bandlimiting frequency approaches infinity, so too does the Darrell. (see the *Technical Introduction*'s section titled *The Darrell As Generalized Gibbs-Dirichlet Kernel*).

But real PESAW data is sampled at a finite time step Δt which corresponds to a finite $f_m = (2\Delta t)^{-1}$ for which, generally, $\alpha(f_m) > 0$. Therefore an analysis of the finite f_m 'lossy Darrell' is of critical import if these CLDP transforms are to be used to perform actual numeric recoveries. A numeric CLDP IE source waveform recovery which uses analytic CLDP transform mathematics is called a Lyons recovery.

1.9 The Behavior of the Darrell

This thesis' analyses assume $0 < \lambda \ll \Lambda < \infty$, in which case the Darrell has

- a central pulse - centered asymmetrically about $z = 0$
  - with full width at first zero crossing (FWZC) $= c(f_m)/f_m = \lambda$
  - with height $\mathrm{H}_D \equiv \lim\{z \rightarrow 0\}[\mathrm{D}(f_m, z)] = 2f_m/c(f_m) = 2/\lambda$
  - with area $\mathrm{A} = \lim\left\{\xi \rightarrow \infty\right\}\left[\int_{-\xi}^{\xi} \mathrm{D}(f_m, z)dz\right]$
    $= 1 = \frac{1}{2}$ FWZC H_D

- with full width at half maximum (FWHM) $\cong \lambda/1.66$

- sidelobes that - oscillate with wavelength λ
  - grow without bound for $z \gg \Lambda$

1.10 The Impact of the Darrell

Applying the Darrell property to a material with N_q spatially impulsive embedded sources (excited by an electric field of short duration)

$$\mathcal{Q}(z) = \sum_{n=1}^{N_q} q_n \, \delta(z - z_n)$$

yields the prediction that the recovery gleaned from noiseless PESAW pressure data sampled and processed 'without numeric error' at a finite time step Δt (and therefore finite $f_m = f_M \equiv (2\Delta t)^{-1}$) will be given by

$$\mathrm{R}(f_m, z) = \sum_{n=1}^{N_q} q_n \, \mathrm{D}(f_m, z - z_n)$$

in the limit as $\Delta t \to 0$ and $(N_t \, \Delta t) \to \infty$, where N_t is the number of time samples.

1.11 The Need for Regularization

Applying this direct version of the Lyons recovery to real PESAW data acquired when $\alpha(f_m)$ does not vanish will result in a source waveform recovery that is desperately in need of regularization.

That is, even if $\mathcal{Q}(z)$ consists of only a single source impulse the recovered waveform will exhibit significant yet unphysical oscillations, especially for positions Λ deep or deeper than that source impulse (see section 8.1.1). The reason is that the $\exp(\alpha(f_m)z)/z$ factor in $\mathrm{D}(f_m, z)$ grows without bound for large z. When multiplied by $\mathrm{D}(f_m, z)$'s oscillatory $\sin(2\pi f_m z/c(f_m))/\pi$ factor, the result is a waveform that oscillates and grows without bound for large z.

Even if $\mathcal{Q}(z)$ is comprised of only two source impulses separated by a width $\mathrm{W} \sim \Lambda$, the recovery of the deeper source may well be completely obfuscated by the oscillations associated with the recovery of the shallower source. Even if $\lambda \leq \mathrm{W} \ll \Lambda$, the λ oscillations associated with the recovery of the shallower source will be detrimental to the recovery of the deeper source. It follows that the recovery of a continuous charge distribution will be troubled as well, especially if its width $\mathrm{W} > \Lambda$.

1.12 Possible Regularization Methods

Because only a material model and a sampling rate are required to compute some material's Darrell, and because the Darrell property involves only convolution of the true source waveform with the Darrell, one possible solution to this problem would seem to be simple deconvolution. Unfortunately, the Darrell has no Fourier transform (because of its $\exp(z\ \alpha(f_m))$ term). Seen another way, deconvolution is impossible to implement because the Darrell, and consequently the entire recovery, are unbounded and impossible to parse.

Further, any parsed approximation to the Darrell would tend to be sinc-like. Because the Fourier transform of a spatial sinc function vanishes for wavenumbers (inverse lengths) greater than some cutoff wavenumber, the usual Fourier domain deconvolution technique of division in the wavenumber domain is ill-posed. This is but a particular instance of the general rule that deconvolution tends to increase noise. The deconvolution problem is discussed in greater detail in the chapter titled *Loss, Dispersion, Deconvolution.*

A second possibility is to use the fact that the usual frequency domain inverse CLDP IE (2.31) can be expressed in the time domain (2.40) as a linear IE with the measured $\mathrm{P}(t)$ as the source, and the fact that causality requires that the plate pressure response to deeper charges arrive later than the response to shallower charges, to legitimize performing separate recoveries for temporally localized 'chunks' of the measured pressure signal, then ensuring that the recovered waveform associated with each chunk does not extend significantly deeper than it ought. A third possibility advocates spatial filtering of the recovered waveform to explicitly suppress the troublesome characteristic wavelength λ.

Many useful linear, spatially independent spatial filters can be described via convolution with a unit-area waveform which has its center of area at the origin. The 'boxcar waveform' with height λ^{-1} in the range $-\lambda/2 \leq z \leq \lambda/2$, and zero height elsewhere, is the member of this class of waveforms which takes most obvious advantage of the fact that the sidelobes go through one complete cycle in one λ range, whereas the central pulse has all positive area in the same range.

The result $\mathrm{D}_\lambda(f_m, z)$ of convolving $\mathrm{D}(f_m, z)$ with this boxcar waveform is

$$\mathrm{D}_\lambda(f_m, z) = \frac{1}{\lambda}\left[\mathrm{I}_D(f_m, z+\lambda/2) - \mathrm{I}_D(f_m, z-\lambda/2) - \left[\mathrm{U}(z+\lambda/2) - \mathrm{U}(z-\lambda/2)\right]\right]$$

where $\mathrm{U}(z)$ is the Heaviside unit step function and the integral $\mathrm{I}_D(f_m, z)$ of $\mathrm{D}(f_m, z)$ is expressed in terms of the exponential integral $\underline{\mathrm{Ei}}(\underline{z})$ [52]:

$$\mathrm{I}_D(f_m, z) \equiv \int_{-\infty}^{z} \mathrm{D}(f_m, z')\, dz'$$
$$= \frac{1}{2\pi \mathrm{j}} \left[\underline{\mathrm{Ei}}(z[\alpha(f_m) + \mathrm{j}\, 2\pi f_m / c(f_m)]) - \underline{\mathrm{Ei}}(z[\alpha(f_m) - \mathrm{j}\, 2\pi f_m / c(f_m)]) \right]$$

The result $\mathrm{I}_D(f_m, z)$ follows directly from the definition of $\underline{\mathrm{Ei}}(\underline{\mathcal{Z}})$ once the sin term in $\mathrm{D}(f_m, z)$ is expanded in terms of complex exponentials via Euler's identity. The unit step component of $\mathrm{D}_\lambda(f_m, z)$ arises from the fact that the exponential integral $\underline{\mathrm{Ei}}(\underline{\mathcal{Z}})$ is not analytic at $\underline{\mathcal{Z}} = 0$. $\underline{\mathrm{Ei}}(\underline{\mathcal{Z}})$ has a branch cut along the negative real axis of $\underline{\mathcal{Z}}$.

The impact of the branch cut is that when computing the definite integral of $\mathrm{D}(f_m, z)$, the result gleaned via $\mathrm{I}_D(f_m, z)$ and the fundamental theorem of calculus is unity greater than the result gleaned via numerical integration of $\mathrm{D}(f_m, z)$ if the integration range includes $z = 0$. Plots of $\mathrm{D}_\lambda(f_m, z)$ show that it exhibits a significant reduction in sidelobe envelope when compared with the unregularized $\mathrm{D}(f_m, z)$. Like $\mathrm{D}(f_m, z)$, $\mathrm{D}_\lambda(f_m, z)$ oscillates and grows without bound for $z \gg \Lambda$.

In addition to standard (linear) wavenumber domain spatial filtering, the nonlinear median filter may also be useful. The median filter operates upon samples in the space domain by replacing the sample at position z_o with the median value of all the samples within some neighborhood $z_o \pm L_n/2$. The result is a filter that tends to remove large (greater than $1/L_n$) wavenumber variations from the waveform, while preserving edges. The median filter preserves slope. If $L_n \cong \lambda$, the procedure of integrating the direct recovery, applying the median filter, then differentiating tends to remove the λ oscillations while preserving the central pulse.

It is also possible to decrease the sidelobe envelope of the recovery $\mathrm{R}(f_m, z)$ by averaging the results of a number of recoveries utilizing various values of f_m (denoted f'_m to distinguish them from the constant f_m) where all the f'_m's are less than or equal to f_m. The basic idea is that the central pulses will tend to add whereas (hopefully) the oscillating sidelobes will tend to cancel. Consider averaging the result of two Darrells: one with $f'_m = f_m$ and one with $f'_m = f_m/2$. The result

$$\mathrm{D}_2(f_m, z) \equiv \frac{\mathrm{D}(f_m, z) + \mathrm{D}(f_m/2, z)}{2} = \cos(2\pi \frac{f_m}{4} z / c(f_m))\ \mathrm{D}(\frac{3}{4}\ f_m, z)$$

corresponds to an effective Darrell whose sidelobes decrease (via the slowly varying cos term) in the vicinity of its central pulse, which is about 33% wider than $\mathrm{D}(f_m, z)$'s central pulse. However, because the cos term is a continuous periodic waveform with range (-1,1), the sidelobes still oscillate everywhere and grow without bound for $z \gg \Lambda$.

The characteristics of the recovery given by averaging all the f'_m's between $f_m/2$ and f_m is determined by the effective Darrell

$$\mathrm{D}_\infty(f_m, z) \equiv \frac{1}{f_m/2} \int_{f_m/2}^{f_m} \mathrm{D}(f'_m, z)\, df'_m = \frac{c(f_m)}{f_m/2}\ \frac{\sin(\pi \frac{f_m}{2} z / c(f_m))}{\pi z}\ \mathrm{D}(\frac{3}{4}\ f_m, z)$$

which has a central pulse width that is still only about 33% wider than $D(f_m, z)$'s central pulse, but which has a sidelobe envelope that is smaller than $D(f_m, z)$'s by a factor of at least order z over all space. Like $D_2(f_m, z)$, $D_\infty(f_m, z)$'s sidelobes oscillate everywhere and grow without bound for $z \gg \Lambda$. But perhaps the slower growth rate of the sidelobe envelope could be used in conjunction with one of the other possible regularization methods to yield an acceptable overall recovery.

1.13 Spatially Dependent BLG (SDB) Filtering

Although the regularization possibilities mentioned in the previous section have shown some promise, they have not been found to be as satisfying and straightforward to implement as operating upon a $\underline{\mathcal{P}}(f)$ which has been lowpass filtered via $B(f_c, f)$, the filter known as Blackman's Lucky Guess (BLG; see appendix B):

$$\underline{\mathcal{P}}(f) \quad \rightarrow \quad \tilde{\underline{\mathcal{P}}}(f_c, f) \equiv \underline{\mathcal{P}}(f)\, B(f_c, f)$$

This technique has been found to regularize the noiseless Lyons recovery *and* it removes high frequencies which often have, at least in the practical PESAW context, a low signal to noise ratio. Its result is called the SIB recovery (Spatially Independent Blackman) and should not be confused with the spatially filtered recovery which operates upon the recovered waveform.

This SIB recovery, although satisfactory in terms of regularization alone, has demonstrated the less-than-optimum property that the full width at half maximum of recovered source impulses are roughly independent of source position – intuition suggests that the FWHM of shallow-source recoveries ought to be smaller than that of deep-source recoveries. This intuition follows from the realization that pressure waves generated by deep sources have to travel through more attenuative, dispersive material than do the pressure waves generated by shallow sources.

Theoretically, in the absence of noise, these deeper sources should be equally as 'recoverable' as shallow sources. But practically, the finite noise level in the measured signal renders the more-attenuated signals generated by arbitrarily deep sources indistinguishable from the measurement noise.

It is possible to implement a modification of the SIB recovery in which the cutoff frequency f_c of the BLG filter $B(f_c, f)$ used on $\underline{\mathcal{P}}(f)$ is a function of z:

$$\underline{\mathcal{P}}(f) \quad \rightarrow \quad \tilde{\underline{\mathcal{P}}}(z, f) \equiv \underline{\mathcal{P}}(f)\, B(f_c(z), f) \tag{1.3}$$

This technique is called spatially dependent BLG (SDB) filtering. The quantity $f_c(z)$ is called the SDB function; see sections 4.14.2 and 4.15.4, or appendix B.

It has been found that the SDB filtered recovery can be made to yield a regularized recovery for which the FWHM of shallow-source recoveries is smaller than that of deep-source recoveries.

There is no inherent tie between the concept of spatially dependent filtering and the BLG filter. Future research may even show that the BLG filter should not be used for Lyons recoveries because its extreme rejection of frequencies above f_c may not be necessary, and may tend to decrease resolution.

Nevertheless, SDB filtering is the only regularization method investigated in this thesis. The SDB filtering method was chosen as the workhorse regularization scheme in this thesis because the BLG filter has an historic association with the PESAW method, it is simple to implement, and it gives reasonable results.

1.14 The Lyons Recovery

A Lyons recovery is defined as the process, or the result, of numerically implementing the analytic CLDP inverse transform relation (2.31) defined by some material's propagation coefficient $\underline{\mathcal{K}}(f)$. There are, therefore, many possible implementations of the Lyons recovery. But unless noted otherwise, in this thesis 'the Lyons recovery' refers to the SDB filtered Lyons recovery given by (4.60).

As defined above, the Lyons recovery does not pertain particularly to the PESAW recovery of the charge waveform $\mathrm{Q}(z)$ from the measured waveform $\mathrm{V}(t)$. Rather, the Lyons recovery pertains to the CLDP inverse source problem of mapping the generic frequency-domain response signal $\underline{\mathcal{P}}(f)$ to the generic space-domain source waveform $\mathcal{Q}(z)$. But as section 2.2 shows, the Lyons recovery is the crux of the PESAW recovery advocated by this thesis.

With this definition, the Lyons recovery is applicable to problems beyond the PESAW context. It is possible to validate the best-case efficacy of the Lyons recovery by synthetically generating a (to within numerical errors) noiseless $\mathcal{P}(t)$ via the standard model (see section 6.2.2) for the propagation coefficient $\underline{\mathcal{K}}_p(f)$ of polyethylene, and then performing a Lyons recovery upon the fast Fourier transform $\underline{\mathcal{P}}(f)$ of the synthetic, sampled $\mathcal{P}(t)$. The following section compares the $\tilde{\mathcal{Q}}(z)$'s gleaned from this best case $\mathcal{P}(t)$ by the dominant recovery, and by the SDB filtered Lyons recovery.

As defined in (1.2), the dominant recovery $\mathrm{R}_d(z)$ does not use $\underline{\mathcal{K}}_p(f)$ whereas the Lyons recovery does. Similarly, $\mathrm{R}_d(z)$ does not use filtering whereas the Lyons recovery does. The approximately noiseless property of the data therefore gives the dominant recovery an unrealistic advantage for $z \cong 0$ where the effects of attenuation and dispersion have not had much distance over which to accumulate. Over larger distances, however, the Lyons recovery's use of $\underline{\mathcal{K}}_p(f)$ will start to overcome the loss of information (in exchange for regularization) imposed by its use of SBD filtering.

1.15 Lyons Recovery *vs* Dominant Recovery

The following figure offers a comparison of the best-case SD filtered Lyons recovery $\mathrm{R}(z)$ to the best-case dominant recovery $\mathrm{R}_d(z)$ for a source waveform comprised of ten impulses placed at half-millimeter increments, from $z = 0.25$ mm to $z = 4.75$

mm, inside a slab of what this thesis has dubbed 'standard polyethylene' (see section 6.2.2). The so-called standard model of polyethylene ultimately amounts to a specific $\{\alpha(f), c(f)\}$ pair. The specific $\{\alpha(f), c(f)\}$ pair selected for the model called 'standard polyethylene' was chosen because its values are typical for polyethylene.

This standard model of polyethylene (PE) will be widely used throughout this thesis. It will be introduced in the chapter titled *Causality And Materials.* This placement of sources is dubbed the standard impulsive source waveform. In this section, each of the sources is a spatial impulse, or Dirac delta function $\delta(z)$. The Dirac delta function is the limit of a (normalized) Gaussian as the Gaussian's width vanishes. Later in this thesis, this standard source waveform will employ Gaussians of nonvanishing width.

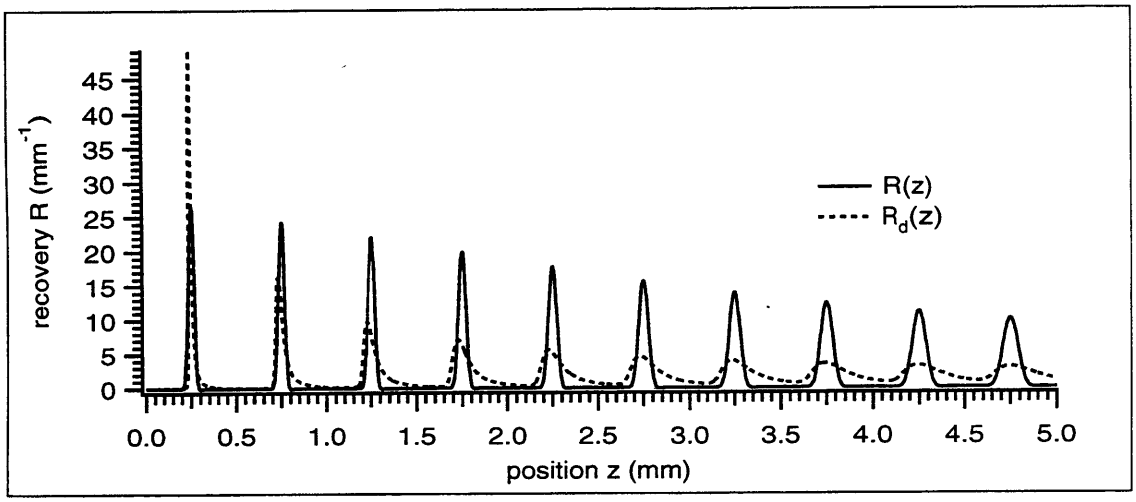

Figure 1.2: Comparison of the noiseless Lyons recovery $\mathrm{R}(z)$ to the noiseless dominant recovery $\mathrm{R}_d(z)$ for the standard source waveform embedded within standard polyethylene.

Note that the SDB filtered Lyons recovery has been denoted $\mathrm{R}(z)$, not $\mathrm{R}(f_m, z)$. The f_m in $\mathrm{R}(f_m, z)$ has been dropped for two reasons. First, because Blackman filtering $\underline{\mathcal{P}}(f)$ does not produce an abruptly bandlimited (*ie* ideal 'square-window' lowpass) signal; rather, Blackman filtering $\underline{\mathcal{P}}(f)$ effects a gradual decrease in $\underline{\mathcal{P}}(f)$'s frequency content, from total inclusion at the zero frequency to total rejection at the cutoff frequency f_c and above. Second, the value of f_c used in the spatial filtering algorithm depends upon the position z; there is no one special frequency associated with SDB filtering so the f_m in $\mathrm{R}(f_m, z)$ has been dropped. These recoveries are called 'best case' because the same standard model of polyethylene was used in both the forward and inverse CLDP IEs, and no noise was introduced into $\underline{\mathcal{P}}(f)$.

Henceforth $\mathrm{R}(f_m, z)$ will denote the Lyons recovery obtained from a $\underline{\mathcal{P}}(f)$ that has been abruptly bandlimited at f_m (f_m a constant independent of position), and $\mathrm{R}(z)$ will denote an SDB filtered Lyons recovery. Unless otherwise noted, the $f_c(z)$ used to implement this thesis' version of the Lyons recovery is 'the standard $f_c(z)$' depicted in

appendix B. Note that SDB filtering reduces to spatially *in*dependent filtering if $f_c(z)$ is a constant f_c', and that SDB filtering reduces to no filtering if $f_c' = \infty$.

The material model and source placement used here is consistent with this thesis' goal of establishing the efficacy of the Lyons recovery to PESAW charge recoveries of up-to-five mm samples of PE. Explicit presentation of $P(t)$ has been omitted here because the $R_d(z)$ presented in Figure 1.2 is simply a version of $P(t)$ which has been scaled by the velocity $c_d = 2.035$ mm/μs. A plot of this $P(t)$ can be found on page 45 in Figure 2.2.

1.15.1 skewness

Returning to Figure 1.2, note that the Lyons recovery is clearly better than the dominant recovery in terms of both the skewness of the recovered source impulses and in terms of their width. As for skewness, the recovered sources determined by the Lyons recovery are all nearly symmetric and have, therefore, nearly vanishing skewness whereas the recovered sources determined by the dominant recovery all have significant positive skewness (they all have long 'tails' extending to the right).

1.15.2 width

As for the width of the recovered source impulses, note that the $z \geqslant 2.5$ mm source impulses recovered by the dominant method fail to have a region between them in which the recovery vanishes, whereas all the source impulses recovered by the Lyons method do have a nearly-vanishing recovery region separating them. More quantitatively, figure 1.3 depicts a comparison of the position dependent FWHM of the source impulses recovered via the Lyons method ($\text{FWHM}_l(z)$) to the FWHM of the sources recovered via the dominant method ($\text{FWHM}_d(z)$).

Note that $\text{FWHM}_l(z) < \text{FWHM}_d(z)$ for all $z \geq .75$ mm. The small width of the $z < .75$ mm source impulses recovered by the dominant method is due to the fact that no filtering was utilized to produce $R_d(z)$.

The small width of these recovered source impulses is an artifact of the known noiselessness of the data – when operating upon real (noisy) data the dominant recovery would presumably employ filtering, which would surely and significantly increase especially the small-z $\text{FWHM}_d(z)$. It is encouraging that the Lyons recovery, which employs a significant degree of filtering, fares as well as it does when compared to the unfiltered $R_d(z)$.

1.15.3 position

Closer inspection of the data depicted in figure 1.2 shows that the Lyons recovery betters the dominant recovery in terms of positional accuracy as well. The value $c_d = 2.035$ mm/μs was chosen to ensure that the dominant recovery's placement of the peak of the 4.75 mm source was exact. Given this constraint, the root-mean-square

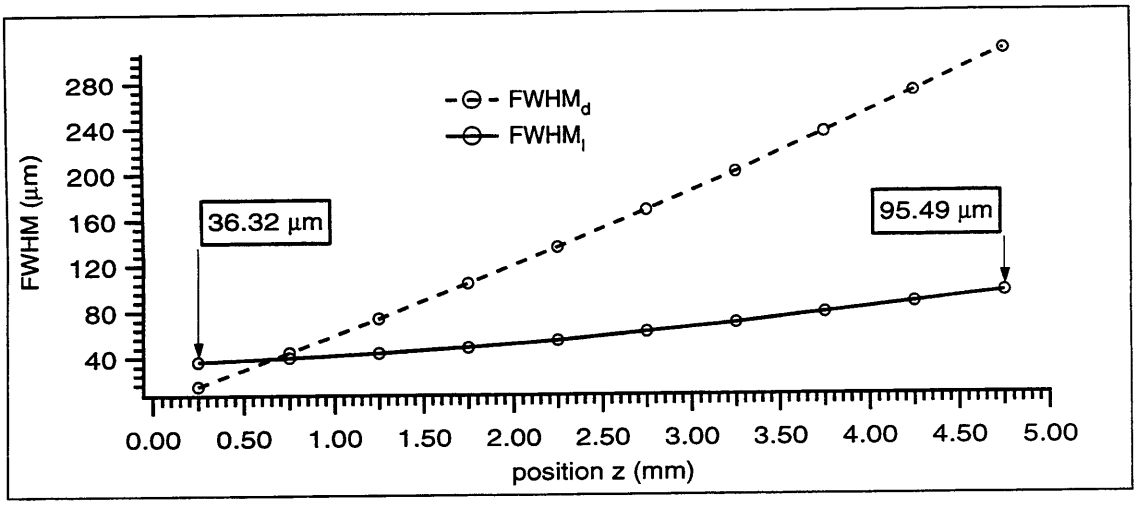

Figure 1.3: Comparison of the position dependent FWHM of the sources recovered via the Lyons method to the FWHM of the sources recovered via the dominant method for the standard impulsive source waveform embedded within a material described by the standard model of PE

error (RMS) in the dominant recovery's placement of the ten source impulses is 16 μm, whereas the Lyons recovery's RMS placement error was just 1 μm.

1.15.4 area

The Lyons recovery bettered the dominant recovery in terms of the raw area of the recovered sources as well. Integrating between -0.25 and 5.25 mm, each raw recovered area fell short of the expected area of ten; the Lyons recovery yielded an area of 9.91 whereas the dominant recovery yielded an area of 9.74.

But note that actual PESAW recoveries are scaled via *a priori* knowledge of the quantity of surface charge on the capacitor plates (see the chapter titled *The PESAW Recovery*). It is, therefore, much more important to the PESAW recovery that the area of a recovered source impulse be independent of position than that the unscaled total area be accurate.

The result of calculating the RMS deviation in the area of each source impulse, as determined by integrating $\pm$ 0.25 mm around the known position of each source, results in the realization that the dominant recovery has an RMS deviation of 1.57 % about its mean whereas the Lyons recovery has an RMS deviation of only 0.15 % about its mean.

In short, for this noiseless numerical experiment, the Lyons recovery is more successful than the dominant recovery in terms of the skewness, width, placement, and area of the recovered source impulses. The Lyons recovery of area betters that of the dominant recovery both in terms of raw recovered area, and in terms of the constancy of the area of each recovered source impulse.

Please remember that the data used in this numerical experiment was as noiseless as a computer can generate, and that the Lyons recovery used filtering (which would reduce high-frequency noise if it existed) whereas the dominant recovery did not. The only category in which the dominant recovery bettered the Lyons recovery was in the recovered width of sources placed very close to the receiving transducer. These gains would not be so great if noise were included in the data and/or if filtering were imposed on the data. The influence of noise will be the subject of the chapters titled *The Lyons Recovery And Noise* and *Experimental Recovery.*

This discussion of the superiority of the Lyons recovery as compared to the dominant recovery is buttressed in the following chapter, where the self consistency of the dominant recovery's placement of recovered sources is questioned. Note that the $R_d(z)$ used in this chapter is denoted $R_d^l(z)$ in the following chapter.

1.16 Preview of Experimental Results

Section 9.2 (*The Double-Sided E-Beam Experiment*) focusses on an $l = 2.121$ mm slab of polymethylmethacrylate which was bombarded with a dose of 0.35 MeV electrons on June 3 1997. The dosage was designed to deliver 200 nC/cm^2 of charge. This irradiated sample was then set aside until June 28'th. Between June 28'th and June 30'th this sample was subjected to the PESAW experimental procedure. Many PESAW signals were measured; some with the DC voltage bias V_o = -2 kV, some with V_o = +2 kV, and some with $V_o = 0$. The temperature was held constant at 22^{o}C throughout. See section 4.3 for an explanation of the meaning of V_o; the current section is only a preview.

Four of the signals were collected with the sample in the EP configuration (*ie*: the sample was mounted with the proximal plate attached to the side of the sample through which the bombarding electrons entered) and four of the signals were collected with the sample in the ED configuration (*ie*: the sample was mounted so that the irradiating electrons entered through the distal plate).

Figure 1.4 (which is identical to page 196's figure 9.22) depicts the bulk region (*ie*: all but the plate region) of the eight charge recoveries corresponding to the eight distinct measured PESAW signals. This plot was included here because whereas these eight recoveries differ in terms of mounting orientation (EP and ED, which 'look into' the sample from opposite sides) and applied DC voltage V_o, these eight recoveries agree on many of the details of the embedded charge distribution.

That is, all eight recoveries agree that bombarding a sample of PMMA with $\sim$ 0.35 MeV electrons, and then allowing the embedded electrons to 'settle' for $\sim$ 25 days, results in a charge distribution dominated by a negative pulse which has a peak value occuring at $z = 1.23$ mm (*ie*: 1.23 mm from the plane of entry of the bombarding electrons) and which has a width (FWHM) $\cong$ 0.26 mm.

The eight recoveries also agree on some of the finer details of the structure of the charge waveform embedded within this irradiated sample, *eg*: there is a region of positive charge in the region between, say, 1.55 and 1.8 mm from the point of entry.

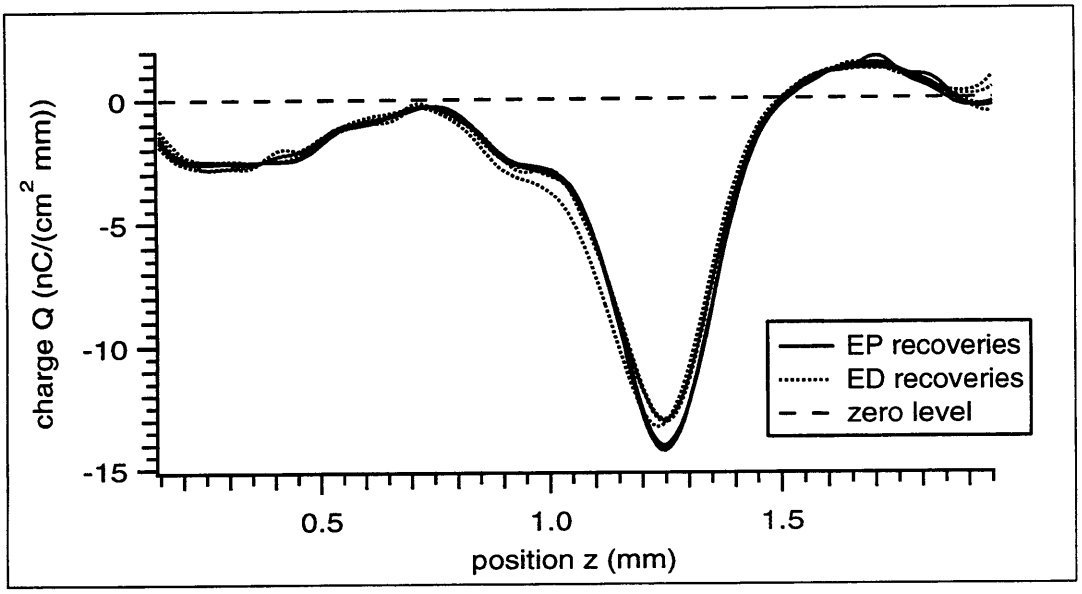

Figure 1.4: Recovered bulk charge distributions corresponding to eight distinct PESAW bulk signals. Solid lines correspond to the four signals acquired with the sample mounted in the EP configuration; dotted lines correspond to the four signals acquired with the sample mounted in the ED configuration.

Further, all eight recoveries roughly agree on the scale of the embedded charge waveform – the peak value of the charge waveform is $\cong$ -13.6 $\pm$ 0.6 nC/(cm^2 mm). The fact that these PESAW recoveries seem to be largely independent of mounting orientation (and V_o) confirms the efficacy of applying the Lyons recovery to the required mapping of measured PESAW signals to charge waveforms.

1.17 Generality of the Lyons Recovery

The mathematics behind the Lyons recovery should be applicable to a class of problems much larger than the polymeric PESAW inverse-source problem. At the very least, the mathematics invoked will apply not only to polymer dielectrics, but to any homogeneous dielectric in which the propagation of plane pressure waves is governed by the wave equation. Further, these mathematics should also prove useful for improving the localization of defects in the field of acoustic emission, and for locating submarines/airplanes emitting active sonar/radar. Insofar as the earth can be modelled as homogeneous with respect to shockwave propagation, these mathematics could prove useful for locating, and quantifying the strength of, earthquakes. In the field of power transmission, these mathematics should prove useful in determining the strength and location of disturbances from the transients they propagate.

In short, any field which seeks to determine the location and strength of a (possibly distributed but, if so, necessarily simultaneous) source which can only be sensed after

propagating through a causal, lossy, dispersive, plane-wave (CLDP) medium may well benefit from these inverse-source mathematics.

The downside of the Lyons recovery as applied to these other fields is that both the time of application, and the shape, of the pulsive, simultaneous stimulus signal must be known so that their influences can be deconvolved out of the measured response signal. Error in the stimulus time leads predominantly to error in the position of recovered features; error in the stimulus shape leads predominantly to error in the shape of recovered features. In the PESAW context, the stimulus time and shape are well enough known that the Lyons recovery gives recoveries that are at least as positionally accurate and well resolved as the dominant method's recoveries.

1.18 Charge Recoveries: Motivation and Review

Electrical discharges in solid dielectrics are often abetted by spacecharge formation [1, 2, 3, 4, 5, 6, 7, 8]. The problem is serious: "picture irradiating [a dielectric device on a satellite] with energetic electrons [from the solar wind] that can penetrate the dielectric and actually remain there. They deposit a charge there. So you can have this charge buildup, and if it gets high enough, the center conductor could arc to the shield and burn a hole right through the shield material. This phenomenon of deep dielectric charging is thought to be responsible for satellite upsets [98]."

Spacecharge formation was also suspected as a possible contributing factor to polymer-dielectric power cable breakdown, which can be disruptive and expensive to fix. Although the charging mechanism itself is less clear, it's existence is manifest. The increase in breakdown voltage with polymer-dielectric cable thickness was found to be less than 'charge-free' electrostatic theory predicted. It was realized that charges inside the cable modify the otherwise divergence-free electric field there, and can possibly increase it so that it has a value greater than the dielectric's breakdown limit somewhere within the dielectric. It seemed prudent to develop a charge monitoring system to investigate the relationship between spacecharge buildup and electrical breakdown.

Researchers have developed a suite of methods for the nondestructive spacecharge profiling of dielectrics. There are five main methods currently in vogue: the Kerr Electro-Optic (KEO) method [2, 9], the Thermally Stimulated Current (TSC) method [10, 11, 12], the Thermal Pulse (TP) method [3, 12, 13, 14, 15], the Pressure Wave Pulse (PWP) method [3, 4, 5, 12, 13], and the Pulsed Electro-Acoustic (PEA) method, referred to here as the Pulsed Electrically Stimulated Acoustic Wave (PESAW) method [1, 3, 6, 7, 8, 16, 17, 18, 19, 20]. These methods allow the monitoring of spacecharge buildup over time, so that the link between charge formation, migration, and breakdown may be investigated.

1.18.1 Non-PESAW Methods

The KEO charge recovery method utilizes the fact that Kerr media exhibit birefringence (polarization dependent phase velocity) in the presence of an applied electric field. The

KEO method uses a three-step procedure to determine the charge distribution which generated the applied electric field – (1) transmit a LASER beam along various paths through the dielectric under test and measure the phase difference between the beam's two polarizations; (2) based on the measured phase shift *vs* path data, reconstruct what the electric field distribution inside the dielectric must be; (3) use Gauss' law to relate the reconstructed electric field to the desired charge distribution. The KEO method is applicable to optically transparent Kerr media.

The TSC method is applicable to dielectrics with a temperature dependent conductivity. The dielectric is sandwiched between two capacitor plates, and the short circuit current is measured as the temperature is slowly varied. The impetus of the measured current is the movement of charges within the dielectric as they arrange themselves in accordance with the internal field and the time-varying conductivity. The image charges on the capacitor plates must change if the *moment* of the internal charge distribution changes. Information about the charge distribution within the dielectric is, therefore, embedded in the resultant current versus time and temperature versus time signals.

The TP and PWP methods are similar to the TSC method in that the charge versus position information is obtained by measuring the short-circuit current of a capacitor containing the dielectric under test. But in the TP and PWP methods the impetus for charges to move from one plate to another is the application of a pulse (thermal for TP; pressure for PWP) at one of the capacitor plates.

As the effects of these applied pulses move through the dielectric (by diffusion for TP; by wave-propagation for PWP) they distort various time-dependent regions. That is, they redistribute the charges in the dielectric (by thermal expansion for TP; by the expansion and compression which is the *sine qua non* of a propagating pressure pulse for PWP), thereby modulating the image charges which must appear on the capacitor plates and generating the measured signal. If the PWP method's pressure pulse is generated piezoelectrically, this method is sometimes called the PIPP method (Piezo-Induced Pressure Pulse); if it is generated by a laser pulse, this method is sometimes called the LIPP method (Laser-Induced Pressure Pulse).

1.18.2 The PESAW Method

The Pulsed Electro-Acoustic (PEA) method is referred to here as the Pulsed Electrically Stimulated Acoustic Wave (PESAW) method to avoid the impression that this method relies on some direct (ie: field to field) electro-acoustic process. As the following discussion will show, this method relies instead upon a time varying electric field launching a travelling pressure wave inside the dielectric material by exerting a time varying force upon the charges embedded within the dielectric.

Although the time varying electric field is the impetus for the resultant travelling pressure wave, the interaction between the electric field and the pressure field is not direct. The PESAW method requires charge as an intermediary between the electric and acoustic fields, and therefore should not strictly be termed electro-acoustic.

The PESAW method is similar to the TP and PWP methods in that some kind of pulse is applied to a capacitor containing the dielectric under test. In the PESAW method the applied pulse is the voltage signal imposed between the two capacitor plates. The temporally pulsive electric field distribution generated inside the dielectric by the pulsed voltage signal interacts with whatever charge distribution may exist there, generating a temporally pulsive force field distribution according to the Coulomb force law $F = Q\ E$.

Because the impetus of the force field is the electric field, and because the electric field is driven by a single voltage source, if the QSA holds then the space and time dependence of the force field $F(z,t)$ must be separable into the product of a waveform and a signal: $F(z,t) \propto Q(z)E_z(z)V_a(t)$ (see section 1).

The stimulus-independent electric field distribution $E_z(z)$ is *a priori* determinable from the experimental configuration. Further, $V_a(t)$ is the (known) applied signal, so knowledge of $F(z,t)$ amounts to knowledge of $Q(z)$; dividing $F(z,t)$ by the product of $E_z(z)$ and $V_a(t)$ yields a quantity proportional to the desired charge waveform $Q(z)$. The problem reduces to that of determining $F(z,t)$. These procedures are actually implemented in the frequency domain; see *The PESAW Recovery* for details.

The current state of PESAW inverse-source theory requires that the internal charge distribution depend solely upon the distance from the capacitor plates. For a planar sample the surfaces of constant distance are planes; for a coaxial sample the surfaces of constant distance are cylinders. In either case the three dimensional charge distribution can be described by a one-dimensional function called the charge waveform $Q(z)$. The spatial dependence of the force field is called the source (pressure) waveform $\mathcal{Q}(z)$.

Because the strength of the pressure waveform is time-varying it launches a travelling pressure wave which propagates through the dielectric, eventually reaching one of the capacitor plates where its influence can be detected as a plate pressure signal by a pressure to voltage transducer. PESAW-CLDP theory currently requires that the spatio-temporal evolution of the pressure wave be governed by the familiar one dimensional wave equation.

Because the temporal forcing function is assumed impulsive the wave equation almost never has a forcing term. The wave equation has a forcing term only for $t \cong 0$, when the excitation voltage signal is applied. Therefore the wave equation is almost always homogeneous, and its short-lived forcing term can be dealt with as a simple change of initial conditions: there is no pressure waveform for negative times, and the pressure wave at any positive time is given by propagating the initial ($t = 0^+$) force distribution forward according to the homogeneous wave equation.

Speaking roughly, charges *nearer* to the transducer launch acoustic waves which arrive at the transducer *earlier* than charges which are farther from the transducer. If the dielectric did not attenuate or disperse acoustic waves propagating through it, and if the pressure to voltage transducer's impulse response function were itself impulsive, then the measured plate pressure versus time signal could, to within a scale factor, be mapped directly to a charge versus position waveform via the frequency-independent velocity of acoustic waves in that dielectric. The problem is that dielectrics

do generally attenuate and disperse acoustic waves. This direct time-to-space mapping algorithm therefore yields only an approximate solution, formally valid only when loss and dispersion are negligible.

1.19 Thesis Outline

This thesis has two related goals: to introduce and establish the novel CLDP mathematics in their own right, and also to explain how to use the proposed CLDP mathematics to perform charge recoveries from measured PESAW data gleaned from ~ 5 mm polymer samples. The procedure, or the result, of numerically implementing the inverse CLDP IE is dubbed the Lyons recovery. The current chapter **chapter 1** *Overview* merely outlines the central topics, goals, and concerns that will be addressed elsewhere in this thesis.

The following chapter **chapter 2** *Technical Introduction* is called an introduction not because its level of discourse is introductory but because, except for one major exception, it simply states and comments upon this thesis' central results but does not actually prove or implement them.

Chapter 2's 'one major exception' is the derivation of the PESAW forward problem IE which shows it to be a CLDP IE. The fact that the PESAW IE is a CLDP IE is this thesis' unifying concept. Without this tie, the novel CLDP transforms would have no particular connection to the PESAW problem.

Chapter 2 therefore begins with the derivation of the PESAW-CLDP IE. It then places the pressure signal to source waveform mapping within the PESAW context. That is, chapter 2 offers an overview of the relation between the actual measured PESAW voltage signal, the CLDP inversion mathematics, and the final mapping to the desired charge waveform. This relationship is examined in more detail in chapter 4. One important point made in chapter 2 is that the actual measured PESAW signal is measured via a finite bandwidth pressure to voltage transducer, and therefore the measured signal must be deconvolved with respect to the transducer's impulse response to arrive at an estimate to the impingent pressure signal.

Chapter 2 also points out the close relationship between delay-only materials (which exhibit no loss or dispersion), the dominant recovery, and the (unilateral) Fourier transform. It also introduces the Darrell property of the inverse CLDP IE, and establishes the Darrell as a generalized Gibbs-Dirichlet kernel (*ie*: it establishes the Darrell as the product of a sinc function and an exponential).

Chapter 3 *Loss, Dispersion, Deconvolution* derives the transfer function and impulse response function of a CLDP material from the assumption that waves propagate according to the one dimensional wave equation. Chapter 3 also discusses the problem of frequency domain deconvolution within this context. That is, chapter 3 addresses the problem of how to determine the signal that was input on one side of a slab of CLDP material given the signal that was output on the other side of the slab and the propagation properties of the slab.

A convolution integral is a special type of linear, first-kind Fredholm IE – one where the value of the kernel $H(z,t)$ depends only on the difference $(z-t/C)$ where C is some velocity. Therefore the generic CLDP IE is not a convolution (the case of a delay-only material is the sole exception; see section 1.6) so the deconvolution problem is not the same as the problem of solving a CLDP IE.

And yet the deconvolution problem has a place in this thesis. One reason is that deconvolution is required to map the measured voltage signal $V(t)$ to an estimated pressure signal $\mathcal{P}(t)$ which may then be submitted to the inverse CLDP IE. Another reason is that value of the recovery at any one position z_o can be expressed in terms of deconvolution with respect to $H(z_o,t)$.

The objective of **Chapter 4** *The PESAW Recovery* is to describe how specifically to perform a PESAW recovery, which includes both the recovery of the required approximate material model $\{\tilde{\alpha}(f),\tilde{c}(f)\}$ and the application of this model to the ultimate goal of recovering the approximate charge waveform $\tilde{Q}(z)$.

Chapter 5 *Inverting Linear, First-Kind Fredholm IEs* gives an overview of the known methods for inverting linear, first-kind Fredholm IEs. The CLDP IEs are a subclass of this set of IEs.

Chapter 6 *Causality And Materials* discusses the frequency domain implications of the requirement that the material impulse function $H(z,t)$ must yield a causal function of time for any positive z. Chapter 6 first introduces the Kramers-Kronig relations, which relate the real and imaginary parts of the Fourier transform of $H(z,t)$. Chapter 6 then introduces the nearly-local Kramers-Kronig relations, which relate the real and imaginary parts of $\underline{\mathcal{K}}(f)$ for a particular subclass of causal materials.

Chapter 6 also introduces the Paley-Wiener criteria, which give some conditions $\Re_e\{\underline{\mathcal{K}}(f)\} = \alpha(f)$ and $\Im_m\{\underline{\mathcal{K}}(f)\} = \beta(f) = 2\pi f/c(f)$ must satisfy if $\underline{\mathcal{K}}(f)$ is to yield a causal $H(z,t)$. The Paley-Wiener criteria constrain the $\underline{s} \to \underline{\infty}$ asymptotic behavior of $\underline{\gamma}(\underline{s}) = -l\ \underline{\mathcal{K}}(\underline{s}/(\mathrm{j}2\pi))$.

Chapter 6 points out that any analytic $\underline{\gamma}(\underline{s})$ with acceptable $\underline{s} \to \underline{\infty}$ asymptotic behavior must yield a causal $H(z,t)$ provided $\underline{\gamma}(\underline{s})$ is analytic throughout the entire right half plane (RHP, inclusive of j ω axis). These results help determine whether some proposed model for $\underline{\mathcal{K}}(f)$ will yield a causal $H(z,t)$.

The generic models for the polymeric, transmission line, and Bromwich materials are introduced in this chapter, as are their standard models (polyethylene, skin effect, and standard Bromwich, respectively). See appendix C for plots of these standard materials' 1 mm impulse response functions $H(1\mathrm{mm},t)$, as well as their attenuation coefficient $\alpha(f)$ and phase velocity $c(f)$ curves. Note that, in this context, 'standard' means standard only within this thesis' context; there is no globally accepted standard brand or model of polyethylene, for example.

Chapter 7 *CLDP Transforms* presents, and attempts to validate, this thesis' novel mathematical results. Chapter 7 starts with 'the principal insight' which concerns 'CLDP paths.' The principal insight is that the temporal output of a CLDP IE can, after Fourier transformation, be interpreted as the values of the spatial Laplace transform of the input source waveform along what has been dubbed a CLDP path.

Appendix D offers a graphical depiction of the principal insight.

It is then shown that the Bromwich Laplace transform inversion path is identical to the CLDP path corresponding to a particular type of CLDP material (dubbed, not surprisingly, a Bromwich material). This thesis proposes that implementing the generic Laplace transform inversion integral along a CLDP path will result in the desired source waveform provided the desired source waveform itself satisfies certain material-dependent conditions.

The forward CLDP IE maps waveforms to signals; it defines a material-dependent forward integral transform relation. The proposed inverse CLDP IE maps signals to waveforms. The question is: for what class of CLDP materials and waveforms does the proposed inverse CLDP IE 'undo' the forward CLDP IE? (Using this terminology, the Fourier synthesis integral would be said to 'undo' the Fourier analysis integral.) This thesis proposes that all CLDP materials (not just Bromwich materials) have this property, and that each CLDP material defines a CLDP integral transform relation.

As a practical matter, any implementation of the proposed inverse CLDP IE will be bandlimited because experimental signals can only be sampled at a finite rate. Two sections of chapter 7 (*The Darrell Property Of The Inverse CLDP IE* and *Deriving The Darrell*) yield surprising results concerning the bandlimited inverse CLDP IE: given a pure but abruptly bandlimited signal, the recovered waveform must be the convolution of the true source waveform with a material-dependent generalized Gibbs-Dirichlet kernel (sinc function) dubbed the Darrell.

In *Validation of the Inverse CLDP IE* the class of CLDP transformable waveforms is determined implicitly via the CLDP criterion, which states that a particular Laplace plane integration path must vanish in a particular limit. In *The Darrell As Delta Convergent Sequence* the Darrell property and the sinc-like form of the Darrell itself is used to examine the class of CLDP transformable waveforms.

The goal of chapter 7's final section is numeric verification of the Darrell property, and the shape of the Darrell, as descriptors for the noiseless but abruptly (*ie*: subjected to an ideal, square window lowpass filter) bandlimited inverse CLDP IE. This final section of chapter 7 verifies the Darrell property, and the shape of the Darrell, for this thesis' three standard CLDP materials (polyethylene, skin effect, and Bromwich).

Chapter 8 *The Lyons Recovery Applied To Standard Polyethylene* starts by focussing on the standard impulsive source waveform: ten unit-area Dirac delta functions of source placed at half-millimeter increments, from $z = 0.25$ mm to $z = 4.75$ mm. First it is shown that the unregularized Lyons recovery is unacceptable due to the Darrell's λ oscillations. Then it is shown that lowpass filtering the measured response signal before executing the Lyons mapping from frequency to space results in an acceptable recovery. Lowpass filtering is implemented via the filter $\mathrm{B}(f_c, f)$ known as Blackman's Lucky Guess (BLG; see appendix B).

The 'acceptable recovery' described above is dubbed the SIB recovery (spatially independent Blackman) because the cutoff frequency f_c of the BLG filter $\mathrm{B}(f_c, f)$ used was not a function of space. Although acceptable, this SIB recovery is not optimum because it does not take advantage of the fact that the signals emitted by shallower

sources require less amplification than do signals emitted by deeper sources and are therefore more stable (they are also relatively less inclusive of the often noisy higher frequencies).

It is then shown that the SDB recovery (spatially dependent Blackman), which uses a spatially dependent BLG cutoff frequency function (*aka*: SDB function) $f_c(z)$, can be made to more accurately resolve shallow sources than can the SIB recovery (assuming the degree of λ-oscillation supression is held constant).

The efficacy of the SDB recovery is also shown for the case of distributed (*ie*: non-impulsive) sources via the standard Gaussian source waveform, which places Gaussian distributions of source at those positions formerly occupied by delta functions of source.

The $z = 0.25$ mm Gaussian source is thin (FWHM = 36.32 μm) and has area -1; the $z = 4.75$ mm Gaussian source is thick (FWHM = 95.49 μm) and has area +1. The standard Gaussian source waveform is defined by repeating this binary base-pair five times. This definition of 'thin' was determined as the width of the standard recovery of a $z = 0.25$ mm delta function of source; this definition of 'thick' corresponds to the standard recovery of a $z = 4.75$ mm delta function of source.

Because the author was unable to analytically calculate standard polyethylene's impulse response $\mathrm{H}_p(z,t)$ corresponding to even an impulsive source (much less a distributed Gaussian source) each Gaussian source is actually modelled via closely spaced (2 nm) delta functions of source. (With l equal to some specific value of z, this thesis proffers modelled versions $\hat{\mathrm{H}}_p[l,t_n]$ of $\mathrm{H}(l,t)$ calculated by inverse fast Fourier transforming $\hat{\underline{h}}[f_k] \equiv \exp(-l\ \underline{\mathcal{K}}_p(f_k)))$

Chapter 8 then proceeds to show that this thesis' standard Lyons recovery subsumes the dominant recovery. That is, it will be shown that the SIB recovery can be regularized (at the expense of increased width and skewness) by *relaxing* (modulating) the model used for the recovery ($\alpha_r(f)$ and $c_r(f)$) smoothly (in terms of width and apparent skewness) between the limits set by the standard model for polyethylene ($\alpha_p(f)$ and $c_p(f)$) and the delay-only model ($\alpha_d(f) = 0$ and $c_d(f) = c_d$).

The final section of chapter 8 shows that the SDB regularized Lyons recovery can be relaxed in a similar manner, and that the recovery (measured in terms of recovered localized area, recovered peak position, and recovered source pulse full-width-at-half-maximum) is most successful when the model used in the forward CLDP IE (to produce the synthetic response signal) is also used in the inverse CLDP IE (to map the synthetic response signal to an approximation to the original waveform).

Although the following result was not confirmed quantitatively (except indirectly, *via* analysis of the recovered localized area), the final section of chapter 8 also shows that the troublesome skewness evident in the dominant recovery is ameliorated when the model used in the inverse CLDP IE is the same as the model used in the forward CLDP IE.

Chapter 10 *Experimental Recovery* ties the thesis together by performing charge recoveries from four PESAW experiments. The goal is to establish the Lyons recovery as a reliable means for processing measured PESAW signals.

Chapter 11 *Conclusions And Surmises* draws conclusions about the CLDP trans-

form theorem, and also about the applicability of the Lyons recovery to the interpretation of measured PESAW signals. It will also make surmises about (1) how the Lyons recovery might be extended to apply to inhomogeneous materials and (2) how other (non-SDB) regularized Lyons recoveries might be implemented.

Chapter 2

Technical Introduction

This thesis has two related goals: one mathematical, one practical. The practical goal is to describe, and verify numerically, a novel signal processing algorithm which subsumes the dominant time-to-space charge recovery algorithm currently in vogue among PESAW researchers (see section 1.6). The mathematical goal is to justify this novel algorithm in its own right.

The novel mathematics are dubbed 'CLDP transform theory.' The novel signal processing algorithm is dubbed 'the Lyons recovery.' This separation of the mathematics from the processing algorithm it advocates allows application of the Lyons recovery to cases where, strictly, the application of CLDP transform theory is either (A) not known to be valid or (B) known not to be valid. These novel mathematics propose both a 'forward' operator dubbed the CLDP IE and an 'inverse' operator dubbed the inverse CLDP IE.

These two goals are linked because the PESAW forward problem can often reasonably be modelled as a CLDP IE. Therefore the inverse CLDP IE may be applied to the PESAW problem of determining the charge waveform which gave rise to a particular pressure signal emitted by a particular material. The following section derives the PESAW IE from a simple model of the PESAW experiment, and then generalizes it into a larger context wherein it is referred to as the CLDP IE.

2.1 The PESAW Problem

Figure 1.1 depicts a simple slab capacitor which has a pressure-to-voltage transducer attached to the external surface of its proximal plate. The capacitor has a surface charge q_1 (nC/cm^2) embedded at position (plane) z_1 within its otherwise homogeneous dielectric region. The spatially impulsive charge per volume Q(z) (nC/(cm^2 mm)) is represented mathematically via the Dirac delta function $\delta(z)$:

$$\mathrm{Q}(z) = q_1 \delta(z - z_1) \tag{2.1}$$

Note that the permittivity of free space ϵ_o rounds to unity in the following units:

$$\epsilon_o = \overbrace{0.8854}^{\cong 1} \frac{\text{nC}}{\text{cm}^2} / \frac{\text{kV}}{\text{mm}} \tag{2.2}$$

If $\epsilon \cong \epsilon_o$, then when applied voltages $\text{V}_a(t) \sim$ kV are applied to slab capacitors with plates separation $l \sim$ mm, the magnitude of the surface charges q_p on each plate will be $\sim$ nC/cm^2. That is, nC/cm^2 is a sensible unit of surface charge when (as is the case here) the applied electric fields are on the order of kV/mm.

Suppose the applied voltage $\text{V}_a(t) = \mathcal{V}\delta(t)$ generates an excitation electric field $\bar{\mathbf{E}}(z,t)$ within the dielectric which can be modelled as temporally impulsive and spatially distributed

$$\bar{\mathbf{E}}(z,t) = \frac{-\mathcal{V}}{l}\ \delta(t)\ \hat{\mathbf{i}}_z \tag{2.3}$$

Please note that the time-varying excitation electric field (described in (2.3)) adds to the non-time-varying electric field (not described) produced by the charges themselves. Also, note that the units of $\delta(t)$ are μs^{-1}, and that the units of $\mathcal{V}$ are [kV μs]. The PESAW charge recovery method focusses on the time-varying components of the problem; the non-time-varying portions do not contribute to the measured signal.

According to the Lorentz force law F = Q E, the excitation force field $\bar{\mathbf{F}}(z,t)$ generated by the excitation electric field interacting with the charge distribution will be given by

$$\bar{\mathbf{F}}(z,t) = \frac{-q_1\mathcal{V}}{l}\ \delta(z-z_1)\ \delta(t)\ \hat{\mathbf{i}}_z \tag{2.4}$$

Due to the symmetry of this configuration, this excitation force field acts as a temporally impulsive pressure (force per area)

$$\text{X}_1(t) = \frac{q_1\mathcal{V}}{l}\ \delta(t) \tag{2.5}$$

which imposes itself in the $-z$ direction at the excitation plane $z = z_1$. Assuming both q_1 and $\mathcal{V}$ are positive, a positive pressure (compression) wave will be launched from the excitation plane toward the proximal plate and a negative pressure (rarefaction) wave will be launched toward the distal plate.

If the slab of material comprising the region $0 \leq z \leq z_1$ may be considered a linear, time-invariant system with impulse response $\text{h}_1(t)$ with respect to plane pressure waves passing through it, and if the pressure wave launched toward the distal plate may be neglected, then the pressure signal $\mathcal{P}(t)$ delivered to the transducer by the internal charge distribution will be given by simple convolution

$$\mathcal{P}(t) = \mathrm{X}_1(t) * \mathrm{h}_1(t) = \frac{q_1 \mathcal{V}}{l}\, \mathrm{h}_1(t) \tag{2.6}$$

This thesis considers only materials for which $\mathrm{h}_1(t)$ is real, causal (vanishes for negative times), and has a Fourier transform $\underline{h}_1(f)$ (see appendix F) of the form

$$\underline{h}_1(f) = \exp(-z_1\, \underline{\mathcal{K}}(f)) \tag{2.7}$$

where $\underline{\mathcal{K}}(f)$ is the complex propagation coefficient. These materials are called causal, lossy, dispersive, plane-wave (CLDP) materials. The term 'causal' refers to the fact that a physical material must have an impulse response $\mathrm{h}_1(t)$ that is causal regardless of the (assumedly positive) value of z_1. See chapter 6 for a discussion of causal materials.

The term 'plane-wave' refers to this thesis' focus on plane pressure waves which propagate according to the familiar, one dimensional linear wave equation. See chapter 3 or appendix A for a derivation of (2.7). The terms 'lossy' and 'dispersive' refer to the fact that $\underline{\mathcal{K}}(f)$'s real and imaginary parts, respectively, can be expressed in terms of the material's attenuation coefficient $\alpha(f)$ and phase velocity $c(f)$:

$$\underline{\mathcal{K}}(f) = \alpha(f) + \mathrm{j}\, \frac{2\pi f}{c(f)} \tag{2.8}$$

Note that the propagation coefficient $\underline{\mathcal{K}}(f)$ given here is related to the familiar complex wavenumber $\underline{k}(f)$ via

$$\underline{\mathcal{K}}(f) = \mathrm{j}\, \underline{k}(f) \tag{2.9}$$

The novel notation $\underline{\mathcal{K}}(f)$ rather than $\mathrm{j}\, \underline{k}(f)$ has been adopted so that the parallel between the Laplace transform and a CLDP IE can be made most clear. This relation to the Laplace transform is demonstrated in section 7.1. Relation (2.9) is derived in appendix A.

A slab of CLDP material may be considered a linear, time invariant system with respect to plane pressure waves passing through it. Recall that when a CLDP material which has a charge distribution of the form

$$\mathrm{Q}(z) = q_1 \delta(z - z_1) \tag{2.10}$$

embedded within it is subjected to the PESAW experimental procedure, the time dependent pressure signal $\mathcal{P}(t)$ transmitted to the proximal plate transducer by the charge layer is given implicitly by (2.7) and (2.6) as

$$\mathcal{P}(t) = \frac{q_1 \mathcal{V}}{l} \mathcal{F}^{-1}\{\exp(-z_1 \underline{\mathcal{K}}(f))\} \tag{2.11}$$

Through linearity it follows that if $\mathrm{Q}(z)$ is composed of M charge layers with relative weights q_m

$$\mathrm{Q}(z) = \sum_{m=1}^{M} q_m \, \delta(z - z_m) \tag{2.12}$$

then the pressure signal $\mathcal{P}(t)$ delivered to the transducer by the internal charge distribution will be composed of sum of M weighted responses

$$\mathcal{P}(t) = \frac{\mathcal{V}}{l} \sum_{m=1}^{M} q_m \, \mathcal{F}^{-1}\{\exp(-z_m \underline{\mathcal{K}}(f))\} \tag{2.13}$$

Please note that this analysis neglects the non-time-varying Coulomb forces generated by the non-time-varying embedded charges, and that (2.13) is but a special case of the more general relation

$$\mathcal{P}(t) = \frac{\mathcal{V}}{l} \int_0^l \mathrm{Q}(z) \, \mathcal{F}^{-1}\{\exp(-z \underline{\mathcal{K}}(f))\} dz \tag{2.14}$$

The result of modifying (2.14) by introducing the time domain CLDP kernel $\mathrm{H}(z,t)$

$$\mathrm{H}(z,t) \qquad \stackrel{\mathcal{F}}{\Longleftrightarrow} \qquad \exp(-z \underline{\mathcal{K}}(f)) \tag{2.15}$$

is

$$\mathcal{P}(t) = \frac{\mathcal{V}}{l} \int_0^l \mathrm{Q}(z) \, \mathrm{H}(z,t) dz \tag{2.16}$$

Equation (2.16) should make it clear that, if the experimenter makes sure that the approximations made in this derivation are reasonable, the measured PESAW pressure versus time signal is the output of a linear, first-kind Fredholm IE (see chapter 5 for a definition of this class of IEs). The special CLDP kernel $\mathrm{H}(z,t)$ justifies calling (2.16) a CLDP IE.

In the interest of generality, the source waveform $\mathcal{Q}(z)$ is proposed as the generic CLDP waveform that subsumes the PESAW charge waveform $\mathrm{Q}(z)$:

$$\mathcal{Q}(z) = \frac{\mathcal{V}}{l} \mathrm{Q}(z) \tag{2.17}$$

so that

$$\mathcal{P}(t) = \int_0^l \mathcal{Q}(z)\ \mathrm{H}(z,t) dz \tag{2.18}$$

may be termed the forward PESAW IE. The PESAW IE is a CLDP IE; CLDP IEs are a subclass of linear, first-kind Fredholm IEs. It is interesting to note that (2.18) implies

$$\int_{-\infty}^{\infty} \mathcal{P}(t)\ dt = \int_{-\infty}^{\infty} \mathcal{Q}(z)\ \exp(-z\ \alpha(0)) dz \tag{2.19}$$

That is, if $\alpha(0) = 0$ then the area of the source waveform equals the area of the response signal. Equation (2.19) may be derived by Fourier transforming both sides of (2.18), inserting (2.15), then focussing on the zero frequency. Equation (2.19) can be useful in evaluating the approximate $\mathcal{Q}(z)$ associated with some $\mathcal{P}(t)$ by some recovery algorithm.

Note that, in theory, both the lower integration limits in (2.19) could be raised from negative infinity to zero due to the assumed causality of both $\mathcal{P}(t)$ and $\mathcal{Q}(z)$. However, in practice, $\mathcal{P}(t)$ is often filtered. Filtering a function can violate its causality (see section 6.3) so the lower limits of (2.19) have been modified to reflect this possibility.

The upper limit of the integral of $\mathcal{Q}(z)$ has been raised from l to infinity for two reasons. First, because the generic (non-PESAW) CLDP IE does not require the source waveform to vanish beyond any particular positive value of z. Second, the PESAW recovery gleaned via some algorithm will not necessarily vanish above $z = l$; again, because filtering can cause the recovery to 'spread' beyond its expected limits.

2.2 From Voltage Signal To Charge Waveform

Determining an estimated charge waveform $\tilde{\mathrm{Q}}(z)$ to the desired charge waveform $\mathrm{Q}(z)$ given a measured voltage signal $\mathrm{V}(t)$ (and a material model) can be viewed as a three step process. This section introduces the three steps; chapter 4 discusses these steps in detail.

The avid reader can find a one-page schematic outline of the PESAW-CLDP relationship in appendix G. The three steps discussed here corresponds to traversing the three trunks of appendix G's Π-shaped schematic in a counter-clockwise direction: first the right leg, then the top bar, then the left leg. The top bar involves only CLDP-specific quantities; the two legs suggest how the measured, and the desired, PESAW-specific quantities relate to the CLDP-specific quantities.

The three steps are as follows:

First, deconvolve the measured $\mathrm{V}(t)$ with respect to some estimate $\tilde{\mathrm{H}}_e(t)$ to the experimental impulse response function $\mathrm{H}_e(t)$, and then perhaps filter, to arrive at an estimated pressure signal $\tilde{\mathcal{P}}(t)$ to the true pressure signal $\mathcal{P}(t)$ which inspired $\mathrm{V}(t)$ (the experimental impulse response $\mathrm{H}_e(t)$ is defined in equation (4.15); $\mathrm{H}_e(t)$ involves the transducer impulse response $\mathrm{H}_T(t)$, the applied voltage signal $\mathrm{V}_a(t)$, and the permittivity ϵ and thickness l of the dielectric).

Second, map the estimated pressure signal $\tilde{\mathcal{P}}(t)$ to an estimated source pressure waveform $\tilde{\mathcal{Q}}(z)$ using an estimated propagation coefficient $\underline{\tilde{\mathcal{K}}}(f)$. Third, map the estimated source pressure waveform $\tilde{\mathcal{Q}}(z)$ to an estimated charge waveform $\tilde{\mathrm{Q}}(z)$.

Note that the estimated source waveform $\tilde{\mathcal{Q}}(z)$ will henceforth be referred to as the recovered waveform, denoted $\mathrm{R}(z)$. These three steps are presented diagrammatically below. The boxed quantities indicate the information required to map the function on the left to the function on the right.

$$\begin{array}{lcccc} \text{Step 1:} & \mathrm{V}(t) & \longrightarrow & \boxed{\tilde{\mathrm{H}}_e(t),\ \text{filter}} & \longrightarrow\ \tilde{\mathcal{P}}(t) \\ \text{Step 2:} & \tilde{\mathcal{P}}(t) & \longrightarrow & \boxed{\underline{\tilde{\mathcal{K}}}(f)} & \longrightarrow\ \tilde{\mathcal{Q}}(z) \equiv \mathrm{R}(z) \\ \text{Step 3:} & \mathrm{R}(z) & \longrightarrow & \boxed{\text{experimental setup}} & \longrightarrow\ \tilde{\mathrm{Q}}(z) \end{array}$$

Figure 2.1: Diagrammatic exposition of the proposed three step method for mapping a measured PESAW signal $\mathrm{V}(t)$ to an estimate $\tilde{\mathrm{Q}}(z)$ of the desired source charge waveform $\mathrm{Q}(z)$.

2.2.1 Step 1

The first step is a well known problem whose familiar frequency-domain-division solution is implemented in this thesis via the Fast Fourier Transform (FFT) and the filter known as Blackman's Lucky Guess (BLG). See chapter 3 for a discussion of deconvolution; see appendix B for an introduction to the BLG filter. Chapter 4 will describe how an estimate $\tilde{\mathrm{H}}_T(t)$ to the true transducer impulse response function $\mathrm{H}_T(t)$ may be gleaned from experimental data.

2.2.2 Step 2

The second step forms the mathematical and numerical core of this thesis. A section of this introduction will present the major results of this thesis' attempt to solve

this problem. Chapter 4 will describe how an estimate $\tilde{\underline{\mathcal{K}}}(f)$ to the true propagation coefficient $\underline{\mathcal{K}}(f)$ may be gleaned from experimental data.

2.2.3 Step 3

At first glance the third step appears trivial. Modifying (2.17), the result is

$$\tilde{\mathrm{Q}}(z) = \frac{l}{\mathcal{V}}\mathrm{R}(z) \tag{2.20}$$

However, (2.17) is but the special (planar) case of the more general relation

$$\mathcal{Q}(z) = \mathrm{E}_z(z)\mathrm{Q}(z) \tag{2.21}$$

where the excitation electric field $\bar{\mathbf{E}}(z,t)$ has separable space and time dependencies:

$$\bar{\mathbf{E}}(z,t) = -\mathrm{E}_z(z)\delta(t)\hat{\mathbf{i}}_z \tag{2.22}$$

In general, therefore,

$$\tilde{\mathrm{Q}}(z) = \frac{\mathrm{R}(z)}{\mathrm{E}_z(z)} \tag{2.23}$$

From (2.22) and (2.3) it follows that in a planar geometry

$$\mathrm{E}_z(z) = \frac{\mathcal{V}}{l} \tag{2.24}$$

so that (2.20) is recovered from (2.23).

In a coaxial cable geometry (where the recovery variable z and the cable radius r are related by $z + r = r_o$) which has the voltage signal $\mathrm{V}_a(t) = \mathcal{V}\delta(t)$ applied to the inner capacitor plate at $r = r_i$, and which has the outer capacitor plate at $r = r_o$ grounded, elementary electrostatics reveals

$$\mathrm{E}_z(z) = \frac{\mathcal{V}}{(r_o - z)\ln(r_o/r_i)} \tag{2.25}$$

so that (2.23) yields

$$\tilde{\mathrm{Q}}(z) = \mathrm{R}(z)\frac{(r_o - z)\ln(r_o/r_i)}{\mathcal{V}} \tag{2.26}$$

Generality is served by focussing on $\mathcal{Q}(z)$ and $\mathrm{R}(z)$ instead of $\mathrm{Q}(z)$ and $\tilde{\mathrm{Q}}(z)$ because then questions about geometry and actual applied voltage strength are sidestepped, and the focus is thrown upon the CLDP IE inversion process rather than experimental details.

Unfortunately, the previous analysis is only approximate: it has assumed that the one dimensional (cylindrical) waves generated by the cylindrical charges 'propagate like plane waves.' *Eg*: the previous analysis assumes that cylindrical waves propagating in a lossless/dispersionless material will have an amplitude that is independent of z.

But because a $-z$ propagating cylindrical wave expands as it travels, conservation of energy requires its amplitude to diminish. A thorough analysis of this effect would require introduction of the Hankel functions [105], and thereby shift this thesis' emphasis from its goal of introducing and applying CLDP theory.

2.3 Dimensions And Units

Focussing on $\mathcal{Q}(z)$ rather than $\mathrm{Q}(z)$ is also seen to serve generality when the dimensions of (2.18) are considered. From the derivation of the PESAW-CLDP IE, the dimension of $\mathcal{P}(t)$ is clearly pressure. As $\mathrm{H}(z,t)$ is defined as the inverse Fourier transform of the dimensionless quantity $\underline{H}(z,f) = \exp(-z\ \underline{\mathcal{K}}(f))$, $\mathrm{H}(z,t)$ must have dimension of frequency, or inverse time. Therefore the dimension of $\mathrm{H}(z,t)dz$ is velocity (length dz over time) So the dimension of $\mathcal{Q}(z)$ must be pressure per velocity, as indeed it is according to (2.17).

Generalizing the PESAW IE (2.18) into the broader CLDP context, if the quantity $\mathcal{P}(t)$ somehow had dimension of, say, voltage, then the associated $\mathcal{Q}(z)$ would have to have dimension of voltage per velocity if both sides of (2.18) are to have the same dimension (which they must).

What is required, fundamentally, is that the quantity $\mathcal{P}(t)/\mathcal{Q}(z)$ have the same dimension as the quantity z/t. In this thesis, z will always have dimension of length and t will always have dimension of time. However, even with this constraint, there is freedom in the dimensions attached to $\mathcal{P}(t)$ and $\mathcal{Q}(z)$ because it is only the dimension of their ratio which is constrained to be velocity. Perhaps pressure and pressure-per-velocity are not the best choices for the dimensions of $\mathcal{P}(t)$ and $\mathcal{Q}(z)$.

In this thesis the units of z will be taken as millimeters (mm), the units of t will be microseconds (μs), the units of $\mathcal{Q}(z)$ will be inverse millimeters (mm^{-1}), and the units of $\mathcal{P}(t)$ will be inverse microseconds ($\mu\mathrm{s}^{-1}$). This $\mathcal{Q}(z)$ is called the source; this $\mathcal{P}(t)$ is called the response. With these dimensions the Fourier and Laplace transforms of both $\mathcal{P}(t)$ and $\mathcal{Q}(z)$ are dimensionless.

This choice for the dimension of $\mathcal{P}(t)$ may seem exotic at first. Yet from an experimental point of view, $\mathcal{P}(t)$ is determined by deconvolving the measured signal $\mathrm{V}(t)$ with respect to the experimental impulse response function $\mathrm{H}_e(t)$, both of which have the same dimension (see chapter 4). Therefore $\mathcal{P}(t)$ must have dimension inverse to that of its argument; the dimension of t is time so, according to this analysis, the natural dimension of the experimental $\mathcal{P}(t)$ is inverse time.

From the computer simulation point of view, as discussed above, $\mathrm{H}(z,t)$ is defined as the inverse Fourier transform of the dimensionless quantity $\underline{H}(z,f) = \exp(-z\,\underline{\mathcal{K}}(f))$ and so has dimension of frequency, or inverse time. Because $\mathcal{P}(t)$ is comprised of a sum of these $\mathrm{H}(z,t)$'s, the natural dimension of the simulated $\mathcal{P}(t)$ is also inverse time.

So inverse time is actually a sensible dimension to attach to $\mathcal{P}(t)$, both from an experimental and a computer simulation point of view. Because the dimension of $\mathcal{P}(t)/\mathcal{Q}(z)$ must be the same as the dimension of z/t, and because the dimension of z/t is length per time, it follows from this choice of dimension for $\mathcal{P}(t)$ that $\mathcal{Q}(z)$ must have dimension of inverse length.

In the forward problem, the dimension of $\mathcal{Q}(z)$ may quite naturally be interpreted as non-dimensional source per length. Similarly, in the inverse problem (where $\mathcal{P}(t)$ is the 'source') the dimension of $\mathcal{P}(t)$ may just as naturally be interpreted as non-dimensional source per time.

Because $\mathcal{P}(t)$ has been generalized out of the PESAW context, it is referred to as 'the response signal' rather than 'the pressure signal.' For the same reason, $\mathcal{Q}(z)$ is referred to as 'the source waveform' rather than 'the charge waveform.'

The units of the phase velocity $c(f)$ will be taken as mm/μs. The units of the Fourier transform variable f will be mega-Hertz (MHz), which are the same as inverse microseconds. The units of the attenuation coefficient $\alpha(f)$ will be Nepers per millimeter (Np/mm).

2.3.1 Nepers and Decibels

Note that, qualitatively, Nepers are to decibels (dB) as radians are to degrees (deg).

That is, Nepers and radians are the natural units of the real and imaginary parts, respectively, of the logarithm of a complex number, whereas decibels and degrees are scaled versions of the natural units. Although the scale factor for translating radians to degrees is greater than the scale factor for translating Nepers to decibels, both scale factors are within an order of magnitude of ten.

To be specific,

$$1\,\mathrm{rad} \quad = \quad \frac{360}{2\pi}\,\mathrm{deg} \quad \cong \quad 57.3\,\mathrm{deg}$$

and

$$1\,\mathrm{Np} \quad = \quad 10\,\log_{10}(e^2)\,\mathrm{dB} \quad \cong \quad 8.686\,\mathrm{dB}$$

The dimensions chosen for $\mathcal{P}(t)$ and $\mathcal{Q}(z)$ reflect a striving towards generality; the units chosen for t and z reflect the reality that much of the work in this thesis involves PESAW modelling of ~mm-thick slabs of polymer which have phase velocities ~mm/μs.

Note that the definitions chosen for the three steps, and the units chosen for the functions and variables involved in step two, all conspire to make step two a separable module which may be focussed upon in its own right. This allows the emphasis to

be placed upon this thesis' novel mathematics, and their numeric implementation and verification, without leaving the PESAW experimenter adrift in abstraction.

2.4 The Need For Improved Recovery

The figure below is offered as a means to understand the deficiency of the dominant time-to-space mapping algorithm mentioned in the general introduction. It depicts the modelled output signal $\mathcal{P}(t)$ corresponding to a source waveform comprised of ten unit-strength source impulses placed at half-millimeter increments inside a polyethylene (PE) slab. The first impulse sits at $z = 0.25$ mm. The last impulse sits at $z = 4.75$ mm. This placement of sources is called the standard constellation.

The standard model for polyethylene was used to produce the plot. This model is introduced in section 6.2.2. For now, suffice to say that the model includes loss and dispersion; the attenuation coefficient $\alpha(f)$ and phase velocity $c(f)$ are frequency dependent.

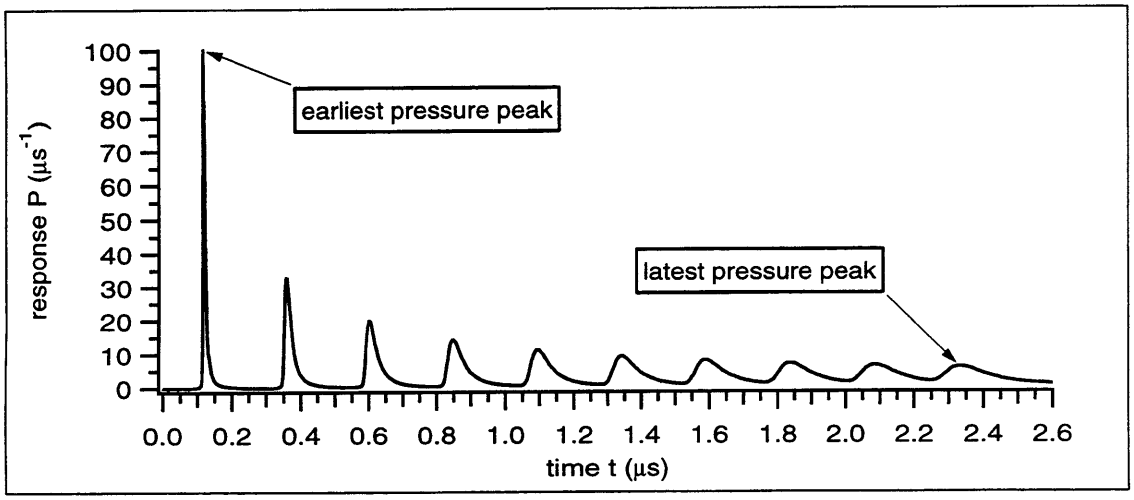

Figure 2.2: Modelled output pressure signal corresponding to the standard impulsive source constellation embedded in standard polyethylene.

The dominant time-to-space pressure waveform recovery $\mathrm{R}_d(z)$ is given by

$$\mathrm{R}_d(z) \equiv \frac{1}{c_d}\,\mathcal{P}(\frac{z}{c_d}) \tag{2.27}$$

where c_d has dimensions of length per time, and represents an effective velocity. But what value should be used for c_d if the phase velocity is frequency dependent? This question points out one of two main problems with this algorithm. The second problem is that, regardless of the value of c_d, the recovery of each pressure impulse will be skewed to the right.

Returning to the question of the value of c_d, one reasonable choice would be to select c_d to ensure that the time of the earliest pressure peak is mapped to the position of the shallowest charge: $z = 0.25$ mm. Denote the value of c_d that ensures this mapping c_d^e and denote its associated recovery $\mathrm{R}_d^e(z)$. It turns out that $c_d^e = 2.119$ mm/μs. Another reasonable choice is to select c_d to ensure that the latest pressure peak is mapped to $z = 4.75$ mm. Denote this value c_l^l and denote its associated recovery $\mathrm{R}_d^l(z)$. It turns out that $c_d^l = 2.035$ mm/μs. The problem is that $c_d^e \neq c_d^l$.

Rather, $c_d^e/c_d^l = 1.041$. The result is that $\mathrm{R}_d^e(z)$ places the recovered peak of the $z = 4.75$ mm charge impulse 196 μm too far to the right, and $\mathrm{R}_d^l(z)$ places the recovered peak of the $z = 0.25$ mm charge impulse 10 μm too far to the left. It seems there can be no single correct value for c_d. Perhaps a time-dependent effective velocity $c_d(t)$ would improve the positioning, but it could not fix the skewness problem.

It is worth noting that $\mathrm{R}_d^l(z)$ gives a better overall recovery than $\mathrm{R}_d^e(z)$, as evidenced by the following figure which depicts these two recoveries. More quantitatively, the root-mean-square error in the recovered locations of the ten source impulses, as measured by the position of each source recovery's peak value, is 109 μm for $\mathrm{R}_d^e(z)$ and only 16 μm for $\mathrm{R}_d^l(z)$.

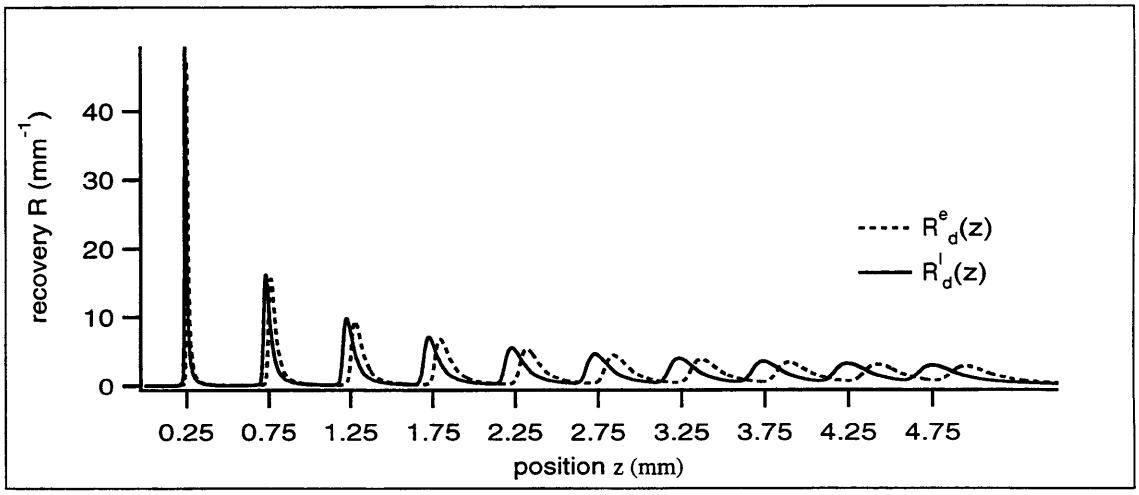

Figure 2.3: Comparison of the dominant recovery $\mathrm{R}_d(z)$ for two values (c_d^e and c_d^l) of the requisite constant velocity c_d.

2.5 CLDP Transforms

The mathematical core of this thesis is CLDP transform theory. The existence, and requirements, of the proposed CLDP transforms are discussed in chapter 7. The remaning portions of the current chapter seek only to illuminate the properties of the proposed CLDP transforms.

CLDP transform theory proposes that, if the propagation coefficient

$$\underline{\mathcal{K}}(f) = \alpha(f) + \mathrm{j}\ \underbrace{2\pi f/c(f)}_{\beta(f)} \tag{2.28}$$

corresponds to a temporally causal, position z dependent impulse response function

$$\mathrm{H}(z,t) = \mathrm{H}(z,t)\ \mathrm{U}(t) \qquad \stackrel{\mathcal{F}}{\Longleftrightarrow} \qquad \underline{H}(z,f) \ \equiv\ \exp(-z\ \underline{\mathcal{K}}(f)) \tag{2.29}$$

and if the response signal $\underline{\mathcal{P}}(f)$ is related to the causal, real, Fourier-transformable source waveform $\mathcal{Q}(z)$ via the CLDP IE

$$\underline{\mathcal{P}}(f) = \int_0^\infty \mathcal{Q}(z)\ \exp(-z\ \underline{\mathcal{K}}(f))\ dz \tag{2.30}$$

then $\mathcal{Q}(z)$ may be determined from $\mathcal{P}(f)$ and $\underline{\mathcal{K}}(f)$ via

$$\mathcal{Q}(z) = \int_{-\infty}^{\infty} \underline{\mathcal{P}}(f)\ [\frac{1}{\mathrm{j}2\pi} \frac{d\ \underline{\mathcal{K}}(f)}{df}]\ \exp(z\ \underline{\mathcal{K}}(f))\ df \tag{2.31}$$

provided $\mathcal{Q}(z)$ satisfies the $\underline{\mathcal{K}}(f)$-dependent CLDP transform criterion (equation (7.73))

$$\lim_{f\to\infty} \left\{ \int_0^{\alpha(f)} \Im_m\{\underline{\tilde{\mathcal{Q}}}([\alpha' + \mathrm{j}\ \beta(f)])d\ \alpha' \right\} = 0 \tag{2.32}$$

where $\underline{\tilde{\mathcal{Q}}}(\underline{\mathcal{K}})$ is the (spatial) Laplace transform of $\mathcal{Q}(z)$ (see appendix F).

It is in this sense that $\mathcal{Q}(z)$ and $\underline{\mathcal{P}}(f)$ are said to be CLDP transforms of each other. This relation is denoted symbolically via

$$\mathcal{Q}(z) \qquad \stackrel{\mathcal{K}}{\Longleftrightarrow} \qquad \underline{\mathcal{P}}(f) \tag{2.33}$$

Note that $\mathcal{Q}(z)$ has been placed on the privileged left hand side of the transform relation commonly reserved for 'direct space' functions. Of course, like all transforms, the answer to the question "which is the direct space function and which is the inverse space function?" is somewhat arbitrary.

The waveform $\mathcal{Q}(z)$ has been designated the direct space function because of its role in the PESAW context, where the *forward* problem involves calculating $\mathcal{P}(f)$ from $\mathcal{Q}(z)$. This is fortuitous because (as section 2.5.6 will show) in the case of the delay-only material for which the CLDP transforms reduce to the Fourier transform, $\mathcal{Q}(z)$ acts like a function of time. Unfortunately, designating $\mathcal{Q}(z)$ as the direct space function forces the measured PESAW signal $\mathcal{P}(t)$ to be designated as an inverse space, or perhaps 'pseudo direct space,' function.

2.5.1 Group Velocity

It is interesting to note that the bracketed quantity in (2.31) is just the inverse of the material's complex, frequency dependent group velocity $\underline{C}_g(f)$. That is,

$$\frac{1}{\mathrm{j}2\pi}\frac{d\,\underline{\mathcal{K}}(f)}{df} = \frac{1}{\underline{C}_g(f)} \tag{2.34}$$

so that

$$\mathcal{Q}(z) = \int_{-\infty}^{\infty} \frac{\mathcal{P}(f)}{\underline{C}_g(f)}\,\exp(z\,\underline{\mathcal{K}}(f))\,df \tag{2.35}$$

Equation (2.34) follows from the realization that [54]

$$\underline{C}_g(f) \equiv \frac{d\,\omega}{d\,\underline{\mathrm{k}}(\omega)} = \frac{d\,[2\pi f]}{d\,[-\mathrm{j}\,\underline{\mathcal{K}}(f)]} \tag{2.36}$$

It follows from (2.34) and

$$\underline{\mathcal{K}}(f) = \alpha(f) + \mathrm{j}\,2\pi f/c(f) \tag{2.37}$$

that

$$\frac{1}{\underline{C}_g(f)} = \frac{1}{c(f)}\left[1 - \frac{f}{c(f)}\,\frac{d\,c(f)}{df}\right] + \frac{1}{\mathrm{j}2\pi}\frac{d\,\alpha(f)}{df} \tag{2.38}$$

The real part of the inverse of the group velocity involves only the phase velocity; the imaginary part of the inverse of the group velocity involves only the attenuation.

2.5.2 Time Domain Recovery

It is possible to express the frequency domain recovery (2.35) in the time domain by applying Fourier theory's initial value and convolution theorems. The result is

$$\mathcal{Q}(z) = \left[\; \mathcal{P}(t) * \overbrace{\mathcal{F}^{-1}\left\{\frac{1}{\underline{C}_g(f)}\right\}(t)}^{\mathrm{g}(t)} * \overbrace{\mathcal{F}^{-1}\{1/\underline{H}(z,f)\}(t)}^{\check{\mathrm{H}}(z,t)} \;\right]_{t=0} \tag{2.39}$$

$$= \left[\, \mathcal{P}(t) * \mathrm{g}(t) * \check{\mathrm{H}}(z,t) \,\right]_{t=0} \tag{2.40}$$

$$= \int_{-\infty}^{\infty} \mathcal{P}(t)\,\mathrm{K}(t,z)\,dt \tag{2.41}$$

where the 'the group signal' $g(t)$ in (2.40) is defined as the second convolved quantity in (2.39), the $\check{H}(z,t)$ in (2.40) is defined as the third convolved quantity in (2.39), and $K(t,z)$ is, for each particular value of z, the temporal reflection of the convolution of the group signal with $\check{H}(z,t)$. That is,

$$K(t,z) = \left\{ g(t) * \check{H}(z,t) \right\} (-t) \tag{2.42}$$

Because the $\mathcal{P}(t)$ in (2.41) must be causal, it follows that (2.41) can be rewritten

$$\mathcal{Q}(z) = \int_0^\infty \mathcal{P}(t)\, K(t,z)\, dt \tag{2.43}$$

Raising the l in (2.18) to infinity (which is valid if, as is assumed, $\mathcal{Q}(z)$ vanishes for $z > l$), it is interesting to note that the proposed time domain inverse CLDP IE (2.43) is a linear, first-kind Fredholm IE just like (2.18):

$$\mathcal{P}(t) = \int_0^\infty \mathcal{Q}(z)\, H(z,t)\, dz \tag{2.44}$$

2.5.3 The Convolution Inverse

Note that, as defined, $\check{H}(z,t)$ is the *convolution inverse* of $H(z,t)$. That is, for any one particular value of $z = z_o$,

$$H(z_o,t) * \check{H}(z_o,t) = \delta(t) \tag{2.45}$$

where (from equation (2.39))

$$\check{H}(z_o,t) \quad \stackrel{\mathcal{F}}{\Longleftrightarrow} \quad \frac{1}{\underline{H}(z_o,f)} = \underline{H}(-z_o,f) = \exp(z_o\, \underline{K}(f)) \tag{2.46}$$

Appendix ?? examines the criterion for the existence of a convolution inverse. But briefly: to verify (2.45), Fourier transform it. The right hand side becomes unity, and the left hand side becomes a product according to Fourier theory's convolution theorem:

$$\underline{H}(z_o,f)\, \frac{1}{\underline{H}(z_o,f)} = 1 \tag{2.47}$$

The time-domain recovery (2.40) makes it clear that the core of the recovery operation for calculating $\mathcal{Q}(z_o)$ involves deconvolution with respect to the material impulse response $H(z_o,t)$ (deconvolution = convolution with the convolution inverse).

Note that if $\mathrm{H}(-z,t) = \mathcal{F}^{-1}\{\exp(z\ \underline{\mathcal{K}}(f))$ is used to justify extending the domain of $\mathrm{H}(z,t) = \mathcal{F}^{-1}\{\exp(-z\ \underline{\mathcal{K}}(f))$ to negative values of z then the inverse CLDP IE may be succinctly expressed in the time domain:

$$\mathcal{Q}(z) = [\ \mathcal{P}(t) * \mathrm{g}(t) * \mathrm{H}(-z,t)\ ]_{t=0} \tag{2.48}$$

Assuming $\Re_e\{\underline{\mathcal{K}}(f)\} > 0$ under the aforementioned conditions yields an $\mathrm{H}(z,t)$ that is causal and stable for $z > 0$, causal and unstable for $z < 0$. This $\mathrm{H}(z,t)$ satisfies $\mathrm{H}(z,t) * \mathrm{H}(-z,t) = \delta(t)$ for all real values of z including $z = 0$, where both $\mathrm{H}(z,t)$ and $\mathrm{H}(-z,t)$ equal $\delta(t)$.

2.5.4 The Group Signal

It is interesting to ponder the meaning and properties of the group signal

$$\mathrm{g}(t) \quad \overset{\mathcal{F}}{\Longleftrightarrow} \quad \underline{g}(f) \equiv \frac{1}{\underline{C}_g(f)} \tag{2.49}$$

Note that $\mathrm{g}(t)$'s dependence on the attenuation coefficient $\alpha(f)$ only includes $d\alpha(f)/df$ (see equation (2.38)). Any constant term in $\alpha(f)$ will have no effect on $\mathrm{g}(t)$. This is important because, as section 6.1 will show, if some $\{\alpha(f), c(f)\}$ pair corresponds to a causal material and if α' is some arbitrary real constant, then the pair $\{\alpha(f)+\alpha', c(f)\}$ will also correspond to a causal system (although, depending on α' and $\alpha(f)$, the resulting material may well not be stable).

The result is that the entire family of materials $\{\alpha(f)+\alpha', c(f)\}$ spanned by different values of α' all share the same group signal. Note also that $\mathrm{g}(t)$ will be real because $\underline{g}(f)$ has conjugate symmetry, and that $\mathrm{g}(t)$ has a "general measure of duration [58]" $\Delta\mathrm{T}_g$ satisfying

$$\Delta\mathrm{T}_g \geq \frac{\sqrt{\int_{-\infty}^{\infty} |\underline{C}_g(f)|^{-2}\ df}}{2\pi\sqrt{\int_{-\infty}^{\infty} f^2\ |\underline{C}_g(f)|^{-2}\ df}} \tag{2.50}$$

In the case of the Bromwich materials (see section 6.1.1), for which $\{\alpha(f), c(f)\} = \{\alpha_b, c_b\}$, the integrals in (2.50) do not converge and (2.49) yields $\mathrm{g}(t) = \delta(t)/c_b$.

For the reductive case of the Bromwich materials, $\mathrm{g}(t)$ is definitely pulsive. If $|\underline{C}_g(f)|$ does does not increase too rapidly with f then, by the duration-bandwidth relationship of Fourier transforms, $\mathrm{g}(t)$ must have a duration $\Delta\mathrm{T}_g$ bound by (2.50). In the case where $\mathrm{g}(t)$ is unimodal (pulsive) and somewhat smooth over its duration, the author wonders whether $\Delta\mathrm{T}_g$ (given either by (2.50), or by $\mathrm{g}(t)$ directly) might not give the experimenter a material-dependent absolute time scale to help determine the minimum useful time step Δt at which to sample $\mathrm{V}(t)$.

The argument is that, regardless of the position z at which $\mathcal{Q}(z)$ is desired, (2.40) recommends first convolving with $\mathrm{g}(t)$. If $\mathrm{g}(t)$ is a smooth pulse the result of convolving $\mathrm{g}(t)$ with $\mathcal{P}(t)$ will be to smooth out temporal variations in $\mathcal{P}(t)$ that occur on a time scale smaller that $\Delta \mathrm{T}_g$. Therefore, given a smooth unimodal $\mathrm{g}(t)$, it does not make sense to sample $\mathrm{V}(t)$ with a time step Δt that is 'too small' a fraction of $\Delta \mathrm{T}_g$.

2.5.5 Conjugate Symmetry

Note that because both $\mathcal{Q}(z)$ and $\mathrm{H}(z,t)$ are assumed real (as they must be if they correspond to physical quantities) it follows that $\underline{\mathcal{K}}(f)$, $\underline{H}(z,f)$, and $\underline{\mathcal{P}}(f)$ must have conjugate symmetry; meaning that, for example,

$$\underline{\mathcal{P}}(-f) = \underline{\mathcal{P}}^*(f) \tag{2.51}$$

where the $*$ denotes complex conjugation. It is possible to use this information to rewrite (2.35) in unilateral form

$$\mathcal{Q}(z) = 2 \int_0^\infty \Re_e \left\{ \frac{\underline{\mathcal{P}}(f)}{\underline{C}_g(f)} \exp(z\, \underline{\mathcal{K}}(f)) \right\} df \tag{2.52}$$

The recoveries performed in this thesis utilize a discretized form of (2.52) which is implemented via the Fast Fourier Transform (FFT). See equation (4.60).

2.5.6 Delay-Only Materials And The Fourier Transform

A Bromwich material has $\alpha(f) = \alpha_b$ and $c(f) = c_b$, where α_b is a non-negative constant and c_b is a positive constant (see section 6.1.1). A delay-only material is a Bromwich material which has $\alpha_b = 0$. Using (2.37), it follows that the delay-only $\underline{\mathcal{K}}(f)$, denoted $\underline{\mathcal{K}}_d(f)$, is given by

$$\underline{\mathcal{K}}_d(f) = \mathrm{j}\, 2\pi f / c_d \tag{2.53}$$

where the subscript 'b' for Bromwich on c_b has been replaced with a 'd' for delay-only (and dominant). Substituting $\underline{\mathcal{K}}_d(f)$ into (2.30) and (2.31) yields

$$\underline{\mathcal{P}}(f) = \int_0^\infty \mathcal{Q}(z)\, \exp(-\mathrm{j}\, 2\pi f z / c_d)\, dz \tag{2.54}$$

and

$$\mathcal{Q}(z) = \frac{1}{c_d} \int_{-\infty}^\infty \underline{\mathcal{P}}(f)\ \exp(\mathrm{j}\, 2\pi f z / c_d)\, df \tag{2.55}$$

Introducing time t via

$$t(z) = \frac{z}{c_d} \tag{2.56}$$

maps (2.54) and (2.55) into

$$\underline{\mathcal{P}}(f) = \int_0^\infty [c_d \mathcal{Q}(tc_d)] \ \exp(-\mathrm{j}\ 2\pi f t)\ dt \tag{2.57}$$

and

$$c_d \mathcal{Q}(tc_d) = \int_{-\infty}^\infty \underline{\mathcal{P}}(f)\ \exp(\mathrm{j}\ 2\pi f t)\ df \tag{2.58}$$

so that it becomes clear that $c_d \mathcal{Q}(t\ c_d)$ and $\underline{\mathcal{P}}(f)$ are Fourier transforms of each other.

The Fourier transform is the special case of the CLDP transforms which corresponds to a lossless, dispersionless (delay-only) materials. Note that the version of the Fourier analysis equation given above is unilateral, whereas the Fourier transform is conventionally defined bilaterally.

Although it is clearly possible to extend this version of the Fourier transform to include negative values of z, this thesis does not require this extension and it is unclear whether the transforms associated with lossy materials can sensibly be extended in this manner.

Further, as chapter 6 will show, assuming $\mathcal{Q}(z)$ is causal (and has a Fourier transform) ensures the right half plane analyticity of the Laplace transform of $\mathcal{Q}(z)$. This is a clear advantage insofar as mathematical tractability is concerned, and so this thesis' versions of the forward CLDP transforms will continue to be defined unilaterally.

2.5.7 Delay-Only Materials And The Dominant Recovery

If $c_d \mathcal{Q}(t\ c_d)$ and $\underline{\mathcal{P}}(f)$ are Fourier transforms of each other, it follows that

$$\mathcal{P}(t) = c_d \mathcal{Q}(t\ c_d) \tag{2.59}$$

Rewriting (2.56) as

$$z(t) = t\ c_d \tag{2.60}$$

and inserting into (2.59) yields

$$\mathcal{Q}(z) = \frac{1}{c_d} \mathcal{P}(\frac{z}{c_d}) \tag{2.61}$$

This expression for $\mathcal{Q}(z)$ is clearly just the dominant recovery $\mathrm{R}_d(z)$ given by (2.27). It is in this sense that the dominant recovery is said to correspond to the assumption of a lossless, dispersionless material.

2.6 The Darrell Property of the Inverse CLDP IE

Referring back to section 2.5, the CLDP transform relations

$$\mathcal{Q}(z) \quad \overset{\mathcal{K}}{\Longleftrightarrow} \quad \underline{\mathcal{P}}(f) \tag{2.62}$$

state that, if the propagation coefficient $\underline{\mathcal{K}}(f)$ corresponds to a causal $\mathrm{H}(z,t)$, and if $\mathcal{Q}(z)$ is real, causal, Fourier transformable *and* satisfies the CLDP criterion (2.32), then the $\underline{\mathcal{P}}(f)$ defined by

$$\underline{\mathcal{P}}(f) = \int_0^\infty \mathcal{Q}(z)\ \exp(-z\ \underline{\mathcal{K}}(f))\ dz \tag{2.63}$$

and the $\mathcal{Q}(z)$ given by

$$\mathcal{Q}(z) = \int_{-\infty}^{\infty} \underline{\mathcal{P}}(f)\ [\frac{1}{\mathrm{j}2\pi}\frac{d\ \underline{\mathcal{K}}(f)}{df}]\ \exp(z\ \underline{\mathcal{K}}(f))\ df \tag{2.64}$$

are CLDP transforms of each other.

The Darrell property of the proposed inverse CLDP IE answers the following question: if a pure but strictly bandlimited version $\mathcal{P}(f_m, f)$ of $\mathcal{P}(f)$ were inserted into (2.64), what would the 'bandlimited recovery' $\mathrm{R}(f_m, z)$ be? Sections 7.6 and 7.7 show that, if

$$\mathcal{P}(f_m, f) \ \equiv\ \mathcal{P}(f)\ [\mathrm{U}(f - f_m) - \mathrm{U}(f + f_m)] \tag{2.65}$$

where $\mathrm{U}(f)$ is the Heaviside step function, then

$$\mathrm{R}(f_m, z) \equiv \int_{-\infty}^{\infty} \underline{\mathcal{P}}(f_m, f)\ [\frac{1}{\mathrm{j}2\pi}\frac{d\ \underline{\mathcal{K}}(f)}{df}]\ \exp(z\ \underline{\mathcal{K}}(f))\ df$$

$$= \int_{-f_m}^{f_m} \underline{\mathcal{P}}(f)\ [\frac{1}{\mathrm{j}2\pi}\frac{d\ \underline{\mathcal{K}}(f)}{df}]\ \exp(z\ \underline{\mathcal{K}}(f))\ df \tag{2.66}$$

$$= \mathcal{Q}(z) * \mathrm{D}(f_m, z) \tag{2.67}$$

where the $*$ denotes spatial convolution, $\mathcal{Q}(z)$ is assumed causal, and "the Darrell" $\mathrm{D}(f_m, z)$ is given by

$$\mathrm{D}(f_m, z) \equiv \int_{-f_m}^{f_m} \left[\frac{1}{\mathrm{j}2\pi} \frac{d\,\underline{\mathcal{K}}(f)}{df}\right] \exp(z\,\underline{\mathcal{K}}(f))\,df \tag{2.68}$$

$$= \frac{\Im_m\{\exp(z\,\underline{\mathcal{K}}(f_m))\}}{\pi z} \tag{2.69}$$

$$= \exp(z\,\alpha(f_m))\,\frac{\sin(2\pi f_m z/c(f_m))}{\pi z} \tag{2.70}$$

The result (2.70) is almost alarming in its simplicity: regardless of $\alpha(f)$ and $c(f)$'s excursions for $f < f_m$, the Darrell depends only upon $f_m, \alpha(f_m)$ and $c(f_m)$.

2.6.1 The Darrell As Generalized Gibbs-Dirichlet Kernel

Siebert [53] points out that Gibbs' phenomenon (which manifests itself when a signal $\mathrm{x}(t)$ is forward Fourier transformed into $\underline{x}(f)$, abruptly bandlimited at f_m, then inverse Fourier transformed into $\tilde{\mathrm{x}}(f_m, t)$) can be described through convolution with a sinc function (*aka* Dirichlet's kernel)

$$\tilde{\mathrm{x}}(f_m, t) = \mathrm{x}(t) * \frac{\sin(2\pi f_m t)}{\pi t} \tag{2.71}$$

Compare this result with the Darrell property (2.67)

$$\mathrm{R}(f_m, z) = \mathcal{Q}(z) * \mathrm{D}(f_m, z) \tag{2.72}$$

$$= \mathcal{Q}(z) * \left[\exp(z\,\alpha(f_m))\,\frac{\sin(2\pi f_m z/c(f_m))}{\pi z}\right] \tag{2.73}$$

Replacing the z in (2.73) with t via

$$t = z/c(f_m) \tag{2.74}$$

yields

$$\tilde{\mathrm{x}}'(f_m, t) = \mathrm{x}'(t) * \left[\exp(\alpha(f_m)c(f_m)\,t)\,\frac{\sin(2\pi f_m t)}{\pi t}\right] \tag{2.75}$$

where

$$\tilde{\mathrm{x}}'(f_m, t) \equiv \mathrm{R}(f_m, c(f_m)\, t) \qquad \text{and} \qquad \mathrm{x}'(t) \equiv \frac{\mathcal{Q}(c(f_m)\, t)}{c(f_m)} \tag{2.76}$$

so that (comparing (2.71) and (2.75)) it is clear that the Darrell operates as a generalized Gibbs-Dirichlet kernel.

Chapter 3

Loss, Dispersion, Deconvolution

This chapter's first section (*Loss And Dispersion*) derives the expression (3.2) for the transfer function $\underline{H}(l, f)$ of a thickness l slab of material in terms of the propagation coefficient $\underline{\mathcal{K}}(f)$ via the line of reasoning used by Staelin *et al* [21]. Appendix A derives this same result in a shorthand manner that emphasizes the importance of the frequency domain to solution of the wave equation.

3.1 Loss And Dispersion

The effects of attenuation and dispersion upon a time-dependent signal $\mathrm{s}(t)$ propagating through a linear medium have long been understood and explained via the frequency domain [21, 22]. With l denoting the propagation length through the medium, $\underline{s}(f)$ denoting the Fourier transform of $\mathrm{s}(t)$, $\alpha(f)$ and $c(f)$ denoting the frequency-dependent attenuation coefficient and phase velocity, respectively, of waves propagating through the medium, and with $\underline{s}'(f)$ denoting the Fourier transform of the output signal $\mathrm{s}'(t)$, the result is

$$\underline{s}'(f) = \underline{H}(l, f)\, \underline{s}(f) \tag{3.1}$$

where the thickness-l dependent propagation transfer function $\underline{H}(l, f)$ is given by

$$\underline{H}(l, f) = \exp(-l\, \underline{\mathcal{K}}(f)) \tag{3.2}$$

and the complex propagation coefficient $\underline{\mathcal{K}}(f)$ is given by

$$\underline{\mathcal{K}}(f) = \alpha(f) + \mathrm{j}\, 2\pi f / c(f) \tag{3.3}$$

Appendix A shows that the $\underline{\mathcal{K}}(f)$ used here is related to the familiar complex wavenumber $\underline{k}(f)$ via

$$\underline{K}(f) = \mathrm{j}\,\underline{k}(f) \tag{3.4}$$

The wavenumber $\underline{k}$ is often used to describe the evolution of single-frequency, one-dimensional solutions $\mathrm{g}(z,t)$ to the homogeneous wave equation

$$\frac{\partial^2}{\partial z^2}\mathrm{g}(z,t) - c^{-2}\frac{\partial^2}{\partial t^2}\mathrm{g}(z,t) = 0 \tag{3.5}$$

which propagate with the phase velocity c. According to the time-harmonic convention, the wavenumber $\underline{k}$ describes propagating solutions via

$$\mathrm{g}(z,t) = \Re\{\underline{g}_o e^{-j\underline{k}z} e^{j2\pi ft}\} = |\underline{g}_o| e^{\mathrm{k}_i z}\cos(2\pi ft - \mathrm{k}_r z + \arg(\underline{g}_o)) \tag{3.6}$$

where $\underline{g}_o$ is a complex constant given in polar form by

$$\underline{g}_o = |\underline{g}_o|\exp(\,\mathrm{j}\,\langle \underline{g}_o \rangle\,) \tag{3.7}$$

and $\underline{k}$ is a complex constant given in cartesian form by

$$\underline{k} = \mathrm{k}_r + \mathrm{j}\,\mathrm{k}_i \tag{3.8}$$

Although the time-harmonic convention pertains only to waves of a single frequency, there is no reason that the Fourier transform may not be invoked to add up the effects of a frequency-dependent $\underline{k}(f)$, so that with

$$\underline{k}(f) = \mathrm{k}_r(f) + \mathrm{j}\,\mathrm{k}_i(f) \tag{3.9}$$

the result (3.6) becomes

$$\mathrm{g}(z,t) = \int_{-\infty}^{\infty} \underline{g}(0,f)\ \exp(\mathrm{j}2\pi ft)\ \exp(-\mathrm{j}z\underline{k}(f))df \tag{3.10}$$

where

$$\underline{g}(0,f) = \int_{-\infty}^{\infty} \mathrm{g}(0,t)\exp(-\mathrm{j}2\pi ft)df \tag{3.11}$$

Inverse Fourier transforming (3.10) yields

$$\underline{g}(z,f) = \underline{g}(0,f)\exp(-\mathrm{j}z\underline{k}(f)) \tag{3.12}$$

so that equations (3.1) through (3.4) are verified with the understanding that

$$c(f) = 2\pi f/\mathrm{k}_r(f) \tag{3.13}$$
$$\alpha(f) = -\mathrm{k}_i(f) \tag{3.14}$$

and

$$\mathrm{s}(t) = \mathrm{g}(0,t) \tag{3.15}$$
$$\mathrm{s}'(t) = \mathrm{g}(l,t) \tag{3.16}$$

This analysis makes it clear that α corresponds most directly to the attenuation of the amplitude of the wave, not its power. The alternative notation $\underline{\mathcal{K}}(f)$ rather than $\mathrm{j}\ \underline{k}(f)$ has been adopted so that the parallel between the PESAW integral equation and the Laplace transform is made most clear (see section 7.1).

3.2 Deconvolution

A common problem related to the PESAW problem is that of recovering $\mathrm{s}(t)$ given $\mathrm{s}'(t)$ and $\underline{H}(l,f)$. This problem is known as deconvolution, which is seen to be a sensible term when (3.1) is inverse Fourier transformed, and the Fourier convolution theorem is applied:

$$\mathrm{s}'(t) = \mathrm{H}(l,t) * \mathrm{s}(t) \tag{3.17}$$

In (3.17), the '*' denotes convolution, and $\mathrm{H}(l,t)$ is the material's thickness-l dependent impulse response function:

$$\mathrm{H}(l,t) \overset{\mathcal{F}}{\Longleftrightarrow} \underline{H}(l,f) = \exp(-l\alpha(f))\ \exp(-j2\pi f l/c(f)) \tag{3.18}$$

This problem arises in the field of acoustic emission, where a pulse generated by a fracture within some material is distorted as it travels to the surface [23, 24], and it arises whenever GHz-range waveforms are acquired electronically through even a short metallic cable, because then skin-effect losses occurring within the cable distort the signal as it passes through the cable (see [25, 26], and section 6.5.1).

The deconvolution problem is known to be ill-posed [27], meaning that even small uncertainties in either $\mathrm{s}'(t)$ or $\underline{H}(l,f)$ can lead to large changes in the estimate $\tilde{\mathrm{s}}(t)$

to $s(t)$ gleaned from $s'(t)$ and $\underline{H}(l,f)$. The ill-posedness of this problem can be seen directly by stating the common frequency domain method of deconvolution

$$\tilde{s}(t) \overset{\mathcal{F}}{\Longleftrightarrow} \underline{\tilde{s}}(f) = \frac{\underline{s'}(f)}{\underline{H}(l,f)} \tag{3.19}$$

$$= \underline{s'}(f)\underline{H}(-l,f) \tag{3.20}$$

$$= \underline{s'}(f)\exp(l\alpha(f))\exp(j2\pi f/c(f)) \tag{3.21}$$

If the product $l\alpha(f)$ is large for some frequencies f_i, even a small positive deviation in either $|\underline{s'}(f_i)|$ or $l\alpha(f_i)$ will lead to a large deviation in $\tilde{s}(t)$. The ill-posedness of the deconvolution operation does not necessarily imply that a meaningful estimate $\tilde{s}(t)$ to $s(t)$ cannot be determined from $s'(t)$ and $\underline{H}(l,f)$.

The science concerned with selecting meaningful solutions to ill-posed IEs is called regularization. Because the convolution IE (and the CLDP IEs) are first-kind Fredholm IEs, Stenger's pronouncement [39] that "Tikhonov regularization has proved to be a powerful practical tool to deal with Fredholm IEs of the first kind, and with other ill-posed linear or nonlinear integral equations of the first kind" suggests that an outline of Tikhonov regularization is in place here.

In this section's context, Tikhonov [40] and Stenger suggest that (3.19) be regularized by first multiplying the numerator and denominator by the complex conjugate $\underline{H}^*(l,f)$ of $\underline{H}(l,f)$, then adding a small positive number τ to the new denominator so that the Tikhonov-regularized recovery is given by

$$\tilde{s}_\tau(t) \overset{\mathcal{F}}{\Longleftrightarrow} \underline{\tilde{s}}_\tau(f) \equiv \frac{\underline{s'}(f)\,\underline{H}^*(l,f)}{\tau + |\underline{H}(l,f)|^2} \tag{3.22}$$

The basic idea is that the inclusion of τ in the denominator of (3.22) lessens the degree of spurious over-amplification of $\underline{s'}(f)$ consonant with $|\underline{H}(l,f)|$'s signal to noise ratio dropping dangerously low.

It may even prove sensible to modify (3.22) by allowing τ to be a function of frequency. An f dependent τ allows inclusion of *a priori* knowledge about where $|\underline{H}(l,f)|$'s signal to noise ratio is likely to drop. In another context (section 4.14.2), it may prove useful to allow τ to be a function of position z (as well as frequency f). This z (and f) dependent τ could be used to execute a SD-filtered alternative to the SD BLG-filtered regularization procedure investigated in this thesis.

More generally, the ill-posedness of this frequency domain deconvolution scheme is often satisfactorily managed by introducing some filter $G(f)$ into (3.21) which will suppress the inclusion of the 'dangerous' frequencies f_i while minimizing the impact of $G(f)$ in the case where the data is trustworthy. That is, the new estimate is given by

$$\tilde{s}(t) \overset{\mathcal{F}}{\Longleftrightarrow} \underline{\tilde{s}}(f) = G(f)\,\underline{s'}(f)\,\exp(l\alpha(f))\exp(j2\pi f/c(f)) \tag{3.23}$$

The task of finding a suitable $G(f)$ for a particular problem requires knowledge of the expected properties of the material and the expected noise in the received waveform. This task is difficult, and there is a large body of literature pertaining to it. [27, 28].

One particular $G(f)$ known as Blackman's Lucky Guess (BLG) [29] has proved useful in analyzing polymeric data, where $\alpha(f)$ increases with f. The BLG filter $B(f_c, f)$ (see appendix B) does a remarkable job of suppressing high frequencies while minimizing the time-domain 'ripple' commensurate with lowpass filtering. High frequencies need to be suppressed where $\alpha(f)$ increases with frequency because, in this situation, it is at high frequencies that the 'boosting term' $\exp(l\alpha(f))$ becomes large while the signal-to-noise ratio drops, so that $|\underline{s}'(f)|$ becomes uncertain. BLG filtering will be this thesis' regularization workhorse; Tikhonov regularization is mentioned for completeness.

The impact of attenuation and dispersion for millimeter-thick slabs of polymer has been noted by PEA researchers Li *et al* [20], who point out that "the acoustic [signal] is obviously distorted as it propagates through the thick polymer." It is important to note that the problem faced by PESAW researchers is greater than that posed by convolution alone. True, the voltage signal produced by the pressure-to-voltage transducer must be deconvolved with respect to the transducer's impulse response function to find an estimate for the plate pressure signal.

But this is a small problem compared to the fact that the plate pressure signal is comprised of a (generally infinite) sum of pressure signals, each one originating from a different point inside the dielectric and, therefore, each one being attenuated and dispersed by a different amount.

The deconvolution problem asks: "given the received signal, and given the properties of the linear, time-invariant system which transmitted the signal, how to find an acceptable estimate for the signal that was sent?" The PESAW problem asks: "given the received signal, the transducer's impulse response function, the applied voltage versus time waveform, and the shape and properties of the material, how to find an acceptable estimate for the distributed source?"

The deconvolution problem seeks to map a signal to a signal; the PESAW problem seeks to map a signal to a waveform under the assumption that the distributed sources emitted simultaneously. As the next section will show, the mathematical relationship between the charge distribution $Q(z)$ inside a dielectric and the plate pressure versus time waveform $\mathcal{P}(t)$ which it generates when stimulated by a quasistatic field is a CLDP IE.

It is worth pausing here to point out that this thesis' analyses assume only one dimension of variation in the charge distribution. For a slab geometry the charge distribution is assumed to depend only upon the radial distance from the slab's surface, not upon either of the other two orthogonal directions. For a cable geometry the charge distribution is assumed to depend only upon the distance from the cable's surface, not upon the distance along the axis of the cable nor upon the rotation angle. Therefore the positive variable 'z' in the following discussion will signify a generic position (surface) inside the dielectric which is a distance z from the proximal capacitor plate surface to

which the pressure-to-voltage transducer is attached.

Chapter 4

The PESAW Recovery

The *General Introduction* includes a lay introduction to the Pulsed Electrically Stimulated Acoustic Wave (PESAW) method of charge profiling in dielectrics. The *Technical Introduction* analyzes the PESAW experiment insofar as needed to derive the CLDP-PESAW IE.

The objective of this chapter is to describe how specifically to perform a PESAW recovery, which includes both the recovery of the required approximate material model $\{\tilde{\alpha}(f), \tilde{c}(f)\}$ and the application of this model to the ultimate goal of recovering the approximate charge waveform $\tilde{\mathrm{Q}}(z)$.

This chapter therefore addresses some practical PESAW issues, such as:

1. how to attempt to ensure the validity of the CLDP IE model of the PESAW forward problem?
2. how to extract the transducer's impulse response function from measured data?
3. how to extract propagation parameters $\alpha(f)$ and $c(f)$ from measured data?
4. what are the experimental requirements that determine whether it will be possible to enact items 2 and 3?
5. given a measured signal, and the results of items 2 and 3, what is the specific algorithm for generating $\tilde{\mathrm{Q}}(z)$?

4.1 Bulk Forces And Plate Forces

The PESAW experiment proceeds by applying a pulsed voltage between the two plates of a parallel plate capacitor containing the dielectric under test (see figure 1.1). Neglecting fringing and succumbing to the quasistatic approximation (see section 4.6), the applied voltage pulse $\mathrm{V}_a(t)$ creates a $-z$ directed, pulsed excitation electric field

$$\mathrm{E}(t) = \frac{\mathrm{V}_a(t)}{l} \tag{4.1}$$

inside the dielectric. The field $\mathrm{E}(t)$ is called the excitation electric field to distinguish it from the static field arising from the static charge q_1. This static field produces no time dependent signal in the measurement apparatus, and so is not included in this analysis. The field $\mathrm{E}(t)$ will therefore be referred to simply as 'the electric field.'

When the electric field interacts with the charge-per-area q_1 at position z_1 inside the capacitor's dielectric it exerts a $-z$ directed force-per-area (pressure)

$$\mathrm{F}_1(t) = \frac{q_1\ \mathrm{V}_a(t)}{l} \tag{4.2}$$

at z_1 according to the Coulomb force law (assuming $q_1 V_a(t)$ is a positive polarity pulse). This pressure signal launches a wave from z_1 that travels toward, and is detected by, the transducer attached to the proximal capacitor plate. The *Technical Introduction* analyzes the more general case of a generic distributed charge $\mathrm{Q}(z)$; this chapter achieves its goals by considering only the special case $\mathrm{Q}(z) = q_1\delta(z - z_1)$ depicted in figure 1.1.

The applied voltage $\mathrm{V}_a(t)$ also generates time dependent surface charges $\mathrm{Q}_-(t)$ and $\mathrm{Q}_+(t)$ at the proximal and distal capacitor plates respectively. According to the boundary condition associated with Gauss' law [80],

$$-\mathrm{Q}_-(t) = \mathrm{Q}_+(t) = \frac{\epsilon \mathrm{V}_a(t)}{l} \tag{4.3}$$

where ϵ is the dielectric's permittivity.

These charges also produce forces. Regardless of the polarity of $\mathrm{V}_a(t)$, the force-per-area or pressure exerted by each capacitor plate is always *in*, towards the opposing plate. The positive charges on one plate and the negative charges on the other plate pull towards each other. The pressure $\mathrm{F}_p(t)$ exerted by each plate can be calculated via the principle of virtual work [81, 82]. The result is

$$\mathrm{F}_p(t) = \frac{1}{2}\ \mathrm{Q}_+(t)\ \mathrm{E}(t) = \frac{\epsilon\ \mathrm{V}_a^2(t)}{2l^2} \tag{4.4}$$

Feynman [82] points out that the factor $1/2$ relating the 'expected' Coulomb-force result $\mathrm{Q}_+(t)\ \mathrm{E}(t)$ to the $\mathrm{F}_p(t)$ given above can be understood by thinking of the surface charges $\mathrm{Q}_-(t)$ and $\mathrm{Q}_+(t)$ as having finite thickness Δ.

Focussing on the positive charge layer $\mathrm{Q}_+(t)$ on the surface of the distal capacitor plate, the electric field in the charge layer decreases linearly from $\mathrm{E}(t)$ at $z = l - \Delta$ down to zero at $z = l$. The average (i.e: effective) value of the field in the charge layer $\mathrm{Q}_+(t)$ will therefore be $\mathrm{E}(t)/2$.

4.2 Bulk And Plate Responses

With $\mathrm{H}(z,t)$ denoting the position z dependent material impulse response function introduced in chapter 2, and with $\mathrm{H}_T(t)$ denoting the transducer's impulse response function, the measured voltage $\mathrm{V}(t)$ in figure 1.1 will be given by

$$\mathrm{V}(t) = \mathrm{H}_T(t) * \Big[\overbrace{\mathrm{F}_p(t) * [\, -\mathrm{H}(0,t) + 2\,\mathrm{H}(l,t)]}^{\text{plates}} + \overbrace{\mathrm{F}_1(t) \;*\; \mathrm{H}(z_1,t)}^{\text{bulk}} \Big]$$

$$= \mathrm{H}_T(t) * \Big[\frac{\epsilon\, \mathrm{V}_a^2(t)}{2l^2} * [\, \underbrace{-\mathrm{H}(0,t)}_{\text{proximal}} + \underbrace{2\,\mathrm{H}(l,t)}_{\text{distal}} \,] + \frac{q_1}{l}\, \mathrm{V}_a(t) \;*\; \mathrm{H}(z_1,t) \Big] \qquad (4.5)$$

The proximal plate response kernel $-\mathrm{H}(0,t)$ comes with a minus sign because $\mathrm{F}_p(t)$ causes the proximal plate to deflect towards positive z. This causes a negative pressure (rarefaction) wave to propagate directly into the transducer. It also causes a positive pressure (compression) wave to propagate toward the distal plate. This positive pressure wave will eventually reflect off the distal plate, and return towards the proximal plate.

But this reflected wave will arrive after all the unreflected waves (from the proximal plate, bulk charge, and distal plate) have arrived. The present analysis is only concerned with the unreflected waves. The reflected waves will be neglected in the service of simplicity under the (hopeful) assumption that the contribution of these reflected waves to the measured signal will be temporally resolvable from the contribution of the unreflected waves.

The zero in $-\mathrm{H}(0,t)$ reflects the fact that the pressure signal $\mathrm{F}_p(t)$ exerted by the proximal plate does not pass through any of the dielectric material before it enters the transducer. Note that $\mathrm{H}(0,t) = \delta(t)$ because $\underline{H}(z,f) = \exp(-z\,\underline{K}(f))$ so $\underline{H}(0,f) = 1$ and $\mathcal{F}^{-1}\{1\} = \delta(t)$. In the next expression of (4.5), $\mathrm{H}(0,t)$ will be replaced by $\delta(t)$.

Whereas the proximal plate response kernel takes the form -$\mathrm{H}(0,t)$, the distal plate response kernel takes the form 2 $\mathrm{H}(l,t)$. The prefactor to the proximal plate response kernel is positive because the plate pressure $\mathrm{F}_p(t)$ causes the distal plate to deflect towards negative z, launching a positive pressure wave toward the transducer at the opposite side of the dielectric sample. The l in 2 $\mathrm{H}(l,t)$ is the width of the dielectric sample through which this wave must pass.

The factor 2 comes via the assumption that whereas the $\mathrm{F}_p(t)$-generated deflection of the proximal plate is equally restrained by *both* the transducer to its left and the dielectric to its right, the $\mathrm{F}_p(t)$-generated deflection of the distal plate is restrained *only* by the dielectric to its left.

The region to the right of the distal plate is assumed to offer no restriction to the deflection of the distal plate. It is assumed to be incapable of supporting a wave so no energy can propagate in that direction.

Because the magnitude of the force $F_p(t)$ applied to both plates differs only in direction ($+z$ at the proximal plate, $-z$ at the distal plate) and because the proximal plate is twice as restrained as the distal plate, it follows from Hooke's law F = - K X [83] that the amplitude of the proximal plate's deflection will be half the amplitude of the distal plate's deflection (and will be the same as what the bulk deflection would be if $F_p(t)$ were somehow exerted at some plane in the bulk).

Stated another way, with $\underline{Z}_T$ denoting the acoustic impedence of the $z < 0$ (transducer) material, with $\underline{Z}_d$ denoting the acoustic impedence of the $0 < z < l$ (dielectric) material, and with $\underline{Z}_u$ denoting the acoustic impedence of the $z > l$ (unrestrictive) material, the factor of two results from the assumption that

$$\underline{Z}_T \cong \underline{Z}_d \gg \underline{Z}_u \tag{4.6}$$

Because the reflection coefficient Γ_{ht} for waves propagating from region here$_h$ to region there$_t$ is [103]

$$\Gamma_{ht} = \frac{\underline{Z}_t - \underline{Z}_h}{\underline{Z}_t + \underline{Z}_h} \tag{4.7}$$

the reflection coefficient vanishes for waves propagating through the proximal plate whereas the reflection coefficient is -1 for waves attempting to pass from the dielectric to the unrestrictive region.

According to this impedence-based analysis, the doubling of the distal plate response can be thought of as being the sum of the original, unit-sized, positive polarity, $-z$ directed pulse and a virtual, unit-sized, negative polarity, $+z$ directed pulse which is immediately reflected back in the $-z$ direction by $\Gamma_{du} = -1$.

At first glance, using this impedence based analysis may seem like killing a fly with a golden brick – the previous 'fly-swatter' analysis did not require the concept of impedence, nor the concept of reflection, nor the concept of a 'virtual pulse.' However, the impedence based analysis may readily by extended to situations where (4.6) does not hold even approximately (the terms may even be complex and frequency dependent), whereas the fly-swatter analysis is tractable only for the special case considered here.

This result concerning the factor 2 is consistent with the realization that whereas pressure pulses exerted at planes in the region $z < l$ launch equal-amplitude, opposite-polarity pulses in both directions, pressure pulses exerted at $z = l$ can launch only one double-strength wave in the $-z$ direction.

The bulk charge response kernel $\sim q_1$ H(z_1, t). If $q_1 = 0$, there will be no bulk response. The strength of the bulk response is modulated by the strength of this charge layer via the Coulomb force law. The quantity z_1 enters because the charge layer q_1 is at position z_1. Therefore the pressure wave generated by this charge layer in the bulk must pass through a thickness-z_1 slab of dielectric before it enters the transducer.

4.3 The Applied Voltage Signal $V_a(t)$

In practice, $V_a(t)$ is often comprised of a 'large' positive DC voltage V_o and a 'small' pulsed voltage $v_p(t)$ which is zero everywhere except for times t satisfying $|t| \leq \mathcal{T}_p/2$ for which $v_p(t) > 0$. Either the sum of V_o and $v_p(t)$, or the negative of their sum, is applied to the capacitor. That is,

$$V_a(t) = \pm [\, V_o + v_p(t) \,] \tag{4.8}$$

where

$$V_o \quad \gg \quad v_p(t) \quad \text{for all times } t \tag{4.9}$$

so that $V_a(t)$ is either always negative or always positive. Neglecting DC terms by assuming the transducer does not respond to a DC pressure, and neglecting 'small' terms via (4.9),

$$V_a(t) = \pm[\, V_o + v_p(t) \,] \quad \longrightarrow \quad \pm v_p(t) \tag{4.10}$$

and

$$V_a^2(t) = [\pm[\, V_o + v_p(t) \,]]^2 = V_o^2 + 2\, V_o\, v_p(t) + v_p^2(t) \quad \longrightarrow \quad 2\, V_o\, v_p(t) \tag{4.11}$$

Using these approximations, and adding a $\pm$ subscript to the $V(t)$ in (4.5) to account for the two possible polarities of $V_a(t)$,

$$V_\pm(t) = H_e(t) * \mathcal{P}_\pm(t) \tag{4.12}$$

where

$$\mathcal{P}_\pm(t) \equiv \underbrace{-\delta(t)}_{\text{proximal}} \pm \underbrace{\frac{q_1}{q_p}\, H(z_1, t)}_{\text{bulk}} + \underbrace{2\, H(l, t)}_{\text{distal}} \tag{4.13}$$

Note that

$$q_p \equiv \frac{\epsilon\, V_o}{l} \tag{4.14}$$

is the magnitude of the DC surface charges on each plate due to V_o, and

$$\mathrm{H}_e(t) \equiv \frac{q_p}{l}\ \mathrm{H}_T(t) * v_p(t) \tag{4.15}$$

is called the experimental impulse response. The quantity q_p is always positive because V_o is defined as positive even when $\mathrm{V}_a(t)$ has negative polarity (see (4.8)).

The $\pm$ in $\mathrm{V}_{\pm}(t)$ only enters into the bulk response component of $\mathcal{P}_{\pm}(t)$ because whereas $v_p(t)$ always acts to increase the inward pressure $\mathrm{F}_p(t)$ exerted by the plates, the polarity of the excitation force acting on charges in the bulk depends upon the polarity of the applied voltage $\mathrm{V}_a(t)$ (and the polarity of q_1).

Whereas the plate force $\mathrm{F}_p(t) \sim \mathrm{V}_a^2(t)$, the bulk force $\mathrm{F}_1(t) \sim \mathrm{V}_a(t)$. This difference arises from the fact that whereas the strength of charges in the bulk is independent of time, the strength of the plate charges vary as $\mathrm{V}_a(t)$.

4.4 Resolving The Two Plate Responses

As a practical matter, the transducer impulse response $\mathrm{H}_T(t)$ will have some minimum temporal width $\mathcal{T}_T \sim f_T^{-1}$ corresponding to the transducer's assumedly finite bandwidth f_T [58]. Because the experimental impulse response $\mathrm{H}_e(t)$ is the convolution of $\mathrm{H}_T(t)$ and $v_p(t)$ (which has width $\mathcal{T}_p$), $\mathrm{H}_e(t)$ will also have some finite width $\mathcal{T}_e$ where [89]

$$\mathcal{T}_e \cong \mathcal{T}_T + \mathcal{T}_p \tag{4.16}$$

With $\mathcal{T}_s$ defined as the temporal increase in pulse width (spreading) imposed upon the pressure pulse launched by the distal plate as a result of traversing the thickness l slab of attenuative, dispersive dielectric, and with C defined as the approximate velocity of pressure waves inside the dielectric, if

$$\mathcal{T}_e + \mathcal{T}_s \quad \ll \quad \frac{l}{C} \tag{4.17}$$

then the temporal response signals $\mathrm{V}_p(t)$ and $\mathrm{V}_d(t)$ due to the forces exerted by the proximal and distal capacitor plates, respectively, will be well resolved in the measured signal $\mathrm{V}_{\pm}(t)$. Such a pair of resolvable plate responses are depicted below, in figure 4.1.

Incidentally, equation (6.26) and its discussion on page 99 suggest that the polymeric $\mathcal{T}_s \cong l\ m/\pi$ where $\alpha(f) = mf$. Further, the polymeric $C \sim 2$ mm/μs.

4.5 Resolving The Bulk Response

If, in addition, the position z_1 of the bulk charge q_1 is not too far from the center of the sample (i.e: not too close to either of the capacitor plates) then the temporal

response signal $V_b(t)$ due to the pressure pulse generated by the bulk charge q_1 will also be resolvable from the plate pressure responses if the inequality (4.17) is sufficiently strong. Such a resolvable bulk response is depicted below, in figure 4.1.

4.6 Temporally Impulsive Electric Field

On page 36, the derivation of the PESAW integral equation asks the reader to "Suppose the applied voltage $V_a(t)$ generates an excitation electric field $\bar{E}(z,t)$ within the dielectric which can be modelled as temporally impulsive and spatially distributed."

Despite this statement, there are two reasons why it is physically impossible for the electric field in the capacitor to truly be temporally impulsive. First, Maxwell's equations require time for the electric field inside the capacitor to build up. Electromagnetic waves travel at a maximum velocity $C_{em} \cong 3\ 10^5$ mm/μs. Let the time constant $\mathcal{T}_{em}$ associated with the finite velocity of electromagnetic waves be given by $\mathcal{T}_{em} \equiv l/C_{em}$.

Second, there will be some finite series resistance R acting in the wires and apparatus delivering $v_p(t)$ to the capacitor. The product of this R with the capacitance $\epsilon A/l$ associated with an area A parallel plate capacitor [84] yields the familiar RC time constant $\mathcal{T}_{rc} \equiv R\epsilon A/l$ which limits the celerity of the capacitor's response to $v_p(t)$ [85]. Yet if the width $\mathcal{T}_p$ of the excitation pulse $v_p(t)$ satisfies

$$\mathcal{T}_{rc} + \mathcal{T}_{em} \quad \ll \quad \mathcal{T}_p \quad \ll \quad \mathcal{T}_T \tag{4.18}$$

then the 'smearing' due to the finite response time of the electric field inside the capacitor will be negligible in comparison to the smearing caused by the finite response time of the transducer and $\bar{E}(z,t)$ may reasonably be modelled as the product of a spatially distributed waveform and a temporal impulse as in equation (2.3).

The inequality (4.18) includes what is called the quasistatic approximation [86], which requires only that

$$\mathcal{T}_{em} \quad \ll \quad \mathcal{T}_p \tag{4.19}$$

4.7 A Sample Pressure-Response Signal

Figure 4.1 depicts the pressure response signal for the situation where equation (4.8) and inequalities (4.9), (4.17) and (4.18) hold. This figure corresponds to an experiment where $l = 5$ mm, $z_1 = 2$ mm, $q_p = q_1$, and $V_a(t) > 0$.

Figure 4.1 was produced using the experimental model (4.12) in conjunction with the fast Fourier transform and the standard model of polyethylene (see section 6.2.2). The $H_e(t)$ used was a truncated Gaussian with full width at half maximum = 0.133 μs. The 'pressure units' used in figure 4.1 are somewhat arbitrary because all the terms defining $H_e(t)$ have not been specified.

In the practical PESAW situation, a signal such as that depicted in figure 4.1 might well have units of Volts upon acquisition because these are the units ultimately registered by many digitizing oscilloscopes. The data depicted in figure 4.1 has been rather arbitrarily normalized so that the area of the proximal pulse is -1, which requires that the dimensions of the data (1/time) be the inverse of the dimensions of the data's argument (time). This normalization procedure will be used throughout this thesis.

Later sections of this chapter will show that, despite the arbitrariness of the scale and units of the measured signal, useful information may still be extracted from measured data such as that depicted in figure 4.1.

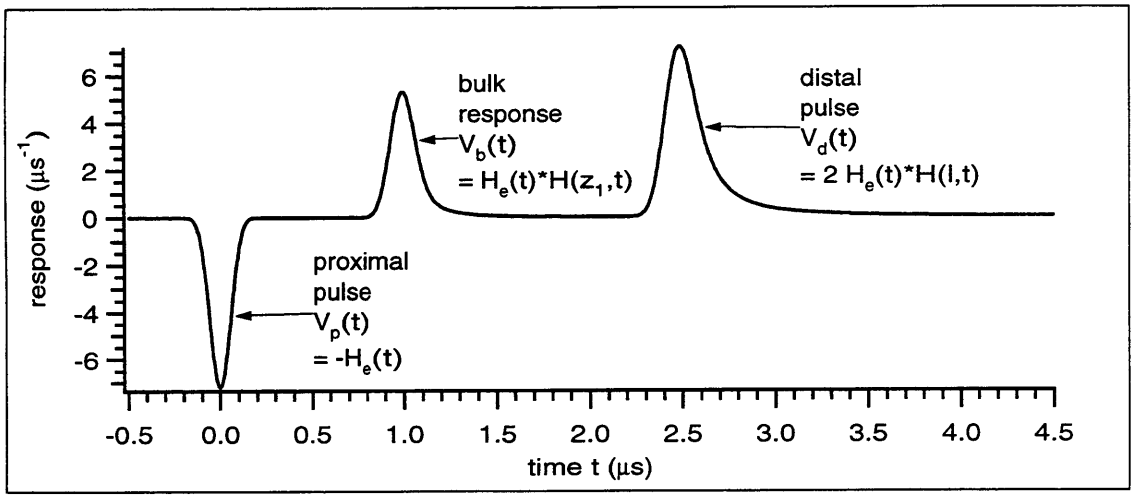

Figure 4.1: Sample PESAW pressure response signal.

4.8 Calibration And Bulk Signals

A pressure signal such as the one depicted in figure 4.1, but which includes only the proximal and distal pulses, is called a calibration signal. The remaining signal, which can only correspond to the charge (or more generally, charges) in the bulk of the dielectric is called the bulk signal.

The Lyons recovery uses the CLDP inverse transform relation defined by the attenuation coefficient $\alpha(f)$ and phase velocity $c(f)$ of plane pressure waves propagating through the bulk of the dielectric. The PESAW recovery requires, in addition, an approximation to the experimental impulse response $\mathrm{H}_e(t)$ so that the measured $\mathrm{V}_{\pm}(t)$ may be deconvolved to yield an estimate for the required response signal $\mathcal{P}_{\pm}(t)$ (see equation (4.12)).

Estimates for $\alpha(f)$, $c(f)$, and $\mathrm{H}_e(t)$ may all be extracted from the calibration signal. The following section will outline this process. For now, note well that the information contained in the calibration signal is of critical import to the PESAW recovery in general.

If the dielectric sample under study is somehow known to have no charge embedded within it then the measured pressure signal is by definition a calibration signal. Therefore, one way to obtain a calibration signal is to apply the PESAW experimental method to a sample that has no embedded charge. Later, after charge has somehow been embedded within the sample, this calibration signal may be subtracted from the pressure response signal obtained from the charged sample. The result is a bulk signal. This method will work well if the initial sample is indeed charge free, and if the experimental conditions ($\mathrm{H}_e(t)$, $\alpha(f)$, $c(f)$, ϵ, l, etc.) do not change significantly during the time between these measurements.

If the bulk charge is somehow known to be located within the sample in such a way that the bulk response is clearly resolvable from both the proximal and distal pulses (as is the case in figure 4.1) then the calibration and bulk signals may simply be separated 'by hand.'

But if the experimenter starts with a sample which is not known to be charge free, or if the known position of the bulk charge is too close to one of the plates, then neither of the two methods mentioned above can be counted on to separate the bulk and calibration signals. One possible method for separating the bulk and calibration signals in this case arises from consideration of equations (4.12) and (4.13). Note that whereas the sign of the bulk response is reversed if the polarity of $\mathrm{V}_a(t)$ is reversed, the plate responses remain unchanged.

It is therefore possible in theory to obtain a measurement $\mathrm{V}_{\pm}(t) \rightarrow \mathrm{V}_{+}(t)$ corresponding to an experiment where $\mathrm{V}_a(t)$ has positive polarity, and another measurement $\mathrm{V}_{\pm}(t) \rightarrow \mathrm{V}_{-}(t)$ corresponding to an experiment where $\mathrm{V}_a(t)$ has negative polarity. According to equation (4.12):

$$\frac{\mathrm{V}_{+}(t) + \mathrm{V}_{-}(t)}{2} = \mathrm{H}_e(t) * \Big[-\delta(t) + 2\,\mathrm{H}(l,t) \Big] \tag{4.20}$$

and

$$\frac{\mathrm{V}_{+}(t) - \mathrm{V}_{-}(t)}{2} = \frac{q_1}{q_p}\,\mathrm{H}_e(t) * \mathrm{H}(z_1,t) \tag{4.21}$$

This procedure should work even in the general case where the bulk charge waveform is continuously distributed throughout the sample, even up to the capacitor plates.

The rather reductive case of a single charge layer in the bulk has been introduced as a pedagogical device to show how bulk charge enters into the experimental model. It is in no way meant to represent a likely physical charge distribution in an actual dielectric sample. Drawing on the results derived in the *Technical Introduction* for a continuous source waveform $\mathcal{Q}(z)$, if the sources are distributed continuously throughout the sample then

$$\frac{\mathrm{V}_{+}(t) - \mathrm{V}_{-}(t)}{2} = \frac{\mathrm{H}_e(t)}{q_p} * \int_0^l \mathcal{Q}(z)\,\mathrm{H}(z,t)\,dz \tag{4.22}$$

This last result is included for completeness only. The proceeding discussion will again return to the simplifying assumption that $\mathcal{Q}(z) \propto q_1\ \delta(z - z_1)$, and will also assume that the experimenter has somehow obtained a calibration signal

$$\mathrm{V}_c(t) = \mathrm{H}_e(t) * \Big[-\delta(t) + 2\ \mathrm{H}(l,t) \Big] \tag{4.23}$$

and a bulk signal

$$\mathrm{V}_b(t) = \frac{q_1}{q_p}\ \mathrm{H}_e(t)\ *\ \mathrm{H}(z_1,t) \tag{4.24}$$

4.9 Sampling Issues

Note well that, depending on how they are obtained, the actual $\mathrm{H}_e(t)$ acting in the calibration signal may not be precisely the same as the $\mathrm{H}_e(t)$ acting in the bulk signal. Further, all of the experimentally determined signals will actually be noisy, sampled versions of the desired signals.

That is, in the practical PESAW context, the desired generic signal $\mathrm{V}(t)$ (which could represent any of a number of desired signals, *eg*: $\mathrm{V}_c(t)$, $\mathrm{V}_b(t)$, $\mathrm{H}_e(t)$) will only be known at a set of points t_n given by $t_n = n\ \Delta t$ where n is an integer satisfying $0 \leq n < N_t$ and N_t is the number of samples obtained. That is, $\mathrm{V}(t)$ will at best be represented by $\mathrm{V}[t_n] = \mathrm{V}(n\ \Delta t)$.

This thesis will use the fast Fourier transform (FFT) to map $\mathrm{V}[t_n]$ into an approximate set of samples $\underline{V}[f_k] \cong \underline{V}(k\ \Delta f)$ of the desired Fourier transform $\underline{V}(f)$ of $\mathrm{V}(t)$. Subsection 4.14.3 will discuss this mapping in more detail. For now, simply note that N_t must be a positive integer power of 2, that $\Delta f = (N_t\ \Delta t)^{-1}$, and that k is an integer satisfying $0 \leq k \leq N_t/2$.

Because the actual number of measured samples obtained from the experimental apparatus is not necessarily a power of 2, it is sometimes necessary to 'pad' the measured data with 'fake data' so that the total number of samples submitted to the FFT is a power of 2. In this thesis, if the last measured sample has value zero then the fake data is taken to be all zeros as well; if the last sample is not zero, then the BLG filter $\mathrm{B}(f_c, f)$ is adapted to the time domain in such a way as to 'connect the dots' in a continuous manner from the last measured sample down to zero at the requisite power of 2. The BLG filter is introduced in appendix B.

The assumption is that, although this procedure will change the DC value $\underline{V}[0]$ of $\mathrm{V}[t_n]$, it will introduce less spurious noise into the higher-frequency components of $\underline{V}[f_k]$ than the sharp cutoff that would result from padding with zeros only.

Although it is often more convenient to use the 'continuous variable notation' ($\mathrm{V}(t)$ and $\underline{V}(f)$), it will sometimes be necessary to use the 'discrete variable notation' ($\mathrm{V}[t_n]$ and $\underline{V}[f_k]$). Please bear this in mind in the proceeding sections, which sometimes alternate between these notations.

4.10 Extracting The Experimental Impulse Response Signal $\mathrm{H}_e(t)$

Modifying the definition of the calibration signal (4.23)

$$\mathrm{V}_c(t) = \mathrm{H}_e(t) * \Big[-\delta(t) + 2\,\mathrm{H}(l,t) \Big] \tag{4.25}$$

$$= \underbrace{-\mathrm{H}_e(t)}_{\mathrm{V}_p(t)} + \underbrace{2\,\mathrm{H}_e(t) * \mathrm{H}(l,t)}_{\mathrm{V}_d(t)} \tag{4.26}$$

and then recognizing the terms associated with the proximal pulse $\mathrm{V}_p(t)$ and distal pulse $\mathrm{V}_d(t)$ depicted in figure 4.1, it should be clear that

$$\mathrm{H}_e(t) = -\mathrm{V}_p(t) \tag{4.27}$$

and

$$\mathrm{V}_d(t) = 2\,\mathrm{H}_e(t) * \mathrm{H}(l,t) \tag{4.28}$$

may be easily obtained by parsing a measured calibration signal, provided the proximal and distal pulses are well resolved. Equation (4.27) gives a simple recipe for extracting $\mathrm{H}_e(t)$: simply parse out $\mathrm{V}_p(t)$, then change its sign. Given $\mathrm{V}_p(t)$, $\mathrm{V}_d(t)$ may be determined from $\mathrm{V}_c(t)$ by subtraction: $\mathrm{V}_d(t) = \mathrm{V}_c(t) - \mathrm{V}_p(t)$.

4.11 Extracting The Attenuation Coefficient $\alpha(f)$

With $\underline{H}_e(f)$ denoting the Fourier transform of $\mathrm{H}_e(t)$, $\underline{V}_d(f)$ denoting the Fourier transform of $\mathrm{V}_d(t)$, and $\underline{H}(l,f)$ denoting the Fourier transform of $\mathrm{H}(l,t)$, it follows from (4.28) and the convolution theorem that

$$\Big(\frac{-1}{2}\Big)\frac{\underline{V}_d(f)}{\underline{V}_p(f)} = \frac{[2\,\underline{H}_e(f)\,\underline{H}(l,f)]}{2\,[-\underline{V}_p(f)]} = \frac{[2\,\underline{H}_e(f)\,\underline{H}(l,f)]}{2\,\underline{H}_e(f)} = \underline{H}(l,f) \tag{4.29}$$

To emphasize that the $\underline{H}(l,f)$ determined experimentally via (4.29) is a numeric result derived by FFTing sampled versions $\mathrm{V}_p[t_n]$ and $\mathrm{V}_d[t_n]$ of $\mathrm{V}_p(t)$ and $\mathrm{V}_d(t)$, respectively, let

$$\underline{H}_c[l;f_k] \equiv \Big(\frac{-1}{2}\Big)\frac{\underline{V}_d[f_k]}{\underline{V}_p[f_k]} = \Big(\frac{-1}{2}\Big)\frac{\mathrm{FFT}\{\mathrm{V}_d[t_n]\}}{\mathrm{FFT}\{\mathrm{V}_p[t_n]\}} \tag{4.30}$$

The notation $\underline{H_c}[l; f_k]$ (using a semicolon) rather than $\underline{H_c}[l, f_k]$ (using a comma) has been adopted to emphasize that knowledge of the thickness l is not explicitly included in $\underline{H_c}[l; f_k]$. It is possible to obtain a pressure response signal without knowing the thickness l of the sample.

A cursory glance at the magnitude of the resultant $\underline{H_c}[l; f_k]$ often gives an estimate for the 'acceptable' frequency range wherein the signal to noise ratio (SNR) is large. For polymers, which exhibit linearly increasing attenuation with frequency (see *Causality And Materials*), there is typically a frequency band $\{f_-, f_+\}$ wherein the magnitude of $\underline{H_c}[l; f_k]$ decreases continuously with f_k. Above f_+, the magnitude of $\underline{H_c}[l; f_k]$ takes on seemingly random values at each value of frequency. There is no point in trying to extract an estimate $\tilde{\alpha}(f)$ to the desired, underlying $\alpha(f)$ outside this range; the result can only be noise.

Comparing (4.30) with appendix A's expression

$$\underline{H}(l, f) = \exp(\ -l\ [\alpha(f) + \mathrm{j}\ 2\pi f/c(f)]\ ) \tag{4.31}$$

it should be clear that information about the numerically-determined approximate attenuation coefficient $\tilde{\alpha}[f_k]$ is contained in the magnitude $|\underline{H_c}[l; f_k]|$ of $\underline{H_c}[l; f_k]$, and that information about the numerically-determined approximate phase velocity $\tilde{c}[f_k]$ is contained in the phase $\langle \underline{H_c}[l; f_k] \rangle$ of $\underline{H_c}[l; f_k]$. It would seem that

$$\tilde{\alpha}[f_k] = \frac{-\ln|\underline{H_c}[l; f_k]|}{l} \tag{4.32}$$

and

$$\tilde{c}[f_k] = \frac{-2\pi f_k l}{\langle \underline{H_c}[l; f_k] \rangle} \tag{4.33}$$

Equation (4.32) has been found to yield a satisfactory experimental method for approximating the dielectric's attenuation coefficient $\alpha[f_k]$ if

$$|\underline{H_c}[l; f_k]| \equiv \sqrt{\Re_e\{\underline{H_c}[l; f_k]\}^2 + \Im_m\{\underline{H_c}[l; f_k]\}^2} \tag{4.34}$$

However, because the phase of a given complex number cannot be determined uniquely, and because (4.33) requires that $\langle \underline{H_c}[l; f_k] \rangle$ be at least approximately equal to the true sampled phase $-2\pi f_k l/c[f_k]$, some care must be taken in determining the experimental $\langle \underline{H_c}[l; f_k] \rangle$ to submit to (4.33).

4.12 Extracting The Phase Velocity $c(f)$

By definition [87], the principal value of the phase $\langle \underline{Z} \rangle_p$ of a complex number $\underline{Z}$ falls in the 'principal range' $\{-\pi, \pi\}$. Without extra information, computers can only determine the phase of a complex number to within some specific 2π range, which is

commonly chosen to be the principal range. Implementation of (4.33) using the principal value of the phase $\langle \underline{H}_c[l; f_k] \rangle_p$ of $\underline{H}_c[l; f_k]$ yields a valid $\tilde{c}[f_k]$ only if the true sampled phase $-2\pi f_k l / c[f_k]$ falls within the principal range for f in the frequency band of interest (a recovered $\tilde{c}[f_k]$ is called valid in some frequency band if the phase error incurred by using the approximate $\tilde{c}[f_k]$ rather than the true $c[f_k]$ is always much less than 2π for positions z of interest).

If the true sampled phase $-2\pi f_k l / c[f_k]$ falls outside the principal range for some frequency band then the $\tilde{c}[f_k]$ gleaned by submitting $\langle \underline{H}_c[l; f_k] \rangle_p$ to (4.33) only yields the correct *principal value* of the phase at the one position $z = l$. In this case the estimated transfer function $\underline{\tilde{H}}[z, f_k]$ gleaned via $\tilde{c}[f_k]$ and $\tilde{\alpha}[f_k]$ produces, after inverse FFTing, a reasonable estimate $\tilde{\mathrm{H}}[z, t_k]$ to the desired, underlying $\mathrm{H}[z, t_k]$ for the case of $z = l$ *only*. The fundamental problem is that the principal value 'wraps' all possible values of the phase into the principal range. The principal value of the phase $\langle \underline{H}_c[l; f_k] \rangle_p$ of $\underline{H}_c[l; f_k]$ should be carefully 'unwrapped' before it is submitted to (4.33) in the hopes of extracting a valid $\tilde{c}[f_k]$.

This thesis invokes a three step process for unwrapping the phase: (1) minimize the tendency for the phase to wrap by subtracting off known components of the phase; (2) unwrap the 'remainder phase' so that the change in slope at each discrete frequency is as small as possible; (3) define the desired unwrapped phase as the sum of the 'smoothed remainder phase' and the known component of the phase that was subtracted off in step (1).

The point of step (1)'s removal of known components of the phase is to leave a remainder phase that is as smooth, and therefore unlikely to 'wrap,' as possible. The problem is one of aliasing: if the true slope of the phase yields a 2π phase-jump in one frequency increment Δf then the principal value of both data points will be the same. The idea is to subtract off known components of the phase so that the assumption that the phase will have at most a shallow slope will be more likely to be valid.

As implemented here, step (1) utilizes the realization that the ratio of the Fourier transforms of two temporally resolvable pulses such as $\mathrm{V}_p(t)$ and $\mathrm{V}_d(t)$ will have a linear phase component $2\pi f \mathcal{T}_{pp}$ corresponding to the temporal duration $\mathcal{T}_{pp}$ separating the time of the peak value of $|\mathrm{V}_p(t)|$ and the time of the peak value of $|\mathrm{V}_d(t)|$. Subtracting $-2\pi f_k \mathcal{T}_{pp}$ from $\langle \underline{H}_c[l; f_k] \rangle_p$ yields a remainder phase

$$\langle \underline{H}_c[l; f_k] \rangle_r \equiv \langle \underline{H}_c[l; f_k] \rangle_p + 2\pi f_k \mathcal{T}_{pp} \tag{4.35}$$

Step (2) utilizes the realization that the $f = 0$ value of the phase of $\underline{H}(l, f)$ must be zero because $\mathrm{H}(l, t)$ is a real function of time, and $\underline{H}(l, 0)$ is proportional to the area of $\mathrm{H}(l, t)$. Therefore $\langle \underline{H}_c[l; 0] \rangle_r = 0$. The value of the remainder phase $\langle \underline{H}_c[l; f_1] \rangle_r$ at the first nonzero frequency $f_k = \Delta f$ can be coerced into the principal range, thereby defining what might be called the 'first principal slope' of the remainder phase.

The value of the remainder phase $\langle \underline{H}_c[l; f_2] \rangle_r$ at the second nonzero frequency can be uniquely determined by adding the (possibly negative) integer number of 2π's that brings about the smallest change in the first principal slope. The slope determined by

the first and second nonzero values of $\langle \underline{H}_c[l; f_k] \rangle_r$ might be called the second principal slope. Choose $\langle \underline{H}_c[l; f_2] \rangle_r$ so that the second principal slope is as close as possible to the first principal slope.

Proceed similarly for $\langle \underline{H}_c[l; f_3] \rangle_r$, and so on for each discrete frequency until step (2) is completed. Step (3) involves adding $-2\pi f_k \mathcal{T}_{pp}$ to the result of step (2). The result is this thesis' best guess as to the $\langle \underline{H}_c[l; f_k] \rangle$ that should be submitted to (4.33) to determine $\tilde{c}[f_k]$.

4.12.1 A Possible Improvement

Note that step (2) could possibly be improved by using knowledge of $\tilde{\alpha}[f_k]$ to make some preliminary guess $\tilde{c}_\alpha[f_k]$ as to what $\tilde{c}[f_k]$ might be (see *Causality And Materials*). With this $\tilde{c}_\alpha[f_k]$ and the sample thickness l in hand, the previous expression (4.35) for the remainder phase $\langle \underline{H}_c[l; f_k] \rangle_r$ could be updated:

$$\langle \underline{H}_c[l; f_k] \rangle_r = \langle \underline{H}_c[l; f_k] \rangle_p + 2\pi f_k l / \tilde{c}_\alpha[f_k] \tag{4.36}$$

Because $l/\tilde{c}_\alpha[f_k]$ can be described by

$$l/\tilde{c}_\alpha[f_k] = \mathcal{T}_{pp} + \mathcal{T}_{\text{disp}}[f_k] \tag{4.37}$$

where $\mathcal{T}_{\text{disp}}[f_k]$ is the frequency dependent excess (with respect to $\mathcal{T}_{pp}$) time delay effected by the frequency dependent velocity, the result of (4.36) may well be a remainder phase that is even less rapidly varying than the remainder phase defined in (4.35).

The additional 'flattening' of the remainder phase potentially afforded by this improvement should be most pronounced in thick (large l) samples where the 'dispersive' time delay $\mathcal{T}_{\text{disp}}[f_k]$ has had a longer distance over which to accrue. It would make sense to validate $\tilde{c}_\alpha[f_k]$ via the time-domain techniques described in section 4.13.2 before supplanting $\mathcal{T}_{pp}$ with $l/\tilde{c}_\alpha[f_k]$.

4.13 Curve Fitting And Parameter Extraction

4.13.1 Frequency Domain Parameter Extraction

Given an approximate $\{\tilde{\alpha}[f_k], \tilde{c}[f_k]\}$ pair, and given closed-form, parameterized models $\{\hat{\alpha}[\overline{\xi}, f_k], \hat{c}[\overline{\zeta}, f_k]\}$ for the desired $\{\alpha(f), c(f)\}$ expressed in terms of the attenuation coefficient parameters $\overline{\xi}$ and the phase velocity parameters $\overline{\zeta}$, it is possible to employ a variety of frequency domain curve fitting procedures to determine a 'best fit' set of parameters $\overline{\xi}'$ from $\tilde{\alpha}[f_k]$ and a best fit set of parameters $\overline{\zeta}'$ from $\tilde{c}[f_k]$.

Note that whereas 'tildes' (as in $\tilde{\alpha}$) correspond to approximate quantities, 'hats' (as in $\hat{\alpha}$) correspond to modelled quantities. In this thesis the closed-form, parameterized polymeric model (see equation (6.23))

$$\hat{\alpha}_p[\underbrace{\{m, b\}}_{\overline{\xi}_p}, f_k] = m\ f_k + b \tag{4.38}$$

and the parameterized phase velocity model (see equation (6.24))

$$\hat{c}_p[\underbrace{\{m, b, f_o, c(f_o)\}}_{\overline{\zeta}_p}, f_k] = c(f_o) + \left[\frac{c(f_o)}{\pi}\right]^2 \left[m \ln(\frac{f_k}{f_o}) + b\left[\frac{1}{f_o} - \frac{1}{f_k}\right]\right] \tag{4.39}$$

are used in conjunction with Powell's method [88] for minimizing multidimensional functions to determine the best-fit polymeric parameters $\{\overline{\xi}_p', \overline{\zeta}_p'\}$ that minimize the RMS difference between the measured frequency domain samples and the sampled closed-form expressions over the SNR-acceptable frequency range $\{f_-, f_+\}$ described previously.

In regards to the curve fit determining $c(f)$, it should be noted that the author implemented the curve fit to $\beta(f) = 2\pi f/c(f)$ (rather than to $c(f)$ directly) because the data *arrives* as the principal value of the phase angle $[-l\beta(f)]$ whereas $c(f)$ is a derived quantity:

$$\tilde{c}(f) = \frac{-2\pi f l}{[-l\beta(f)]} \tag{4.40}$$

It is known *a priori* (from the fact that the material's impulse response $\mathrm{H}(l, t)$ must be real) that

$$\lim_{f \to \infty} \{\beta(f)\} = 0 \tag{4.41}$$

It follows that even a 'small' error in the measured low frequency value of $[-l\beta(f)]$ will lead to a relatively large error in the low frequency $c(f)$.

4.13.2 Time Domain Parameter Extraction

Note that because $\overline{\xi}_p'$ is determined from $\tilde{\alpha}[f_k]$ alone, and because $\overline{\zeta}_p'$ is determined from $\tilde{c}[f_k]$ alone, it is entirely possible to extract m and b values from $\tilde{\alpha}[f_k]$ that do not agree with the m and b values extracted from $\tilde{c}[f_k]$. In this case (and others) it is sometimes useful to employ Powells' method in the time domain as a 'tie-breaker' when in doubt as to what one set of parameters gives the 'best fit.' The idea is to search for the one set of parameters $\overline{\varsigma}_p'$ that minimizes the RMS values of

$$\eta[\overline{\varsigma}_p, t_n] \equiv \mathrm{V}_d[t_n] - \hat{\mathrm{V}}_d[\overline{\varsigma}_p, t_n] \tag{4.42}$$

where

$$\overline{\varsigma}_p \equiv \overline{\xi}_p \cup \overline{\zeta}_p = \{m, b, f_o, c(f_o)\} \tag{4.43}$$

includes all the parameters involved in the model. The quantity $\hat{\mathrm{V}}_d[\overline{\varsigma}_p, t_n]$ is meant to represent the samples of a modelled version $\hat{\mathrm{V}}_d(\overline{\varsigma}_p, t)$ of $\mathrm{V}_d(t)$ which can be calculated using equation (4.28), the measured samples $\mathrm{H}_e[t_n]$ of $\mathrm{H}_e(t)$, and the modelled transfer function $\underline{\hat{H}}(\overline{\varsigma}_p, l, f)$ determined by the parameters $\overline{\varsigma}_p$. Fourier transforming (4.28) using the convolution theorem,

$$\underline{V}_d(f) = 2\, \underline{H}_e(f)\, \underline{H}(l, f) \tag{4.44}$$

so that

$$\hat{\mathrm{V}}_d[\overline{\varsigma}_p, t_n] = \mathrm{FFT}^{-1}\left\{ 2\, \underline{H}_e[f_k]\, \underline{\hat{H}}[\overline{\varsigma}_p, l, f_k] \right\} \tag{4.45}$$

4.13.3 Final Note On Parameter Extraction

It is important to realize that the 'best attenuation fit' set of parameters $\overline{\xi}'$ determined from $\tilde{\alpha}[f_k]$, the 'best velocity fit' set of parameters $\overline{\zeta}'$ determined from $\tilde{c}[f_k]$, and the 'best time domain fit' set of parameters $\overline{\varsigma}'$ determined from $\mathrm{H}_e[t_n]$ and $\mathrm{V}_p[t_n]$ will not, in general, agree with each other. Also, the 'best fit' will depend on the frequency range $\{f_-, f_+\}$ used in the case of $\overline{\xi}$ and $\overline{\zeta}$, and on the time range used in the case of $\overline{\varsigma}$.

A forthcoming paper by Cooke and Lyons [69] presents evidence supporting the efficacy of these parameter extraction techniques. The results of this paper which concern polyethylene, the principal material investigated in this thesis, are summarized in table 6.1. The specifics of the procedure used to determine the set of coefficients presented in table 6.1 are not yet well defined; they involve at least as much art as science.

But regardless of the precise details of the procedure used to define the 'true best fit' set of parameters, the result is a closed form expression for the estimated attenuation coefficient $\tilde{\alpha}(f)$ and phase velocity $\tilde{c}(f)$. This is useful in terms of data reduction, and also for calculating the required approximate derivatives $d\tilde{\alpha}(f)/df \equiv \tilde{\alpha}_f(f)$ and $d\tilde{c}(f)/df \equiv \tilde{c}_f(f)$ which may then be used to produce their respective sampled versions $\tilde{\alpha}_f[f_k]$ and $\tilde{c}_f[f_k]$. The proceeding discussion assumes that such a model has somehow been established, and reverts to denoting that model as $\alpha(f)$ and $c(f)$.

4.14 Implementing The Lyons Recovery

A Lyons recovery is defined as the process, or the result, of numerically implementing the analytic CLDP inverse transform relation determined by the propagation coefficient

$$\underline{\mathcal{K}}(f) = \alpha(f) + \mathrm{j}\, 2\pi f/c(f) \tag{4.46}$$

The CLDP inverse transform uses $\underline{\mathcal{K}}(f)$ (and its derivative $\underline{\mathcal{K}}_f(f)$) to define the following mapping (see equation (2.52)) between the Fourier transform $\underline{\mathcal{P}}(f)$ of some real of time function $\mathcal{P}(t)$ and a real function of space $\mathcal{Q}(z)$:

$$\mathcal{Q}(z) = 2\int_0^\infty \Re_e\left\{\frac{\underline{\mathcal{P}}(f)}{\underline{C}_g(f)}\ \exp(z\ \underline{\mathcal{K}}(f))\right\} df \tag{4.47}$$

where the group velocity $\underline{C}_g(f)$ is given by

$$\frac{1}{\underline{C}_g(f)} = \frac{\underline{\mathcal{K}}_f(f)}{\mathrm{j}2\pi} = \frac{1}{c(f)}\left[1 - \frac{f}{c(f)}\ \frac{d\,c(f)}{df}\right] + \frac{1}{\mathrm{j}2\pi}\frac{d\,\alpha(f)}{df} \tag{4.48}$$

Given $\underline{\mathcal{K}}(f)$, $\underline{\mathcal{K}}_f(f)$, and samples $\mathcal{P}[t_n]$ of $\mathcal{P}(t)$, there are many possible ways to numerically implement the CLDP inverse transform relation. There are, therefore, many possible versions of 'the Lyons recovery.'

These versions will differ chiefly on the details of

I. How the recovery (4.47) is regularized to mollify the oscillations associated with the Darrell property of the bandlimited CLDP inverse transform

II. How the recovery (4.47) is regularized to decrease the influence of noise

III. How approximate values for $\underline{\mathcal{P}}(f)$ are determined from the measured $\mathcal{P}[t_n]$

IV. How the frequency domain integration (4.47) is implemented

4.14.1 Relationship To The PESAW Experiment

The four items listed above are generic; they have no specific connection to the PESAW experiment. All researchers possessed of a time-sampled CLDP response signal (and a material model) who are interested in implementing a Lyons recovery must address these four issues. These four issues will be discussed in turn in the following subsections. The point of this subsection of to place 'the Lyons recovery' within the context of 'the PESAW charge recovery.'

Section 2.2 introduces an approach which breaks the process of mapping a measured PESAW pressure signal $\mathrm{V}(t)$ to an estimate $\tilde{\mathrm{Q}}(z)$ of the desired charge waveform $\mathrm{Q}(z)$ into a three step process.

Step 1 involves deconvolving the measured signal $\mathrm{V}(t)$ with respect to the experimental impulse response $\mathrm{H}_e(t)$ to gain some estimate $\tilde{\mathcal{P}}(t)$ to the response signal

$\mathcal{P}(t)$. This thesis uses the familiar frequency domain deconvolution scheme discussed in *Loss, Dispersion, Deconvolution*, and bypasses the much-touted Tikhonov regularization scheme also discussed in that chapter in favor of the more familiar lowpass filtering scheme discussed in the next subsection. Because the deconvolution is enacted in the frequency domain the natural result is not the time-domain $\tilde{\mathcal{P}}(t)$ mentioned above but, fortuitously, a frequency domain version $\underline{\tilde{\mathcal{P}}}(f)$ ripe for submission to (4.47).

Step 2 is concerned with how to map $\underline{\tilde{\mathcal{P}}}(f)$ to an estimate $\mathrm{R}(z)$ of the source waveform $\mathcal{Q}(z)$, and step 3 is concerned with how to map $\mathrm{R}(z)$ to the charge waveform estimate $\tilde{\mathrm{Q}}(z)$. Step 2 is the focus of all but this specific subsection 4.14.1 of this section 4.14; step 2 can be completely decoupled from the PESAW experiment, and so will not be discussed further here. Step three is a relatively trivial space-to-space mapping that must be performed as the final step of a PESAW recovery, and so its discussion will be deferred to the final section of this chapter *Putting It All Together.*

4.14.2 SDB Filtering (Items I & II)

This thesis' version of the Lyons recovery answers items I and II via a spatially-dependent implementation of the filter known as Blackman's Lucky Guess (BLG). That is, the $\underline{\mathcal{P}}(f)$ in (4.47) is replaced by

$$\underline{\tilde{\mathcal{P}}}(z,f) \quad \equiv \quad \underline{\mathcal{P}}(f)\,\mathrm{B}(f_c(z),f) \tag{4.49}$$

where both the BLG filter $\mathrm{B}(f_c,f)$ and the standard SDB function $\grave{f}_c(z)$ are introduced in appendix B. Applying the familiar frequency domain deconvolution scheme discussed in the previous chapter to equation (4.12) yields

$$\underline{\mathcal{P}}(f) = \frac{\underline{V}(f)}{\underline{H}_e(f)} \tag{4.50}$$

Note that because $\mathrm{H}_e(t)$ is parsed from the calibration signal $\mathrm{V}_c(t)$, and because $\mathrm{V}_c(t)$ has the same dimensions as the generic $\mathrm{V}(t)$ in (4.50) (in the case of a plate-charge recovery, $\mathrm{V}(t)$ *is* $\mathrm{V}_c(t)$), the ratio $\underline{\mathcal{P}}(f)$ in (4.50) must be dimensionless. It follows that the inverse Fourier transform $\mathcal{P}(t)$ of $\underline{\mathcal{P}}(f)$ must have dimensions of frequency, or inverse-time.

Substituting (4.50) into (4.47) yields

$$\tilde{\mathcal{Q}}(z) = 2\int_0^\infty \Re_e\left\{\frac{\underline{V}(f)\,\mathrm{B}(f_c(z),f)}{\underline{H}_e(f)\,\underline{C}_g(f)}\,\exp(z\,\underline{\mathcal{K}}(f))\right\}df \tag{4.51}$$

where equation (4.47)'s left hand side has been replaced with $\tilde{\mathcal{Q}}(z)$ to emphasize that the result of the integration in (4.47) is generally only a recovered approximation to the desired $\mathcal{Q}(z)$.

4.14.3 Time Samples To Frequency Samples (Item III)

The generic quantity $\underline{V}(f)$ in equation (4.51) may correspond to any number of signals, including $\underline{V}_c(f)$ and $\underline{V}_b(f)$ (see section 4.8). Item III is concerned with how information about $\underline{V}(f)$ is extracted from the measured samples $\mathrm{V}[t_n]$ of the underlying $\mathrm{V}(t)$.

This thesis' version of the Lyons recovery answers item III by implementing equation *(13.9.6)* of Press *et al* [90]. In short, *(13.9.6)* advocates FFTing the list of numbers $\mathrm{V}[t_n]$ into another list of numbers $\underline{V}[f_k]$ which are then taken as samples of the desired Fourier transform $\underline{V}(f)$ of $\mathrm{V}(t)$. This thesis' definition of the FFT is introduced in the following subsection *High-Frequency Inaccuracy.*

Press *et al* do not recommend this approach. They point out: "equation *(13.9.6)* becomes systematically inaccurate as ω $[= 2\pi f]$ increases." Yet equation *(13.9.6)* is simple to implement, and this thesis only uses the results of *(13.9.6)* at low frequencies where its results are presumably more reliable.

Press *et al* suggest a more sophisticated approach that future researchers may choose to implement. This 'more sophisticated approach' is called 'the dftcor approach' here because dftcor is the name of the sophisticated approach's workhorse subroutine.

High-Frequency Inaccuracy

It is worth drawing attention to one specific example of the inaccuracy (at high frequency) of approximating $\underline{V}(f)$ with the $\underline{V}[f_k]$ determined via Press *et al*'s equation *(13.9.6)*. Please recall that N_t, the number of samples of $\mathrm{V}(t)$ comprising the $\mathrm{V}[t_n]$ submitted to the FFT, must be an integer power of 2, and that if (as is the case here) all the numbers comprising $\mathrm{V}[t_n]$ are real then $\underline{V}[f_k]$ will have conjugate symmetry.

The practical result of this symmetry is that only the first $(1 + N_t/2)$ elements $\{\underline{V}[0], \underline{V}[f_1], \ldots, \underline{V}[f_{N_t/2}]\}$ of $\underline{V}[f_k]$ are unique; the last $(-1 + N_t/2)$ elements of $\underline{V}[f_k]$ may be determined from the first $(1 + N_t/2)$ elements simply by reversing their order, discarding the first and last elements, then taking the complex conjugate of each element.

Therefore the number of unique frequency values $N_f = 1 + N_t/2$, and the maximum frequency f_M available through the FFT of data sampled with time step Δt is

$$f_M = \Delta f\,(N_f - 1) = \left(\frac{1}{N_t\,\Delta t}\right)\left(\frac{N_t}{2}\right) = \frac{1}{2\,\Delta t} \tag{4.52}$$

corresponding to $k' \equiv N_t/2$, so that $f_M = f_{k'}$ (defining k' allows the unattractive notation $f_{N_t/2}$ to be replaced by $f_{k'}$).

Now consider the proposition

$$\underline{V}(f_M) \cong \underline{V}[f_{k'}] \tag{4.53}$$

in light of the fact that

$$\underline{V}[f_k] = \mathrm{FFT}\{\mathrm{V}[t_n]\} \equiv \Delta t \sum_{n=0}^{N_t-1} \mathrm{V}[t_n]\ \exp(-\mathrm{j}\ 2\pi\ k\ n/N_t) \tag{4.54}$$

so that

$$\underline{V}[f_{k'}] = \Delta t \sum_{n=0}^{N_t-1} \mathrm{V}[t_n]\ (-1)^n \tag{4.55}$$

$$= \Delta t\,[\ \mathrm{V}[t_0] - \mathrm{V}[t_1] + \cdots + \mathrm{V}[t_{N_t-2}] - \mathrm{V}[t_{N_t-1}]\ ]$$

Whereas the $f = f_M$ value of the imaginary part $\Im_m\{\underline{V}(f)\}$ of the Fourier transform $\underline{V}(f)$ of some arbitrary real function $\mathrm{V}(t)$ is itself arbitrary, $\Im_m\{\underline{V}[f_{k'}]\}$ must be zero if all the elements of $\mathrm{V}[t_n]$ are real. Therefore equation (4.53) cannot be generally valid.

Note that the FFT operation introduced in equation (4.54) is actually implemented in the computer in a less direct but more efficient manner which yields the same results. See [91] or [92] for information concerning the FFT and the inverse FFT, introduced below:

$$\mathrm{FFT}^{-1}\{\underline{V}[f_k]\} \equiv \Delta f \sum_{k=0}^{N_t-1} \underline{V}[f_k]\ \exp(\mathrm{j}\ 2\pi\ k\ n/N_t) \tag{4.56}$$

The prefactor to this thesis' 'dimensioned' version of the FFT (4.54) is Δt; the prefactor to the IFT (4.56) is Δf. In general, the definition of an FFT/IFT pair requires that the product of these prefactors be $1/N_t$. Note that because $\Delta f \equiv (N_t \Delta t)^{-1}$, the prefactor product of this thesis' versions of the FFT and IFT satisfy the general constraint.

Consequences

If the true material impulse response $\mathrm{H}(l', t)$ (l' some specific value of l) is sampled to yield $\mathrm{H}[l'; t_n]$, and if $\mathrm{H}[l'; t_n]$ is then FFT'd to yield a set of samples $\underline{H}[l'; f_k]$ which are meant to satisfy

$$\underline{H}[l'; f_k] \cong \underline{H}(l', f_k) \equiv \exp(-l'\ [\alpha(f_k) + \mathrm{j}\ 2\pi f_k / c(f_k)]) \tag{4.57}$$

it should be clear from the results presented in the previous section that, unless

$$0 = \Im_m\{\underline{H}(l'; f_{k'})\} = -\exp(-l'\ \alpha(f_{k'}))\ \sin(2\pi f_{k'} l' / c(f_{k'})) \tag{4.58}$$

it cannot possibly be true that $\underline{H}[l'; f_{k'}] = \underline{H}(l', f_{k'})$.

The implications of the "high-frequency inaccuracy" associated with this thesis' approach to calculating $\tilde{\alpha}[f_k]$ and $\tilde{c}[f_k]$ are clear: these numeric approximations to the desired $\alpha(f)$ and $c(f)$ will generally fail in the limit as $f \to f_{k'}$

4.14.4 Frequency Domain Integration (Item IV)

The frequency domain integral expression (4.51) for the PESAW source waveform recovery $\mathrm{R}(z)$ is re-presented below for consideration.

$$\tilde{\mathcal{Q}}(z) = 2 \int_0^\infty \Re_e \left\{ \frac{\underline{V}(f)\, \mathrm{B}(f_c(z), f)}{\underline{H}_e(f)\, \underline{C}_g(f)} \exp(z\, \underline{\mathcal{K}}(f)) \right\} df \tag{4.59}$$

In this thesis, only equally-spaced approximate samples $\underline{V}[f_k]$ and $\underline{H}_e[f_k]$ of the desired quantities $\underline{V}(f)$ and $\underline{H}_e(f)$ are available. Because $\underline{\mathcal{K}}(f)$ is assumed to be represented by closed-form, parameterized models $\alpha(f)$ and $c(f)$ extracted from measured data, both $\underline{\mathcal{K}}(f)$ and $1/\underline{C}_g(f)$ (which is proportional to the derivative of $\underline{\mathcal{K}}(f)$) are assumed to be known continuous functions of frequency. The BLG filter $\mathrm{B}(f_c, f)$ is also a known continuous function of frequency (see appendix B). But the end result is that equation (4.59)'s integrand is known only at the equally spaced set of frequencies $f_k = k\, \Delta f$.

This thesis uses a simple approach to the numerical integration of (4.59):

$$\mathrm{R}(z) \equiv \Delta f \sum_{k=0}^{k'} \mathrm{two}[k]\, \Re_e \left\{ \frac{\underline{V}[f_k]\, \mathrm{B}(f_c(z), f_k)}{\underline{H}_e[f_k]\, \underline{C}_g[f_k]} \exp(z\, \underline{\mathcal{K}}(f_k)) \right\} \tag{4.60}$$

where $\mathrm{two}[0] = \mathrm{two}[k'] = 1$, and $\mathrm{two}[k] = 2$ for $k \neq \{0, k'\}$.

The function $\mathrm{two}[k]$ arises from the assumed conjugate symmetry of $\underline{V}[f_k]$ (recall that $\mathrm{V}[t_n]$ is assumed real); if the real-part operator $\Re_e$ were removed and the summation over k was extended from 0 to $2k'-1$ (so that the summation includes all $N_t = 2k'$ values produced by the FFT) then the function $\mathrm{two}[k]$ could be removed.

The left hand side $\tilde{\mathcal{Q}}(z)$ of (4.59) has been replaced with $\mathrm{R}(z)$ in (4.60) to reflect the fact that whereas $\tilde{\mathcal{Q}}(z)$ is an approximate *analytic* expression for the PESAW source waveform, $\mathrm{R}(z)$ is an approximate *numeric* expression. $\mathrm{R}(z)$ defines this thesis' implementation of the Lyons recovery for determination of the PESAW source waveform.

This definition of the function $\mathrm{two}[k]$ follows from the realization that, from (4.56),

$$\mathrm{V}[t_n] = \Delta f \sum_{k=0}^{N_t-1} \underline{V}[f_k]\, \exp(\mathrm{j}\, 2\pi\, k\, n/N_t) \tag{4.61}$$

$$= \Delta f \sum_{k=0}^{k'} \mathrm{two}[k]\, \Re_e \{ \underline{V}[f_k]\, \exp(\mathrm{j}\, 2\pi\, k\, n/N_t) \} \tag{4.62}$$

in the case where $\mathrm{V}[t_n]$ is a real sequence of numbers and, consequently, $\underline{V}[f_k]$ has conjugate symmetry. Using $\mathrm{two}[k]$ rather than 2 avoids double-counting of the special-case frequency components f_0 and $f_{k'}$.

If $f_c(z)$ is 'significantly' less than $f_M (= f_{k'})$, then the errors associated with the "high-frequency inaccuracy" of this thesis' naive identification $\underline{V}(f_k) \cong \underline{V}[f_k]$ should be mollified if not quelled.

Possible Frequency Domain Integration Improvement

Press *et al* [100] highly recommend Romberg integration. Unfortunately, as envisioned by these authors, Romberg integration requires knowledge of the integrand at arbitrary abscissa's. Romberg integration could provide an alternative to (4.60) for numerically integrating (4.59) if $\underline{V}(f)$ and $\underline{H}_e(f)$ were calculable at arbitrary f instead of only at $f_n = n\Delta f = n/(N_t\Delta t)$.

Fortunately, Press *et al* (see section 4.14.3, or [90]) provide a relatively high accuracy (compared to Press *et al*'s equation *(13.9.6)*) 'dftcor method' for computing estimates to the Fourier transform $\underline{\mathcal{P}}(f)$ of some signal $\mathcal{P}(t)$ given knowledge of $\mathcal{P}(t)$ only at the set of sampled points $\mathcal{P}[t_n] = \mathcal{P}(n\Delta t)$.

It would be possible to improve this thesis' SDB-filtered version of the Lyons recovery, and other frequency-domain implementations of the proposed CLDP inverse IE as well, by using Romberg integration to perform the frequency domain integration of an integrand whose values are computed from $\mathrm{V}[t_n]$ and $\mathrm{H}_e[t_n]$ via the dftcor method.

4.15 Putting It All Together

4.15.1 Overview

Given a calibration signal $\mathrm{V}_c[t_n]$, a bulk signal $\mathrm{V}_b[t_n]$, and the plate charge q_p generated by the DC component V_o of the applied voltage (see equation (4.14)), the first step of the suggested algorithm for determining estimated samples $\tilde{\mathrm{Q}}[z_i]$ of the desired PESAW charge distribution $\mathrm{Q}(z)$ is to solve the *inverse medium* problem of estimating the dielectric's propagation parameter $\underline{\mathcal{K}}(f) = \alpha(f) + \mathrm{j}\ 2\pi f/c(f)$.

The information required to solve the inverse medium problem is contained in $\mathrm{V}_c[t_n]$. $\mathrm{V}_c[t_n]$ must be parsed into its proximal plate component $\mathrm{V}_p[t_n]$ and its distal plate component $\mathrm{V}_d[t_n]$, which must then be analyzed to determine models for $\alpha(f)$, $\mathrm{c}(f)$ and, ultimately, $\underline{\mathcal{K}}(f)$. Sections 4.10 through 4.13.3 explain this process.

Having solved the inverse medium problem, the next task is the *inverse source* problem of determining the normalized, estimated source pressure waveform $\mathrm{R}[z_i]$. $\mathrm{R}[z_i]$ must then be scaled (by $\mathrm{E}_z(z)$; see equation (2.23)) to yield the normalized estimated charge waveform $\tilde{\mathrm{Q}}_n[z_i]$ – which must then be un-normalized to yield $\tilde{\mathrm{Q}}[z_i]$.

As described in section 1.11, the Darrell property of the bandlimited CLDP inverse transform necessitates that the recovery be regularized. This thesis has implemented the BLG (Blackman's Lucky Guess) filter $\mathrm{B}(f_c, f)$ as a means to this end. This filter appears in $\mathrm{R}(z)$'s defining expression (4.60) as $\mathrm{B}(f_c(z), f)$. The process of determining the spatially-dependent BLG filter frequency cutoff function $f_c(z)$ will be deferred to section 4.15.4.

4.15.2 The Need For Spatially Dependent Scaling

The scaling by $\mathrm{E}_z(z)$ takes into account the fact that (generalizing equation (2.21))

$$\mathcal{Q}(z) \equiv \left| \int_{-\mathcal{T}_p/2}^{\mathcal{T}_p/2} \overline{\mathrm{F}}(z,t)dt \right| = \mathrm{Q}(z) \left| \int_{-\mathcal{T}_p/2}^{\mathcal{T}_p/2} \overline{\mathrm{E}}(z,t)dt \right| = \mathrm{Q}(z)\ \mathrm{E}_z(z) \tag{4.63}$$

is the true impetus of the measured $\mathrm{V}_b[t_n]$. Note that the $\overline{\mathrm{F}}(z,t)$ (and, likewise, the $\overline{\mathrm{E}}(z,t)$) in (4.63) is the excitation field due to the excitation voltage $v_p(t)$ – not the DC field due to the static charge $\mathrm{Q}(z)$, and not the DC field due to V_o.

The temporal width $\mathcal{T}_p$ of the excitation voltage pulse $\mathrm{V}_p(t)$ is introduced in section 4.3. The $\mathrm{Q}(z) = q_1\ \delta(z - z_1)$ special case of $\overline{\mathrm{F}}(z,t)$ is given in equation (2.4). The implicit definition of $\mathrm{E}_z(z)$ given above is a generalization of the special case ($\mathrm{V}_a(t) = \mathcal{V}\delta(t)$) implicit definition given in equation (2.22).

For a parallel plate capacitor $\mathrm{E}_z(z)$ is a constant and there is, therefore, no need for spatially dependent scaling. For a coaxial (cable) capacitor, $\mathrm{E}_z(z) \sim 1/(r_o - z)$, where r_o is the radius of the outer conductor; see equation (2.25).

In short: because the impetus of the measured bulk signal $\mathrm{V}_b[t_n]$ is the initial, distributed *pressure* waveform $\overline{\mathrm{F}}(z,t)$, and because $\overline{\mathrm{F}}(z,t)$ is the product of the (possibly spatially dependent) excitation electric field $\mathrm{E}_z(z)$ and the desired charge waveform $\mathrm{Q}(z)$, the recovered, normalized pressure waveform $\mathrm{R}[z_i]$ must divided by the excitation electric field to determine (the shape of) $\tilde{\mathrm{Q}}[z_i]$. It will be shown that only the shape of $\mathrm{E}_z(z)$ is needed; the overall scale of $\mathrm{E}_z(z)$ is effectively determined by the un-normalization procedure described in section 4.15.5.

4.15.3 SD Filtering And The Spatial Sampling Interval

Note that sampled abscissa's z_i at which $\mathrm{R}[z_i]$ is to be determined need not be spaced evenly in z. According to (4.60), each $\mathrm{R}[z_i = z_i']$ can be determined independently of all the other $\mathrm{R}[z_i]$'s. This section discusses how to select a spatial sampling rate.

The Nyquist Interval

Adapting the results of section 2.6 to the the current case, where

$$\underline{\mathcal{P}}(f) = \frac{\underline{V_b}(f)}{\underline{H_e}(f)} \tag{4.64}$$

If $\underline{\mathcal{P}}(f)$ is abruptly bandlimited at f_m but otherwise noise-free, then

$$\mathrm{R}(f_m, z) = \mathcal{Q}(z) * \mathrm{D}(f_m, z) \tag{4.65}$$

where

$$\mathrm{D}(f_m, z) = \exp(z\ \alpha(f_m))\ \frac{\sin(2\pi f_m z/c(f_m))}{\pi z} \tag{4.66}$$

$$= \exp(z/\Lambda)\ \frac{\sin(2\pi z/\lambda)}{\pi z} \tag{4.67}$$

and

$$\lambda = \lambda(f_m) \equiv \frac{c(f_m)}{f_m} \tag{4.68}$$

$$\Lambda = \Lambda(f_m) \equiv \frac{1}{\alpha(f_m)} \tag{4.69}$$

Note that, according to Stenger's definition [94] of the sinc function,

$$\lim_{\Lambda\to\infty} \mathrm{D}(f_m, z) = \frac{\sin(2\pi z/\lambda)}{\pi z} = \frac{2}{\lambda}\ \mathrm{sinc}(\frac{2}{\lambda}\ z) \tag{4.70}$$

so that, when $\Lambda \equiv 1/\alpha(f_m) = \infty$,

$$\mathrm{R}(f_m, z) = \frac{2}{\lambda}\ \mathcal{Q}(z) * \mathrm{sinc}(\frac{2}{\lambda}\ z) \tag{4.71}$$

The results of the sampling theorem [93] to this special (sharp bandlimiting, $\alpha(f_m) = 0$) case are clear: information about $\mathrm{R}(f_m, z)$ will be irretrievably lost to aliasing if the spacing Δz between consecutive z_i's is larger than the Nyquist interval

$$\Delta z_n \equiv \frac{\lambda}{2} = \frac{c(f_m)}{2f_m} \tag{4.72}$$

It is, therefore, recommended that the sampling interval Δz be some 'small' fraction χ of Δz_n:

$$\Delta z_\chi = \chi\ \Delta z_n \tag{4.73}$$

where

$$0 < \chi \ll 1 \tag{4.74}$$

Adapting the well-known results associated with the sampling theorem, the recommended procedure for the sharp bandlimiting, $\alpha(f_m) = 0$ case is to oversample the unregularized $\mathrm{R}(z)$ at the rate Δz_χ and then apply a lowpass spatial filter with cutoff wavenumber $1/\lambda$.

Spatially Dependent Nyquist Interval

The previous discussion assumed sharp bandlimiting and $\alpha(f_m) = 0$, so that the Darrell reduced to a sinc function. It then followed that the sampling interval Δz between successive sampling abscissa's z_i should be Δz_χ, and that filtering to remove the λ oscillations could successfully be performed post-recovery, in the inverse space domain.

These results do not apply to the $\alpha(f_m) > 0$ case because the $\alpha(f_m) > 0$ Darrell is not a sinc function. The $\alpha(f_m) > 0$ Darrell grows exponentially for

$$z \quad > \quad \Lambda \equiv 1/\alpha(f_m) \tag{4.75}$$

and the unregularized Δz_χ-sampled recovery $\mathrm{R}[z_i]$ can become dominated by the Darrell's $\exp(z/\Lambda)$ term when $z > \Lambda$. Inverse space domain filtering cannot be counted upon to remove this exponential growth.

This thesis advocates pre-recovery frequency domain BLG filtering of $\underline{\mathcal{P}}(f)$. This procedure produces a non-sharp bandlimited $\underline{\mathcal{P}}(f)$. Carefully applied, this procedure has been found to remove the $\exp(z/\Lambda)$ growth associated with the Darrell. It also removes the λ oscillations, and it inherently quells the often noise-ridden higher frequency components of the experimental $\underline{\mathcal{P}}(f)$.

Further, it is a simple matter to introduce spatially dependent filtering into the BLG filter $\mathrm{B}(f_c, f)$ via the SDB function $f_c(z)$ so that $\mathrm{B}(f_c, f) \rightarrow \mathrm{B}(f_c(z), f)$. Carefully applied, this procedure has been found to result in recoveries with the intuitively appealing (see section 1.13) property that the width of a recovered source impulse decreases with its placement depth.

But what should the interval Δz between successive sampled abscissa's z_i be for the SD BLD filtered Lyons recovery? Experience has shown that the experimenter will be rewarded if she takes a small leap of faith and extends the results of the sampling theorem to the SD BLG filtered recovery. Although the BLG filter $\mathrm{B}(f_c, f)$ does not introduce a sharp cutoff, it's f_c-dependent 3 dB point $f_3(f_c)$ $(= \kappa_3 f_c$, where $\kappa_3 \cong 0.24445)$ may reasonably be interpreted as f_m.

The result is a position z dependent quasi-Nyquist interval

$$\Delta z_q(z) \equiv \frac{c(\kappa_3\ f_c(z))}{2\ \kappa_3\ f_c(z)} \tag{4.76}$$

which is a spatially-dependent factor of approximately $f_m/(\kappa_3\ f_c(z))$ times larger than the true Nyquist interval Δz_n in the case where $c(f_m) \cong c(\kappa_3 f_c(z))$ for all z.

Rather than use (4.76) to implement a spatially dependent sampling interval, this thesis advocates determining the smallest value $\Delta z_q'$ of $\Delta z_q(z)$ (which should be near $z = 0$ because $f_c(z)$ decreases monotonically with z), and then sampling at a constant interval $\Delta z_o = \chi \Delta z_q'$ where χ is some small fraction as in (4.74).

Using equation (4.76) in this manner for the case of standard polyethylene (see section 6.2.1) and the standard $f_c(z)$ (see appendix B) has resulted in the choice $\Delta z_o = 2$ nanometers.

4.15.4 Determining The SDB Function $f_c(z)$

Calculation of some sample $R(z_i')$ of $R(z)$ via (4.60) requires z_i' and the signals $\underline{V}[f_k]$, $\underline{H}_e[f_k]$, $\underline{\mathcal{K}}[f_k]$, $\underline{C}_g[f_k]$, and the SDB function $f_c(z_i')$.

This section assumes that the proximal plate signal $\underline{V}_p[f_k]$ and the distal plate signal $\underline{V}_p[f_k]$ have been determined; these are the two signals that will, in turn, play the role of the generic $\underline{V}[f_k]$ in (4.60). It is also assumed that the experimental impulse response $\underline{H}_e[f_k]$, the propagation coefficient $\underline{\mathcal{K}}(f)$, and the complex group velocity $\underline{C}_g(f)$ have been determined. Given these signals, this section's goal is to describe one method of determining $f_c(z)$.

The Proximal Plate Recovery: Determining $f_c(0)$

Start by letting $\underline{V}[f_k] \rightarrow \underline{V}_p[f_k]$ and $f_c(z) = \infty$. Calculate $R[z_i]$ at a sequence of positions z satisfying $|z| < 5\lambda$. Use a spatial sampling rate of Δz_o, as determined in section (4.15.3).

Because $V_p[t_n] = -H_e[t_n]$ (see equation (4.27)), the operant data signal $\underline{\mathcal{P}}_p[f_k]$ in (4.60) must be

$$\underline{\mathcal{P}}_p[f_k] \equiv \frac{\underline{V}_p[f_k]}{\underline{H}_e[f_k]} = -1 \tag{4.77}$$

Substituting (4.77) and $B(\infty, f) = 1$ in (4.59), then comparing with (2.68):

$$D(f_m, z) \equiv \int_{-f_m}^{f_m} \left[\frac{1}{j2\pi} \frac{d\,\underline{\mathcal{K}}(f)}{df}\right] \exp(z\,\underline{\mathcal{K}}(f))\, df \tag{4.78}$$

$$= \int_{-f_m}^{f_m} \frac{\exp(z\,\underline{\mathcal{K}}(f))}{\underline{C}_g(f)}\, df \tag{4.79}$$

$$= 2\int_{0}^{f_m} \Re_e \left\{\frac{\exp(z\,\underline{\mathcal{K}}(f))}{\underline{C}_g(f)}\right\} df \tag{4.80}$$

results in the realization that the resulting sequence $R[z_i] = -D[f_m, z_i]$.

That is, the operation described above will result in a set of numerically approximate samples of the Darrell. Because the selected z_i's oversampled a range extending over many λ about $z = 0$, the Darrell's λ oscillations will be clearly visible. Now, experiment with various decreasing $f_c(z) =$ constant values and observe the lessening of the λ oscillations and commensurate increase in the central pulse width of the recovery. The tradeoff between the degree of allowable λ oscillation and the degree of allowable pulse spread is up to the experimenter's discretion.

The author chose to decrease $f_c(z)$ = constant just until the oscillations could not be seen on a plot showing the recovery of the entire pulse, and then another 20% reduction was executed 'for good measure.' This process is not yet an exact science. Denote the resulting value of $f_c(z)$ = constant as $f_c^{\rm hi}$. This value gives the first datapoint in $f_c(z)$: $f_c(0) = f_c^{\rm hi}$.

The Distal Plate Recovery: Determining $f_c(l)$

Now let $\underline{V}[f_k] \rightarrow \underline{V}_d[f_k]$, $f_c(z) = f_c^{\rm hi}$, and compute R$[z_i]$ for $|z-l| < 5\lambda$. The resultant recovery will look noisy in part because the operant data signal

$$\underline{\mathcal{P}}_d[f_k] \equiv \frac{\underline{V}_d[f_k]}{\underline{H}_e[f_k]} = 2\,\underline{H}[l, f_k] + \underline{\rm noise}[f_k] \tag{4.81}$$

The inclusion of the $\underline{\rm noise}[f_k]$ term in $\underline{\mathcal{P}}_d[f_k]$ follows from the assumption that the frequency dependence of the random noise signal injected into the measured calibration signal $V_c[t_n]$ for times t_n corresponding to the arrival of the proximal pulse was not precisely the same as the frequency dependence of the random noise signal injected into $V_c[t_n]$ for times t_n corresponding to the arrival of the distal pulse.

In the case of the proximal plate recovery the operant data signal was a noiseless $\underline{\mathcal{P}}_p[f_k] = -1$ and the range of z_i's sampled in that case were all presumably much less than l (assuming $5\lambda \ll l$) so that the frequency dependent 'boosting term' $\exp(z_i\ \alpha(f))$ in $\exp(z_i\ \underline{\mathcal{K}}(f))$ was relatively small for all the z_i's.

But now the mean position of the range of sampled z_i's is $\sim l$, so the boosting term is a relatively larger quantity $\sim \exp(l\ \alpha(f))$. The combined effect of the larger boosting term combined with the existence of noise in $\underline{\mathcal{P}}_d[f_k]$ results in a distal plate recovery that is noisier than the proximal plate recovery.

However, just as in the case of the proximal plate recovery, lowering $f_c(z)$ = constant will reduce the recovered noise at the expense of a wider (than the proximal plate recovery) distal plate recovery. The observed decrease in noise, λ oscillation, and Λ growth in the presence of a decreased $f_c(z)$ = constant selection are all consistent with the increased suppression of the relatively noisy higher frequencies that would otherwise be overamplified by the recovery's $\exp(z_i\ \alpha(f))$ term.

Again, decrease $f_c(z)$ = constant just until the oscillations cannot be seen on a plot showing the recovery of the entire pulse, and then execute another 20% reduction. Denote the resulting value of $f_c(z)$ = constant as $f_c^{\rm lo}$. This value gives the second datapoint in $f_c(z)$: $f_c(l) = f_c^{\rm lo}$.

Intermediate Values

When $f_c(0) > f_c(l)$ the proximal plate recovery will be thinner than the distal plate recovery. This is entirely in agreement with the *General Introduction*:

"Intuition suggests that the FWHM of shallow-source recoveries ought to be smaller than that of deep-source recoveries. This intuition follows from the realization that pressure waves generated by deep sources have to travel through more attenuative, dispersive material than do the pressure waves generated by shallow sources. Theoretically, in the absence if noise these deeper sources could be recovered equally as well as shallow sources. Practically, the finite noise level in the measured signal renders the more-attenuated signals generated by arbitrarily deep sources indistinguishable from the measurement noise."

In cases where the quantity $[l\ \alpha(f_c(l))] \ll 1$ the distortion caused by propagation loss through the dielectric is small, so $f_c(0)$ will approximately equal $f_c(l)$ and the two plate recoveries will have approximately the same width. But this special low-loss case is not the general case. This thesis focusses on the high loss case where $[l\ \alpha(f_c(l))] \geq 1$, in which case $f_c(0) > f_c(l)$.

It seems reasonable to expect that the cutoff function $f_c(z)$ will decrease monotonically, be concave up, and approach zero only asymptotically. The line connecting the two known values of $f_c(z)$ would not be appropriate because this line will cross zero at a finite value of z. Some function similar to

$$f_c'(z) = f_c^{\mathrm{hi}}\ \exp(-z/z^{\mathrm{e}}) \tag{4.82}$$

where

$$z^{\mathrm{e}} = \frac{l}{\ln(f_c^{\mathrm{hi}}/f_c^{\mathrm{lo}})} \tag{4.83}$$

would be more appropriate.

It is possible to 'test' this $f_c'(z)$ by computing modelled impulse responses $\hat{\mathrm{H}}[z_o; t_n]$ for various values of z_o, and then sampling the $\mathrm{R}(z)$ gleaned by submitting $\underline{\hat{H}}[z_o; f_k]$ as $\underline{V}[f_k]$ in (4.60) at abscissa's z_i satisfying $|z - z_o| < 5\lambda$ to determine whether or not observed degree of λ oscillation is the same that given by using $f_c(z) = f_c'(z_o)$ and following the approach used to determine $f_c(0)$ and $f_c(l)$.

The standard SDB function $\grave{f}_c(z)$ presented in figure B.2 was determined by performing this process, changing the value of $f_c'(z_o)$ in those cases where the test failed, then performing some additional hand-modifications to promote an apparently intrinsic tendency towards linear FWHM *vs* z behavior .

The $\mathrm{V}_p[t_n]$ and $\mathrm{V}_d[t_n]$ used were the same as that which generated the polymeric model presented in table 6.1. The resultant $\grave{f}_c(z)$ was found to be steeper than $f_c'(z)$ for z_i's near $z = 0^+$, and less steep than $f_c'(z)$ for z_i's near $z = l^-$. The value of $\grave{f}_c(z)$ for $z < 0$ was set at the constant value $f_c(0)$ to ensure continuity of $f_c(z)$. The value of $\grave{f}_c(z)$ for $z > l$ was extrapolated using the same method used to determine the intermediate, interpolated values.

4.15.5 The Un-Normalization Procedure

The Lyons recovery (4.60) produces a set of spatial samples $\mathrm{R}[z_i]$ corresponding to some pair of measured time samples $\{\mathrm{V}[t_n], \mathrm{H}_e[t_n]\}$ obtained from a material with a known (or at least approximately known; see sections 4.10 through 4.13.3) propagation coefficient $\underline{\mathcal{K}}(f)$. The units of $\mathrm{V}[t_n]$ and $\mathrm{H}_e[t_n]$ must be the same (because they are measured by the same apparatus) so the units of $\mathrm{R}[z_i]$ must be mm^{-1} (because z is measured in mm).

Presumably $\underline{\mathcal{K}}(f)$ was determined from a calibration signal $\mathrm{V}_c[t_n]$ which had been broken up into a proximal pulse $\mathrm{V}_p[t_n]$ and a distal pulse $\mathrm{V}_d[t_n]$ (see sections 4.8 and 4.10), and the goal is to determine estimates $\tilde{\mathrm{Q}}[z_i]$ to the bulk charge waveform $\mathrm{Q}(z)$ given samples $\mathrm{V}_b[t_n]$ of the bulk signal $\mathrm{V}_b(t)$ and knowledge of the capacitor's geometry (parallel-plate or coaxial-cable). It is assumed that $\mathrm{V}_c[t_n]$, $\mathrm{V}_b[t_n]$, and $\mathrm{H}_e[t_n]$ were obtained under similar experimental conditions ($\mathrm{V}_a(t)$, $\mathrm{H}_T(t)$, $\alpha(f)$, $c(f)$, ϵ, etc.; see section 4.8).

Generalizing equation (4.14)'s q_p beyond the planar geometry by defining it as the magnitude of the surface charge on the capacitor plate the transducer is attached to (ie: the proximal plate), the PESAW researcher knows *a priori* that the area ($\Delta z \sum_i \tilde{\mathrm{Q}}_p[z_i]$) of $\tilde{\mathrm{Q}}_p[z_i]$ should equal $-q_p$ where $\tilde{\mathrm{Q}}_p[z_i]$ is the un-normalized version of $\mathrm{R}_p[z_i]$ gleaned from $\mathrm{V}_p[t_n]$ (see section 4.2).

With q_d defined as the quantity of surface charge on the distal capacitor plate (for coaxial-cable geometry, $q_d > q_p$; for planar geometry, $q_d = q_p$) the PESAW researcher also knows *a priori* that the area of $\tilde{\mathrm{Q}}_d[z_i]$ should equal $2q_d$ where $\tilde{\mathrm{Q}}_d[z_i]$ is the un-normalized version of $\mathrm{R}_d[z_i]$ gleaned from $\mathrm{V}_d[t_n]$ (see section 4.2).

Drawing on the results of sections 2.2.3 and 4.15.2, the recovery $\mathrm{R}[z_i]$ must be divided by a geometry-dependent function of space $\mathrm{E}_z[z_i]$ before the quantity $\mathrm{R}[z_i]/\mathrm{E}_z[z_i]$ can be un-normalized (scaled by a constant ν) to represent samples of the desired charge waveform estimate $\tilde{\mathrm{Q}}[z_i]$.

Because the un-normalization procedure will take care of the overall scale (to ensure that $\Delta z \sum_i \tilde{\mathrm{Q}}_p[z_i] \cong -q_p$ and $\Delta z \sum_i \tilde{\mathrm{Q}}_d[z_i] \cong 2q_d$) only the *shape* of $\mathrm{E}_z(z)$ is important. For the planar case, $\mathrm{E}_z(z)$ is a constant so there is no need to change the shape of $\mathrm{R}[z_i]$ before un-normalizing it. For the cable case, $\mathrm{E}_z(z) \sim r_o/(r_o - z)$ (see equation (2.25)) so multiplying $\mathrm{R}[z_i]$ by $(r_o - z_i)/r_o$ prepares that $\mathrm{R}[z_i]$ for un-normalization.

There are two ways to select the un-normalization constant ν. First option: choose $\nu \equiv \nu_p$ to ensure that $\Delta z \sum_i \tilde{\mathrm{Q}}_p[z_i] = -q_p$. Second option: choose $\nu \equiv \nu_d$ to ensure that $\Delta z \sum_i \tilde{\mathrm{Q}}_d[z_i] = 2q_d$. In theory, ν_p should equal ν_d. In practice, experimental errors often conspire to violate the equivalence $\nu_p = \nu_d$.

Using these two values of ν (and the same 'shape change function' $\mathrm{E}_z(z)$), the PESAW researcher can determine two bulk recoveries $\tilde{\mathrm{Q}}_b[z_i]$: $\tilde{\mathrm{Q}}_b^{(p)}[z_i]$, corresponding to ν_p; and $\tilde{\mathrm{Q}}_b^{(d)}[z_i]$ corresponding to ν_d. The PESAW researcher must use her own discretion in determining which recovery is 'more valid.'

Chapter 5

Inverting Linear, First-Kind Fredholm IEs

A linear first-kind Fredholm integral equation (IE) has the form [30]

$$y(\tau) = \int_a^b K(\xi, \tau) x(\xi) d\xi \tag{5.1}$$

where a and b are constants. The function $K(\xi, \tau)$ is called the kernel of the IE. It is clear from this definition that the PESAW IE is a linear first-kind Fredholm IE, whether expressed in the time domain (7.3) or the frequency domain (7.6). To solve such an IE is to determine $x(\xi)$ given knowledge of $y(\tau)$, $K(\xi, \tau)$, a and b.

An IE is said to be singular "when one or both limits of integration become infinite or when the kernel approaches infinity at one or more points within the range of integration." [31] A kernel is said to be separable if [31]

$$K(\xi, \tau) = \sum_{k=1}^{n} g_k(\xi) h_k(\tau) \tag{5.2}$$

where the functions $g_1(\xi), \ldots, g_n(\xi)$ and the functions $h_1(\tau), \ldots, h_n(\tau)$ are linearly independent. A kernel is said to be Hermitian [31] if it satisfies $K(\xi, \tau) = K^*(\tau, \xi)$.

There are some theorems pertaining to the analytic solution of singular, linear first-kind Fredholm IEs, and to linear IEs with kernels which are either separable or Hermitian. Unfortunately the PESAW IE meets none of these criteria, except for the fact that the upper limit l may be taken as infinite because of the *a priori* knowledge that Q(z) vanishes for $z > l$. This fact will be taken up later, when the parallels between the PESAW IE and the Laplace transform are discussed. Otherwise, none of these theorems pertain to the PESAW IE and will, therefore, not be discussed.

The following quote from Numerical Recipes in C (NRiC,[30]) neatly outlines the difficulties posed by first-kind Fredholm IEs: "Fredholm equations of the first kind are often extremely ill-conditioned. Applying the kernel to a function is generally a

smoothing operation, so the solution, which requires inverting the operator, will be extremely sensitive to small changes or errors in the input. Smoothing often actually loses information, and there is no way to get it back in an inverse operation."

The Laplace transform is a linear, first-kind Fredholm IE. Chapter 7 shows that the CLDP IE inversion problem is a particular type of Laplace transform inversion problem (one where path of integration is a CLDP path). Stenger's warning about this class of problems is blunt: "it is a simple fact that all methods of inversion of the Laplace transform are ill-posed. [43]"

NRiC points out that "almost all methods for solving IEs numerically make use of quadrature rules" which discretize (5.1) into a set of linear equations which could, theoretically, be solved via linear algebra. However, Hansen [32] has pointed out that "all the classical numerical methods, such as LU and Cholesky factorization, fail to compute a meaningful solution once (5.1) has been discretized."

Hansen surveys "several numerical tools that can be used for the analysis and solution of systems of linear algebraic equations derived from Fredholm IEs of the first kind" and finds that if a regularized or 'smooth' solution is desirable, then the singular value decomposition (SVD) and the generalized singular value decomposition are the preferred tools for selecting a regularization parameter and a solution. Among the methods to which these results pertain are Tikhonov's method, truncated SVD, iterative methods, and "a whole class of regularization methods ... of which the most promising are semi-iterative methods and the method of conjugate gradients."

Convolution equations are the subclass of linear, first-kind Fredholm IEs for which $K(\xi, \tau)$ in (5.1) reduces to $K(\xi - \tau)$, while a and b take on the values $-\infty$ and $+\infty$, respectively. A frequency domain adaptation of Tikhonov's method to the problem of deconvolving signals modified by transmission through CLDP materials is introduced in chapter 3. NRiC [41] provides an overview and analysis of frequency domain deconvolution schemes.

NRiC notes that, until recently, the numerical solution of (non-convolution) IEs was almost never treated in numerical analysis textbooks. It is a relatively young science. "There are many different kinds of equations, each with many possible pitfalls; often many different algorithms have been proposed to deal with a single case." Given that this is the state of IE theory in general, and given that first-kind Fredholm IEs are among the most difficult of these equations to solve, it should come as no surprise that Hansen's is not the only authoritative voice to speak on this topic.

Tarantola [33] is one of these voices. He proposes a probabilistic approach to the solution of first-kind IEs and compares it to the Backus-Gilbert method, summarizing "I feel the probabilistic approach to be much richer than the mathematical approach of Backus and Gilbert, but they probably feel the contrary." NRiC also discusses the Backus-Gilbert method, and they both also discuss the Maximum Entropy method for the solution of first kind IEs. Wavelet analysis has also been proposed as a method for obtaining approximate numerical solutions to discretized first-kind Fredholm IEs [34]. On this topic, NRiC says: "wavelet transforms ... can ... be used to transform some classes of integral equations into sparse linear problems that allow fast solution [30]"

Stenger [59] uses Sinc-based methods to perform and analyze the inversion of linear, first-kind Fredholm IEs in general, and in the particular case of the inverse Laplace transform. Krylov [111] also discusses the numerical inversion of Laplace transforms.

Despite all these approaches to the numerical solution of linear first-kind Fredholm IEs, to the best of this author's knowledge no-one but those executing a Bromwich inversion [42, 75, 44] of the Laplace transform has considered the inversion of CLDP IEs ... except for the recent attempt by PEA researchers Li *et al* [20]. Li approached the inversion problem from the time-domain perspective by producing a time-domain kernel from frequency-domain values for $\alpha(f)$ and $c(f)$ gleaned from an effective time-domain through-transmission pulse pair.

Li generated the forward discretization matrix from her time-domain kernel, and solved it for her known plate pressure versus time waveform via the Jacobi relaxation method. She apparently met with success, as evidenced by the fact that her relaxation-recovery of the impulsive plate-charge distributions were thinner and taller than those gleaned via the dominant recovery, and yet had the same area. That is, her relaxation-recovery of the plate charges more closely approximated the spatially impulsive nature of these plate charges than did the dominant recovery.

Her success can be understood by realizing that even when attenuation and dispersion are non-negligible, the forward time-domain discretization matrix will tend to be diagonally dominant and, therefore, relatively easy to solve. Further: she used an iterative method, as recommended by Hansen. Forward time-domain discretization matrices tend to be diagonally dominant because charges *nearer* the proximal plate have the time of their peak plate pressure *sooner* than charges farther from the proximal plate; if dispersion were absent, the forward time-domain discretization matrix would be purely diagonal. See section 9.2.3 for a more complete discussion of these discretization matrices.

Chapter 6

Causality And Materials

The goal of this chapter is to outline the frequency domain (see appendix F) relationships pertaining to real, causal functions and materials. This discussion is relevant because this thesis is concerned only with waveforms (functions of space alone), signals (functions of time alone), and materials that are real and causal. A function is called causal if it vanishes for negative values of its argument. A material is called causal if its thickness l dependent transfer function

$$\underline{H}(l,f) = \exp(-l\,\underline{\mathcal{K}}(f)) \tag{6.1}$$

where

$$\underline{\mathcal{K}}(f) = \alpha(f) + \mathrm{j}\,\underbrace{2\pi f/c(f)}_{\beta(f)} \tag{6.2}$$

yields a causal temporal impulse response function $\mathrm{H}(l>0,t)$ when it is inverse Fourier transformed:

$$\mathrm{H}(l,t) \quad \overset{\mathcal{F}}{\Longleftrightarrow} \quad \underline{H}(l,f) \tag{6.3}$$

Materials which satisfy these conditions are called CLDP materials (Causal, Lossy, Dispersive, Plane-wave). See chapter 3 for proof and explanation of the terms and equations discussed above.

The results presented in this chapter will help in determining whether some given $\underline{\mathcal{K}}(f)$ corresponds to a causal material. Most of the results presented in this section have been culled from the excellent discussions of the frequency domain implications of causality found in Guillemin [45] and Hahn [47]. The section on the nearly-local Kramers-Kronig relations is the sole exception.

6.1 The Kramers-Kronig Relations

Although this material is covered by Guillemin and Hahn, the presentation given here was inspired especially by Siebert [65]. This section uses the definitions of the Fourier and Laplace transformations given in appendix F. Using the notation introduced there, the Kramers-Kronig (KK) relations state that the real and imaginary parts of the Fourier transform $\underline{G}(\aleph)$ of a causal $\mathrm{G}(x)$ must be a Hilbert transform pair. To see this, start with the following direct-space statement that $\mathrm{G}(x)$ is causal:

$$\mathrm{G}(x) = \mathrm{G}(x)\ \mathrm{U}(x) \tag{6.4}$$

where $\mathrm{U}(x)$ is the Heaviside unit step function satisfying

$$\mathrm{U}(x) \quad \overset{\mathcal{F}}{\Longleftrightarrow} \quad \frac{\delta(\aleph)}{2} + \frac{1}{\mathrm{j}2\pi\aleph} \tag{6.5}$$

The result of Fourier transforming equation (6.4) via the convolution theorem, then inserting (6.5), is

$$\underline{G}(\aleph) = \underline{G}(\aleph) * \left[\frac{\delta(\aleph)}{2} + \frac{1}{\mathrm{j}2\pi\aleph}\right] \tag{6.6}$$

where the $*$ denotes convolution. Applying Dirac's identity to (6.6), then rearranging, yields:

$$\underline{G}(\aleph) = \underline{G}(\aleph) * \frac{1}{\mathrm{j}\pi\aleph} \tag{6.7}$$

Separating $\underline{G}(\aleph)$ into its real and imaginary parts $G_r(\aleph)$ and $G_i(\aleph)$, respectively, yields

$$\left[G_r(\aleph) + \mathrm{j}\ G_i(\aleph)\right] = \left[G_r(\aleph) + \mathrm{j}\ G_i(\aleph)\right] * \frac{1}{\mathrm{j}\pi\aleph} \tag{6.8}$$

Separating (6.8) into its real and imaginary components yields the Hilbert transform relations $\mathcal{H}$:

$$G_r(\aleph) = G_i(\aleph) * \frac{1}{\pi\aleph} \quad \overset{\mathcal{H}}{\Longleftrightarrow} \quad G_i(\aleph) = G_r(\aleph) * \frac{-1}{\pi\aleph} \tag{6.9}$$

where the principal value of the convolution integral is to be taken in the case of a singular integrand.

This derivation of the KK relations is reversible, meaning that if some propagation coefficient $\underline{K}(f)$ yields an $\underline{H}(l,f)$ with real and imaginary parts that satisfy the KK relations then that $\underline{H}(l,f)$ corresponds to a causal material.

Note that the Hilbert transform relations are linear, implying (in part) that if $\underline{H}(l,f)$ satisfies the KK relations then $\Upsilon\underline{H}(l,f)$ (where Υ is some positive constant) will also satisfy the KK relations. It follows that if some $\{\alpha(f), c(f)\}$ pair corresponds to a causal material, then the material described by $\{\alpha(f) - \ln(\Upsilon)/l, c(f)\}$ will also be causal.

Adding a constant to the $\alpha(f)$ associated with a causal material will result in another causal material. However, depending on the original $\alpha(f)$ and the constant added, the resulting material may or may not be stable (if $\alpha(f) > 0$ for some band of frequencies, then the amplitude of those frequencies will grow exponentially as the wave propagates).

6.1.1 Example: Bromwich Materials

A Bromwich material is defined as a material for which $\alpha(f) = \alpha_b$ and $c(f) = c_b$, where α_b and c_b are constants satisfying $\alpha_b \geq 0$ and $c_b > 0$. These materials bear the name 'Bromwich' because, as section 7.4 will show, the so-called CLDP path associated this choice of form for $\alpha(f)$ and $c(f)$ corresponds to the Bromwich Laplace transform inversion path [42, 75, 44].

Inserting the Bromwich models for $\alpha(f)$ and $c(f)$ into (6.1), it follows that the real and imaginary parts of the Bromwich material's transfer function $\underline{H}_b(l,f)$, denoted $\mathrm{H}_{br}(l,f)$ and $\mathrm{H}_{bi}(l,f)$ respectively, are given by

$$\mathrm{H}_{br}(l,f) = \exp(-l\ \alpha_b)\ \cos(2\pi f l/c_b) \tag{6.10}$$

and

$$\mathrm{H}_{bi}(l,f) = -\exp(-l\ \alpha_b)\ \sin(2\pi f l/c_b) \tag{6.11}$$

From the fact that

$$\cos(2\pi f l/c_b) \quad \overset{\mathcal{H}}{\Longleftrightarrow} \quad -\sin(2\pi f l/c_b) \tag{6.12}$$

it follows via the KK relations that the Bromwich material is causal.

Note that c_b must be positive because, otherwise, the combined effect of the even symmetry of $\mathrm{H}_{br}(l,f)$'s cos term and the odd symmetry of $\mathrm{H}_{bi}(l,f)$'s sin term would be to remove the leading minus sign on $\mathrm{H}_{bi}(l,f)$. In this case $\mathrm{H}_{br}(l,f)$ and $\mathrm{H}_{bi}(l,f)$ would not be a Hilbert transform pair, so the material would not be causal.

This same result may be seen more directly by inserting the Bromwich model directly into equations (6.1),(6.2), and (6.3) to arrive at

$$\mathrm{H}(z,t) = \exp(-z\alpha_b)\ \delta(t - z/c_b) \tag{6.13}$$

It should be clear that (assuming $z > 0$) if c_b is positive then $\delta(t - z/c_b)$ will be a causal signal, whereas if $c_b < 0$ then $\delta(t - z/c_b)$ will be an acausal signal. Also, the constraint $\alpha_b \geq 0$ follows from the requirement that

$$\lim_{z\to\infty}\{\mathrm{H}(z,t)\} \tag{6.14}$$

remain bounded.

6.2 The Nearly-Local KK Relations

Whereas the KK relations exactly relate the real and imaginary parts of the entire spectrum of any causal material's transfer function $\underline{H}(l,f)$, the nearly local Kramers-Kronig (NLKK) relations [66, 67, 68, 69] state approximate relations between $\alpha(f)$ and $c(f)$ for a particular subclass of materials over some frequency range. A derivation of these relations can be found in O'Donnell [35].

According to the NLKK relations, if some material has no sharp resonances in the frequency range of interest, and if

$$\left[\frac{\alpha(f)c(f)}{2\pi f}\right]^2 \ll 1 \tag{6.15}$$

is valid for all frequencies, then:

$$\alpha(f) \cong \frac{\pi^2 f^2}{c^2(f)}\ \frac{dc(f)}{df} \tag{6.16}$$

Integrating (6.16) yields

$$\frac{1}{c(f_o)} - \frac{1}{c(f)} \cong \frac{1}{\pi^2}\int_{\phi=f_o}^{f} \frac{\alpha(\phi)}{\phi^2}\ d\phi \tag{6.17}$$

If, for frequencies f of interest,

$$|c(f_o)| \gg |c(f) - c(f_o)| \tag{6.18}$$

then the left hand side of (6.17) is approximately $[c(f) - c(f_o)]/c^2(f_o)$, and

$$c(f) \cong c(f_o) + \left[\frac{c(f_o)}{\pi}\right]^2 \int_{\phi=f_o}^{f} \frac{\alpha(\phi)}{\phi^2}\, d\phi \tag{6.19}$$

Note that whereas the KK relations are global (require information over all frequencies), (6.19) is nearly local because it allows the calculation of an approximate $c(f)$ given knowledge of $\alpha(f)$ over a finite range (between f_o and f). Equation (6.16) is almost entirely local; it allows the calculation of an approximate $\alpha(f)$ at some frequency f' given knowledge of $c(f)$ over an infinitesimal range of frequencies about f'.

Following Hahn's discussion [47] of minimum phase transfer functions, the NLKK relations seem to rely on the fact that the real and imaginary parts $\alpha(f)$ and $\beta(f)$ of a propagation coefficient

$$\underline{\mathcal{K}}(f) = \alpha(f) + \mathrm{j}\,\beta(f) \tag{6.20}$$

which corresponds to a causal $\mathrm{H}(l,t)$, and which corresponds to a $\underline{\mathcal{K}}(\underline{s}/(\mathrm{j}2\pi))$ which has all its zeros in the left half plane, form a Hilbert transform pair:

$$\alpha(f) \quad \overset{\mathcal{H}}{\Longleftrightarrow} \quad \beta(f) \tag{6.21}$$

Quoting Hahn directly: "These relations [between $\alpha(f)$ and $\beta(f)$] can be converted to take the form of the well-known Bode phase-integral theorem:

$$\beta(f_o) = \frac{\pi}{2}\left|\frac{d\alpha}{du}\right|_o + \frac{1}{\pi}\int_{-\infty}^{\infty}\left[\left|\frac{d\alpha}{du}\right| - \left|\frac{d\alpha}{du}\right|_o\right]\ln\left(\coth\left(\left|\frac{u}{2}\right|\right)\right)\, du \tag{6.22}$$

where $u = \ln(f/f_o)$ is the normalized logarithmic frequency scale, and $d\alpha/du$ is the slope of the α-curve in a ln-ln scale. The Bode formula shows that for the minimum-phase transfer functions the phase depends on the slope of the α-curve ... The factor $\ln(\coth(|u/2|))$ is peaked at $u = 0$ (or $f = f_o$) and hence the phase at a given f_o is mostly influenced by the slope $d\alpha/du$ in the vicinity of f_o." The principal value of the integral (6.22) is to be taken in the case of a singular integrand.

O'Donnell [35] does not explicitly invoke the Bode phase-integral in his derivation of the NLKK relations, but he does explicitly invoke the KK relations. Like Bode and Hahn, he also introduces the normalized log frequency scale $u = \ln(f/f_o)$ and arrives at an integral involving the function $\ln(\coth(|u/2|))$.

O'Donnell proffers a plot of $\ln(\coth(|u/2|))$ and observes that "the function has a sharp singularity at $u = 0$, and thus the magnitude of the integral is dominated by the value of the integrand at $u = 0$." O'Donnell therefore Taylor-expands $\ln(\coth(|u/2|))$ about $u = 0$ and, after making some approximations, arrives at the NLKK relations.

The following quote from O'Donnell places the entire situation in context: "Bode [104] demonstrated that at any frequency the phase shift is approximately related to

the local rate of change of the gain with frequency. The approximation is quite accurate if both the gain and phase shift are sufficiently well behaved (*ie*, exhibit no resonances) over a limited frequency range centered at the frequency of interest."

6.2.1 Example: Polymeric Materials

Assuming that hysteresis absorption is the dominant loss process manifesting itself in some polymer, the polymeric attenuation coefficient may be modelled as [71, 70, 69]

$$\alpha_p(f) = m\, f + b \tag{6.23}$$

where m and b are constants which depend on the polymer under study. Inserting (6.23) into (6.19) yields

$$c_p(f) = c_p(f_o) + \left[\frac{c_p(f_o)}{\pi}\right]^2 \left[m \ln(\frac{f}{f_o}) + b\left[\frac{1}{f_o} - \frac{1}{f}\right]\right] \tag{6.24}$$

This model for $\alpha(f)$ and $c(f)$ clearly includes no resonances. Submitting (6.23) and (6.24) to (6.15), and setting $b = 0$ for simplicity, yields

$$\left[\frac{m}{2\pi}\left[c_p(f_o) + m\left[\frac{c_p(f_o)}{\pi}\right]^2 \ln(\frac{f}{f_o})\right]\right]^2 \ll 1 \tag{6.25}$$

This is the $b = 0$ requirement that m, f_o, and $c_p(f_o)$ must satisfy within the frequency range f for the hysteresis absorption model for $\alpha_p(f)$ and the resultant NLKK model for $c_p(f)$ to satisfy the NLKK relations.

It is interesting to note that submitting the $b = 0$ polymeric model to equations (6.1), (6.2), and (6.3), then applying Fourier theory's convolution theorem, yields the following expression for the polymeric thickness l dependent impulse response function:

$$\mathrm{H}_p(l,t) = \left[\frac{2\, l\, m}{(lm)^2 + (2\pi t)^2}\right] * \left[\mathcal{F}^{-1}\{\exp(-\mathrm{j}2\pi f l / c_p(f))\}(t)\right] \tag{6.26}$$

where $c_p(f)$ is given by (6.24) and the $*$ denotes temporal convolution.

The $b = 0$ polymeric model for $\mathrm{H}(l,t)$ is the convolution of the term associated with dispersion and the term associated with attenuation. The term associated with attenuation is a Lorentzian with full width at half maximum lm/π and peak output $2/(lm)$.

The Lorentzian term is acausal; it does not vanish for any finite value of t. The dispersive term modulates the acausal Lorentzian term, making the entire temporal response (approximately) causal for each $l > 0$.

This analysis suggests that the temporal width of the impulse response of a $b = 0$ polymer should increase approximately linearly with l, and that the value of its peak output should vary as the inverse of l. The expected linear increase in temporal FWHM with l is implicit in the exhibited linear increase in spatial FWHM with l depicted in figure 1.3's $\mathrm{R}_d(z)$; $\mathrm{R}_d(z)$ uses a linear mapping from time to space.

6.2.2 The Standard Model For Polyethylene

Cooke and Lyons [69] applied chapter 4's inverse medium techniques to more than one sample of polyethylene, averaged the results for m, b, and $c(f_o)$, and arrived at the following model:

m	=	6.29	±5%	dB/(cm MHz)
b	=	-2.5	±50%	dB/cm
f_o	=	1		MHz
$c(f_o)$	=	1.982	±0.2%	mm/μs

Table 6.1: Cooke & Lyons' experimentally determined values for the hysteresis absorption/nearly local Kramers-Kronig model of polyethylene.

Setting $b = 0$ and changing units yields

m	=	0.073	Np/(mm MHz)
f_o	=	1	MHz
$c(f_o)$	=	1.982	mm/μs

Table 6.2: Values for the hysteresis absorption/nearly local Kramers-Kronig model of standard polyethylene.

This thesis' standard model of PE is determined by submitting these values (and $b = 0$) to the polymeric model for $\alpha(f)$ and $c(f)$ given by (6.23) and (6.24). The resulting functions are denoted $\alpha_p(f)$ and $c_p(f)$. Submitting $\alpha_p(f)$ and $c_p(f)$ into (6.2) yields the standard model for PE's propagation coefficient, denoted $\underline{\mathcal{K}}_p(f)$.

Similarly, standard PE's thickness l dependent transfer function is denoted $\underline{H}_p(l, f)$ and standard PE's thickness l dependent impulse response function is denoted $\mathrm{H}_p(l, t)$.

Submitting the standard PE model to the NLKK requirement (6.25) and allowing $(0.1)^2 \ll 1$ yields the generous result that the frequency range acceptable to the NLKK relations is $\{10^{-158}, 10^{99}\}$ MHz.

6.3 The Paley-Wiener Criterion

The Paley-Wiener criterion [47, 72, 45]is given by

$$\int_0^\infty \frac{\alpha(f)}{1+f^2}\,df \quad < \quad \infty \tag{6.27}$$

An important corollary of this Paley-Wiener theorem is that no real, physical (ie: causal) system can absolutely filter out a finite frequency range. This would correspond to $\alpha(f) \rightarrow \infty$ for that frequency range, and so (6.27) would automatically fail. Guillemin points out that if the asymptotic behavior of $\alpha(f)$ is described by

$$\alpha(f) \rightarrow f^n \qquad \text{for} \quad f \rightarrow \infty \tag{6.28}$$

then the integral (6.27) can have a finite value only if $n < 1$.

6.3.1 Failure Of The Polymeric Model

It follows immediately that the hysteresis absorption model of polymeric attenuation (6.23) cannot be valid over all frequencies.

However: first, this model is just barely on the wrong side of the border $n < 1$; this Paley-Wiener criterion would be satisfied if $\alpha(f) = \tilde{m} f^{(1-\diamond)}$ where $\diamond$ is an arbitrarily small positive number (perhaps the hysteresis absorption model should be modified in this manner). Second, this model seems to agree well with experimental results (see [69]), at least for frequencies in the MHz range. Third, the NLKK relations are not meant to apply to all frequencies; they are nearly local. Fourth, this thesis' numeric recoveries do not seem to suffer from the 'acausal' nature of the standard model of PE. Therefore this thesis will continue to use the standard model of PE in spite of its seeming inconsistency.

6.3.2 Existence Theorem

Siebert [72] points out that, for every $\alpha(f)$ satisfying (6.27) there exists a corresponding $\beta(f)$ such that the corresponding $\mathrm{H}(l,t)$ is causal. The NLKK relations give one approximate method for determining this $\beta(f)$. Guillemin [45] also addresses this problem, as does the Bode phase integral theorem (6.22).

6.4 The Paley-Wiener-Guillemin Criterion

Guillemin [45] submits another version of the Paley-Wiener criterion which speaks to the asymptotic behavior of $\beta(f)$. He points out that if the asymptotic behavior of $\beta(f) \equiv 2\pi f / c(f)$ is described by

$$\beta(f) \rightarrow f^m \qquad \text{for} \quad f \rightarrow \infty \tag{6.29}$$

then there exists a corresponding $\alpha(f)$ such that the related $\mathrm{H}(l,t)$ is causal only if $1 \leq m < 2$. The $m = 1$ case corresponds to the delay-only material for which $c(f)$ is constant. Again, both Guillemin and the NLKK relations offer suggestions about how to determine the $\alpha(f)$ which corresponds to an acceptable $\beta(f)$.

6.4.1 Existence Theorem

According to Hahn [47], the Bode phase integral theorem (6.22) follows from the fact that the $\alpha(f)$ and $\beta(f)$ of a minimum phase transfer function must be a Hilbert transform pair (6.21).

Although the author has not found this stated explicitly in the literature, it seems that if some given $\beta(f)$ satisfies the Paley-Wiener-Guillemin criterion then there must exist at least one $\alpha(f)$ such that the corresponding $\mathrm{H}(l,t)$ is causal. From the results of section 6.1, it follows that if there exists even one such associated $\alpha(f)$ then there must exist an infinite number of associated $\alpha(f)$'s which differ from each other by only a constant.

6.5 Analytic Propagation Coefficients

Guillemin [45] uses Cauchy's integral formula and the assumption of a

$$\underline{\gamma}(\underline{s}) = -l\, \underline{\mathcal{K}}(\underline{s}/(\mathrm{j}2\pi)) \tag{6.30}$$

that has acceptable $\underline{s} \rightarrow \underline{\infty}$ asymptotic behavior (*ie*: satisfies the Paley-Wiener criteria) and is analytic in the entire right half plane (RHP, inclusive of $\mathrm{j}\omega$ axis) as a starting point for a rigorous inspection of the Hilbert transform relations between the real and imaginary parts of

$$\underline{H}(l,f) = \exp(\underline{\gamma}(\mathrm{j}2\pi f)) = \exp(-l\, \underline{\mathcal{K}}(f)) \tag{6.31}$$

Because a function $\underline{H}(l,f)$ that satisfies the Hilbert transform relations must be causal (see section 6.1), it follows that if $\underline{\mathcal{K}}(\underline{s}/(\mathrm{j}2\pi))$ is analytic in the RHP and has acceptable $\underline{s} \rightarrow \underline{\infty}$ asymptotic behavior then it must correspond to a causal $\mathrm{H}(l,t)$.

This result justifies investigation of the so-called transmission line materials. Their $\underline{\gamma}(\underline{s})$'s are analytic in the entire RHP (simply let $f \rightarrow \underline{s}/(\mathrm{j}2\pi)$ in (6.38) and (6.39)), and the $f \rightarrow \infty$ asymptotic behavior of their $\alpha(f)$'s is either $\sim \sqrt{f}$ (if $\mathrm{S}' > 0$) or $\sim$ constant (if $\mathrm{S}' = 0$). In either case, their $\alpha(f)$'s $f \rightarrow \infty$ asymptotic behavior is well within the $\alpha(f) \sim f^1$ limit set by the Paley-Weiner criterion.

6.5.1 Example: The Standard Skin-Effect Material

Extending Staelin *et al* [49], a periodic transmission line (TL) with lumped parallel admittance $\underline{Y}'(f)\Delta z$ and lumped series impedance $\underline{Z}'(f)\Delta z$ per length Δz will yield a propagation coefficient

$$\underline{\mathcal{K}}(f) = \sqrt{\underline{Y}'(f)\,\underline{Z}'(f)} \tag{6.32}$$

in the limit $\Delta z \to 0$.

Using the following result [55] for real numbers X_r and X_i,

$$\sqrt{X_r + j\,X_i} = \sqrt{\frac{\sqrt{X_r^2 + X_i^2} + X_r}{2}} + j\sqrt{\frac{\sqrt{X_r^2 + X_i^2} - X_r}{2}} \tag{6.33}$$

if the product $\underline{Y}'(f)\,\underline{Z}'(f)$ can be separated into real and imaginary parts $X_r(f)$ and $X_i(f)$

$$\underline{Y}'(f)\,\underline{Z}'(f) = X_r(f) + j\,X_i(f) \tag{6.34}$$

then the attenuation coefficient $\alpha(f)$ and phase velocity $c(f)$ determined by $\underline{Y}'(f)$ and $\underline{Z}'(f)$ through

$$\underline{\mathcal{K}}(f) = \alpha(f) + j\,2\pi f/c(f) \tag{6.35}$$

will be

$$\alpha(f) = \frac{1}{\sqrt{2}}\sqrt{X_r(f)}\sqrt{1 + \sqrt{1 + [\frac{X_i(f)}{X_r(f)}]^2}} \tag{6.36}$$

and

$$c(f) = \frac{\sqrt{2}\,2\pi f}{X_i(f)}\sqrt{X_r(f)}\sqrt{1 + \sqrt{1 + [\frac{X_i(f)}{X_r(f)}]^2}} \tag{6.37}$$

The TL model presented here uses

$$\underline{Y}'(f) = \overbrace{j\,2\pi f C'}^{\text{capacitor}} \tag{6.38}$$

$$\underline{Z}'(f) = \underbrace{R'}_{\text{resistor}} + \underbrace{j\,2\pi f L'}_{\text{inductor}} + \underbrace{S'\sqrt{j\,2\pi f}}_{\text{skin effect}} \tag{6.39}$$

In a coaxial cable, the capacitive and inductive terms correspond to the cables' inherent per-length capacitance and inductance. The resistive term corresponds to the assumed-finite conductivity of the cable walls. This model does not include dielectric leakage; there is no shunt conductance. The remaining term S′ models high frequency skin-effect impedance in the conducting walls [50, 51].

For this model,

$$X_r(f) = -2\pi f C' \left[L'\, 2\pi f + S'\sqrt{\pi f} \right]$$

$$X_i(f) = 2\pi f C' \left[R' + S'\sqrt{\pi f} \right]$$

The resultant model for the attenuation coefficient and phase velocity is

$$\alpha(f) = \sqrt{C'\pi f}\sqrt{L'\, 2\pi f + S'\sqrt{\pi f}}\sqrt{-1 + \sqrt{1 + \left[\frac{R' + S'\sqrt{\pi f}}{L'\, 2\pi f + S'\sqrt{\pi f}} \right]^2}} \tag{6.40}$$

and

$$c(f) = \frac{2\sqrt{\pi f}}{\sqrt{C'}\left[R' + S'\sqrt{\pi f} \right]}\sqrt{L'\, 2\pi f + S'\sqrt{\pi f}}\sqrt{-1 + \sqrt{1 + \left[\frac{R' + S'\sqrt{\pi f}}{L'\, 2\pi f + S'\sqrt{\pi f}} \right]^2}} \tag{6.41}$$

It is worth pointing out that if $\{R', C', L'\} > 0$, and if $S' \geq 0$, then

$$\lim_{f \to \infty} c(f) = \frac{1}{\sqrt{L'C'}} \tag{6.42}$$

Further, if $S' = 0$

$$\lim_{f \to \infty} \alpha(f) = \frac{R'}{2}\sqrt{\frac{C'}{L'}} \tag{6.43}$$

These TL materials are introduced only to allow comparison of the Lyons recovery for standard PE with the Lyons recovery of some other causal materials – to show that the results are general.

	skin-effect	units
R′	0.378503	Ω/mm
S′	0.378503	$\Omega/(\text{mm}\sqrt{\text{MHz}})$
C′	0.471105	$1/(\Omega\ \text{mm MHz})$
L′	0.471105	$\Omega/(\text{mm MHz})$

Table 6.3: Values of the transmission line components which yield this thesis' 'standard skin-effect material.'

Therefore, rather than choose 'physical' values for the example TL material, the example TL material will adopt values that put it roughly on the same scale as standard PE. The example TL material is called the standard skin effect material, and its four parameters $\{\text{R}', \text{S}', \text{C}', \text{L}', \}$ are given by

Note that, in these units, the numeric value of R′ is the same as that of S′, and the numeric value of C′ is the same as that of L′. The standard skin-effect materials' specific component values were selected by requiring that the standard skin effect material and standard polyethylene have the same $f = 25$ MHz value for both the attenuation coefficient and the phase velocity. That is,

$$\alpha_p(25\ \text{MHz}) = \alpha_s(25\ \text{MHz}) = 1.825\ \text{Np/mm} \tag{6.44}$$

and

$$c_p(25\ \text{MHz}) = c_s(25\ \text{MHz}) = 2.07553\ \text{mm}/\mu\text{s} \tag{6.45}$$

The standard Bromwich material's constant values for $\alpha(f)$ and $c(f)$ were selected to agree with this constraint, so all three materials investigated in this thesis (polyethylene, skin-effect, Bromwich) have the same 25 MHz values for the attenuation coefficient and phase velocity. Appendix C compares these three materials' $\alpha(f)$ and $c(f)$ curves, and also depicts each of their $l = 1$ mm impulse response functions $\text{H}(1\ \text{mm}, t)$.

Chapter 7

CLDP Transforms

7.1 The Principal Insight

The principal insight which led to this thesis' approach to the inversion of CLDP IEs (and, by extension, to the inversion PESAW IEs as well) was the realization that

$$\underline{\mathcal{P}}(f) = \underline{\tilde{\mathcal{Q}}}(\underline{\mathcal{K}}(f)) \tag{7.1}$$

That is, the frequency dependent values of the Fourier transform $\underline{\mathcal{P}}(f)$ of the temporal CLDP response signal $\mathcal{P}(t)$ may be interpreted as the values of the spatial Laplace transform $\underline{\tilde{\mathcal{Q}}}(\underline{\mathcal{K}})$ of the source waveform $\mathcal{Q}(z)$ along a path in the spatial Laplace plane $\underline{\mathcal{K}}$ given parametrically by the propagation coefficient $\underline{\mathcal{K}}(f)$.

Equation (D.1) constitutes CLDP theory's requisite link between space and time (or frequency). This link subsumes the dominant recovery's fundamental link c_d between space and time (see equation (1.6)).

To derive (D.1), start with the PESAW-CLDP IE (2.18):

$$\mathcal{P}(t) = \int_0^l \mathcal{Q}(z)\ \mathrm{H}(z,t)dz \tag{7.2}$$

Outside the PESAW context there is no reason for the source waveform $\mathcal{Q}(z)$ to vanish for $z > l$ so the upper integration limit l of (7.2) may be raised to infinity to reflect the possibility of a source extending throughout all $z \geq 0$.

Thinking another way, if it is known that $\mathcal{Q}(z)$ vanishes for $z > l$ then raising the upper integration limit l to infinity cannot change the result of the integration. Either way, replacing the upper integration limit l with infinity is justified. This thesis is only concerned with causal source waveforms so the lower integration limit $z = 0$ remains.

With this modification, (7.2) becomes

$$\mathcal{P}(t) = \int_0^\infty \mathcal{Q}(z)\ \mathrm{H}(z,t)dz \tag{7.3}$$

Using (2.15) to justify replacing

$$\mathrm{H}(z,t) = \mathcal{F}^{-1}\{\exp(-z\,\underline{\mathcal{K}}(f))\}(t) \tag{7.4}$$

in (7.3) yields

$$\mathcal{P}(t) = \int_0^\infty \mathcal{Q}(z)\,\left[\mathcal{F}^{-1}\{\exp(-z\,\underline{\mathcal{K}}(f))\}(t)\right]\,dz \tag{7.5}$$

Fourier transforming both sides of (7.5) results in

$$\underline{\mathcal{P}}(f) = \int_0^\infty \mathcal{Q}(z)\,\exp(-z\,\underline{\mathcal{K}}(f))\,dz \tag{7.6}$$

The validity of this result follows from the fact that the Fourier transform is an integral over *time*, whereas (7.5) is an integral over *space*. For each position $z = z_o$ the Fourier transform integral may be taken inside the spatial integral (7.5).

Now compare (7.6) with appendix F's definition of the spatial Laplace transform $\underline{\tilde{\mathcal{Q}}}(\underline{\mathcal{K}})$ of the source waveform $\mathcal{Q}(z)$:

$$\underline{\tilde{\mathcal{Q}}}(\underline{\mathcal{K}}) = \int_0^\infty \mathcal{Q}(z)\,\exp(-z\,\underline{\mathcal{K}})\,dz \tag{7.7}$$

Defining

$$\underline{\mathcal{P}}_o \equiv \underline{\mathcal{P}}(f_o) \tag{7.8}$$

and

$$\underline{\mathcal{K}}_o \equiv \underline{\mathcal{K}}(f_o) \tag{7.9}$$

it should be clear that, for $f = f_o$,

$$\underline{\mathcal{P}}_o = \underline{\tilde{\mathcal{Q}}}(\underline{\mathcal{K}}_o) \tag{7.10}$$

and that, for the generic frequency f,

$$\underline{\mathcal{P}}(f) = \underline{\tilde{\mathcal{Q}}}(\underline{\mathcal{K}}(f)) \tag{7.11}$$

as advertised.

7.2 CLDP Paths

The spatial Laplace transform variable

$$\underline{\mathcal{K}} = \alpha + \mathrm{j}\,\beta = \alpha + \mathrm{j}\,2\pi\flat \tag{7.12}$$

denotes a generic position in the spatial Laplace plane $\underline{\mathcal{K}}$ just as the temporal Laplace transform variable

$$\underline{s} = \sigma + \mathrm{j}\,\omega = \sigma + \mathrm{j}\,2\pi f \tag{7.13}$$

denotes a generic position in the temporal Laplace plane $\underline{s}$. However, contemplation of the principal insight

$$\underline{\mathcal{P}}(f) = \underline{\tilde{\mathcal{Q}}}(\underline{\mathcal{K}}(f)) \tag{7.14}$$

results in the realization that $\underline{\mathcal{P}}(f)$ only contains information about the values of $\underline{\tilde{\mathcal{Q}}}(\underline{\mathcal{K}})$ along a particular path in the $\underline{\mathcal{K}}$ plane defined by the propagation coefficient $\underline{\mathcal{K}}(f)$. This path is called a CLDP path because the propagation coefficient

$$\underline{\mathcal{K}}(f) = \alpha(f) + \mathrm{j}\,\underbrace{2\pi f/c(f)}_{\equiv\beta(f)} \tag{7.15}$$

is assumed to correspond to a CLDP material.

Note that because the attenuation coefficient $\alpha(f)$ and the phase velocity $c(f)$ are dependent upon the CLDP material under consideration, the CLDP path is likewise dependent upon the CLDP material under consideration. Appendix D proffers a graphical depiction of the principal insight.

7.3 The Bromwich Path

Siebert states that $\mathcal{Q}(z)$ may be recovered from its spatial Laplace transform $\underline{\tilde{\mathcal{Q}}}(\underline{\mathcal{K}})$ via the Laplace synthesis integral (see appendix F)

$$\mathcal{Q}(z) = \frac{1}{\mathrm{j}2\pi}\int_{\mathcal{C}} \underline{\tilde{\mathcal{Q}}}(\underline{\mathcal{K}})\exp(z\,\underline{\mathcal{K}})\,d\,\underline{\mathcal{K}} \tag{7.16}$$

"where the integral is a line integral along an appropriate [path] $\mathcal{C}$ in the complex plane. [74]"

Stenger [42], Seely [75], and LePage [44] each point out that the Bromwich path

$$\Re_e\{\underline{\mathcal{K}}\} = \alpha', \text{ a constant} \tag{7.17}$$

is an appropriate path provided it passes through the region of convergence of $\underline{\tilde{\mathcal{Q}}}(\underline{\mathcal{K}})$.

Note that this thesis only considers causal waveforms $\mathcal{Q}(z)$ which have a convergent Fourier transform. It follows that $\underline{\tilde{\mathcal{Q}}}(\underline{\mathcal{K}})$ will be convergent and analytic in the entire right half plane [57, 75], inclusive of the j β axis. Therefore, for this thesis, the Bromwich path $\Re_e\{\underline{\mathcal{K}}\} = \alpha'$ is an appropriate path to use in the Laplace synthesis equation provided $\alpha' \geq 0$.

Appendix D's figure D.2 depicts the CLDP path corresponding to standard polyethylene. If it were plotted in figure D.2, the generic Bromwich path would appear as a vertical line in the RHP.

7.4 The Bromwich Inversion

The Bromwich inversion, defined by (7.16) where $\mathcal{C}$ is given by $\Re_e\{\underline{\mathcal{K}}\} = \alpha' \geq 0$, may be expressed [42]

$$\mathcal{Q}(z) = \int_{\alpha'-\mathrm{j}\infty}^{\alpha'+\mathrm{j}\infty} \underline{\tilde{\mathcal{Q}}}(\underline{\mathcal{K}}) \exp(z\,\underline{\mathcal{K}})\,\frac{d\,\underline{\mathcal{K}}}{\mathrm{j}2\pi} \tag{7.18}$$

Introducing

$$\underline{\mathcal{K}}'(f) = \alpha' + \mathrm{j}\,2\pi f/c' \tag{7.19}$$

where c' is some positive constant, it is possible to write (7.18) parametrically [76]:

$$\mathcal{Q}(z) = \int_{-\infty}^{\infty} \underline{\tilde{\mathcal{Q}}}(\underline{\mathcal{K}}'(f))\,\left[\frac{1}{\mathrm{j}2\pi}\frac{d\,\underline{\mathcal{K}}'(f)}{df}\right]\,\exp(z\,\underline{\mathcal{K}}'(f))\,df \tag{7.20}$$

Now recall that the Bromwich material was defined as having $\alpha(f) = \alpha_b$ and $c(f) = c_b$ where $\alpha_b \geq 0$ and $c_b > 0$ so the propagation coefficient $\underline{\mathcal{K}}_b(f)$ determined by inserting the Bromwich material's model into (7.15) yields the realization that the Bromwich material's CLDP path will be identical to the Bromwich path discussed by Stenger, Seely, and LePage provided $\alpha_b = \alpha'$ and $c_b = c'$.

In this case, $\underline{\mathcal{K}}'(f) = \underline{\mathcal{K}}_b(f)$. Using this relation and (D.1) it is possible to rewrite (2.31) as

$$\mathcal{Q}(z) = \int_{-\infty}^{\infty} \underline{\mathcal{P}}(f)\,\left[\frac{1}{\mathrm{j}2\pi}\frac{d\,\underline{\mathcal{K}}_b(f)}{df}\right]\,\exp(z\,\underline{\mathcal{K}}_b(f))\,df \tag{7.21}$$

Note that, if $\alpha_b = 0$, (7.21) reduces to

$$\mathcal{Q}(z) = \int_{-\infty}^{\infty} \underline{\mathcal{P}}(f)\ \exp(\mathrm{j}\ 2\pi z[\frac{f}{c'}])\ d[\frac{f}{c'}] \tag{7.22}$$

which is clearly just the inverse Fourier transform.

7.5 The Proposed Inverse CLDP IE

Note that (7.21), which follows directly from the results stated by Stenger, Seely, and LePage, is but a special case of the proposed general case (2.31)

$$\mathcal{Q}(z) = \int_{-\infty}^{\infty} \underline{\mathcal{P}}(f)\ [\frac{1}{\mathrm{j}2\pi}\frac{d\,\underline{\mathcal{K}}(f)}{df}]\ \exp(z\,\underline{\mathcal{K}}(f))\ df \tag{7.23}$$

which corresponds to the causal Bromwich materials (see section 6.1.1).

CLDP transform theory proposes that if some generic $\underline{\mathcal{K}}(f)$ yields a causal $\mathrm{H}(z,t)$ via (7.4), then the $\underline{\mathcal{P}}(f)$ determined by

$$\underline{\mathcal{P}}(f) = \int_{0}^{\infty} \mathcal{Q}(z)\ \exp(-z\,\underline{\mathcal{K}}(f))\ dz \tag{7.24}$$

and the $\mathcal{Q}(z)$ determined by (7.23) constitute a transform pair provided $\mathcal{Q}(z)$ is real, causal, Fourier-transformable, and also satisfies the $\underline{\mathcal{K}}(f)$)-dependent relation

$$\lim_{f\to\infty}\left\{\int_{0}^{\alpha(f)} \underline{\tilde{\mathcal{Q}}}(\alpha' + \mathrm{j}\ 2\pi f/c(f))\ d\ \alpha'\right\} = 0 \tag{7.25}$$

where $\underline{\tilde{\mathcal{Q}}}(\underline{\mathcal{K}})$ is the spatial Laplace transform of $\mathcal{Q}(z)$. Equation (7.23) is the proposed inverse CLDP IE. The relevance of 'the CLDP transform constraint' (7.25) is explained in section 7.8.

If some trinity $\{\underline{\mathcal{K}}(f), \mathcal{Q}(z), \underline{\mathcal{P}}(f)\}$ meets all the criterion listed above then, according to CLDP transform theory, $\mathcal{Q}(z)$ and $\underline{\mathcal{P}}(f)$ can be said to form a transform pair under the CLDP path parameterized by $\underline{\mathcal{K}}(f)$. This relationship is denoted symbolically as

$$\mathcal{Q}(z) \quad \overset{\mathcal{K}}{\Longleftrightarrow} \quad \underline{\mathcal{P}}(f) \tag{7.26}$$

7.6 The Darrell Property of the Inverse CLDP IE

The goal of this section is to prove that if $\mathcal{Q}(z)$ and $\underline{\mathcal{P}}(f)$ are a CLDP transform pair

$$\mathcal{Q}(z) \quad \overset{\mathcal{K}}{\Longleftrightarrow} \quad \underline{\mathcal{P}}(f) \tag{7.27}$$

where

$$\underline{\mathcal{P}}(f) = \int_0^\infty \mathcal{Q}(z)\ \exp(-z\ \underline{\mathcal{K}}(f))\ dz \tag{7.28}$$

and

$$\mathcal{Q}(z) = \int_{-\infty}^{\infty} \underline{\mathcal{P}}(f)\ [\frac{1}{\mathrm{j}2\pi}\frac{d\ \underline{\mathcal{K}}(f)}{df}]\ \exp(z\ \underline{\mathcal{K}}(f))\ df \tag{7.29}$$

then the result of inserting a strictly bandlimited version $\underline{\mathcal{P}}(f_m, f)$ of $\underline{\mathcal{P}}(f)$

$$\underline{\mathcal{P}}(f_m, f) \ \equiv\ \underline{\mathcal{P}}(f)\ [\mathrm{U}(f - f_m) - \mathrm{U}(f + f_m)] \tag{7.30}$$

into (7.29) will yield a recovery

$$\mathrm{R}(f_m, z) \equiv \int_{-\infty}^{\infty} \underline{\mathcal{P}}(f_m, f)\ [\frac{1}{\mathrm{j}2\pi}\frac{d\ \underline{\mathcal{K}}(f)}{df}]\ \exp(z\ \underline{\mathcal{K}}(f))\ df$$

$$= \int_{-f_m}^{f_m} \underline{\mathcal{P}}(f)\ [\frac{1}{\mathrm{j}2\pi}\frac{d\ \underline{\mathcal{K}}(f)}{df}]\ \exp(z\ \underline{\mathcal{K}}(f))\ df \tag{7.31}$$

$$= \mathcal{Q}(z) * \mathrm{D}(f_m, z) \tag{7.32}$$

where the $*$ denotes spatial convolution, $\mathcal{Q}(z)$ is assumed causal, and "the Darrell" $\mathrm{D}(f_m, z)$ is some material dependent waveform.

To see this, start by inserting (7.28) into (7.31). Note that there are two distinct z's; one in the forward problem (7.28) and one in the inverse problem (7.31). To ensure that these two invocations of z do not get confused, change the z in (7.28) to a ξ. The result is

$$\mathrm{R}(f_m, z) = \int_{-f_m}^{f_m} \left[\int_0^\infty \mathcal{Q}(\xi)\ \exp(-\xi\ \underline{\mathcal{K}}(f))\ d\xi \right] [\frac{1}{\mathrm{j}2\pi}\frac{d\ \underline{\mathcal{K}}(f)}{df}]\ \exp(z\ \underline{\mathcal{K}}(f))\ df \tag{7.33}$$

Changing the order of integration, rearranging, and combining yields

$$\mathrm{R}(f_m, z) = \int_0^\infty \mathcal{Q}(\xi) \underbrace{\left[\int_{-f_m}^{f_m} [\frac{1}{\mathrm{j}2\pi} \frac{d\,\underline{\mathcal{K}}(f)}{df}] \exp([z-\xi]\,\underline{\mathcal{K}}(f))\, df \right]}_{\equiv\, \mathrm{D}(f_m, z-\xi)} d\xi \tag{7.34}$$

where the bracketed quantity is defined as the Darrell $\mathrm{D}(f_m, z-\xi)$. Therefore

$$\mathrm{D}(f_m, z) = \int_{-f_m}^{f_m} [\frac{1}{\mathrm{j}2\pi} \frac{d\,\underline{\mathcal{K}}(f)}{df}] \exp(z\,\underline{\mathcal{K}}(f))\, df \tag{7.35}$$

Note that $\mathrm{D}(f_m, z)$ must be real because $\underline{\mathcal{K}}(f)$ has conjugate symmetry, and the limits of integration of (7.35) are symmetric about $f = 0$. Using the assumed causality of $\mathcal{Q}(z)$ to justify lowering the lower limit of the ξ integration in (7.34) to minus infinity,

$$\mathrm{R}(f_m, z) = \mathcal{Q}(z) * \mathrm{D}(f_m, z) \tag{7.36}$$

as required.

7.7 Deriving the Darrell

First note that

$$[\frac{d\,\underline{\mathcal{K}}(f)}{df}] df = d\,\underline{\mathcal{K}} \tag{7.37}$$

So that

$$\mathrm{D}(f_m, z) \equiv \int_{-f_m}^{f_m} [\frac{1}{\mathrm{j}2\pi} \frac{d\,\underline{\mathcal{K}}(f)}{df}] \exp(z\,\underline{\mathcal{K}}(f))\, df \tag{7.38}$$

$$= \frac{1}{\mathrm{j}2\pi} \int_{\underline{\mathcal{K}}(-f_m)}^{\underline{\mathcal{K}}(f_m)} \exp(z\,\underline{\mathcal{K}})\, d\underline{\mathcal{K}} \tag{7.39}$$

$$= \frac{\exp(z\,\underline{\mathcal{K}}(f_m)) - \exp(z\,\underline{\mathcal{K}}(-f_m))}{\mathrm{j}\,2\pi\,z} \tag{7.40}$$

Now recall that $\underline{\mathcal{K}}(f)$ satisfies

$$\underline{\mathcal{K}}(-f) = \underline{\mathcal{K}}^*(f) \tag{7.41}$$

where the $*$ denotes complex conjugation. Therefore (7.40) can be rewritten

$$\mathrm{D}(f_m, z) = \frac{\exp(z\ \underline{\mathcal{K}}(f_m)) - \exp(z\ \underline{\mathcal{K}}^*(f_m))}{\mathrm{j}\ 2\pi\ z} \tag{7.42}$$

$$= \frac{\mathrm{j}\ 2\ \Im_m\{\exp(z\ \underline{\mathcal{K}}(f_m))\}}{\mathrm{j}\ 2\pi\ z} \tag{7.43}$$

$$= \frac{\Im_m\{\exp(z\ \underline{\mathcal{K}}(f_m))\}}{\pi\ z} \tag{7.44}$$

Or, substituting

$$\underline{\mathcal{K}}(f) = \alpha(f) + \mathrm{j}\ 2\pi f/c(f) \tag{7.45}$$

the result is

$$\mathrm{D}(f_m, z) = \exp(z\ \alpha(f_m))\ \frac{\sin(2\pi f_m z/c(f_m))}{\pi z} \tag{7.46}$$

$$= \exp(z/\Lambda)\ \frac{\sin(2\pi z/\lambda)}{\pi z} \tag{7.47}$$

where

$$\lambda = \lambda(f_m) \equiv \frac{c(f_m)}{f_m}$$

$$\Lambda = \Lambda(f_m) \equiv \frac{1}{\alpha(f_m)}$$

7.8 Validation of the Inverse CLDP IE

It has been proposed that the so-called 'inverse CLDP IE' yields a valid inversion (*ie*: a valid inverse CLDP transform) in the case of the (causal) Bromwich materials because,

in this case, the Bromwich inversion integral results. But the class of waveforms $\mathcal{Q}(z)$ to which this alleged transform relationship applies has not yet been specified. Nor has Bromwich inversion been validated in its own right.

The argument for the validity of the proposed inverse CLDP IE starts by investigating the argument for the validity of the Bromwich inversion, and then extending that argument to the generic CLDP inversion. The argument for the validity of the Bromwich inversion can be made by extending Fourier theory into the Laplace plane.

Siebert [106] points out that it is "exceedingly difficult" to rigorously justify Fourier's transformation theorem, and that the first of many versions of a 'Fourier theorem' was proposed by Dirichlet in the form of conditions on the functions to which the Fourier transformation relationship applies. The Dirichlet conditions ("a set of sufficient but not necessary conditions" [75]) require $\mathcal{Q}(z)$ to be absolutely integrable ($\int_{-\infty}^{\infty} |\mathcal{Q}(z)|\, dz < \infty$) and also to have a finite number of maxima and minima in a finite interval.

The conditions on Laplace transformable functions (according to Greenberg [109]) are also sufficient but not necessary: $\mathcal{Q}(z)$ must be piecewise smooth over every finite interval, and $\mathcal{Q}(z)$ must also be of exponential order (*ie*: there must exist real constants K, C, and Z such that $|\mathcal{Q}(z)| < \mathrm{K}\exp(\mathrm{C}\ \mathrm{z})$ for all $z > \mathrm{Z}$).

These 'Laplace transform conditions,' and the Dirichlet (Fourier transform) conditions, are called "sufficient but not necessary." In the case of the Laplace transforms, this term means that all functions which are of exponential order and are piecewise smooth over every interval are Laplace transformable. But the converse is not necessarily true. That is, there may exist functions which are Laplace transformable but fail to satisfy the stated 'Laplace transform conditions.'

A function $\mathcal{Q}(z)$ is said to be Laplace transformable (*ie*: has a Laplace transform $\underline{\tilde{\mathcal{Q}}}(\underline{\mathcal{K}})$) if the Bromwich inversion (defined below) converges to $\mathcal{Q}(z)$ almost everywhere (*eg*: converges to $\mathcal{Q}(z)$ everywhere except at a finite set of points). A function is said to be Fourier transformable if it is Laplace transformable *and* the region of convergence includes the j-axis, so that $\underline{\mathcal{Q}}(\flat) = \underline{\tilde{\mathcal{Q}}}(\mathrm{j}2\pi\flat)$ can meaningfully be called the Fourier transform of $\mathcal{Q}(z)$.

The goal here is not to study Fourier and Laplace transform theorems themselves but, instead, to point out the necessity to specify the functions to which some proposed transformation relation (such as the CLDP transform corresponding to some particular CLDP path $\underline{\mathcal{K}}(f)$) will apply. The proposed proof of the validity of the CLDP transforms utilizes Laplace transform theory – and it is with respect to the Laplace transform $\underline{\tilde{\mathcal{Q}}}(\underline{\mathcal{K}})$ of some given $\mathcal{Q}(z)$ that the forthcoming 'CLDP criterion' (7.73) will be stated – and so Guillemin's outline [46] of the relationship between Fourier and Laplace transform theory is deemed relevant:

> "Fourier theory is introduced as a method of creating a desired interference pattern from steady sinusoids, by applying this theory first to periodic functions and then extending the method to aperiodic ones. The paramount issue here is the evaluation of error and its depencence upon the spectral width, which results in the fact that one can make the error

arbitrarily small, although not zero, with a sufficiently large but still finite spectral width [*note that the Darrell property, and the delta-convergence of the Darrell, speak directly to this 'paramount issue'*]. Through the simple use of Cauchy's integral law one can then extend the procedure to constructing such interference patterns with sinusoids involving complex frequencies; that is to say, through the use of sinusoids having exponentially modulated amplitudes. This amounts to extending the Fourier integral to a double-ended Laplace transform, and one thus recognizes that the Fourier transform is the Laplace transform evaluated along the j-axis."

This thesis considers only causal, real, Fourier-transformable $\mathcal{Q}(z)$'s. The (spatial) Laplace transforms $\underline{\tilde{\mathcal{Q}}}(\underline{\mathcal{K}})$ for this class of $\mathcal{Q}(z)$'s

- have conjugate symmetry [107]: $\underline{\tilde{\mathcal{Q}}}(\underline{\mathcal{K}}^*) = \underline{\tilde{\mathcal{Q}}}^*(\underline{\mathcal{K}})$
- converge in the entire right half plane [57, 75] (RHP, inclusive of the j-axis)
- are the same, regardless of whether the Laplace transformation is defined unilaterally or bilaterally ('double-ended'-ly)

Stenger [42] offers a quotable explanation of how the inverse Fourier transform relates to the Bromwich inversion integral:

Let $\Re_+ = (0, \infty)$, let $\mathcal{Q}(z)$ be defined on $\Re_+$ [*ie*: let $\mathcal{Q}(z)$ be causal], and let $\underline{\tilde{\mathcal{Q}}}(\underline{\mathcal{K}})$ be defined by the integral

$$\underline{\tilde{\mathcal{Q}}}(\underline{\mathcal{K}}) = \int_0^\infty \exp(-z\ \underline{\mathcal{K}})\ \mathcal{Q}(z)\ dz \tag{7.48}$$

Upon setting $\underline{\mathcal{K}} = \alpha + \mathrm{j}\ \beta$ in (7.48), we get

$$\underline{\tilde{\mathcal{Q}}}(\alpha + \mathrm{j}\ \beta) = \int_0^\infty [\exp(-z\ \alpha)\ \mathcal{Q}(z)]\ \exp(-\mathrm{j}\ \beta\ z)\ dz \tag{7.49}$$

We may thus think of the Laplace transform (7.48) as a Fourier transform; this analogy immediately leads to the inversion formula

$$\mathcal{Q}(z) = \frac{1}{2\pi} \int_{-\infty}^\infty \underline{\tilde{\mathcal{Q}}}([\alpha + \mathrm{j}\ \beta])\ \exp([\alpha + \mathrm{j}\ \beta]\ z)\ d\beta \tag{7.50}$$

That is, we get the Bromwich inversion integral

$$\mathcal{Q}(z) = \frac{1}{\mathrm{j}\ 2\pi} \int_{\alpha - \mathrm{j}\infty}^{\alpha + \mathrm{j}\infty} \underline{\tilde{\mathcal{Q}}}(\underline{\mathcal{K}})\ \exp(z\ \underline{\mathcal{K}})\ d\ \underline{\mathcal{K}} \tag{7.51}$$

Note that the frequency f parameterized Bromwich/CLDP path

$$\underline{\mathcal{K}}_b(f) = \alpha_b + \mathrm{j}\overbrace{2\pi f/c_b}^{\equiv\beta_b(f)} \quad , -\infty \geq f \geq \infty, \text{ where } \alpha_b \geq 0 \text{ and } c_b > 0 \tag{7.52}$$

is an *open* path (contour), as is the path associated with the Fourier transform inversion integral (which simply specifies $\alpha_b = 0$). According to Seely [75], for positions $z > 0$ the evaluation of the Bromwich inversion integral usually proceeds by using Cauchy's integral theorem, which specifies that

$$\mathcal{Q}(z) = \lim_{f_m \to \infty} \left\{ \oint_{\Gamma_1(f_m)} \frac{1}{\mathrm{j}2\pi} \underline{\tilde{\mathcal{Q}}}(\underline{\mathcal{K}}) \, \exp(z \, \underline{\mathcal{K}}) \, d \, \underline{\mathcal{K}} \right\} \tag{7.53}$$

$$= \sum \text{residues of } \underline{\tilde{\mathcal{Q}}}(\underline{\mathcal{K}}) \, \exp(z \, \underline{\mathcal{K}}) \text{ at the singularities to the left of } \alpha_b \tag{7.54}$$

where the path $\Gamma_1(f_m)$ consists of a vertical path (extending from $\underline{\mathcal{K}}_b^*(f_m) = \alpha_b - \mathrm{j}\beta_b(f_m)$ to $\underline{\mathcal{K}}_b(f_m)$), and a constant radius $|\underline{\mathcal{K}}_b(f_m)|$ semi-circular path (extending from $\underline{\mathcal{K}}_b(f_m)$ back to $\underline{\mathcal{K}}_b^*(f_m)$) in a mathematically positive (counter-clockwise) sense.

The semi-circular portion of $\Gamma_1(f_m)$ includes only points to the *left* of α_b. The arc subtended in this semi-circular integration decreases from slightly more than π radians (when $\alpha_b c_b \ll f_m < \infty$) to exactly π radians in the limit as $f_m \to \infty$. When $f_m < \infty$ and $\alpha_b > 0$ the semi-circular portion of $\Gamma_1(f_m)$ extends into the RHP. If it can be shown that the $f_m \to \infty$ limit of the semi-circular integration described by $\Gamma_1(f_m)$ vanishes then the Bromwich inversion is validated.

For positions $z < 0$ the appropriate path is $\Gamma_2(f_m)$, which differs from $\Gamma_1(f_m)$ only in that the semi-circular portion is traversed in a mathematically negative (clockwise) sense, so that the semi-circular portion of $\Gamma_2(f_m)$ includes only points to the *right* of α_b. For the RHP-analytic $\underline{\tilde{\mathcal{Q}}}(\underline{\mathcal{K}})$'s considered here the result of the $\Gamma_2(f_m)$ integration vanishes independently of f_m (by the Cauchy-Goursat theorem [79]) so that the $\mathcal{Q}(z)$ recovered via $\Gamma_2(f_m)$ in the limit as $f_m \to \infty$ will be causal, as required.

This thesis considers only Fourier transformable functions, defined above as being those functions for which the Fourier transform inversion integral (*aka* the $\alpha_b = 0$ Bromwich/CLDP inverse IE) yields $\mathcal{Q}(z)$ almost everywhere. From the discussion above, it follows that the $f_m \to \infty$ limit of the semi-circular integration described by $\Gamma_1(f_m)$ must vanish for these $\mathcal{Q}(z)$'s. The Bromwich inversion is valid for the waveforms considered in this thesis (provided that, as specified, $\alpha_b \geq 0$ so that the Bromwich path falls in the region of convergence of $\underline{\tilde{\mathcal{Q}}}(\underline{\mathcal{K}})$).

For the case of a Bromwich material $\underline{\mathcal{K}}_b(f)$, the Bromwich inversion integral (7.51) may be expressed parametrically as

$$\mathcal{Q}(z) = \int_{-\infty}^{\infty} \underline{\tilde{\mathcal{Q}}}(\underline{\mathcal{K}}_b(f)) \, \frac{1}{\mathrm{j}2\pi} \frac{d \, \underline{\mathcal{K}}_b(f)}{df} \, \exp(z \, \underline{\mathcal{K}}_b(f)) \, df \tag{7.55}$$

By the principal insight (section 7.1) the response signal $\underline{\mathcal{P}}_b(f)$ produced by a waveform $\mathcal{Q}(z)$ embedded in a Bromwich material is given by

$$\underline{\mathcal{P}}_b(f) = \underline{\tilde{\mathcal{Q}}}(\underline{\mathcal{K}}_b(f)) = \int_0^\infty \mathcal{Q}(z)\ \exp(-z\ \underline{\mathcal{K}}_b(f))\ dz \tag{7.56}$$

Now the Bromwich inversion (7.55) may be re-written

$$\mathcal{Q}(z) = \int_{-\infty}^{\infty} \underline{\mathcal{P}}_b(f)\ \frac{1}{\mathrm{j}2\pi} \frac{d\ \underline{\mathcal{K}}_b(f)}{df}\ \exp(z\ \underline{\mathcal{K}}_b(f))\ df \tag{7.57}$$

so that $\mathcal{Q}(z)$ and $\underline{\mathcal{P}}_b(f)$ effectively form a CLDP transform relationship under the Bromwich propagation coefficient $\underline{\mathcal{K}}_b(f)$.

Insofar as the validity of the proposed inverse CLDP IE is concerned, the question is whether (7.56) and (7.57) form a valid transform relationship when the $\underline{\mathcal{K}}_b(f)$ acting in these equations is replaced by a generic, stable ($\alpha(f) \geq 0$) CLDP propagation coefficient $\underline{\mathcal{K}}(f)$. *Ie*: for what $\{\mathcal{Q}(z), \underline{\mathcal{K}}(f)\}$ pairs do

$$\mathcal{Q}(z) = \lim_{f_m \to \infty} \left\{ \overbrace{\int_{-f_m}^{f_m} \underline{\mathcal{P}}(f)\ \frac{1}{\mathrm{j}2\pi} \frac{d\ \underline{\mathcal{K}}(f)}{df}\ \exp(z\ \underline{\mathcal{K}}(f))\ df}^{\equiv \mathcal{Q}(f_m, z)} \right\} \tag{7.58}$$

and

$$\underline{\mathcal{P}}(f) = \underline{\tilde{\mathcal{Q}}}(\underline{\mathcal{K}}(f)) = \int_0^\infty \mathcal{Q}(z)\ \exp(-z\ \underline{\mathcal{K}}(f))\ dz \tag{7.59}$$

form a valid CLDP transform relation?

In addressing this question, note first that the generic CLDP path corresponding to a stable material does not depart the known-analytic RHP (which is defined as including the j-axis). Now consider the generic finite-length Laplace plane integration path traversed in calculating $\mathcal{Q}(f_m, z)$ when f_m is finite.

Because the integrand is analytic in the RHP, and because no stable CLDP path departs the RHP, the result is independent of path. The resultant, generic CLDP $\mathcal{Q}(f_m, z)$ will be identical to the Bromwich path result which could be obtained by vertical integration from $\underline{\mathcal{K}}(-f_m) = \underline{\mathcal{K}}^*(f_m)$ to $\underline{\mathcal{K}}(f_m)$ if $\underline{\tilde{\mathcal{Q}}}(\underline{\mathcal{K}})$ were known along that path.

Of course, if only the non-Bromwich $\underline{\mathcal{P}}(f) = \underline{\tilde{\mathcal{Q}}}(\underline{\mathcal{K}}(f))$ is known then this hypothetical Bromwich integration cannot be executed (except possibly via analytic continuation of $\underline{\mathcal{P}}(f)$) but this fact in no way contradicts the statement that *if* $\underline{\tilde{\mathcal{Q}}}(\underline{\mathcal{K}}_b(f))$ were known *then* the two $\mathcal{Q}(f_m, z)$'s (one obtained via the hypothetical Bromwich CLDP path, and one obtained via the given CLDP path) would be identical.

If some generic CLDP material's

$$\underline{\mathcal{K}}(f) = \alpha(f) + \mathrm{j}\, 2\pi f/c(f) = \alpha(f) + \mathrm{j}\, \beta(f) \tag{7.60}$$

satisfies

$$\lim_{f\to\infty}\Big\{\alpha(f)\Big\} \equiv \alpha_\infty < \infty \quad \text{and} \quad \lim_{f\to\infty}\Big\{\beta(f)\Big\} = \infty \tag{7.61}$$

then the validity of the inverse CLDP IE (for these materials) follows directly from the validity of the Bromwich inversion by analogy to the Bromwich path described by $\alpha_b = \alpha_\infty$.

Now note that causality, via the Paley-Wiener-Guillemin criterion (PWG, see section 6.4), ensures that $\lim_{f\to\infty}\{\beta(f)\} = \infty$; the PWG criterion requires that, as $f \to \infty$, $\beta(f)$ must increase *at least* as rapidly as f (and less rapidly than f^2). Unfortunately, the Paley-Wiener criterion does not ensure the finiteness of α_∞; the Paley-Wiener criterion only states that, as $f \to \infty$, $\alpha(f)$ cannot approach infinity as fast as f.

The validity of the inverse CLDP IE is ensured for materials with $\alpha_\infty < \infty$. So consider now the general case, which includes the case $\alpha_\infty = \infty$. Taken together, the Paley-Wiener criteria ensure that, as $f \to \infty$, $|\underline{\mathcal{K}}(f)| \to \infty$ and $\langle\underline{\mathcal{K}}(f)\rangle \to \pi/2$ (where $|\underline{Z}|$ denotes the magnitude of the complex variable $\underline{Z}$ and $\langle\underline{Z}\rangle$ denotes the principal value of its phase: $\underline{Z} = |\underline{Z}|\, \exp(\mathrm{j}\, \langle\underline{Z}\rangle)$).

Note that this generic result holds for the Bromwich materials as well. That is, for *all* causal materials, the CLDP path starts at $-\mathrm{j}\infty$ and ends at $+\mathrm{j}\infty$. Because the result of the inversion integral depends only upon its endpoints, and because the endpoints are the same regardless of the (stable) CLDP material under consideration, it seems that the the general validity of the inverse CLDP IE follows immediately.

The author prefers to be more cautious, noting that these results do not depend upon the $\{\mathcal{Q}(z), \underline{\mathcal{K}}(f)\}$ pair under consideration. Intuition suggests that the waveforms $\mathcal{Q}(z)$ which are 'CLDP transformable' under some particular $\underline{\mathcal{K}}(f)$ should depend upon that $\underline{\mathcal{K}}(f)$.

First, recall that the spatial Laplace transforms $\tilde{\underline{\mathcal{Q}}}(\underline{\mathcal{K}})$ of the the class of $\mathcal{Q}(z)$'s under discussion are known to be analytic in the RHP (where the RHP is defined as including the j axis). The function $\exp(z\, \underline{\mathcal{K}})$ is also known to be analytic in the finite RHP (and elsewhere; it is *entire* [108]). Therefore their product is also analytic in the RHP [96]. It follows from the Cauchy-Goursat theorem [79] that

$$\oint_{\square} \underbrace{\frac{1}{\mathrm{j}\, 2\pi}\, \tilde{\underline{\mathcal{Q}}}(\underline{\mathcal{K}})\, \exp(z\, \underline{\mathcal{K}})}_{\equiv \underline{\mathcal{Y}}(\underline{\mathcal{K}})}\, d\, \underline{\mathcal{K}} = 0 \tag{7.62}$$

where $\oint_{\square}$ denotes the sum of the following four integrations, none of which need depart the RHP:

- the 'top path' **tp**, extending from $\underline{\mathcal{K}}(f_m) = \alpha(f_m) + \mathrm{j}\beta(f_m)$ to $\mathrm{j}\beta(f_m)$
- the 'left path' **lp**, extending from $\mathrm{j}\beta(f_m)$ to -$\mathrm{j}\beta(f_m)$
- the 'bottom path' **bp**, extending from -$\mathrm{j}\beta(f_m)$ to $\underline{\mathcal{K}}^*(f_m) = \alpha(f_m) - \mathrm{j}\beta(f_m)$
- the 'right path' **rp**, extending from $\underline{\mathcal{K}}^*(f_m)$ to $\underline{\mathcal{K}}(f_m)$

That is, re-writing (7.62) using the definition of $\underline{\mathcal{Y}}(\underline{\mathcal{K}})$ given there (for compactness) and the four paths described above,

$$\oint_{\square} \underline{\mathcal{Y}}(\underline{\mathcal{K}})\, d\,\underline{\mathcal{K}} = \int_{\mathrm{tp}} \underline{\mathcal{Y}}(\underline{\mathcal{K}})\, d\,\underline{\mathcal{K}} + \int_{\mathrm{lp}} \underline{\mathcal{Y}}(\underline{\mathcal{K}})\, d\,\underline{\mathcal{K}} + \int_{\mathrm{bp}} \underline{\mathcal{Y}}(\underline{\mathcal{K}})\, d\,\underline{\mathcal{K}} + \int_{\mathrm{rp}} \underline{\mathcal{Y}}(\underline{\mathcal{K}})\, d\,\underline{\mathcal{K}} = 0 \tag{7.63}$$

Note that, except for a change in sign corresponding to the direction of integration, the $f_m \to \infty$ limit of the integration along the left path is identical to the integration in (7.57) when $\alpha_b = 0$ because $\lim_{f_m \to \infty}\{\beta(f_m)\} = \infty$. That is,

$$\lim_{f_m \to \infty} \left\{ \int_{\mathrm{lp}} \underline{\mathcal{Y}}(\underline{\mathcal{K}})\, d\,\underline{\mathcal{K}} \right\} = \lim_{f_m \to \infty} \left\{ \int_{\mathrm{lp}} \frac{1}{\mathrm{j}2\pi}\, \underline{\tilde{\mathcal{Q}}}(\underline{\mathcal{K}})\, \exp(z\,\underline{\mathcal{K}})\, d\,\underline{\mathcal{K}} \right\} = -\mathcal{Q}(z) \tag{7.64}$$

Therefore, any waveform $\mathcal{Q}(z)$ with a Laplace transform $\underline{\tilde{\mathcal{Q}}}(\underline{\mathcal{K}})$ satisfying

$$\lim_{f_m \to \infty} \left\{ \int_{\mathrm{tp}} \underline{\tilde{\mathcal{Q}}}(\underline{\mathcal{K}})\, \exp(z\,\underline{\mathcal{K}})\, d\,\underline{\mathcal{K}} + \int_{\mathrm{bp}} \underline{\tilde{\mathcal{Q}}}(\underline{\mathcal{K}})\, \exp(z\,\underline{\mathcal{K}})\, d\,\underline{\mathcal{K}} \right\} = 0 \tag{7.65}$$

must have the property

$$\lim_{f_m \to \infty} \left\{ \int_{\mathrm{rp}} \frac{1}{\mathrm{j}2\pi}\, \underline{\tilde{\mathcal{Q}}}(\underline{\mathcal{K}})\, \exp(z\,\underline{\mathcal{K}})\, d\,\underline{\mathcal{K}} \right\} = \mathcal{Q}(z) \tag{7.66}$$

Equation (7.65) is the necessary and sufficient condition which ensures the validity of the Bromwich recovery for the class of $\mathcal{Q}(z)$'s under discussion. Because of its importance (it is the basis of the CLDP criterion), it is re-written below in a form which takes advantage of the conjugate symmetry of the quantity $\underline{\mathcal{Y}}(\underline{\mathcal{K}}) = \frac{1}{\mathrm{j}2\pi}\, \underline{\tilde{\mathcal{Q}}}(\underline{\mathcal{K}})\, \exp(z\,\underline{\mathcal{K}})$.

Rewriting (7.65),

$$0 = \lim_{f_m \to \infty} \left\{ \int_{\text{tp}} \underline{\mathcal{Y}}(\underline{\mathcal{K}})\, d\, \underline{\mathcal{K}} + \int_{\text{bp}} \underline{\mathcal{Y}}(\underline{\mathcal{K}})\, d\, \underline{\mathcal{K}} \right\} \tag{7.67}$$

$$= \lim_{f_m \to \infty} \left\{ \int_{\alpha(f_m)}^{0} \underline{\mathcal{Y}}(\alpha' + \mathrm{j}\, \beta(f_m))\, d\, \alpha' + \int_{0}^{\alpha(f_m)} \underline{\mathcal{Y}}(\alpha' - \mathrm{j}\, \beta(f_m))\, d\, \alpha' \right\} \tag{7.68}$$

$$= \lim_{f_m \to \infty} \left\{ \int_{0}^{\alpha(f_m)} \left[\underline{\mathcal{Y}}(\alpha' - \mathrm{j}\, \beta(f_m)) - \underline{\mathcal{Y}}(\alpha' + \mathrm{j}\, \beta(f_m)) \right] d\, \alpha' \right\} \tag{7.69}$$

$$= \lim_{f_m \to \infty} \left\{ \int_{0}^{\alpha(f_m)} \left[\underline{\mathcal{Y}}^{*}(\alpha' + \mathrm{j}\, \beta(f_m)) - \underline{\mathcal{Y}}(\alpha' + \mathrm{j}\, \beta(f_m)) \right] d\, \alpha' \right\} \tag{7.70}$$

$$= -\, 2\, \mathrm{j} \lim_{f_m \to \infty} \left\{ \int_{0}^{\alpha(f_m)} \Im_m\{\underline{\mathcal{Y}}(\alpha' + \mathrm{j}\, \beta(f_m))\}\, d\, \alpha' \right\} \tag{7.71}$$

results in the realization that (7.66) (by way of (7.65)) requires that the Laplace transform $\underline{\tilde{\mathcal{Q}}}(\underline{\mathcal{K}})$ of some $\mathcal{Q}(z)$ satisfy

$$\lim_{f \to \infty} \left\{ \int_{0}^{\alpha(f)} \Im_m\{\underline{\tilde{\mathcal{Q}}}([\alpha' + \mathrm{j}\, \beta(f)])\, \exp(z\, [\alpha' + \mathrm{j}\, \beta(f)])\}\, d\, \alpha' \right\} = 0 \tag{7.72}$$

(where f_m has been replaced by f) in addition to being causal, real, and Fourier-transformable.

The appearance of the variable z in (7.72) suggests that the inverse CLDP recovery may be valid only for certain specific values (or perhaps ranges) of z. However, the Darrell property of the inverse CLDP IE implies that if the $f_m \to \infty$ limit of the inverse CLDP recovery converges anywhere, then it converges everywhere. Therefore (7.72) may be re-written with z replaced by zero:

$$\lim_{f \to \infty} \left\{ \int_{0}^{\alpha(f)} \Im_m\{\underline{\tilde{\mathcal{Q}}}([\alpha' + \mathrm{j}\, \beta(f)])\, d\, \alpha' \right\} = 0 \tag{7.73}$$

Equation (7.73) is dubbed the CLDP criterion. A real, causal, Fourier transformable $\mathcal{Q}(z)$ will be CLDP transformable under some given, analytic $\underline{\mathcal{K}}(f)$ if the CLDP criterion is satisfied.

7.9 The Darrell As Delta Convergent Sequence

The previous section adopted a Laplace plane approach to answering the question of when (*ie*: for which $\{\underline{\mathcal{K}}(f), \mathcal{Q}(z)\}$ pairs) the inverse CLDP IE yields the desired $\mathcal{Q}(z)$ from the given $\underline{\mathcal{P}}(f)$. The result of section 7.8's analysis was the CLDP criterion (equation (7.73)).

The current section approaches the same question via the Darrell property, and the fact (to be shown) that the Darrell $\mathrm{D}(f_m, z)$ converges to a Dirac delta function $\delta(z)$ in the limit as $f_m \rightarrow \infty$ for a particular, $\underline{\mathcal{K}}(f)$-dependent class of $\mathcal{Q}(z)$'s.

As in section 7.8, the goal is to determine the $\underline{\mathcal{K}}(f)$-dependent constraints on $\mathcal{Q}(z)$ such that the $\underline{\mathcal{P}}(f)$ produced by submitting $\mathcal{Q}(z)$ to the $\underline{\mathcal{K}}(f)$-dependent forward CLDP IE will reliably yield $\mathcal{Q}(z)$ when this particular $\{\underline{\mathcal{P}}(f), \underline{\mathcal{K}}(f)\}$ pair is submitted to the inverse CLDP IE. The previous section's results seem complete so the author feels justified in adopting a 'hand-waving' posture in the current section.

7.9.1 The Basic Idea

It is clear from the Darrell property of the inverse CLDP IE

$$\mathrm{R}(f_m, z) = \mathcal{Q}(z) * \mathrm{D}(f_m, z) \tag{7.74}$$

that if

$$\lim_{f_m \rightarrow \infty} \left\{ \mathrm{D}(f_m, z) = \exp(z\ \alpha(f_m))\ \frac{\sin(2\pi f_m z / c(f_m))}{\pi z} \right\} = \delta(z) \tag{7.75}$$

then the inverse CLDP IE's recovery $\mathrm{R}(f_m, z)$ will yield the desired $\mathcal{Q}(z)$. In this case the Darrell is said to be delta convergent.

7.9.2 Interpreting The Dirac Delta Function

A legitimate question is, what is the Dirac delta function $\delta(z)$? Siebert [60], following Dirac and Heaviside, recommends defining what $\delta(z)$ *is* by what $\delta(z)$ *does*. He says: "Mathematically, the effect of a unit impulse function inside an integral is to pick out the value of the remainder of the integrand where the impulse 'is.'"

That is, to test whether some waveform $\Delta(z)$ 'is' a Dirac delta function, Siebert recommends integrating the product of $\Delta(z)$ with some test function $\mathcal{Q}(z)$ to see whether $\Delta(z)$ exhibits the sifting property [95]

$$\mathcal{Q}(z_o) = \int_{-\infty}^{\infty} \Delta(z - z_o)\ \mathcal{Q}(z)\ dz \tag{7.76}$$

If (7.76) holds for all z_o and $\mathcal{Q}(z)$ under consideration then, Siebert would argue, $\Delta(z)$ might as well be thought of as $\delta(z)$ for those $\mathcal{Q}(z)$'s. It is also possible to select $z_o = 0$ in (7.76) without loss of generality (rather than shifting $\Delta(z)$ to the right by z_o, shift the arbitrary test function $\mathcal{Q}(z)$ to the left by z_o). The result is:

$$\mathcal{Q}(0) = \int_{-\infty}^{\infty} \Delta(z)\ \mathcal{Q}(z)\ dz \tag{7.77}$$

Now let

$$\Delta(z) \quad \rightarrow \quad \lim_{f_m \to \infty} \left\{ \overbrace{\exp(z\ \alpha(f_m))\ \frac{\sin(2\pi f_m z/c(f_m))}{\pi z}}^{\mathrm{D}(f_m,z)} \right\} \tag{7.78}$$

so that it can be seen that the Darrell will be delta convergent if and only if

$$\mathcal{Q}(0) = \int_{-\infty}^{\infty} \mathcal{Q}(z) \left[\lim_{f_m \to \infty} \left\{ \exp(z\ \alpha(f_m))\ \frac{\sin(2\pi f_m z/c(f_m))}{\pi z} \right\} \right] dz$$

$$= \lim_{f_m \to \infty} \left\{ \int_{-\infty}^{\infty} \mathcal{Q}(z)\ \exp(z\ \alpha(f_m))\ \frac{\sin(2\pi f_m z/c(f_m))}{\pi z}\ dz \right\} \tag{7.79}$$

for the $\mathcal{Q}(z)$'s of interest. The goal is to determine the $\{\alpha(f_m), c(f_m)\}$-dependent constraints on $\mathcal{Q}(z)$ which ensure the validity of (7.79).

7.9.3 Darrell-Determined Constraints on $\mathcal{Q}(z)$

A causal material's Darrell will be delta convergent with respect to some $\mathcal{Q}(z)$ if

$$\sum_{n=-\infty}^{\infty} \mathcal{Q}_n = \mathcal{Q}(0) \tag{7.80}$$

where

$$\mathcal{Q}_n \equiv \lim_{f_m \to \infty} \left\{ \int_{(2n-1)\Delta z_D(f_m)}^{(2n+1)\Delta z_D(f_m)} \mathcal{Q}(z)\ \mathrm{D}(f_m, z)\ dz \right\}$$

$$= \lim_{f_m \to \infty} \left\{ \int_{(2n-1)\Delta z_D(f_m)}^{(2n+1)\Delta z_D(f_m)} \mathcal{Q}(z)\ \exp(z\ \alpha(f_m))\ \frac{\sin(2\pi f_m z/c(f_m))}{\pi z}\ dz \right\} \tag{7.81}$$

and

$$\Delta z_D(f_m) \equiv \frac{c(f_m)}{2f_m} \tag{7.82}$$

because $\sum \mathcal{Q}_n$ is just a handy way of expressing the right hand side of (7.79).

To perceive this, note that

I. $\Delta z_D(f_m)$ is the distance between $\sin(2\pi f_m z/c(f_m))$'s zero crossings

II. $\mathcal{Q}_n$ is the area of $\mathcal{Q}(z)\mathrm{D}(f_m, z)$ extant between zero crossing $2n-1$ and zero crossing $2n+1$

III. the range of z's associated with each $\mathcal{Q}_n$ is distinct, and the range of z's associated with *all* the $\mathcal{Q}_n$'s is $-\infty \leq z \leq \infty$

IV. $\sum \mathcal{Q}_n$ represents the sum of all these infinitesimal 'chunks' of area, and is therefore identical to the right hand side of (7.79)

Equation (7.80) ensures that $\lim[f_m \rightarrow \infty]\{\mathrm{D}(f_m, z)\}$ will act like a Dirac delta function $\delta(z)$ with respect to $\mathcal{Q}(z)$ because they ensure that $\delta(z)$'s sifting property ($\sum \mathcal{Q}_n = \mathcal{Q}(0)$) will hold.

In brief, the argument is that the Darrell is approximately a sinc function for $z < 1/\alpha(f_m)$ (*ie*: where the effect of the Darrell's exp term is small). It is known that the $f_m \rightarrow \infty$ limit of the sinc function is a Dirac delta function [53] so that, except for the troublesome $z > 1/\alpha(f_m)$ region of the Darrell, the $f_m \rightarrow \infty$ limit of the Darrell is also a Dirac delta function. Constraints are placed on $\mathcal{Q}(z)$ satisfy the 'non delta function like' aspect of the Darrell for $z > 1/\alpha(f_m)$.

Although the following quote from Siebert [60] refers to the Fourier transform, it is deemed relevant because it brings important issues to the foreground:

> Attempts to state and prove mathematically rigorous forms of Fourier's Theorem that apply to some general class of $\mathcal{Q}(z)$ must cope with a dual problem. On the one hand, the "tails" of $\mathcal{Q}(z)$ must be adequately constrained as $|z| \rightarrow \infty$ so that the infinite integral defining $\underline{\mathcal{Q}}(\flat)$ exists in some appropriate sense; we shall call this a *global* condition. On the other hand, $\mathcal{Q}(z)$ must not be too "wiggly" or else the "tails" of $\underline{\mathcal{Q}}(\flat)$ as $|\flat| \rightarrow \infty$ will be so badly behaved that the inverse transform integral will have no satisfactory meaning; we shall call this a *local* condition.

The first requirement on $\mathcal{Q}(z)$ will be that it must not be too wiggly; it must be 'smooth' in a sense that will become clear in the forthcoming discussion. This requirement is local in the sense of Siebert. It is to be expected that $\mathcal{Q}(z)$ must also satisfy some global requirement. This global requirement will also become clear in the forthcoming discussion.

The argument starts by showing that

I $\quad \mathcal{Q}_n \cong 0$ for all $n \neq 0$

II $\quad \mathcal{Q}_0 \cong \mathcal{Q}(0)$

and then proceeds to deduce (7.80) by 'borrowing' from the known delta convergence of the sinc function.

The discussion supporting I and II utilizes

$$\lim_{f_m \to \infty} \left\{ \Delta z_{_D}(f_m) = \frac{c(f_m)}{2f_m} = \frac{\pi}{\beta(f_m)} \right\} = 0 \tag{7.83}$$

which follows directly from the causality constraint of CLDP materials by way of the the Paley-Wiener-Guillemin criterion (PWG, section 6.4). The PWG criterion states that, as $f_m \to \infty$, $\beta(f_m) \equiv 2\pi f_m / c(f_m)$ must increase at least as rapidly as f_m (and less rapidly that f_m^2). But $\beta(f_m)$ is directly proportional to the inverse of $\Delta z_{_D}(f_m)$, so (7.83) follows directly.

Requirement I

For n such that

$$2n\Delta z_{_D}(f_m) = \frac{nc(f_m)}{f_m} \equiv z_n(f_m) \qquad < \qquad 1/\alpha(f_m) \tag{7.84}$$

two effects conspire to satisfy I for smooth, finite-valued $\mathcal{Q}(z)$'s which are roughly constant over the range of z defining the arbitrary $\mathcal{Q}_{n\neq 0}$:

- the integrand defining $\mathcal{Q}_n$ is negative for z satisfying $(2n-1)\Delta z_{_D}(f_m) < z < z_n(f_m)$, and negative for z satisfying $z_n(f_m) < z < (2n+1)\Delta z_{_D}(f_m)$; the total integral defining $\mathcal{Q}_n$ therefore tends to cancel
- equation (7.83) ensures that the range of integration defining $\mathcal{Q}_n$ vanishes; therefore, $\mathcal{Q}_n$ itself tends to vanish

The following analysis confirms these observations mathematically, and points out the need for a global constraint on $\mathcal{Q}(z)$ for $z_n(f_m) \gg 1/\alpha(f_m)$ (in which case the Darrell varies rapidly with z due to its exp term). Equation (7.85) is an approximation to (7.81). Equation (7.85) exploits (7.83) and the assumed smoothness of $\mathcal{Q}(z)$, and also makes use of the fact that the average value of the sin function between zero crossings is $\pm 2/\pi$:

$$\mathcal{Q}_n \cong \lim_{f_m \to \infty} \left\{ \Delta z_{_D}(f_m) \left[\mathcal{Q}(z_n^+(f_m))\ \exp(z_n^+(f_m)\ \alpha(f_m))\ \frac{2/\pi}{\pi z_n^+(f_m)} \right.\right.$$

$$\left.\left. - \mathcal{Q}(z_n^-(f_m))\ \exp(z_n^-(f_m)\ \alpha(f_m))\ \frac{2/\pi}{\pi z_n^-(f_m)} \right] \right\} \tag{7.85}$$

where

$$z_n^{\pm}(f_m) \quad \equiv \quad (2n \pm \frac{1}{2})\,\Delta z_{_D}(f_m) = z_n(f_m) \pm \frac{1}{2}\Delta z_{_D}(f_m) \tag{7.86}$$

Equation (7.85) may be approximated further by noting that

$$\frac{\mathcal{Q}(z_n^+(f_m))}{z_n^+(f_m)} \cong \frac{\mathcal{Q}(z_n^-(f_m))}{z_n^-(f_m)} \cong \frac{\mathcal{Q}(z_n(f_m))}{z_n(f_m)} \tag{7.87}$$

The result is:

$$\mathcal{Q}_n \cong \frac{2}{\pi^2} \lim_{f_m \to \infty} \left\{ \Delta z_{_D}(f_m) \frac{\mathcal{Q}(z_n(f_m))}{z_n(f_m)} \left[\exp(z_n^+(f_m)\alpha(f_m)) - \exp(z_n^-(f_m)\alpha(f_m)) \right] \right\} \tag{7.88}$$

Equation (7.86) allows the square bracketed quantity in (7.88) to be re-written:

$$\exp(z_n(f_m)\ \alpha(f_m)) \Big[\exp(\frac{1}{2}\Delta z_{_D}(f_m)\ \alpha(f_m)) - \exp(-\frac{1}{2}\Delta z_{_D}(f_m)\ \alpha(f_m)) \Big] \tag{7.89}$$

The Paley-Wiener criterion (PW, section 6.3, which also holds for all causal materials) implies that, as $f_m \to \infty$, $\alpha(f_m)$ cannot increase as rapidly as f_m. But by the PWG criterion, $\Delta z_{_D}(f_m)$ must decrease faster than $1/f_m$ so the product quantity

$$\eta(f_m) \quad \equiv \quad \Delta z_{_D}(f_m)\ \alpha(f_m) = \frac{\alpha(f_m)c(f_m)}{2f_m} = \pi \frac{\alpha(f_m)}{\beta(f_m)} \tag{7.90}$$

must satisfy $0 < \eta(f_m) \ll 1$ for large f_m. That is,

$$\lim_{f_m \to \infty} \left\{ \eta(f_m) = \Delta z_{_D}(f_m)\ \alpha(f_m) = \frac{\alpha(f_m)c(f_m)}{2f_m} = \pi \frac{\alpha(f_m)}{\beta(f_m)} \right\} = 0 \tag{7.91}$$

Using this information, and approximating

$$\exp(\eta) \cong 1 + \eta \tag{7.92}$$

allows (7.89) (the square bracketed quantity in (7.88)) to be approximated as

$$\eta(f_m)\ \exp(z_n(f_m)\ \alpha(f_m)) \tag{7.93}$$

Replacing the square bracketed quantity in equation (7.88) with (7.93) yields:

$$\mathcal{Q}_n \cong \frac{2}{\pi^2} \lim_{f_m \to \infty} \left\{ \mathcal{Q}(z_n(f_m)) \left[\Delta z_D(f_m) \eta(f_m) \right] \frac{\exp(z_n(f_m)\alpha(f_m))}{z_n(f_m)} \right\} \tag{7.94}$$

The square bracketed quantity in equation (7.94) approaches zero at least as rapidly as $(f_m)^{-h}$ (where $h \geq 1$) as $f_m \to \infty$. When $z_n(f_m) < 1/\alpha(f_m)$ (and assuming $\mathcal{Q}(z_n(f_m)) < \infty$), it follows that $\mathcal{Q}_n \to 0$ and I is satisfied. When $z_n(f_m) \gg 1/\alpha(f_m)$, however, the exponential term dominates and only a global constraint on $\mathcal{Q}(z)$ can ensure I.

Using (7.82), (7.86), and (7.90) to re-write (7.94) in terms of $\alpha(f_m)$ and $c(f_m)$ yields:

$$\mathcal{Q}_n \cong \lim_{f_m \to \infty} \left\{ \mathcal{Q}(\frac{nc(f_m)}{f_m}) \left[\frac{\alpha(f_m)}{2(\pi n)^2} \frac{nc(f_m)}{f_m} \right] \exp(\frac{nc(f_m)}{f_m} \alpha(f_m)) \right\} \tag{7.95}$$

For I to hold, $\mathcal{Q}_n$ must vanish when n and f_m approach infinity in such a manner that

$$\lim_{\substack{f_m \to \infty \\ n \to \infty}} \left\{ z_n(f_m) = \frac{nc(f_m)}{f_m} \right\} = \infty \tag{7.96}$$

That is: I requires not only that $\mathcal{Q}(z)$ be smooth compared to the $f_m \to \infty$ oscillations of the Darrell, but also that

$$\lim_{\substack{f_m \to \infty \\ z \to \infty}} \left\{ \frac{\mathcal{Q}(z)}{2} \left[\frac{\alpha(f_m)\, c(f_m)}{\pi\, f_m} \right]^2 \frac{\exp(z\, \alpha(f_m))}{z\, \alpha(f_m)} \right\} \quad = \quad 0 \tag{7.97}$$

It follows from (7.91) that

$$\lim_{f_m \to \infty} \left\{ \left[\frac{\alpha(f_m)\, c(f_m)}{\pi\, f_m} \right]^2 \right\} = 0 \tag{7.98}$$

However, the fact that the square bracketed quantity in (7.97) (*ie*: the curly-bracketed quantity in (7.98)) vanishes as the inverse of some positive power of f_m as $f_m \to \infty$ is not enough to ensure (7.97) because (7.97)'s $\exp(z\alpha(f_m))/(z\alpha(f_m))$ term grows exponentially with z when

$$\lim_{f_m \to \infty} \{\alpha(f_m)\} \equiv \alpha_\infty \quad \neq \quad 0 \tag{7.99}$$

So that, besides smoothness, I (by way of (7.97)) requires that $\mathcal{Q}(z)$'s $z \to \infty$ asymptotic "tail" approach zero faster than

$$z\, \alpha_\infty\, \exp(-z\, \alpha_\infty) \tag{7.100}$$

Requirement II

Setting $n = 0$ in (7.81) yields

$$\mathcal{Q}_0 = \lim_{f_m \to \infty} \left\{ \int_{-\Delta z_D(f_m)}^{+\Delta z_D(f_m)} \mathcal{Q}(z)\ \exp(z\ \alpha(f_m))\ \frac{\sin(2\pi f_m z / c(f_m))}{\pi z}\ dz \right\} \tag{7.101}$$

Because the range of integration vanishes as $f_m \to \infty$, the smoothness requirement on $\mathcal{Q}(z)$ ensures that $\mathcal{Q}(z) \cong \mathcal{Q}(0)$ for all the z's in (7.101). It is therefore legitimate to move $\mathcal{Q}(z)$ outside the integral as the constant $\mathcal{Q}(0)$. Performing this operation, and using (7.82) (the definition of $\Delta z_D(f_m)$) yields

$$\mathcal{Q}_0 \cong \mathcal{Q}(0) \lim_{f_m \to \infty} \left\{ \int_{-c(f_m)/(2f_m)}^{+c(f_m)/(2f_m)} \exp(z\ \alpha(f_m))\ \frac{\sin(2\pi f_m z / c(f_m))}{\pi z}\ dz \right\} \tag{7.102}$$

Now note that

$$|z| \leq \frac{c(f_m)}{2f_m} \tag{7.103}$$

for all z's in (7.102). Equation (7.102)'s monotonic $\exp(z\alpha(f_m))$ function therefore takes its $\pm$ extremum values

$$\exp^{\pm}_{\text{extremum}} \quad = \quad \exp\left(\pm \frac{\alpha(f_m) c(f_m)}{2f_m} \right) \tag{7.104}$$

at $z = \pm c(f_m)/(2f_m)$. By equation (7.91), therefore, $\exp(z\alpha(f_m)) \cong 1$ for all the z's in (7.102). Using this approximation, (7.102) becomes

$$\mathcal{Q}_0 \cong \mathcal{Q}(0) \lim_{f_m \to \infty} \left\{ \int_{-c(f_m)/(2f_m)}^{+c(f_m)/(2f_m)} \frac{\sin(2\pi f_m z / c(f_m))}{\pi z}\ dz \right\} \tag{7.105}$$

Changing variables from z to

$$x(z) \quad \equiv \quad z\ \frac{2\pi f_m}{c(f_m)} = z\ \beta(f_m) \tag{7.106}$$

yields

$$\mathcal{Q}_0 \cong \frac{\mathcal{Q}(0)}{\pi} \lim_{f_m \to \infty} \left\{ \int_{-\pi}^{+\pi} \frac{\sin(x)}{x} dx \right\}$$

$$\cong \frac{\mathcal{Q}(0)}{\pi} \left[\mathrm{Si}(\pi) - \mathrm{Si}(-\pi) \right]$$

$$\cong 1.179 \; \mathcal{Q}(0) \tag{7.107}$$

where $\mathrm{Si}(\xi) \equiv \int_0^\xi [\sin(t)/t] dt$ is the sine integral [110]. Note that $\mathcal{Q}_0 \cong \mathcal{Q}(0)$, as required by II.

Borrowing From The Delta Convergence Of The Sinc Function

Consider now the discrete valued function

$$\mathcal{I}_{\mathcal{Q}}[n] \equiv \sum_{n'=-n}^{n} \mathcal{Q}_n$$

$$= \lim_{f_m \to \infty} \left\{ \int_{-(2n+1)\Delta z_D(f_m)}^{+(2n+1)\Delta z_D(f_m)} \mathcal{Q}(z) \; \mathrm{D}(f_m, z) \; dz \right\} \tag{7.108}$$

for which

$$\mathcal{I}_{\mathcal{Q}}[0] = \mathcal{Q}_0 \tag{7.109}$$

$$\mathcal{I}_{\mathcal{Q}}[1] = \mathcal{Q}_{-1} + \mathcal{Q}_0 + \mathcal{Q}_1 \tag{7.110}$$

$$\mathcal{I}_{\mathcal{Q}}[2] = \mathcal{Q}_{-2} + \mathcal{Q}_{-1} + \mathcal{Q}_0 + \mathcal{Q}_1 + \mathcal{Q}_2 \tag{7.111}$$

It should be clear from (7.108) and the discussion leading to (7.107) that if $\mathcal{Q}(z)$ is nearly constant for z's falling between $-(2n+1)\Delta z_D(f_m)$ and $+(2n+1)\Delta z_D(f_m)$ then

$$\mathcal{I}_{\mathcal{Q}}[n] \cong \frac{\mathcal{Q}(0)}{\pi} \Big[\mathrm{Si}(\pi[2n+1]) - \mathrm{Si}(-\pi[2n+1]) \Big] \tag{7.112}$$

For sufficiently smooth $\mathcal{Q}(z)$, the series

$$\frac{\mathcal{I}_{\mathcal{Q}}[n]}{\mathcal{Q}(0)} \cong \{1.179, 1.066, 1.040, 1.029, 1.022, 1.018, 1.016, 1.014, 1.012, 1.011, \cdots\} \tag{7.113}$$

approaches unity monotonically.

Using (7.112), the odd symmetry of $\mathrm{Si}(\xi)$, and the fact that [110]

$$\lim_{\xi \to \infty} \{\mathrm{Si}(\xi)\} = \frac{\pi}{2} \tag{7.114}$$

it follows immediately that

$$\lim_{n \to \infty} \{\mathcal{I}_{\mathcal{Q}}[n]\} = \sum_{n=-\infty}^{\infty} \mathcal{Q}_n \cong \mathcal{Q}(0) \tag{7.115}$$

for sufficiently smooth $\mathcal{Q}(z)$ satisfying (7.97), as required by (7.80).

A CLDP material's Darrell will be delta convergent with respect to all the causal $\mathcal{Q}(z)$'s for which the sinc function is delta convergent (*ie*: the Fourier transformable $\mathcal{Q}(z)$'s) provided these $\mathcal{Q}(z)$'s also satisfy constraint (7.97), which itself reduces to an α_∞-dependent constraint on the $z \to \infty$ asymptotic behaviour of $\mathcal{Q}(z)$. If $\alpha_\infty = \infty$, $\mathcal{Q}(z)$ must have finite support (*ie*: $\mathcal{Q}(z)$ must not only be causal, but must also vanish for $z > z'$ where z' is some positive constant).

Comparing Laplace-plane And Darrell-Determined Constraints On $\mathcal{Q}(z)$

It is worth pointing out that section 7.8's discussion (which culminated with equation (7.73), page 120; the CLDP criterion) also contains local and global constraints on $\mathcal{Q}(z)$. Section 7.8 required that $\mathcal{Q}(z)$ be Fourier transformable, and Siebert has pointed out that Fourier transformable functions must satisfy both a local and a global constraint.

Furthermore: like (7.97), the CLDP criterion places especially stringent requirements on $\mathcal{Q}(z)$ in the case where α_∞ is large. The $\beta \to \infty$ Laplace plane integral which comprises the CLDP criterion (and which registers the high frequency behaviour of $\mathcal{Q}(z)$) is then relatively long and is therefore less likely to vanish as required unless $\underline{\tilde{\mathcal{Q}}}(\underline{\mathcal{K}})$ has small values at large β. $\underline{\tilde{\mathcal{Q}}}(\underline{\mathcal{K}})$ is unlikely to satisfy the CLDP criterion unless $\mathcal{Q}(z)$ satisfies stringent local and global constraints.

7.10 Numeric Verification Of The Darrell Property

This section's goal is to numerically verify the Darrell property, and the shape of the Darrell, as descriptors for the noiseless but abruptly (*ie*: subjected to an ideal, square window lowpass filter) bandlimited inverse CLDP IE. That is, with

$$\mathcal{P}(t) \quad \overset{\mathcal{F}}{\Longleftrightarrow} \quad \underline{\mathcal{P}}(f) = \int_0^\infty \mathcal{Q}(z)\ \exp(-z\ \underline{\mathcal{K}}(f))\ dz \tag{7.116}$$

and

$$\mathrm{R}(f_m, z) = \int_{-f_m}^{f_m} \underline{\mathcal{P}}(f) \left[\frac{1}{\mathrm{j}\, 2\pi} \frac{d\, \underline{\mathcal{K}}(f)}{df} \right] \exp(z\, \underline{\mathcal{K}}(f))\, df$$

$$= 2 \int_0^{f_m} \Re_e \left\{ \underline{\mathcal{P}}(f)\, \frac{\exp(z\, \underline{\mathcal{K}}(f))}{\underline{C}_g(f)} \right\} df \tag{7.117}$$

where

$$\frac{1}{\underline{C}_g(f)} = \frac{1}{\mathrm{j}\, 2\pi} \frac{d\, \underline{\mathcal{K}}(f)}{df} \tag{7.118}$$

and

$$\underline{\mathcal{K}}(f) = \alpha(f) + \mathrm{j}\, 2\pi f / c(f) \tag{7.119}$$

this section's goal is to numerically verify chapter 7's analytic result that

$$\mathrm{R}(f_m, z) = \mathcal{Q}(z) * \mathrm{D}(f_m, z) \tag{7.120}$$

where

$$\mathrm{D}(f_m, z) = \frac{\Im_m \{\exp(z\, \underline{\mathcal{K}}(f_m))\}}{\pi\, z}$$

$$= \exp(z\, \alpha(f_m))\, \frac{\sin(2\pi f_m z / c(f_m))}{\pi z} \tag{7.121}$$

In the practical PESAW context the actual measured signals are time sampled versions $\mathcal{P}[t_n] \equiv \mathcal{P}(n\Delta t)$ of $\mathcal{P}(t)$. In this thesis, estimates $\tilde{\underline{\mathcal{P}}}(f)$ to the desired $\underline{\mathcal{P}}(f)$ are determined from the measured (or synthetic) $\mathcal{P}[t_n]$ via the FFT

$$\tilde{\underline{\mathcal{P}}}(f_k) = \underline{\mathcal{P}}[f_k] = \mathrm{FFT}\{\mathcal{P}[t_n]\} \tag{7.122}$$

and equation (7.117)'s integration is implemented straightforwardly:

$$\mathrm{R}(f_m, z) = \Delta f \sum_{f_k=0}^{f_m} \mathrm{two}[f_k]\, \Re_e \left\{ \underline{\mathcal{P}}[f_k]\, \frac{\exp(z\, \underline{\mathcal{K}}(f_k))}{\underline{C}_g(f_k)} \right\} \tag{7.123}$$

As introduced in section 4.14.4, the discrete-valued function two$[f_k]$ has value 2 for all $k \neq \{0, k'\}$ (where $k' = N_t/2$). When $k = 0$ or $k = k'$, two$[k]$ has the value unity.

Please recall from section 4.14.3 and appendix E.9.1 that $f_M \equiv (2\Delta t)^{-1}$ is the maximum frequency available from the FFT of time sampled data. So whereas f_m is the generic abrupt-bandlimiting frequency appearing in (7.117), f_M is the specific maximum value of f_m that can reasonably be submitted to this thesis' numeric approximation (7.123) to (7.117).

It is of course impossible to exhaustively verify the Darrell property (7.120) and the shape of the Darrell (7.121) for all materials $\underline{\mathcal{K}}(f)$, all bandlimiting frequencies f_m, and all source waveforms $\mathcal{Q}(z)$.

However, for any one particular material model, bandlimiting frequency, and source waveform, it is possible to calculate the error between the expected, analytic recovery given by $\alpha(f_m)$, $c(f_m)$ and $\mathcal{Q}(z)$ via (7.120) and (7.121) with the actual numeric recovery given by (7.122) and (7.123).

For example, the $\hat{\mathrm{H}}_p[1\text{ mm}, t_n]$ depicted in figure C.1 was calculated using $\Delta t = 2$ ns, $N_t = 4096$, $\mathcal{Q}(z) = \delta(z - 1\text{ mm})$, and the $\underline{\mathcal{K}}_p(f)$ model for standard polyethylene described in section 6.2.2 and depicted in figures C.2 through C.5. More explicitly,

$$\hat{\mathrm{H}}_p[1\text{ mm}, t_n] = \mathrm{FFT}^{-1}\{\exp(\,-1\text{ mm}\,[\alpha_p(f_k) + \mathrm{j}\,2\pi f_k/c_p(f_k)])\} \tag{7.124}$$

where $f_k = k/(N_t\ \Delta t)$ and the inverse fast Fourier transform FFT^{-1} is defined in section F.3.

Submitting $\mathrm{FFT}\{\hat{\mathrm{H}}_p[1\text{ mm}, t_n]\} \rightarrow \underline{\mathcal{P}}[f_k]$, $\underline{\mathcal{K}}_p(f) \rightarrow \underline{\mathcal{K}}(f)$, and $f_m \rightarrow f_M$ in equation (7.123) yields the $\mathrm{R}[f_M, z_i]$ depicted in figure 7.1. The analytically expected recovery $\mathrm{D}_p[f_M, z_i - 1\text{ mm}]$ is also depicted in figure 7.1. The RMS error between these two waveforms is 2.474 mm^{-1} over the approximately 10 λ's plotted.

The central (*ie*: $z = 0$) height H_D of $\mathrm{D}_p(f_m, z)$ may be determined analytically from the form of the Darrell as $2f_m/c_p(f_m)$. Because $\Delta t = 2$ ns, $f_M \equiv (2\Delta t)^{-1}$ = 250 MHz. Table C.1 yields $c_p(f_M) = 2.14243$ mm/μs so standard polyethylene's $\mathrm{H}_D(f_M) = 233.4\ \mathrm{mm}^{-1}$ and the normalized RMS error (raw/peak) associated with this numeric experiment is the dimensionless quantity

$$1.06\ 10^{-2} = \frac{2.47\ \mathrm{mm}^{-1}}{233.4\ \mathrm{mm}^{-1}}$$

that appears in table 7.1.

It is also possible to prematurely truncate the summation in (7.123) so that the effective value of f_m in (7.117) is $\grave{f}_m \equiv 25$ MHz. In this case the expected shape of the Darrell changes (see equation (7.121)) but the expected location ($z = 1$ mm) of the center of the Darrell stays the same. The normalized RMS error between the expected, analytic $\mathrm{D}_p(\grave{f}_m, z - 1\text{ mm})$ and the numeric $\mathrm{R}(\grave{f}_m, z)$ determined from $\mathrm{FFT}\{\hat{\mathrm{H}}_p[1\text{ mm}, t_n]\}$ is $4.22\ 10^{-4}$.

This value appears as the second (of six) normalized RMS errors appearing in the $f_m = 25$ MHz column, just to the right of the $1.06\ 10^{-2}$ entry. This value ($4.22\ 10^{-4}$)

happens to be the same as the normalized error culled from the numeric experiment for standard polyethylene where $f_m = 25$ MHz and $\mathcal{Q}(z) = \delta(z)$. Therefore $4.22\ 10^{-4}$ also appears as the first entry in the $f_m = 25$ MHz column.

In each of the twelve numeric experiments alluded to in table 7.1 the recovery was compared over a region of about 10λ (5λ to either side of the source impulse) at a spatial sampling rate $\Delta z \cong \lambda/25$. Perusing table C.1 (or figures C.2 through C.5), please note that the values for $\alpha(\hat{f}_m)$ and $c(\hat{f}_m)$ agree for all three materials. Therefore the expected shape of the Darrell is the same for the entire $f_m = 25$ MHz column.

Reviewing all the entries in table 7.1, it seems clear that both the Darrell property and the shape of the Darrell have been confirmed numerically. The largest normalized RMS error in the table is only $1.06\ 10^{-2}$. The agreement between the numeric and analytic waveforms associated with this entry is good enough that a cursory glance could fail to discern that there are two distinct waveforms plotted.

The next largest entry in the table ($1.36\ 10^{-3}$) is less than one seventh of the largest entry, and the smallest entry in the table ($7.58\ 10^{-6}$) is nearly 1400 times smaller than the largest entry.

It is interesting to note that both the largest and the smallest entries in table 7.1 are associated with standard polyethylene intrinsically bandlimited at f_M. The largest error is associated with a source placed at $z = 1$ mm. The smallest error is associated with a source placed at $z = 0$ mm. These two entries are the only pair of entries that differ from each other (all the other entries are independent of source placement depth, but differ according to the propagation model or bandlimiting frequency used).

It is possible to parlay knowledge of the fact that, at high frequencies,

I. the approximation $\mathcal{F}\{\mathcal{P}(t)\} \equiv \underline{\mathcal{P}}(f_k) \quad \cong \quad \underline{\mathcal{P}}[f_k] \equiv \mathrm{FFT}\{\mathcal{P}[n\Delta t]\}$ becomes systematically inaccurate (see section 4.14.3)

II. standard polyethylene's attenuation coefficient is significantly larger (at least thrice for $f > 200$ MHz; see figure C.2) than either the Bromwich or skin effect material's attenuation coefficient

into an explanation for why table 7.1's entry ($1.06\ 10^{-2}$) corresponding to difference between the recovery $\mathrm{R}(f_M, z)$ (gleaned from $\hat{\mathrm{H}}_p[1\mathrm{mm}, t_n]$ and (7.123)) and the analytically expected result $\mathrm{D}_p(f_M, z - 1\ \mathrm{mm})$ should be the largest in the table.

With $|\underline{Z}|$ denoting the magnitude of the complex number $\underline{Z}$, with $\langle \underline{Z} \rangle$ denoting its phase (so that $\underline{Z} = |\underline{Z}| \exp(\mathrm{j}\ \langle \underline{Z} \rangle)$), and with $\underline{\mathcal{K}}(f) = \alpha(f) + \mathrm{j}\ \beta(f)$, equation (7.123) may be re-expressed:

$$\mathrm{R}(f_m, z) = \Delta f \sum_{f_k=0}^{f_m} |\underline{\mathcal{P}}[f_k]|\ \exp(z\ \alpha(f_k))\ \frac{\mathrm{two}[f_k]}{|\underline{C}_g(f_k)|}\ \cos\left(z\ \beta(f_k) + \langle \underline{\mathcal{P}}[f_k] \rangle - \langle \underline{C}_g(f_k) \rangle\right) \tag{7.125}$$

Assuming the high-frequency error in $|\underline{\mathcal{P}}[f_k]||$ is of the same order of magnitude for all three materials and for both source depths, then that error is amplified most significantly by the $\exp(z\ \alpha(f_k))$ term acting in the calculation of the $\mathrm{R}(f_M, z_i)$'s gleaned from $\hat{\mathrm{H}}_p[1\mathrm{mm}, t_n]$. This follows because the product of the z_i's calculated with the $\alpha_p(f_k)$'s involved is larger for this entry than any other. Inspection of figure 7.1 confirms this hypothesis: the difference between the numeric and expected (analytic) waveforms increases with z.

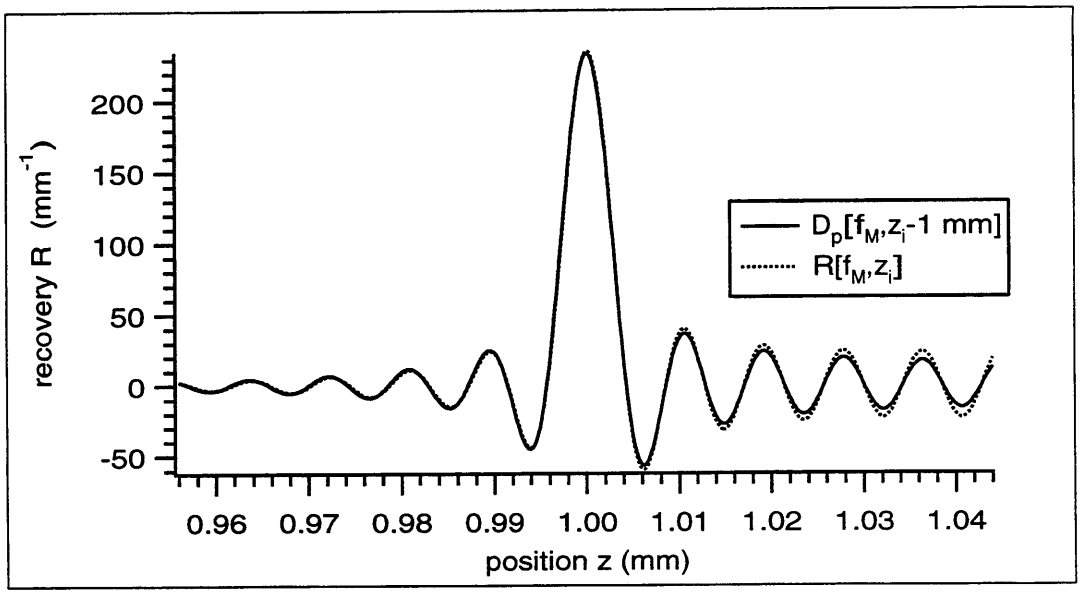

Figure 7.1: Comparison of $R[f_M, z_i]$ (calculated numerically from $FFT\{\hat{H}_p[1\text{ mm}, t_n]\}$) with the expected, analytic $D_p[f_M, z_i - 1\text{ mm}]$. $\Delta z = 0.2\ \mu$m.

	$f_m = f_M$ **250 MHz**	$f_m = \grave{f}_m$ **25 MHz**	$R(f_m, z)$ calculated from
Polyethylene	$7.58\ 10^{-6}$	$4.22\ 10^{-4}$	$\hat{H}_p[0\text{mm}, t_n]$
	$1.06\ 10^{-2}$	$4.22\ 10^{-4}$	$\hat{H}_p[1\text{mm}, t_n]$
Skin Effect	$2.22\ 10^{-4}$	$1.36\ 10^{-3}$	$\hat{H}_s[0\text{mm}, t_n]$
	$2.22\ 10^{-4}$	$1.36\ 10^{-3}$	$\hat{H}_s[1\text{mm}, t_n]$
Bromwich	$1.72\ 10^{-4}$	$4.30\ 10^{-4}$	$\hat{H}_b[0\text{mm}, t_n]$
	$1.72\ 10^{-4}$	$4.30\ 10^{-4}$	$\hat{H}_b[1\text{mm}, t_n]$

Table 7.1: Normalized RMS error (raw/peak) between numerically and analytically computed Darrells. Results presented show the dependence of this error on the material (polyethylene, skin effect, Bromwich), the bandlimiting frequency f_m (250 MHz, 25 MHz), and the source placement depth (0 mm, 1mm).

Chapter 8

The Lyons Recovery Applied To Synthetic Data

8.1 The Standard Impulsive Source Waveform

The standard impulsive source waveform $\mathcal{Q}_i(z)$ is discussed in sections 1.15 and 2.4, and also on page 33 (thesis outline). Mathematically,

$$\begin{aligned}\mathcal{Q}_i(z) &= \sum_{n=1}^{10} \delta(z - [\frac{n}{2} - \frac{1}{4}] \text{ mm}) \\ &= \delta(z - 0.25 \text{ mm}) + \delta(z - 0.75 \text{ mm}) + \cdots + \delta(z - 4.75 \text{ mm}) \end{aligned} \tag{8.1}$$

The response signal $\hat{\mathcal{P}}_i[t_n] = \hat{\mathcal{K}}_p\{\mathcal{Q}_i(z)\}$ corresponding to this standard impulsive source waveform embedded in standard polyethylene is depicted in figure 2.2.

8.1.1 The Unregularized Recovery

The Darrell is defined by the three quantities $\{f_m, \alpha(f_m), c(f_m)\}$:

$$\mathrm{D}(f_m, z) = \exp(z\ \alpha(f_m))\ \frac{\sin(2\pi f_m z / c(f_m))}{\pi z} \tag{8.2}$$

Every Darrell has a unique central (*ie*: $z = 0$) height H_D

$$\mathrm{H}_D \equiv \lim_{z \to 0}\{\mathrm{D}(f_m, z)\} = \frac{2 f_m}{c(f_m)} = \frac{2}{\lambda(f_m)} \tag{8.3}$$

and envelope function $\mathrm{E}_D(z)$

$$\mathrm{E}_D(z) \equiv \frac{\exp(z\ \alpha(f_m))}{\pi z} \tag{8.4}$$

Defining 'the safety length of the Darrell' l_D as that value of z which satisfies

$$\mathrm{E}_D(z) = \mathrm{H}_D \tag{8.5}$$

it follows from the Darrell property that if two source impulses are separated by a distance l_D or greater then the λ oscillations associated with the recovery of the shallower source will significantly obfuscate the recovery of the deeper source.

Equation (8.5) is transcendental so it is not possible to analytically solve for l_D in terms of $f_m, \alpha(f_m)$, and $c(f_m)$. But it is possible to find approximate numeric solutions to (8.5). For standard polyethylene abruptly bandlimited at $f_m = f_M = 250$ MHz, $l_D(f_M) \cong 0.29452$ mm (see table C.1 for the requisite values $\alpha(f_m)$ and $c(f_m)$). Standard polyethylene abrupted bandlimited at $f_m = \grave{f}_m = 25$ MHz yields $l_D(\grave{f}_m) \cong 2.9665$ mm.

Because the sources in $\mathcal{Q}_i(z)$ are separated by 0.5 mm (which is greater than standard polyethylene's $l_D(f_M)$), the unregularized $\mathrm{R}[f_m, z]$ determined from $\hat{\mathcal{P}}_i[t_n]$ will be unsatisfactory: the λ oscillations associated with the recovery of the $z = 0.25$ mm source impulse will significantly obfuscate all the other nine sources.

Figure 8.1 demonstrates that this is so by depicting the recovery of the two shallowest sources. As expected, the recovery of the second source impulse is completely obfuscated by the λ oscillations associated with the recovery of the first source impulse.

Figure 8.2 is a closeup of figure 8.1 which demonstrates that the recovery of the first (*ie*: $z = 0.25$ mm) source appears as expected (*ie*: it appears as $\mathrm{D}_p(f_M, z - 0.25 \text{ mm})$) when the scale has been changed ... actually, the first pulse in the recovery should appear as

$$\mathrm{D}_p(f_M, z - 0.25 \text{ mm}) + \underbrace{\mathrm{D}_p(f_M, z - 0.75 \text{ mm}) + \cdots + \mathrm{D}_p(f_M, z - 4.75 \text{ mm})}_{\text{influence of deeper sources}}$$

but, practically, the influence of these deeper sources for the z's plotted in figure 8.2 is on the order of the negligible quantity $\exp([-0.5 \text{ mm}]\ [\alpha_p(f_M) = 18.25 \text{ Np/mm}]) \sim 10^{-4}$.

Figure 8.3 depicts the error waveform (numeric - expected) between the two waveforms depicted in figure 8.2. The error waveform has a negative average value reflecting the fact that the area ($\Delta z = 0.5$ μm times the sum of the 183 points plotted) of the numeric waveform (1.0122) is slightly less than the area of the analytic, or expected, waveform (1.0135). The RMS value of this error waveform is $4.55\ 10^{-2}$ mm^{-1}. The central value $\mathrm{H}_D = 2/\lambda$ of the expected waveform is 233.4 mm^{-1} so this raw RMS error corresponds to a normalized RMS error of $1.95\ 10^{-4}$. Note that the error waveform increases with z.

Figure 8.4 demonstrates the $f_m = \grave{f}_m = 25$ MHz version of this same 'obfuscation' effect, which manifests itself in the unregularized Lyons recovery of extended sources. Figure 8.4 demonstrates this obfuscation effect, *and* it numerically confirms

the Darrell property by comparing the numeric $\mathrm{R}[\grave{f}_m, z]$ determined by submitting $\underline{\mathcal{P}}[f_k] \equiv \mathrm{FFT}\{\mathcal{P}_i[t_n]\}$ to (7.123) with the expected $\mathrm{R}[\grave{f}_m, z]$ given by submitting the standard impulsive source waveform $\mathcal{Q}_i(z)$ to the Darrell property. That is, figure 8.4's expected $\mathrm{R}[\grave{f}_m, z]$ is given by

$$\text{expected, analytic} \quad \mathrm{R}(\grave{f}_m, z) = \mathcal{Q}_i(z) * \mathrm{D}_p(\grave{f}_m, z) \tag{8.6}$$

Because $l_D(\grave{f}_m) \cong 2.9665$ mm, figure 8.4 only plots $\mathrm{R}[\grave{f}_m, z]$ from $z = 0$ mm to $z = 3$ mm. This range of z includes the recovery of the first six source impulses.

In accordance with (8.6), figure 8.4 confirms that the numeric recovery from $\mathcal{P}_i[t_n]$ is almost exactly the sum of a set of shifted Darrells: the naked eye can just barely discern that there are actually two waveforms plotted. The RMS difference between the two waveforms plotted is 1.83 mm^{-1}.

Figure 8.5 is an 'error waveform.' It depicts the difference between the two waveforms plotted in figure 8.4. Figure 8.5 confirms the expectation (see page 7.10) that this error should increase with z. Perhaps surprisingly, the error waveform depicted in figure 8.5 has an oscillatory nature that would be reasonably well characterized by the product of a sin and an exponential.

Figure 8.6's closeup of the 'large z' portion of figure 8.4 shows that the error between these two waveforms is due more to a difference in phase (*ie*: shifting) than a difference in amplitude: it appears that the two waveforms would overlap if the numeric waveform were shifted ~ 2 μm to the left (of course, actually shifting the numeric recovery in this manner would throw the 'small z' portion of figure 8.4 out of kilter).

This behavior contrasts with the behavior exhibited in figure 7.1, where the error appears to be due more to a difference in amplitude than phase. The author offers no explanation for these disparate behaviors, but notes that they correspond to disparate values of f_m and result in errors that increase with z.

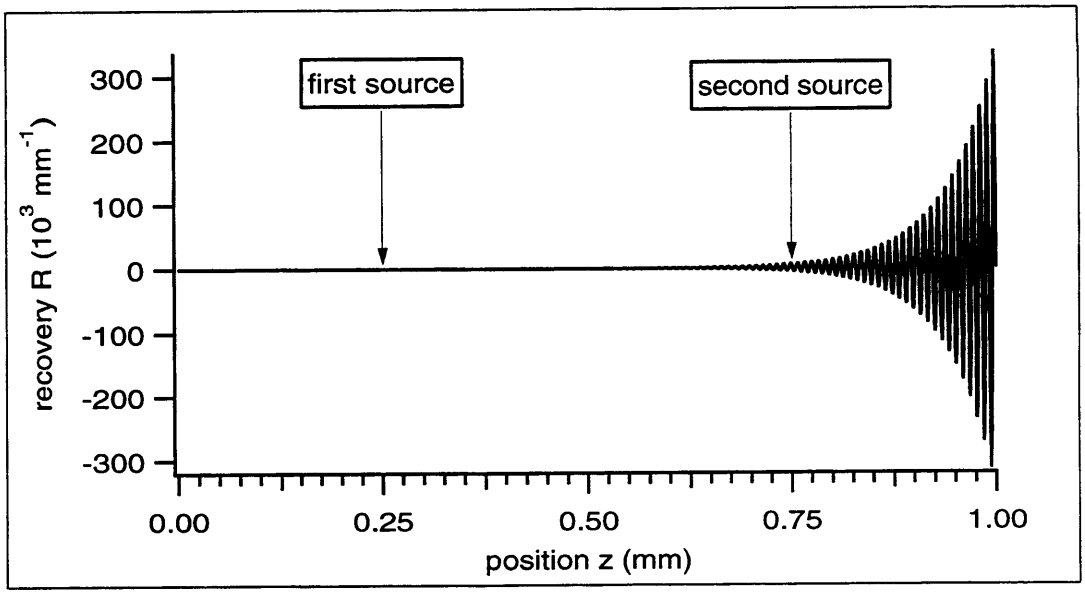

Figure 8.1: The unregularized recovery R$[f_M, z]$ of $\mathcal{Q}_i(z)$ determined from FFT$\{\hat{\mathcal{P}}_i[t_n]\}$.

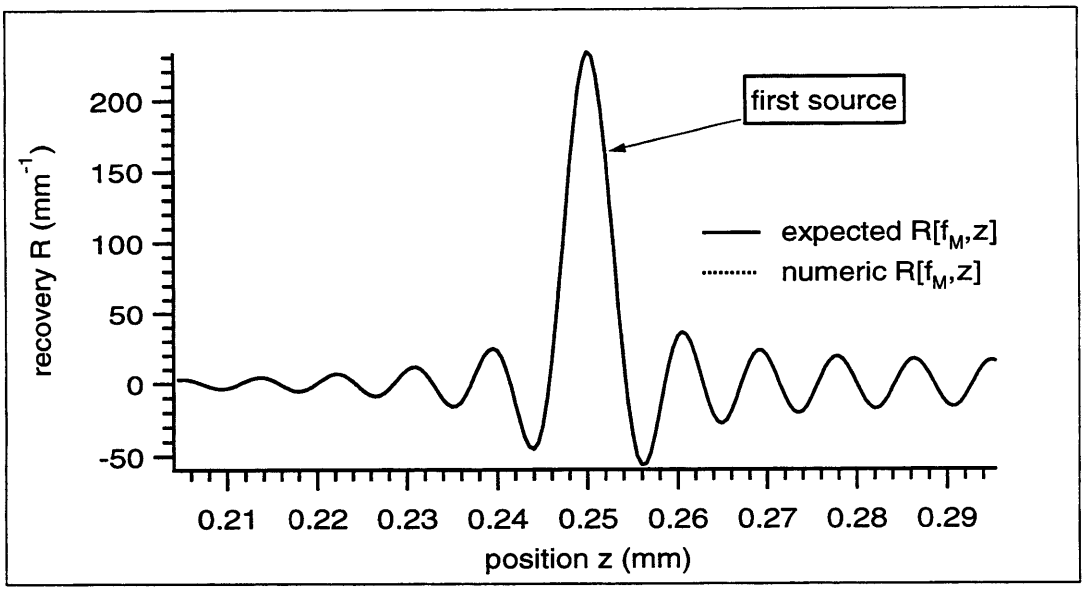

Figure 8.2: Closeup ($z = 0.2$ to 0.3 mm) of figure 8.1.

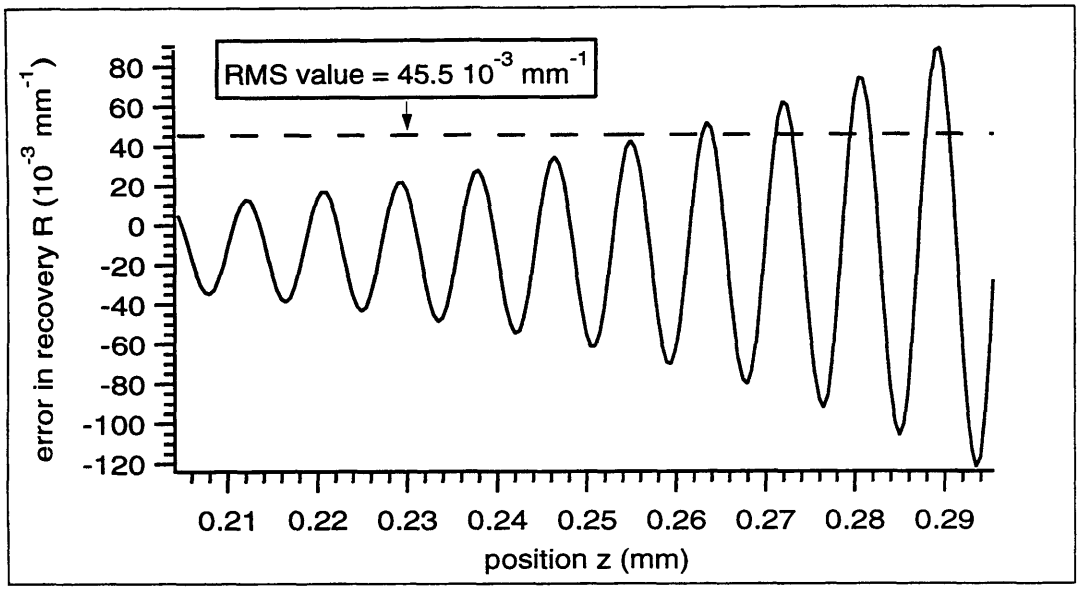

Figure 8.3: Error waveform representing the difference (numeric-analytic) between the two waveforms depicted in figure 8.2.

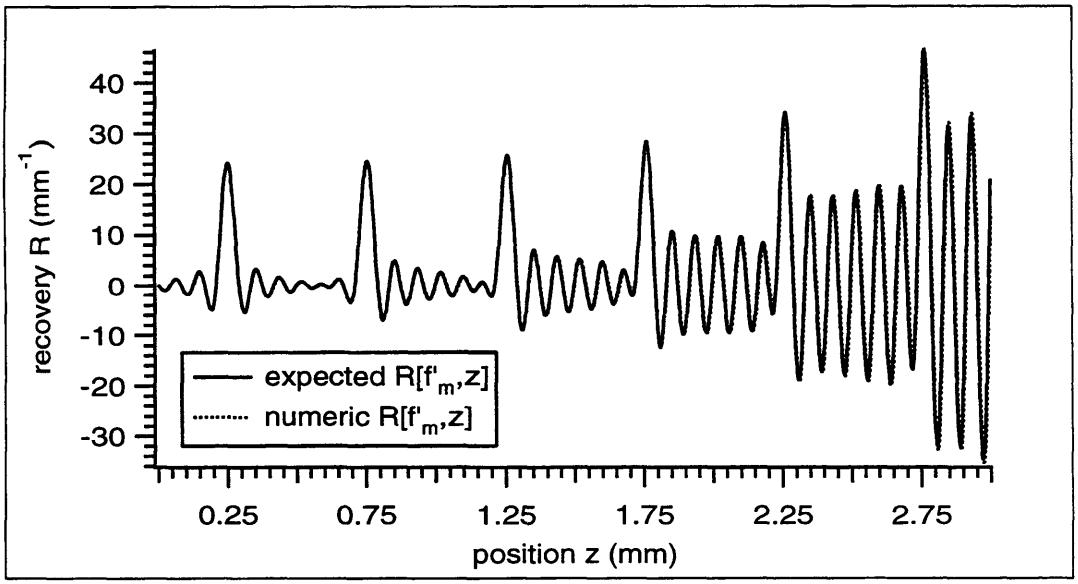

Figure 8.4: Comparison of the unregularized numeric recovery $\mathrm{R}[\hat{f}_m, z]$ of $\mathcal{Q}_i(z)$ determined from $\mathrm{FFT}\{\hat{\mathcal{P}}_i[t_n]\}$ with the expected, analytic recovery.

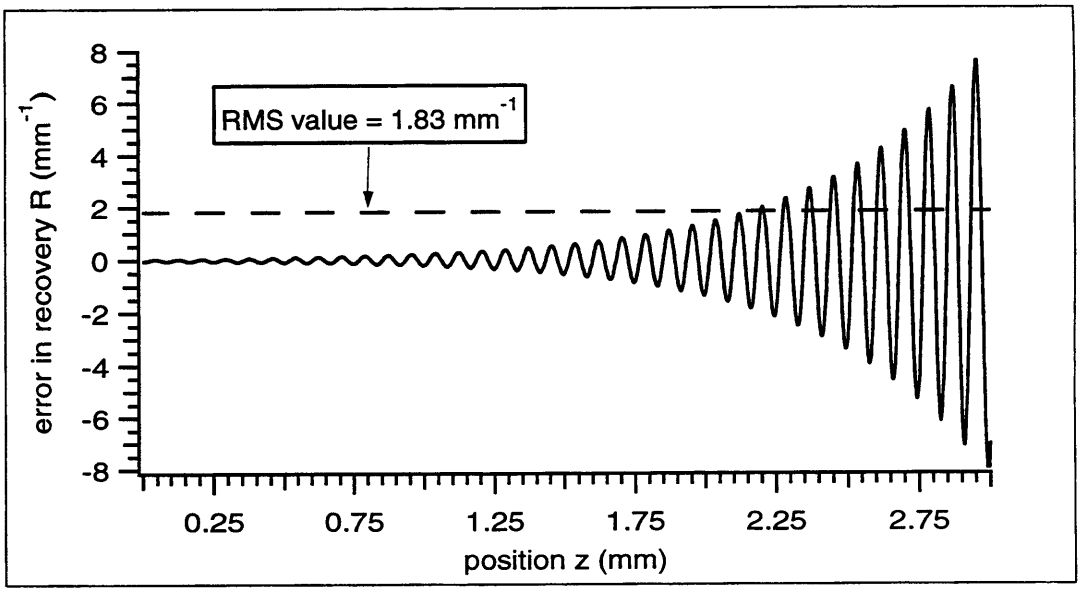

Figure 8.5: Error waveform representing the difference (numeric-analytic) between the two waveforms depicted in figure 8.4.

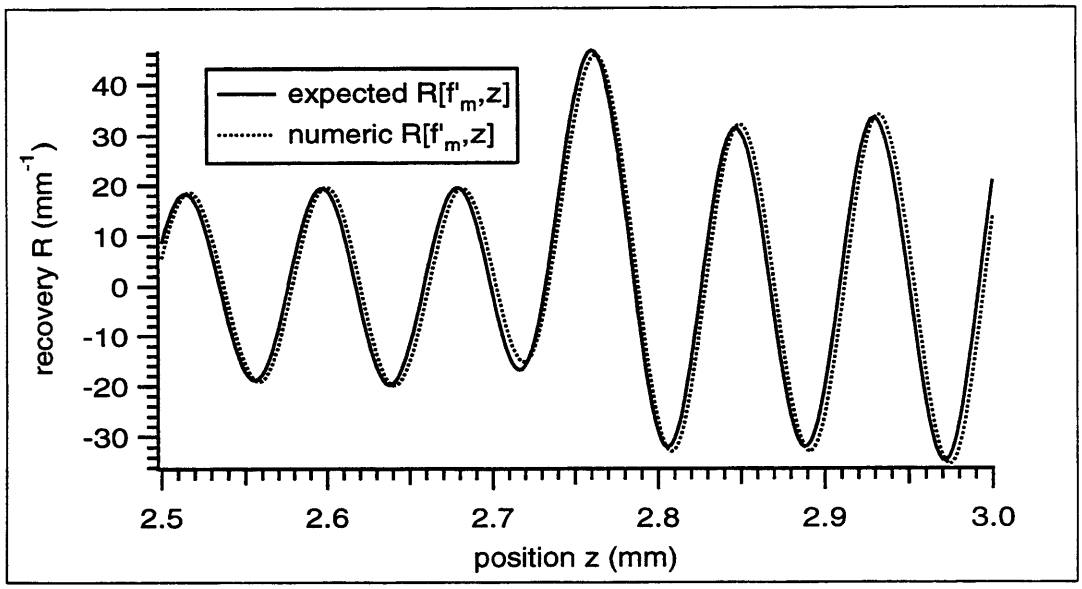

Figure 8.6: Closeup (z = 2.5 to 3 mm) of figure 8.4.

8.2 The Standard Gaussian Source Waveform

Having determined that the unregularized Lyons recovery is unsatisfactory via analysis of the standard impulsive source waveform $\mathcal{Q}_i(z)$, it seems clear that the unregularized Lyons recovery of any source waveform (especially an extended one) will be unsatisfactory as well. Focus now shifts to the SIB and SDB regularized Lyons recoveries of the more realistic (extended) standard Gaussian source waveform $\mathcal{Q}_g[z_i]$:

$$\mathcal{Q}_g[z_i] = \int_{z_i-\Delta z/2}^{z_i+\Delta z/2} \left[\sum_{n=1}^{10} (-1)^n \, \mathcal{G}(\text{FWHM}[n], z - [\frac{n}{2} - \frac{1}{4}] \text{ mm}) \right] dz \qquad (8.7)$$

where

$$\mathcal{G}(\text{FWHM}, z) \equiv \frac{2\sqrt{\ln 2}}{\text{FWHM}\sqrt{\pi}} \exp\left(- \left[\frac{2\sqrt{\ln 2}\, z}{\text{FWHM}} \right]^2 \right) \qquad (8.8)$$

and FWHM$[n]$ = 36.32 μm for n odd whereas FWHM$[n]$ = 95.49 μm for n even.

These rather arbitrary values (36.32 μm and 95.49 μm) correspond, respectively, to the z = 0.25 mm and z = 4.75 mm values of the FWHM of the standard SDB recovery of the standard impulsive sorce waveform embedded in standard polyethylene (see figure 1.3).

Note that $\mathcal{G}(\text{FWHM}, z)$ is a normalized (*ie*: unit area) Gaussian waveform independent of FWHM. This can be seen by starting with the standard deviation σ dependent normalized Gaussian

$$\mathcal{G}'(\sigma, z) \equiv \frac{1}{\sigma\sqrt{2\pi}} \exp\left(-\frac{1}{2} \left[\frac{z}{\sigma} \right]^2 \right)$$

used by Stark and Woods [101], then realizing that FWHM$\{\mathcal{G}'(\sigma, z)\} = \sigma\, 2\sqrt{2\ln 2}$.

The standard Gaussian source waveform $\mathcal{Q}_g[z_i]$ depicted in figure 8.7 was calculated at the set of points $z_i = i\Delta z$ (where $\Delta z = 2$ μm and $0 \leq i \leq 2500$) via the error function erf [101]. The area of each Gaussian pulse is $\pm$ unity.

The modelled response signal $\hat{\mathcal{P}}_g[t_n] = \hat{\mathcal{K}}_p\{\mathcal{Q}_g[z_i]\}$ corresponding to this standard Gaussian source waveform embedded in standard polyethylene is depicted in figure 8.8.

In figure 8.8, the response signals due to the deeper Gaussian sources overlap significantly. The dominant recovery, which maps signals to waveforms without changing their shape (see sections 1.6 or 2.4), will certainly yield a poor deep-source recovery from $\hat{\mathcal{P}}_g[t_n]$.

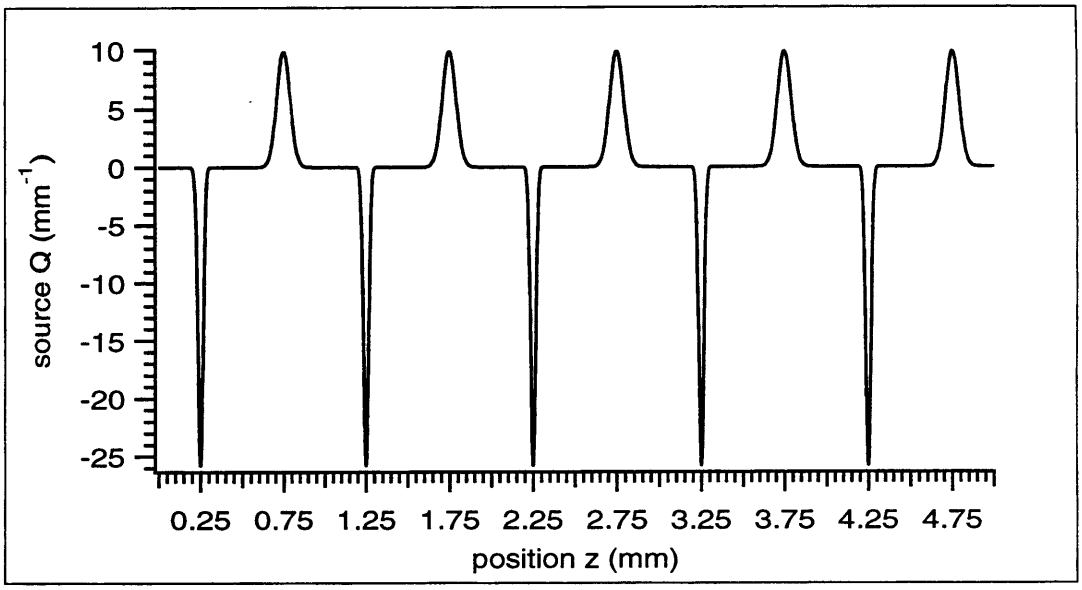

Figure 8.7: The standard Gaussian source waveform $\mathcal{Q}_g[z_i]$.

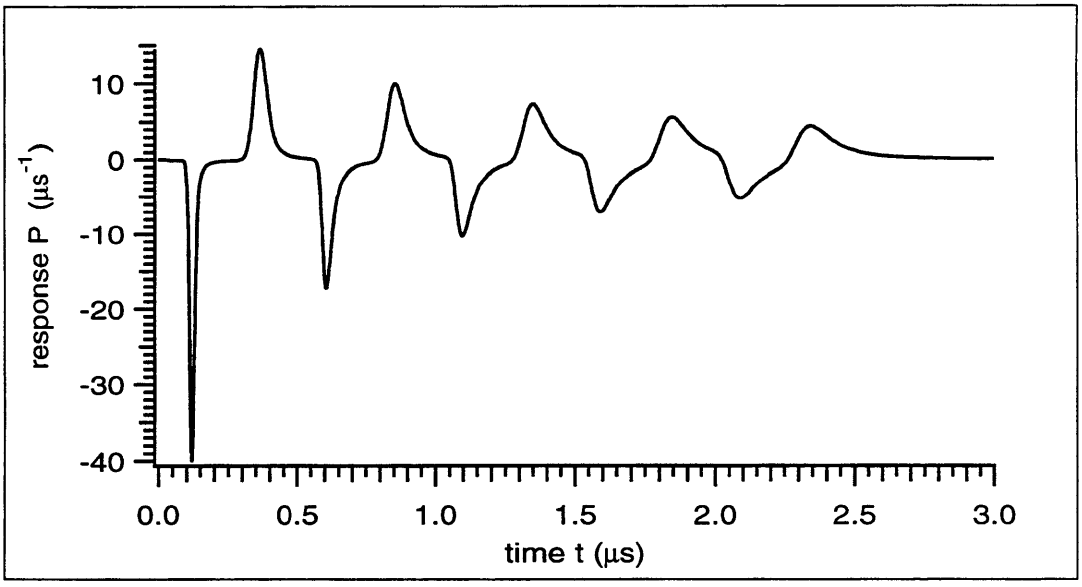

Figure 8.8: The modelled response signal $\hat{\mathcal{P}}_g[t_n] = \hat{\mathcal{K}}_p\{\mathcal{Q}_g(z)\}$. Only the first 3 μs of a total of 8.192 μs are shown. $\Delta t = 2$ ns.

8.3 The SIB Recovery

Section 8.1.1 made it clear that the unregularized Lyons recovery is unsatisfactory. This section investigates SIB (spatially independent frequency domain filtering via the filter known as Blackman's Lucky Guess) regularization. The filter $B(f_c, f)$ known as Blackman's Lucky Guess (BLG) is defined in appendix B. The BLG filter's parameter f_c is the *cutoff frequency*, above which the BLG filter has value zero. The BLG filter's attenuation increases steadily with f up to f_c, at which point the BLG filter's attenuation jumps to infinity (*ie*: all frequencies above f_c are set to zero).

SIB filtering is readily implemented: simply replace the $\underline{\mathcal{P}}[f_k]$ in (7.123) with $\underline{\mathcal{P}}[f_k]\ B(f_c, f_k)$ so that (7.123) becomes

$$R_{sib}(z) = \Delta f \sum_{f_k=0}^{f_m} \text{two}[f_k]\ \Re_e\left\{ \underline{\mathcal{P}}[f_k]\ B(f_c, f_k)\ \frac{\exp(z\ \underline{\mathcal{K}}(f_k))}{\underline{C}_g(f_k)} \right\} \tag{8.9}$$

The previous section's unsatisfactory recoveries correspond to using $f_c = \infty$ in (8.9) because $B(\infty, f) = 1$. The following two figures (8.9 and 8.10) depict the SIB recoveries $R_{sib}(z)$ gleaned using (8.9) with f_c set at two distinct frequencies: $f_c = 52.8$ MHz and $f_c = 28.8$ MHz, respectively.

The last recovered Gaussian in figure 8.9 is 'troubled;' it exhibits something akin to the λ oscillations that filtering was meant to remove. Decreasing the SIB filtering cutoff frequency f_c from 52.8 to 28.8 MHz (*ie*: from figure 8.9 to 8.10) removes the λ oscillations from this troubled recovered pulse at the expense of an increased pulse width (which increases from 104.1 to 133.0 μm).

The area of this troubled recovered pulse ($\Delta z = 2$ μm times the sum of the 251 samples between $z = 4.5$ and 5.0 mm) is 1.005. The peak position of this troubled recovered pulse (which was calculated to the nearest μm via a 3-point quadratic fit) is 4.754 mm. Analagous definitions for the recovered pulse area and peak position are used throughout (*eg*: for the $z = 2.75$ mm pulse, the relevant range is $z = 2.5$ to 3 mm).

The following comments on the area, peak position, and FWHM (width) of the recovered pulses pertain to all nineteen of the 'untroubled' recovered pulses depicted in figures 8.9 and 8.10. All the areas fell within (in many cases, well within) 0.1 % of their expected areas ($\pm$ 1). The peak position was always 1 μm too deep, except for the first three positive pulses in figure 8.9, which were exact (to the nearest μm).

All the recovered thick (*ie*: positive) pulses in figure 8.9 have a FWHM of 107.8 μm (13% wider than source). All the recovered thin (*ie*: negative) pulses in figure 8.9 have a FWHM of 63.05 μm (74% wider than source). All the recovered thick (*ie*: positive) pulses in figure 8.10 have a FWHM of 133.0 μm (39% wider than source). All the recovered thin (*ie*: negative) pulses in figure 8.10 have a FWHM of 101.5 μm (180% wider than source).

It is remarkable that SIB filtering so accurately produces recovered pulses with widths that are independent of source depth (when original source pulse width and f_c are held constant). Reviewing figures 8.9 and 8.10, it seems clear that SIB filtering

produces recoveries with a resolution that is independent of source placement depth and determined by the degree of λ oscillation supression desired for the deepest source.

The fact that the resolution of the SIB recovery at all positions is determined by the resolution of the deepest source (once the desired degree of λ oscillation supression has been specified) forms a recommendation for investigation of the spatially dependent BLG (SDB) recovery which uses a cutoff frequency f_c which is a function of z: $f_c \rightarrow f_c(z)$ in (8.9). The spatially dependent BLG filter cutoff frequency $f_c(z)$ is often simply referred to as the SDB function.

Before investigating the SDB recovery, it will be shown that the SIB recovery can be 'smoothly relaxed' to the dominant recovery by modulating the model used for the recovery ($\alpha_r(f)$ and $c_r(f)$) between the limits set by the standard model for polyethylene ($\alpha_p(f)$ and $c_p(f)$) and the delay-only model ($\alpha_d(f) = 0$ and $c_d(f) = c_d$).

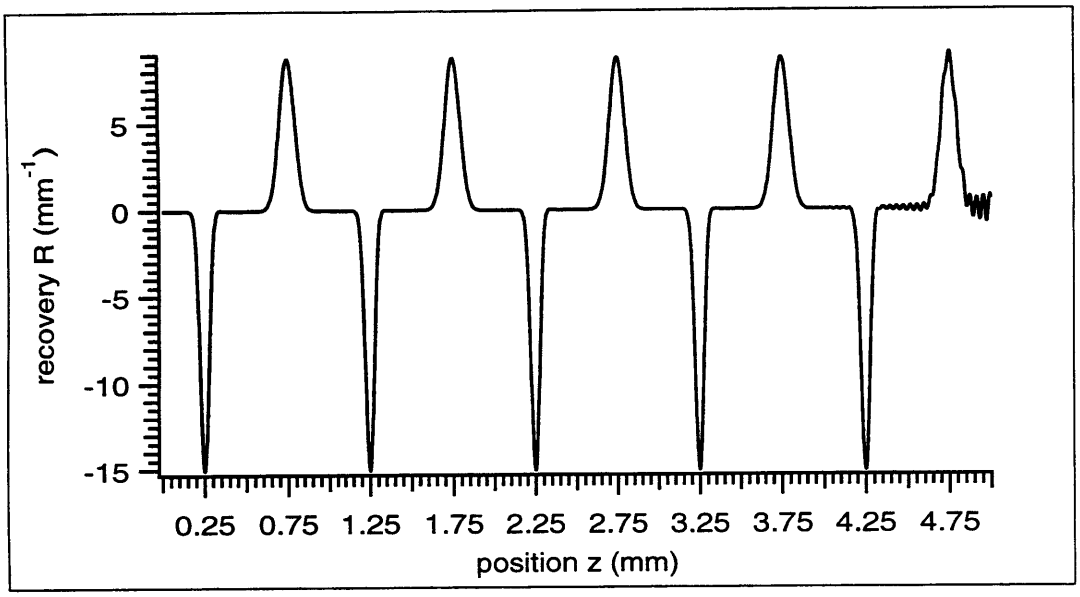

Figure 8.9: The $f_c = 52.8$ MHz $R_{sib}[z_i]$ gleaned from $\hat{\mathcal{P}}_g[t_n]$.

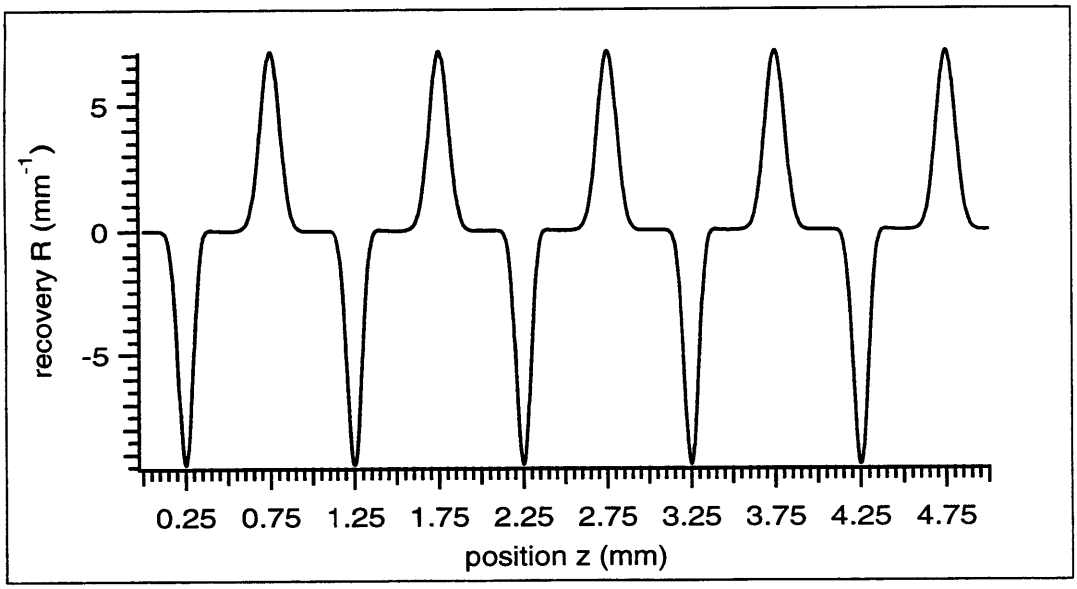

Figure 8.10: The $f_c = 28.8$ MHz $R_{sib}[z_i]$ gleaned from $\hat{\mathcal{P}}_g[t_n]$.

8.3.1 Relaxation To The Dominant Recovery

This section demonstrates that the SIB recovery can be 'smoothly relaxed' to the dominant recovery by modulating the model used for the recovery ($\alpha_r(f)$ and $c_r(f)$) between the limits set by the standard model for polyethylene ($\alpha_p(f)$ and $c_p(f)$) and the delay-only model ($\alpha_d(f) = 0$ and $c_d(f) = c_d$).

Both $\alpha_p(f)$ and $c_p(f)$ are discussed and defined in section 6.2.2 and in appendix C. The delay-only (*aka*: dominant) recovery is discussed in sections 1.6 and 2.4. Section 2.4 verifies $c_d = 2.035$ mm/μs as a resonable value to use for standard polyethylene. The quantity X will be used as the modulation parameter, so that

$$\{\alpha_r(f), c_r(f)\} \quad \rightarrow \quad \{\alpha_r(\mathrm{X}, f), c_r(\mathrm{X}, f)\} \tag{8.10}$$

where

$$\alpha_r(\mathrm{X}, f) \equiv \mathrm{X}\ \alpha_p(f) + [1 - \mathrm{X}]\ \alpha_d(f) \tag{8.11}$$

$$c_r(\mathrm{X}, f) \equiv \mathrm{X}\ c_p(f) + [1 - \mathrm{X}]\ c_d(f) \tag{8.12}$$

so that, when X = 0, the dominant recovery results and, when X = 1, the 'standard polyethylene' SIB recovery investigated in section 8.3 results. The response signal $\hat{\mathcal{P}}_g[t_n]$ depicted in figure 8.8 will be submitted to the $\mathrm{R}_{sib}[z]$ defined in equation (8.9). The SIB recovery given by submitting $\hat{\mathcal{P}}_g[t_n]$ and $\{\alpha_r(\mathrm{X}, f), c_r(\mathrm{X}, f)\}$ to (8.9) will be denoted $\mathrm{R}_{sib}[\mathrm{X}, z_i]$.

Figure 8.11 depicts $\mathrm{R}_{sib}[1.00, z_i]$ and $\mathrm{R}_{sib}[0.75, z_i]$. Figure 8.12 depicts $\mathrm{R}_{sib}[0.75, z_i]$ and $\mathrm{R}_{sib}[0.50, z_i]$. Figure 8.13 depicts $\mathrm{R}_{sib}[0.5, z_i]$ and $\mathrm{R}_{sib}[0.25, z_i]$. Figure 8.14 depicts $\mathrm{R}_{sib}[0.25, z_i]$ and $\mathrm{R}_{sib}[0.00, z_i]$. For all these SIB recoveries, $f_c = 28.8$ MHz.

Reviewing figures 8.11 through 8.14: it seems clear that both the recovered pulse width and the recovered pulse asymmetry increase steadily with decreasing X, and that the manifestation of these effects increases steadily with source position z.

For example: the $z = 0.25$ mm Gaussian pulse recovery is relatively unaffected by the value of X, whereas the $z = 4.75$ mm Gaussian pulse recovery degenerates from fairly successful at X = 1 (FWHM = 133.0 μm, peak position = 4.751 mm, and area = 1.0009, in agreement with the positive pulses in figure 8.10) to quite poor at X = 0 (FWHM = 308 μm, peak position = 4.775 mm, area = 0.518).

It is expected that the X = 0 recovery should have this behavior because X = 0 corresponds to the dominant recovery, which does not change the shape of $\mathcal{P}(t)$ (except possibly through frequency domain filtering). It is also expected that the X = 1 recovery should have the behavior it exhibited because X = 1 corresponds to the 'unrelaxed' SIB recovery investigated in section 8.3.

What is surprising and gratifying is that figures 8.11 through 8.14 demonstrate that there is a reasonably smooth transition between the X = 0 recovery and the

X = 1 recovery. This behaviour is exhibited in figures 8.15,8.16, and 8.17 which depict, respectively, the X dependent behavior of the $z = 4.75$ mm pulses' recovered FWHM, area, and position. In each plot, moving from X = 0 to X = 1 effects a transition towards the correct value.

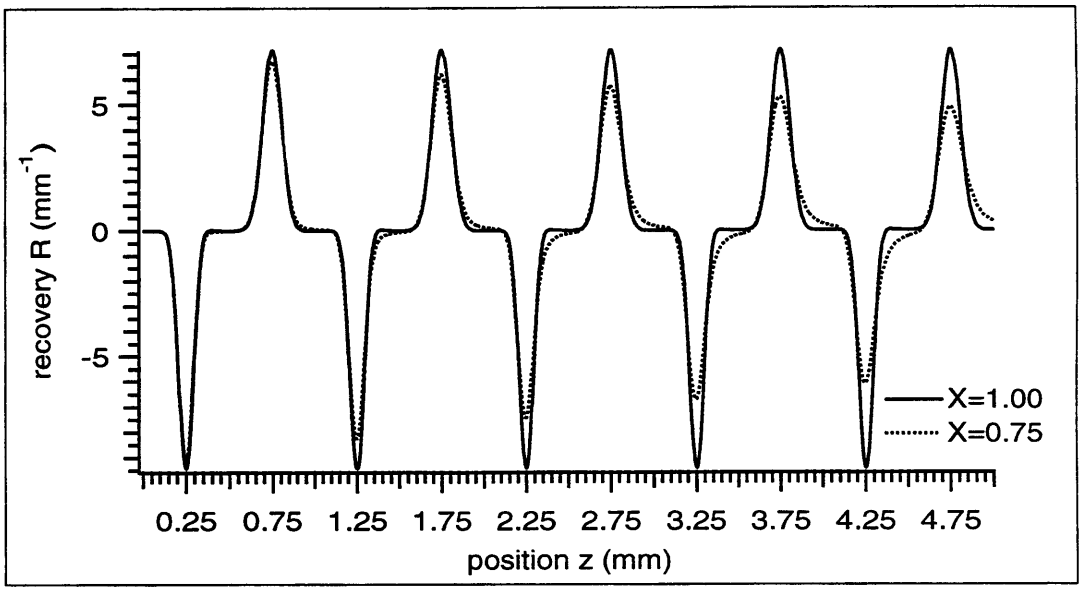

Figure 8.11: 'Relaxed' SIB recoveries $R_{sib}[1.00, z_i]$ (labelled X=1.00) and $R_{sib}[0.75, z_i]$ (labelled X=0.75).

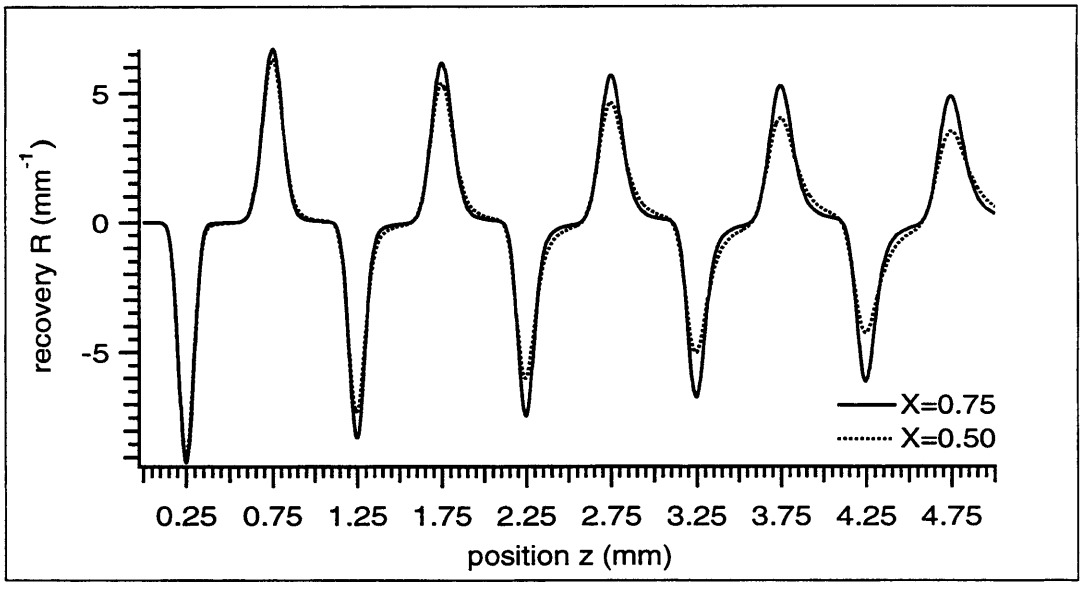

Figure 8.12: 'Relaxed' SIB recoveries $R_{sib}[0.75, z_i]$ (labelled X=0.75) and $R_{sib}[0.50, z_i]$ (labelled X=0.50).

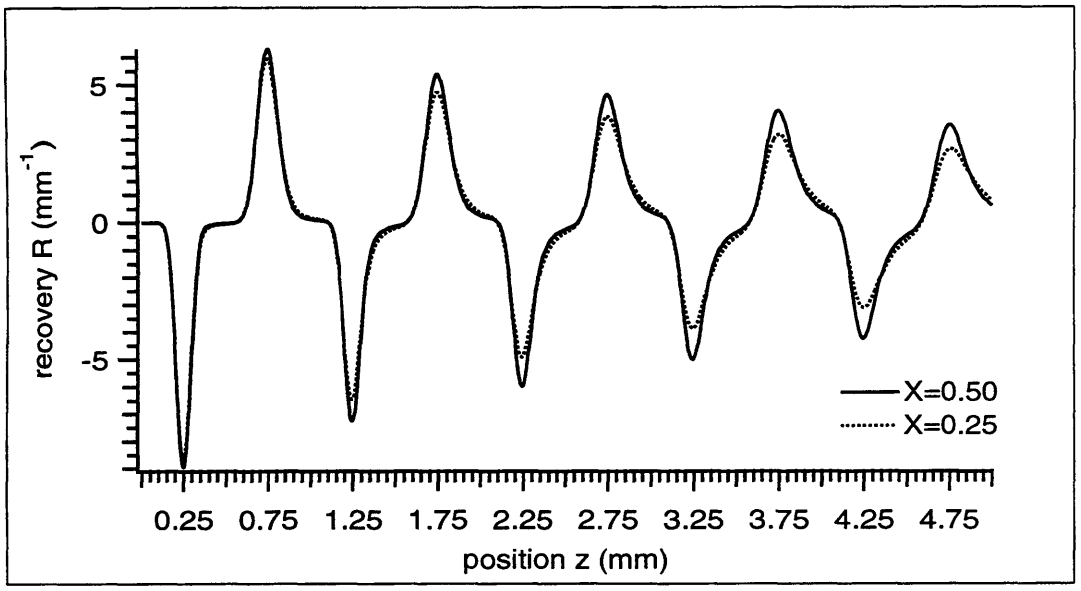

Figure 8.13: 'Relaxed' SIB recoveries $R_{sib}[0.50, z_i]$ (labelled X=0.50) and $R_{sib}[0.25, z_i]$ (labelled X=0.25).

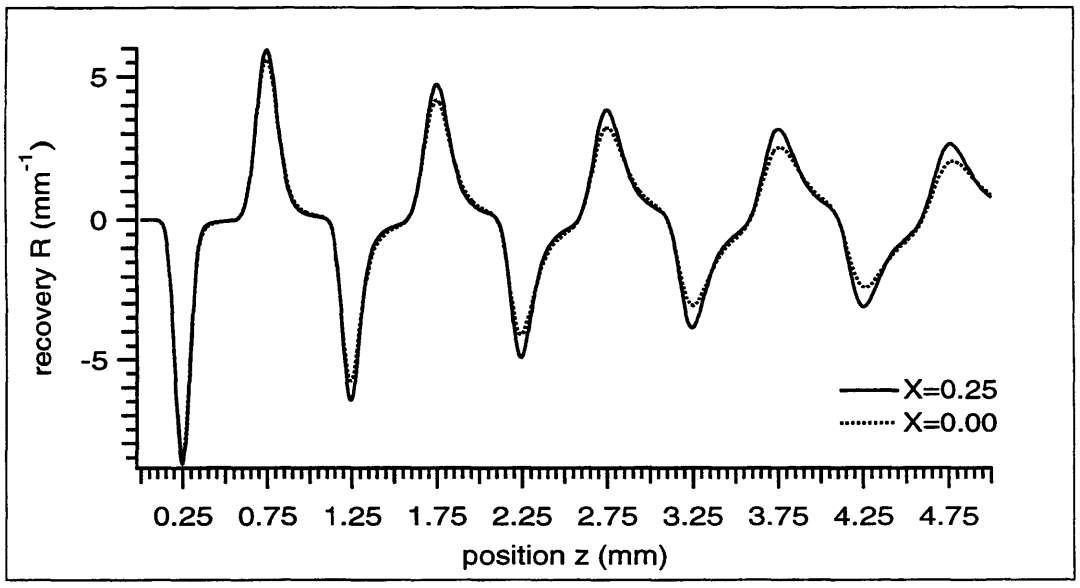

Figure 8.14: 'Relaxed' SIB recoveries $R_{sib}[0.25, z_i]$ (labelled X=0.25) and $R_{sib}[0.00, z_i]$ (labelled X=0.00).

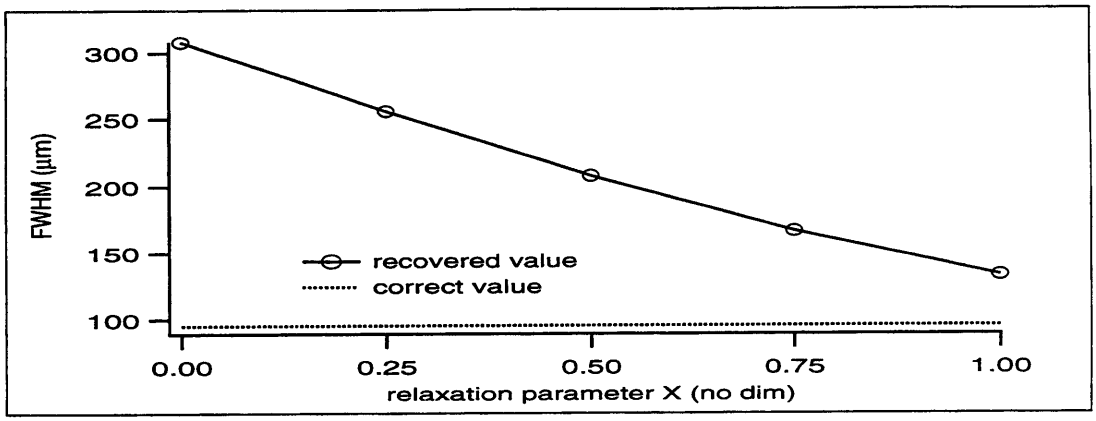

Figure 8.15: Dependence of the FWHM of the $z = 4.75$ mm Gaussian pulse recovery on the SIB 'relaxation parameter' X. Correct value = 95.49 μm.

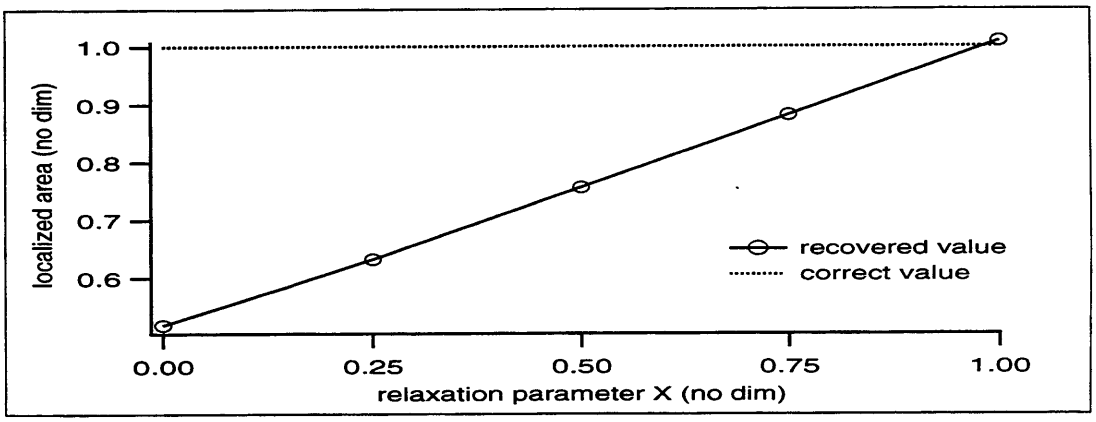

Figure 8.16: Dependence of the localized area ($\pm$ 0.25 mm) of the $z = 4.75$ mm Gaussian pulse recovery on the SIB 'relaxation parameter' X. Correct value = 1.

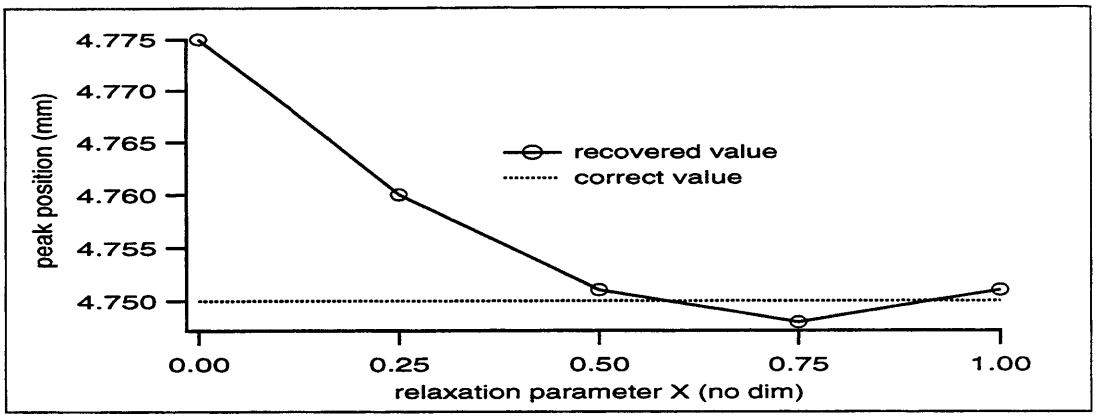

Figure 8.17: Dependence of the position of the $z = 4.75$ mm Gaussian pulse recovery on the SIB 'relaxation parameter' X. Correct value = 4.75 mm.

8.4 The SDB Recovery

Section 8.3 ended by recommending replacing the SIB cutoff frequency f_c used in $R_{sib}(z)$ with some SDB function $f_c(z)$, so that (8.9) becomes

$$R_{sdb}(z) = \Delta f \sum_{f_k=0}^{f_m} \text{two}[f_k]\ \Re_e\left\{ \underline{\mathcal{P}}[f_k]\ B(f_c(z), f_k)\ \frac{\exp(z\ \underline{\mathcal{K}}(f_k))}{\underline{C}_g(f_k)} \right\} \tag{8.13}$$

In the special case where the SDB function $f_c(z)$ used in (8.13) is the standard SDB function $\hat{f}_c(z)$ (see appendix B), the resultant recovery is called the standard SDB recovery. The standard SDB recovery is denoted $R(z)$.

It is possible to 'relax' the standard SDB recovery in the same manner as the SIB recovery was relaxed in section 8.3.1. That is, with $\{\alpha_p(f), c_p(f)\}$ denoting the standard model of polyethylene (see sections 6.2.2 and appendix C) and with $\{\alpha_d(f), c_d(f)\}$ denoting the $c_d = 2.035$ mm/μs delay-only material (see sections 1.6 and 2.4), it is possible to insert into (8.13) a 'relaxation model'

$$\alpha_r(X, f) \equiv X\ \alpha_p(f) + [1 - X]\ \alpha_d(f) \tag{8.14}$$

$$c_r(X, f) \equiv X\ c_p(f) + [1 - X]\ c_d(f) \tag{8.15}$$

which yields the delay-only model when $X = 0$, and which yields the standard model of polyethylene when $X = 1$. The nondimensional quantity X is called the relaxation parameter.

This section investigates two of these relaxed SDB recoveries: the 'standard relaxed SDB recovery' which uses $f_c(z) = \hat{f}_c(z)$ (denoted $R(X, z)$) and the 'overfiltered relaxed SDB recovery' which uses $f_c(z) = 0.65\hat{f}_c(z) \equiv f'_c(z)$ (denoted $R'(X, z)$).

As in section 8.3, relaxed recoveries will be gleaned from the modelled response signal $\hat{\mathcal{P}}_g[t_n]$ arising from the standard Gaussian source waveform $\mathcal{G}[z_i]$ for the values $X = \{0, 0.25, 0.5, 0.75, 1\}$. Please recall that $\mathcal{G}[z_i]$ is comprised of five 'thick' (FWHM = 95.49 μm) Gaussians with area +1 placed at $z = 0.75$, 1.75, 2.75, 3.75, and 4.75 mm and five 'thin' (FWHM = 36.32 μm) Gaussians with area -1 placed at $z = 0.25$, 1.25, 2.25, 3.25, and 4.25 mm.

The recovery $R(1, z)$ is the standard SDB recovery $R(z)$. But whereas the recovery $R_{sib}(0, z)$ investigated in section 8.3 is a $f_c = 28.8$ MHz BLG-filtered, frequency domain implementation of the dominant recovery, $R(0, z)$ does not reduce to the dominant recovery. Like $R_{sib}(0, z)$, $R(0, z)$ uses $\{\alpha_d(f), c_d(f)\}$. But whereas $R_{sib}(0, z)$ uses the constant $f_c = 28.8$ MHz, $R(0, z)$ uses the SDB function $\hat{f}_c(z)$.

8.4.1 Plots Pertaining To The Relaxed SDB Recovery

Pages 154 and 155 depict the standard (*ie*: $f_c(z) = \hat{f}_c(z)$) relaxed SDB recoveries $R[X, z_i]$ where $X = \{1.00, 0.75, 0.50, 0.25, 0.00\}$.

Pages 156 and 157 depict the overfiltered (*ie*: $f_c(z) = f'_c(z) = 0.65\hat{f}_c(z)$) relaxed SDB recoveries R[X, z_i] where X = $\{1.00, 0.75, 0.50, 0.25, 0.00\}$.

Pages 158 and 159 contain four plots. Each plot consists of five lines. Each line depicts the relaxation parameter X dependent FWHM of one of the twenty recovered pulses depicted on pages 154 through 157. The two plots on the even (left-hand) side correspond to the $f_c(z) = \hat{f}_c(z)$ 'standard relaxed SDB' experiment. The two plots on the odd (right-hand) side correspond to the $f_c(z) = f'_c(z) = 0.65\hat{f}_c(z)$ 'overfiltered relaxed SDB experiment' experiment.

The two upper plots on pages 158 and 159 correspond to the thin pulses; the lower plots correspond to the thick pulses. On each of these four plots (which corresponds only to either thin/negative pulses or thick/positive pulses), information pertaining to the first (*ie*: shallowest) source recovery is indicated with a solid line; information pertaining to the second (*ie*: next shallowest) source recovery is indicated with a dotted line; and so on, in accordance with figure 8.18.

Pages 160 and 161 also contain four plots. But whereas the four plots on pages 158 and 159 pertain to the FWHM of the Gaussian pulse recoveries depicted on pages 154 through 157, the four plots on pages 160 and 161 pertain to the area of the recovered pulses. The four plots on pages 162 and 163 contain four plots pertain to the error in recovered peak position (calculated-expected) of the Gaussian pulse recoveries depicted on pages 154 through 157

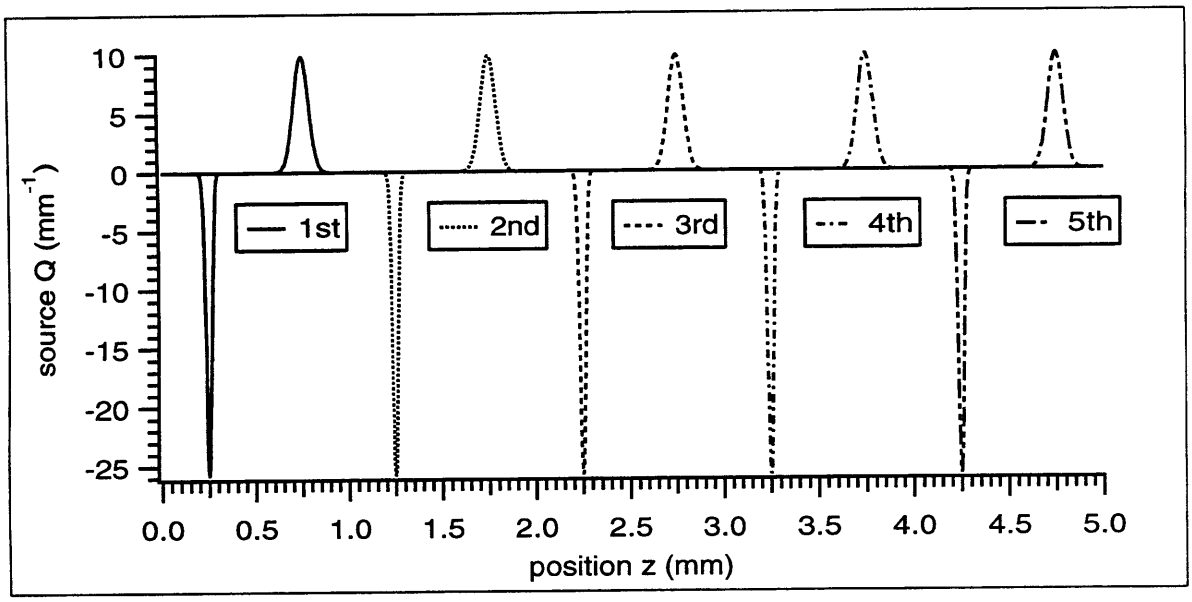

Figure 8.18: The standard Gaussian source waveform (figure 8.7) broken up into the five thick (95.49 μm) positive pulses and the five thin (36.32 μm), negative pulses. The first pulse (whether negative and thin, or positive and thick) is plotted with lines described as: solid; second pulse: dotted; third: dashed; fourth: dash-dot; fifth: dash-dot-dot.

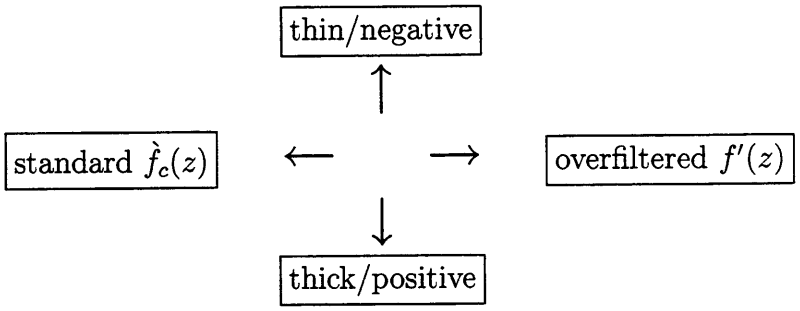

Table 8.1: Significance of the arrangement (left/right,top/bottom) of the sets of four plots found on pages 158 and 159 (FWHM), 160 and 161 (localized area), and 162 and 163 (numeric - expected error in peak position). The two left-handed (even-sided) plots depict data corresponding to the relaxed SDB recovery where the standard SDB function $\hat{f}_c(z)$ was used; the two right-handed (odd-sided) plots depict data corresponding to the relaxed SDB recovery where the overfiltered SDB function $f'_c(z)$ was used. The two upper plots correspond to the thin/negative pulses; the two lower plots correspond to the thick/negative pulses.

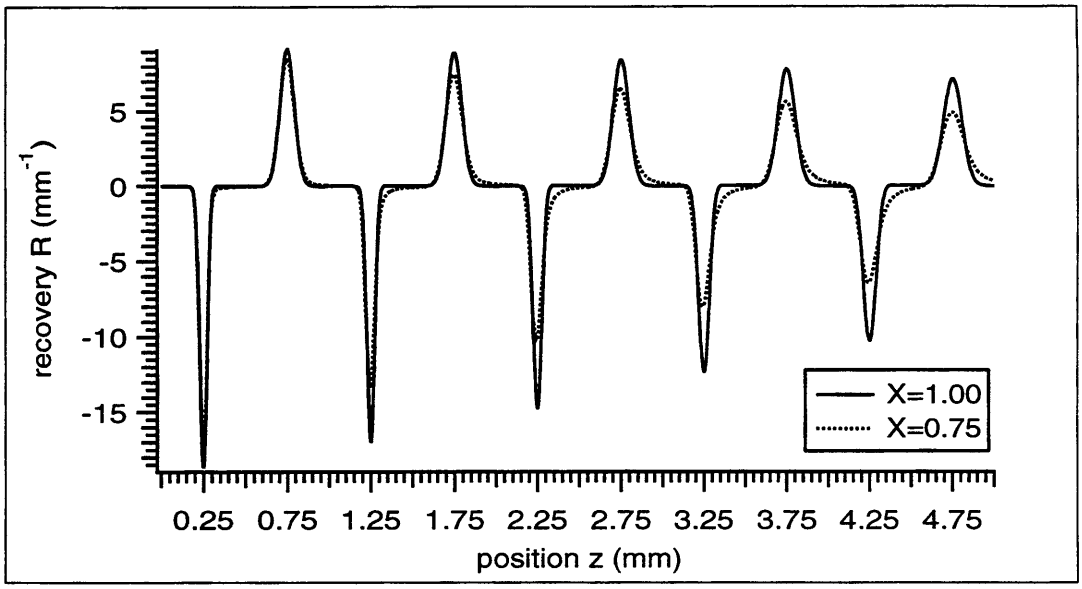

Figure 8.19: Standard ($f_c(z) = \grave{f}_c(s)$) relaxed SDB recoveries R[1.00, z_i] (labelled X=1.00) and R[0.75, z_i] (labelled X=0.75).

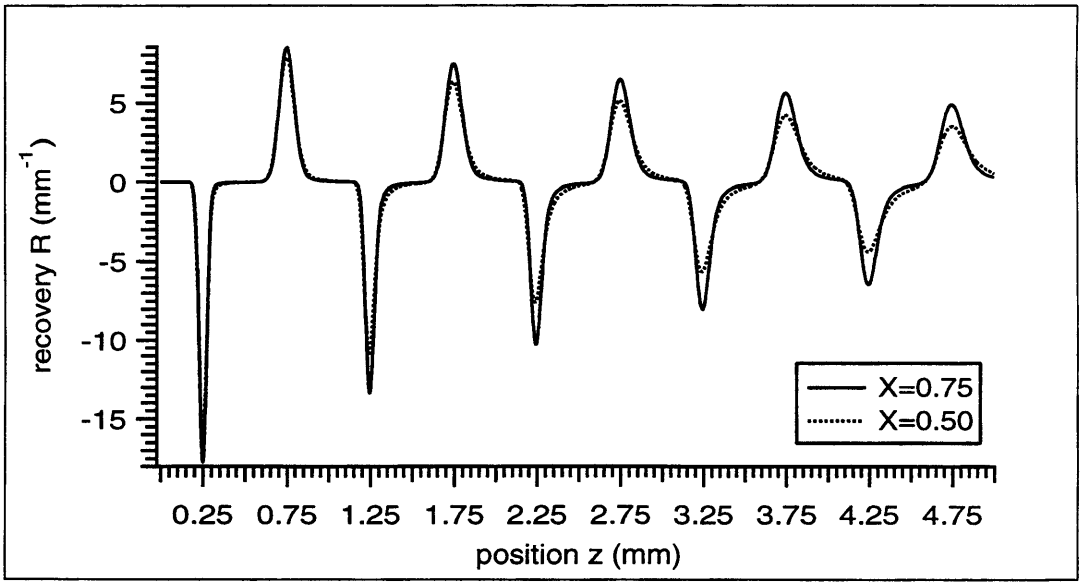

Figure 8.20: Standard ($f_c(z) = \grave{f}_c(s)$) relaxed SDB recoveries R[0.75, z_i] (labelled X=0.75) and R[0.50, z_i] (labelled X=0.50).

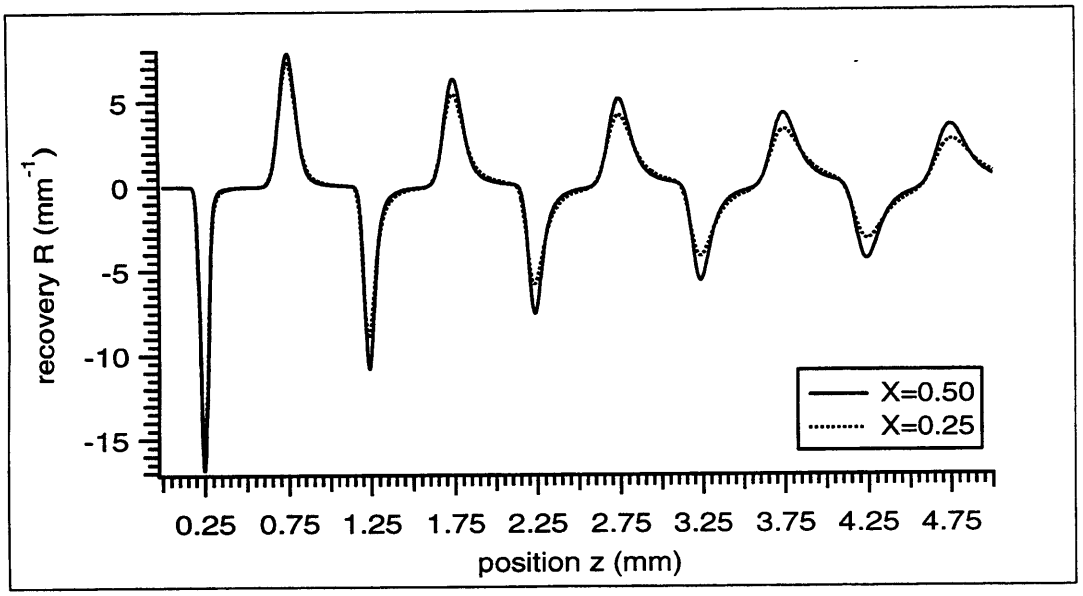

Figure 8.21: Standard ($f_c(z) = \grave{f}_c(s)$) relaxed SDB recoveries R$[0.50, z_i]$ (labelled X=0.50) and R$[0.25, z_i]$ (labelled X=0.25).

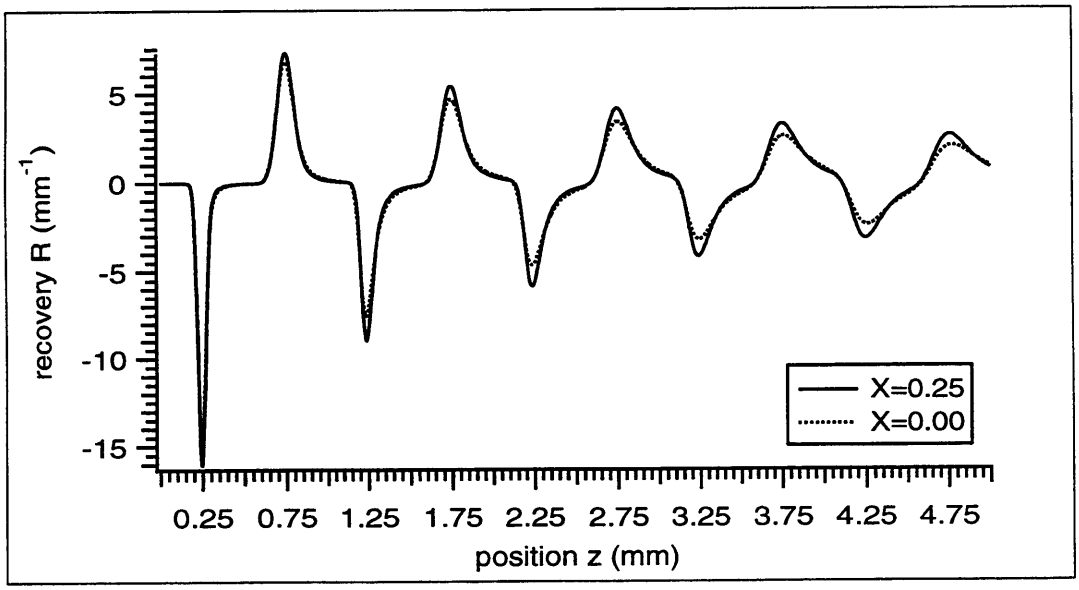

Figure 8.22: Standard ($f_c(z) = \grave{f}_c(s)$) relaxed SDB recoveries R$[0.25, z_i]$ (labelled X=0.25) and R$[0.00, z_i]$ (labelled X=0.00).

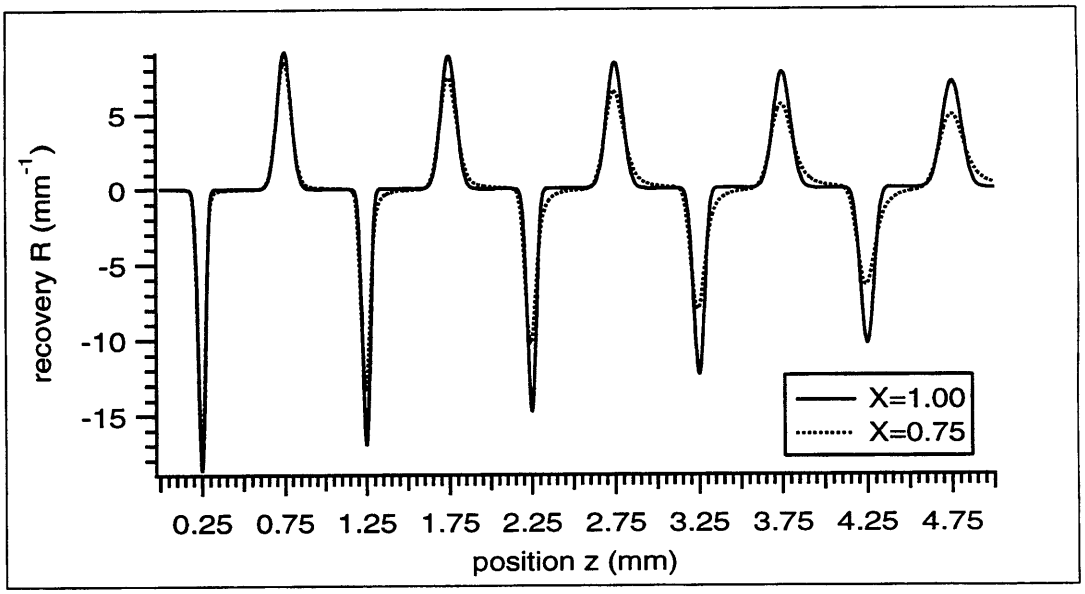

Figure 8.23: Overfiltered ($f_c(z) = f'_c(z) = 0.65\grave{f}_c(s)$) relaxed SDB recoveries R$'[1.00, z_i]$ (labelled X=1.00) and R$'[0.75, z_i]$ (labelled X=0.75).

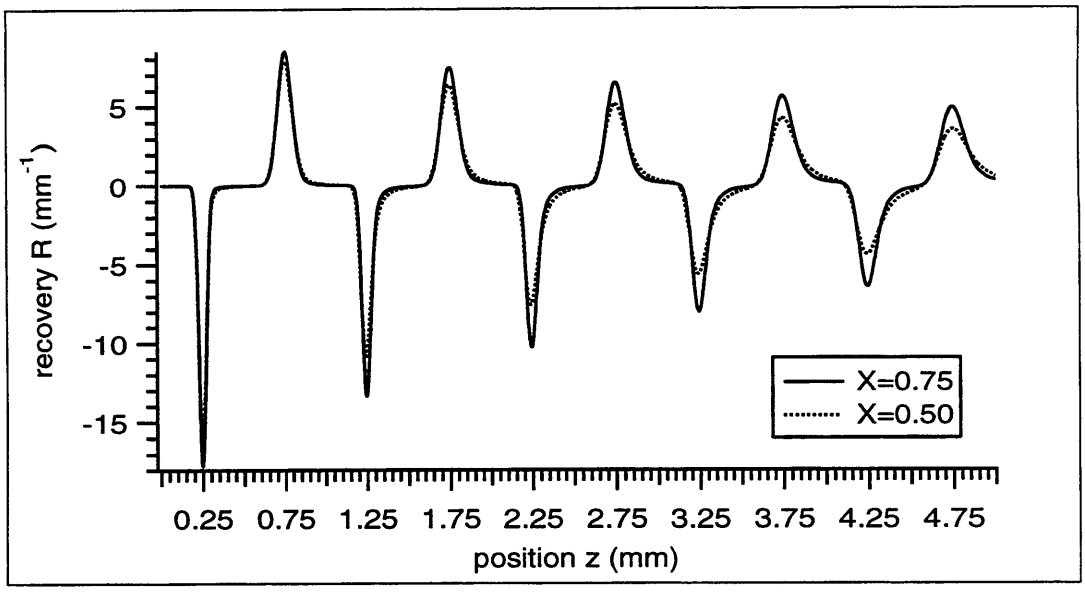

Figure 8.24: Overfiltered ($f_c(z) = f'_c(z) = 0.65\grave{f}_c(s)$) relaxed SDB recoveries R$'[0.75, z_i]$ (labelled X=0.75) and R$'[0.50, z_i]$ (labelled X=0.50).

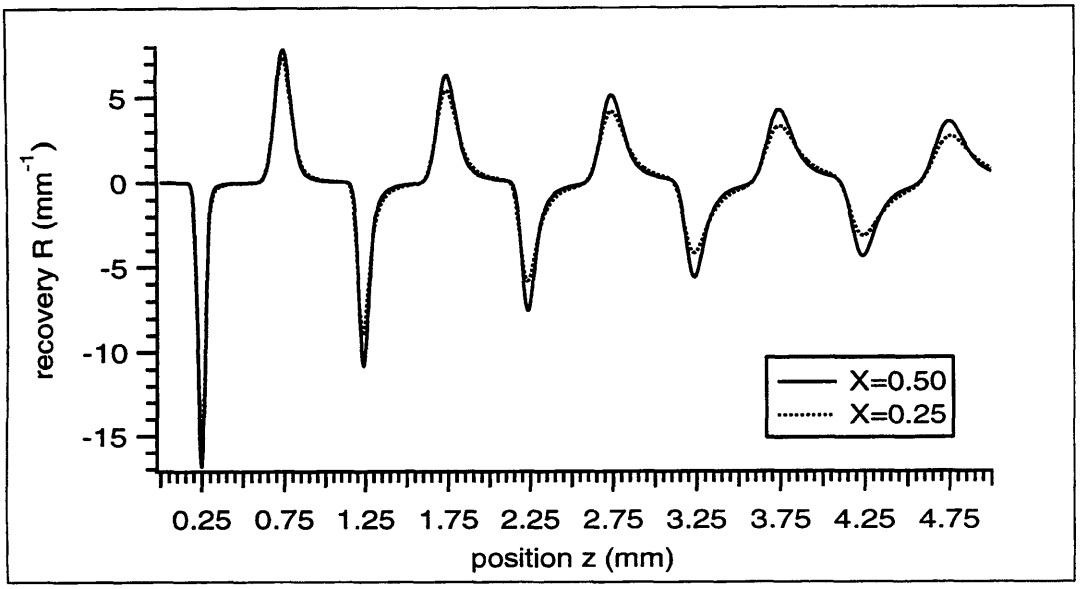

Figure 8.25: Overfiltered ($f_c(z) = f'_c(z) = 0.65\grave{f}_c(s)$) relaxed SDB recoveries R$'[0.50, z_i]$ (labelled X=0.50) and R$'[0.25, z_i]$ (labelled X=0.25).

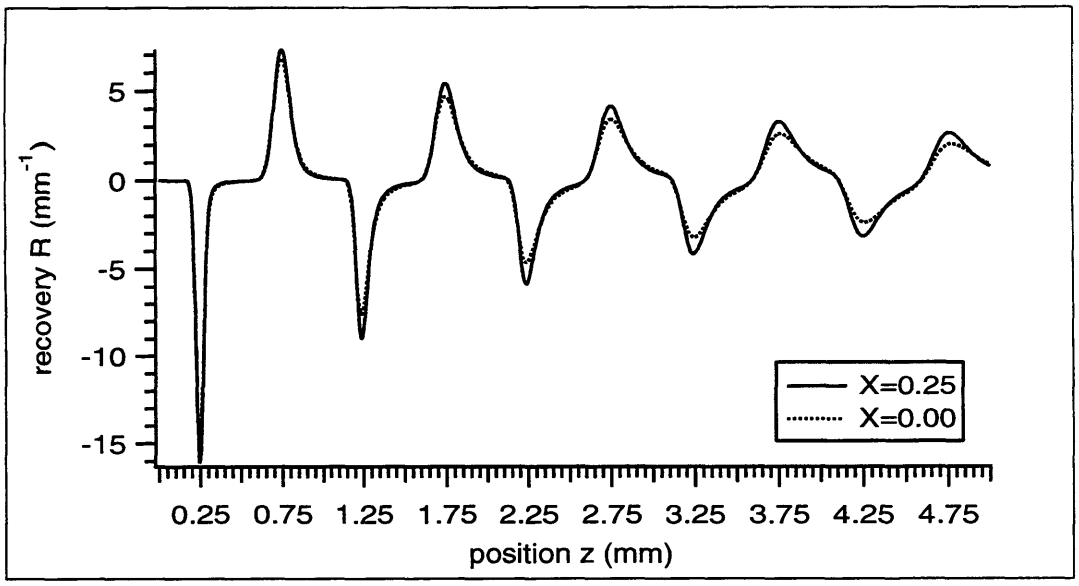

Figure 8.26: Overfiltered ($f_c(z) = f'_c(z) = 0.65\grave{f}_c(s)$) relaxed SDB recoveries R$'[0.25, z_i]$ (labelled X=0.25) and R$'[0.00, z_i]$ (labelled X=0.00).

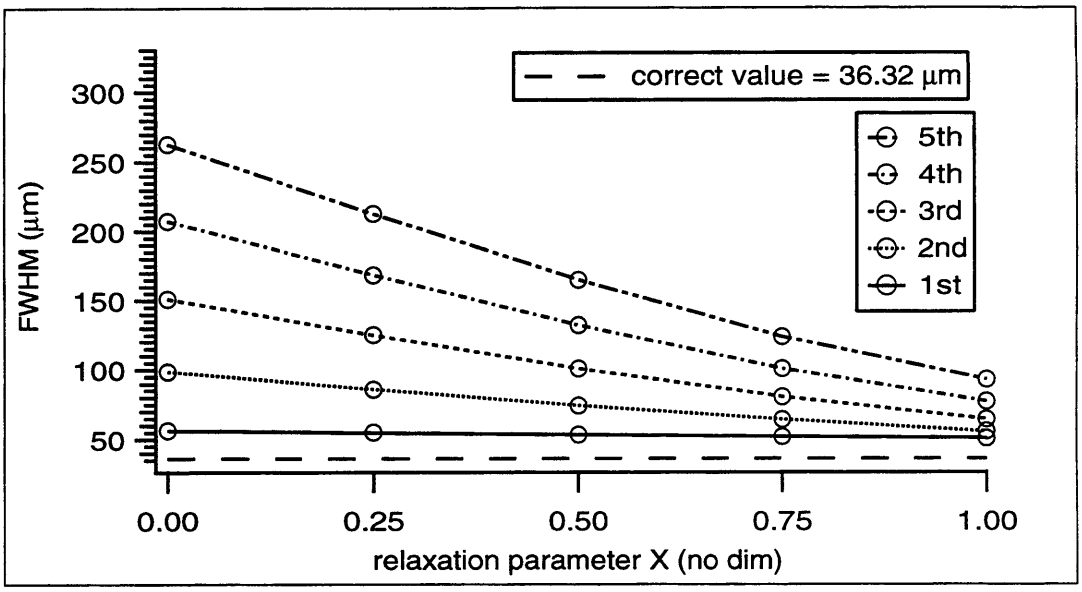

Figure 8.27: Relaxation parameter X dependent width (FWHM) of the thin/negative pulse recoveries gleaned via the standard (*ie*: $f_c(z) = \grave{f}_c(z)$) SDB recovery.

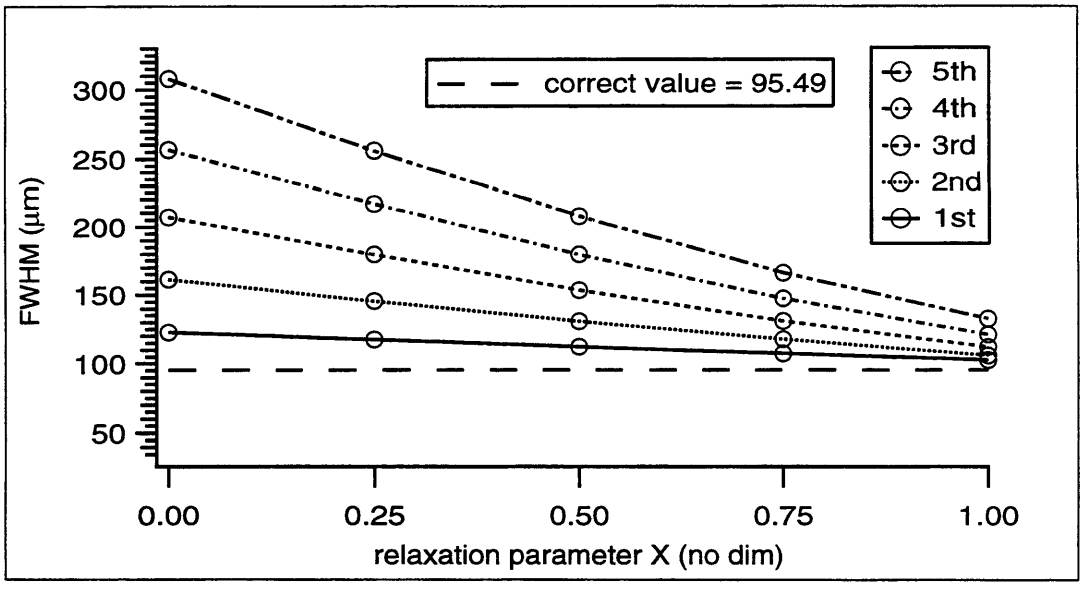

Figure 8.28: Relaxation parameter X dependent width (FWHM) of the thick/positive pulse recoveries gleaned via the standard (*ie*: $f_c(z) = \grave{f}_c(z)$) SDB recovery.

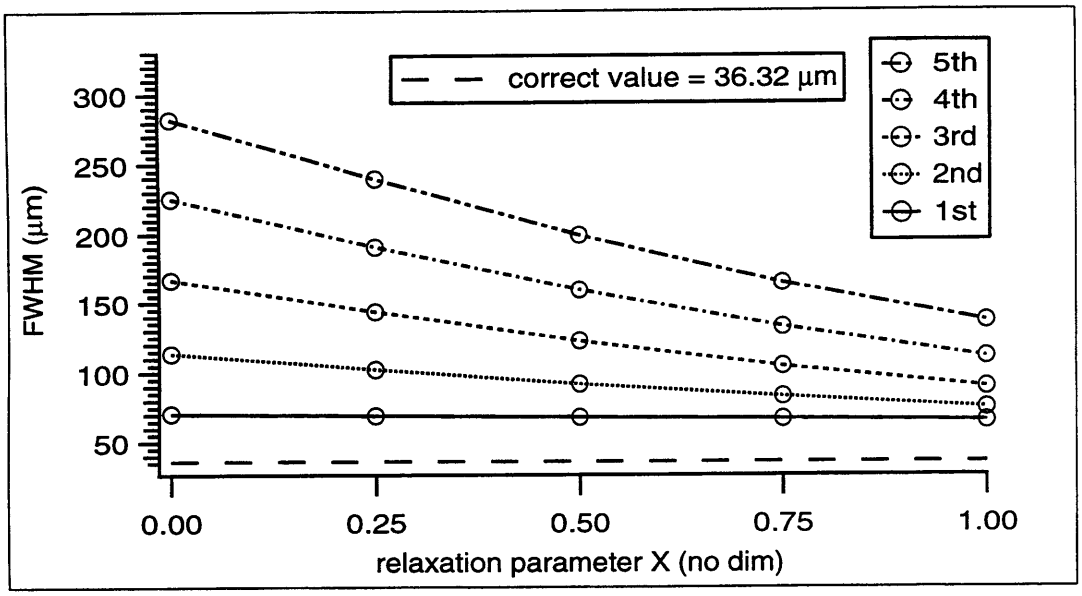

Figure 8.29: Relaxation parameter X dependent width (FWHM) of the thin/negative pulse recoveries gleaned via the overfiltered (*ie*: $f_c(z) = f_c'(z) = 0.65\grave{f}_c(z)$) SDB recovery.

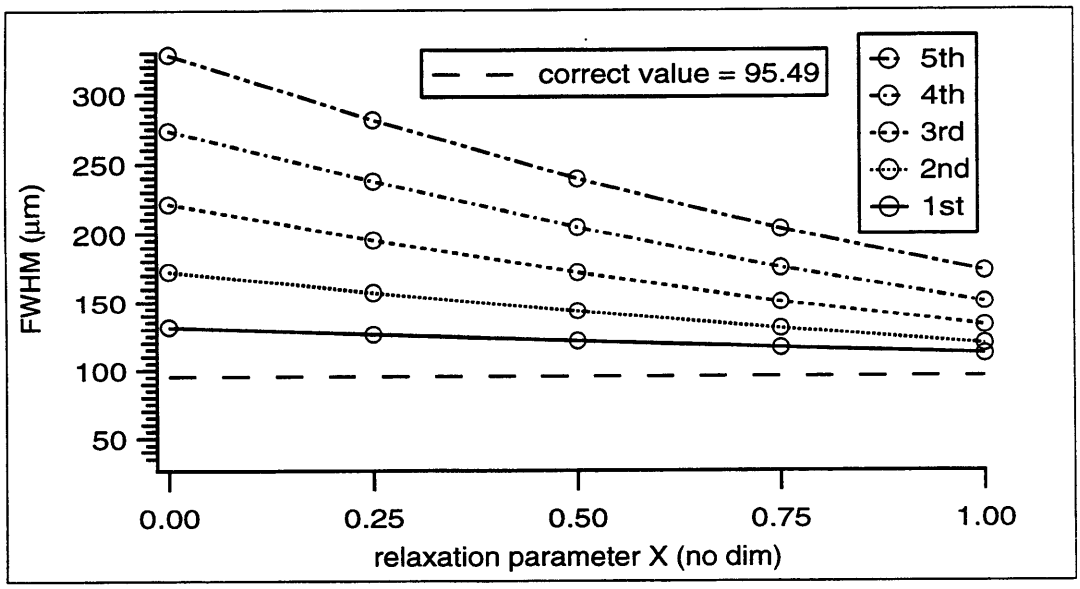

Figure 8.30: Relaxation parameter X dependent width (FWHM) of the thick/positive pulse recoveries gleaned via the overfiltered (*ie*: $f_c(z) = f_c'(z) = 0.65\grave{f}_c(z)$) SDB recovery.

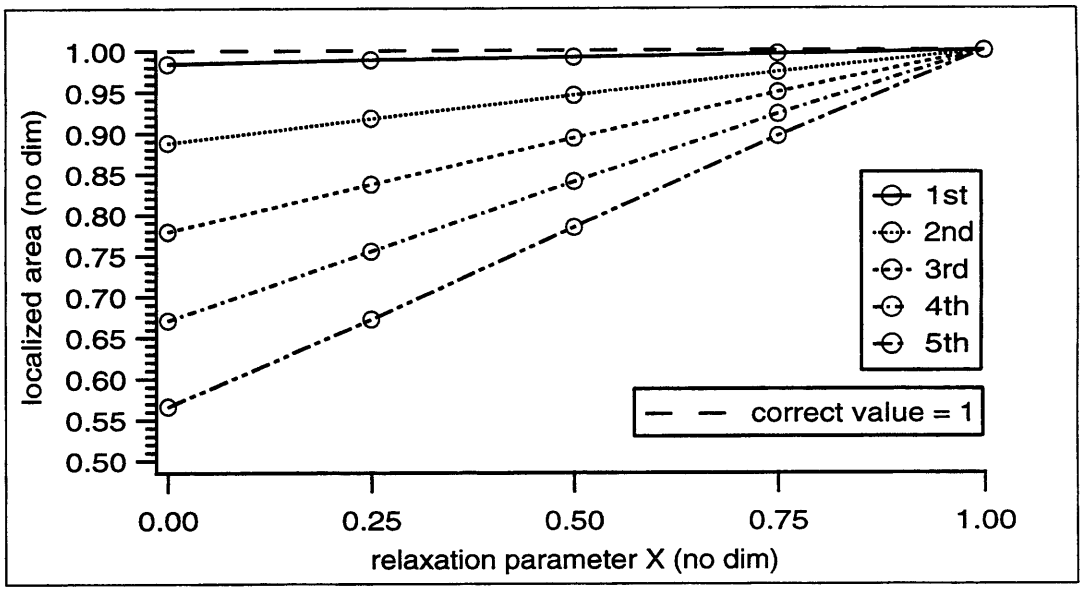

Figure 8.31: Relaxation parameter X dependent area of the thin/negative pulse recoveries gleaned via the standard (*ie*: $f_c(z) = \hat{f}_c(z)$) SDB recovery.

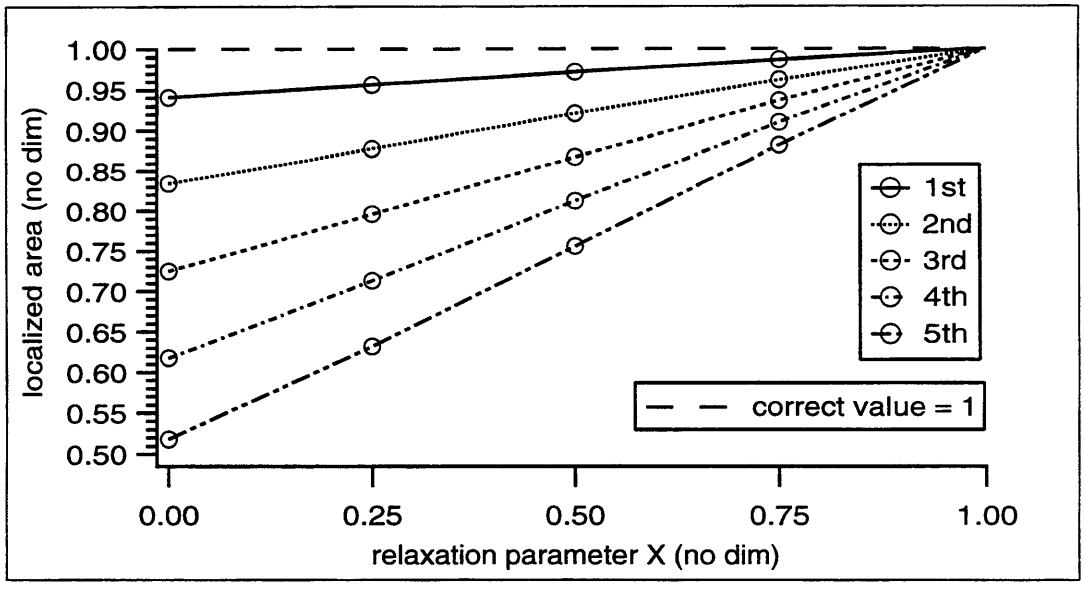

Figure 8.32: Relaxation parameter X dependent area of the thick/positive pulse recoveries gleaned via the standard (*ie*: $f_c(z) = \hat{f}_c(z)$) SDB recovery.

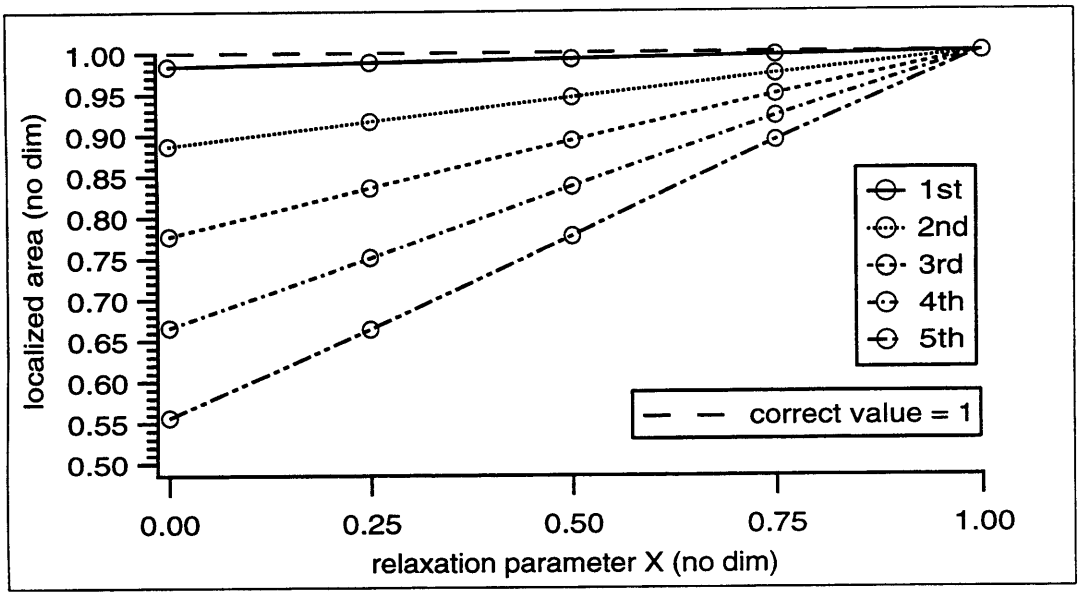

Figure 8.33: Relaxation parameter X dependent area of the thin/negative pulse recoveries gleaned via the overfiltered (*ie*: $f_c(z) = f'_c(z) = 0.65\hat{f}_c(z)$) SDB recovery.

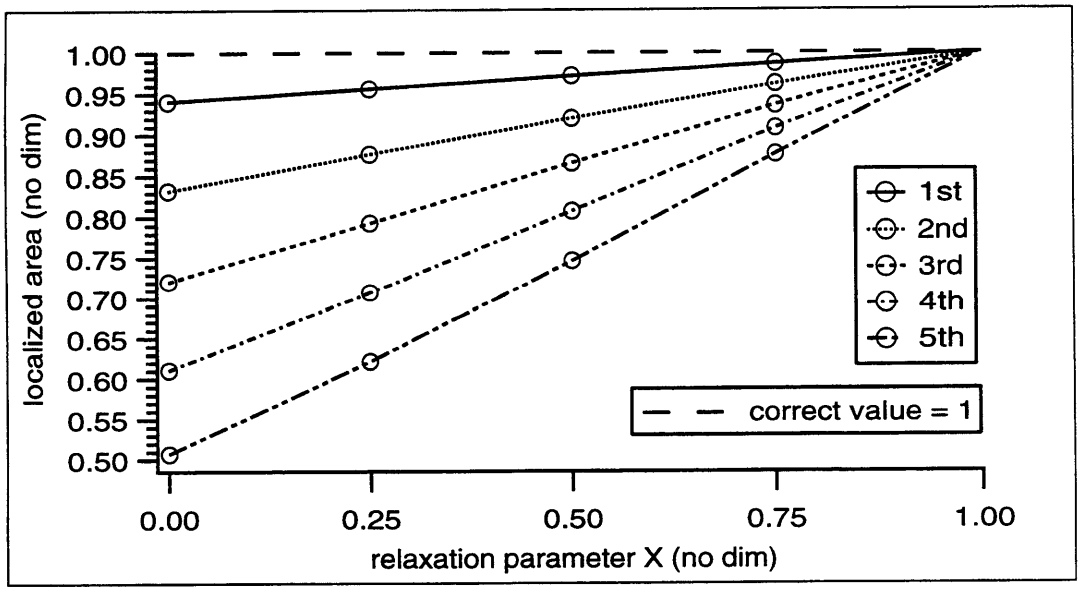

Figure 8.34: Relaxation parameter X dependent area of the thick/positive pulse recoveries gleaned via the overfiltered (*ie*: $f_c(z) = f'_c(z) = 0.65\hat{f}_c(z)$) SDB recovery.

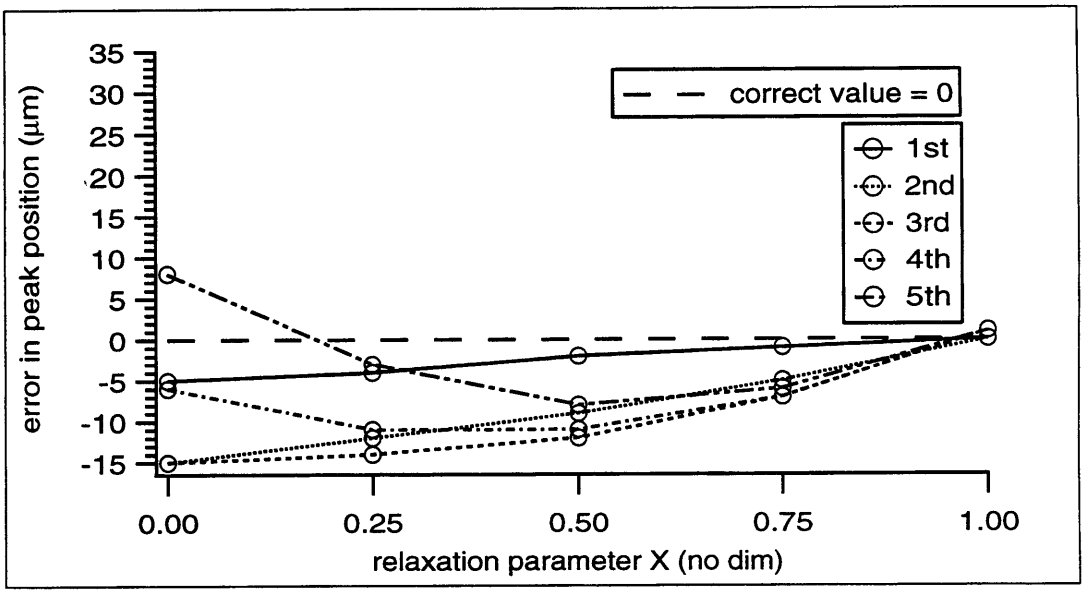

Figure 8.35: Relaxation parameter X dependent error (measured - expected) in peak position of the thin/negative pulse recoveries gleaned via the standard (*ie*: $f_c(z) = \hat{f}_c(z)$) SDB recovery.

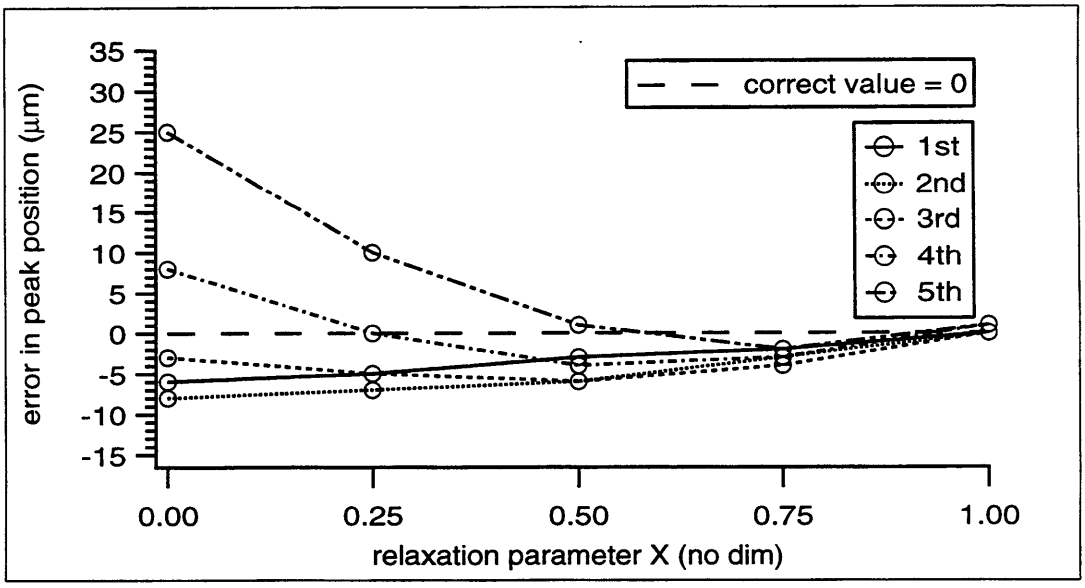

Figure 8.36: Relaxation parameter X dependent error (measured - expected) in peak position of the thick/positive pulse recoveries gleaned via the standard (*ie*: $f_c(z) = \hat{f}_c(z)$) SDB recovery.

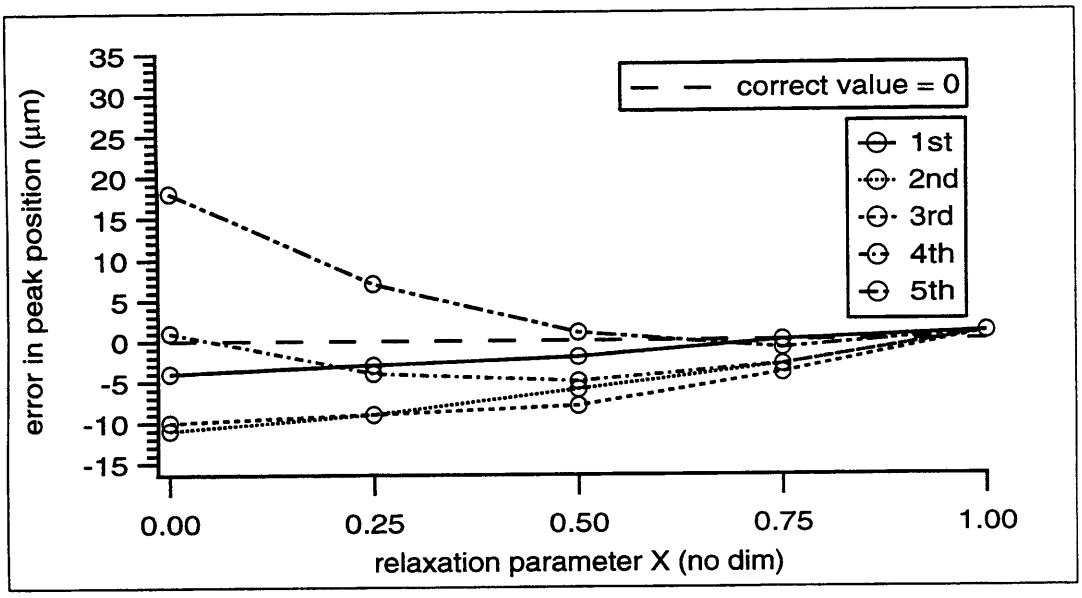

Figure 8.37: Relaxation parameter X dependent error (measured - expected) in peak position of the thin/negative pulse recoveries gleaned via the overfiltered (*ie*: $f_c(z) = f_c'(z) = 0.65\grave{f}_c(z)$) SDB recovery.

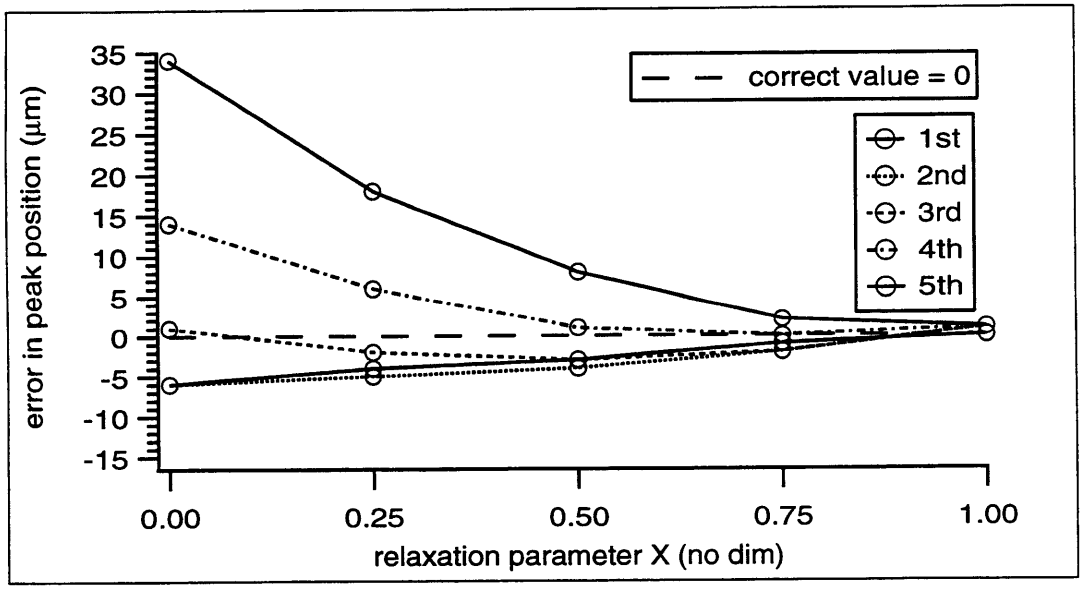

Figure 8.38: Relaxation parameter X dependent error (measured - expected) in peak position of the thick/positive pulse recoveries gleaned via the overfiltered (*ie*: $f_c(z) = f_c'(z) = 0.65\grave{f}_c(z)$) SDB recovery.

Chapter 9

The Lyons Recovery Applied To Experimental Data

This chapter only analyzes PESAW data obtained from planar samples assumed to be homogeneous both electrically (in terms of their dielectric permittivity ϵ) and acoustically (in terms of their material propagation parameter $\underline{\mathcal{K}}(f)$). The embedded charge distribution is not assumed homogeneous, but it is assumed one-dimensional (*ie*: the charge distribution is assumed to depend only on the distance z from the proximal plate).

Section 4.15 includes the following overview of this thesis' proposed procedure for mapping a measured PESAW pressure (usually detected as voltage) signal $V[t_n]$ to a set of approximate samples $\tilde{Q}[z_i]$ of the desired charge waveform $Q(z)$ embedded within, and existing at the surface of, the dielectric sample:

> Given a calibration signal $V_c[t_n]$, a bulk signal $V_b[t_n]$, and the plate charge q_p generated by the DC component V_o of the applied voltage (see equation (4.14)), the first step of the suggested algorithm for determining estimated samples $\tilde{Q}[z_i]$ of the desired PESAW charge distribution $Q(z)$ is to solve the *inverse medium* problem of estimating the dielectric's propagation parameter $\underline{\mathcal{K}}(f) = \alpha(f) + \mathrm{j}\, 2\pi f/c(f)$.
>
> The information required to solve the inverse medium problem is contained in $V_c[t_n]$. $V_c[t_n]$ must be parsed into its proximal plate component $V_p[t_n]$ and its distal plate component $V_d[t_n]$, which must then be analyzed to determine models for $\alpha(f)$, $c(f)$ and, ultimately, $\underline{\mathcal{K}}(f)$. Sections 4.10 through 4.13.3 explain this process.
>
> Having solved the inverse medium problem, the next task is the *inverse source* problem of determining the normalized, estimated source pressure waveform $R[z_i]$. $R[z_i]$ must then be multiplied by some dimensioned constant to yield an estimated charge waveform $\tilde{Q}[z_i]$.

This chapter's goal is to legitimize application of the Lyons recovery to measured PESAW data. The most definitive validation of a charge recovery method would be to

'successfully' recover a known charge distribution. It would be helpful if the relative success of various recoveries could be quantified via comparison with the known charge waveform $Q(z)$.

Unfortunately, the author knows of no way to accurately embed a one dimensional charge waveform $Q(z)$ inside a sample without violating the requisite homogeneity of the samples' electric and acoustic propagation properties.

However: (part one) it *is* possible to embed an 'approximately known,' approximately one dimensional charge waveform within a homogeneous dielectric sample via E-beam irradiation; (part two) it is *also* possible to attempt to recover the known proximal and distal surface plate charges associated with a measured calibration signal $V_c[t_n]$.

In 'the E-beam experiment' the test charge waveform is known to be embedded within the dielectric, but the shape of the waveform is not well known. In 'the calibration experiment' the shape and size of the test charge waveform is well known (at least theoretically, at macroscopic space scales), but contains no bulk charge.

One measure of the success of the recoveries gleaned from either of these two experiments is whether the recovered charge waveform, integrated twice and appropriately scaled, meets the known, applied DC voltage boundary condition (see section 9.1). Another way to attempt to validate a charge recovery is to make sure that the total charge vanishes (again, see section 9.1).

In the case of the E-beam experiment it is also possible to check whether the recovery gleaned when the proximal plate is attached to the side of the slab through which the E-beam entered (the EP configuration) is 'similar to' the recovery gleaned when the distal plate is attached to the side of the slab through which the E-beam entered (the ED configuration).

Note that the ED recovery must be translated (reversed and shifted, so that the pre-translation ED position $z' = l$ maps to the EP position $z = 0$ and the pre-translation position $z' = 0$ maps to $z = l$; *ie*: $z = l - z'$) before it can be compared with the EP recovery, which is awarded primacy. The need for one of the recoveries to be translated before comparison with the other arises from the fact that the EP and ED sub-experiments 'look into' the dielectric from opposite sides.

If both the charge distribution and the experimental conditions (see section 4.8) can be assumed or shown to be roughly constant over the time between the EP and ED sub-experiments, then the success of the Lyons recovery is, in essence, independently confirmed and therefore validated to some degree.

Although the spatially impulsive charge distribution extant in the calibration experiment is well known in advance, it does not extend into the bulk of the dielectric. Yet according to PESAW theory (and excepting an overall multiplication factor of two; see section 4.2) a charge layer at the distal plate $z = l$ acts like a charge layer at any other position $0 \leq z < l$. Therefore the worst case ($z = l$) efficacy of the Lyons recovery of PESAW data can be determined via the calibration experiment.

In this thesis, the double-sided E-beam experiment is performed on relatively low-loss polymethylmethacrylate (PMMA) and the calibration experiment is performed on

relatively high-loss polyethylene (PE). Hopefully, these results will convince the reader that the Lyons recovery is a legitimate method to apply to experimental PESAW data.

The section following both *The Double-Sided E-Beam Experiment* and *The Calibration Experiment* presents the results of two more experiments. These latter experiments explore the range of application of the Lyons recovery.

9.1 The Voltage Boundary Condition

The total charge waveform $\mathrm{Q}(z)$ associated with the PESAW experiment (see figure 1.1, page 10. Note polarity of applied voltage) is assumed to be comprised of the sum of a bulk charge waveform $\mathrm{Q}_b(z)$ and two impulsive plate charges, so that

$$\mathrm{Q}(z) = \mathrm{Q}_b(z) + q_p\delta(z) + q_d\delta(z-l) \tag{9.1}$$

where q_p denotes the quantity of surface charge ($\mathrm{nC/cm^2}$) on the proximal capacitor plate and q_d denotes the quantity of surface charge on the distal capacitor plate. It is assumed that the electric field inside each capacitor plate vanishes so that, by Gauss' law, it follows that the net charge must vanish as well:

$$0 = q_p + q_d + \int_0^l \mathrm{Q}_b(z)\, dz \tag{9.2}$$

According to (9.2), if the sample has net bulk charge embedded within it then $|q_p|$ cannot equal $|q_d|$. With $\phi(z)$ denoting the one dimensional electric potential which satisfies

$$\mathrm{E}(z) = -\frac{d\phi(z)}{dz} \tag{9.3}$$

the DC component V_o of the applied voltage signal $\mathrm{V}_a(t)$ (see section 4.3) must equal the potential drop across the capacitor:

$$\phi(l) - \phi(0) = \mathrm{V}_o \tag{9.4}$$

Integrating (9.3) and inserting Gauss' law (9.5)

$$\mathrm{E}(z) = \frac{1}{\epsilon}\int_0^z \mathrm{Q}(z')\, dz' \tag{9.5}$$

yields

$$\phi(z) - \phi(0) = -\int_0^z \left[\frac{1}{\epsilon}\int_0^{z'} \mathrm{Q}(z'')dz''\right] dz' \qquad (9.6)$$

Considering $z = l$ in (9.6), then inserting (9.4), yields:

$$\mathrm{V}_o = \frac{-1}{\epsilon}\int_0^l \int_0^z \mathrm{Q}(z')dz'dz \qquad (9.7)$$

Equation (9.7) is the known voltage boundary condition that the experimental recovery $\tilde{\mathrm{Q}}(z)$ must satisfy. As a practical matter, the resolution of the recovery will be finite. That is, although the plate charges are known to be impulsive, the recovery of each plate charge will have finite thickness. The range of integration must be extended beyond the physical dielectric region $0 \leq z \leq l$.

With $z = 0^-$ denoting some position on the order of one resolution FWHM to the left of $z = 0$, and with $z = l^+$ denoting some position on the order of one resolution FWHM to the right of $z = l$, equation (9.7) can be re-written in terms of the recovered charge waveform estimate $\tilde{\mathrm{Q}}(z)$

$$\mathrm{V}_o \cong \frac{-1}{\epsilon}\int_{0^-}^{l^+} \int_{0^-}^{z} \tilde{\mathrm{Q}}(z')\, dz'\, dz \qquad (9.8)$$

9.2 The Double-Sided E-beam Experiment

The double-sided E-Beam experiment focusses on an $l = 2.121$ mm slab of polymethylmethacrylate (PMMA) which was bombarded with a dose of 0.35 MeV electrons on June 3 1997. The dosage was designed to deliver 200 nC/cm^2 of charge. This irradiated sample was then set aside until June 28'th. Between June 28'th and June 30'th this sample was subjected to the PESAW experimental procedure. Many PESAW signals were measured; some with the DC voltage bias V_o = -2 kV, some with V_o = +2 kV, and some with $\mathrm{V}_o = 0$. The temperature was held constant at 22°C throughout.

Some of the signals were collected with the sample in the EP configuration (*ie*: the sample was mounted with the proximal plate attached to the side of the sample through which the bombarding electrons entered) and some of the signals were collected with the sample in the ED configuration (*ie*: the sample was mounted so that the irradiating electrons entered through the distal plate).

9.2.1 Inverse Medium Solution

Figure 9.1 depicts the EP and ED calibration signals $\mathrm{V}_c[t_n]$ for this experiment. Note that, although the sample was remounted between the measurement of the EP and the

ED calibration signals, these two signals are remarkably similar. A cursory inspection could fail to discern that there are actually two signals plotted.

A theoretic, hysteresis absorption/NLKK model for the polymeric attenuation coefficient $\alpha_p(f)$ and phase velocity $c_p(f)$ was extracted from these two measured calibration files via the techniques described in chapter 4. The proximal pulse is defined by the samples falling between $t = 0$ and $t = t_p$; the distal pulse is defined by samples falling between $t = t_p$ and $t = t_d$ (see figure 9.1).

The parameters selected to define the theoretic model for this sample of PMMA are given in table 9.1.

m	=	0.011	Np/(mm MHz)
$c(f_o)$	=	2.7534	mm/μs
f_o	=	1	MHz
b	=	0	Np/mm

Table 9.1: Polymeric model selected to describe the slab of polymethylmethacrylate analyzed in *The Double Sided E-Beam Experiment.*

See section 6.2.1 for an introduction to the polymeric hysteresis absorption/NLKK model.

Figure 9.3 depicts measured (EP and ED) and theoretic values of the attenuation coefficient $\alpha[f_k]$ corresponding to this slab of PMMA. Figure 9.4 is analogous to figure 9.3, except the phase velocity $c(f)$ plays the role of $\alpha(f)$. Visual inspection of these two plots confirms this model for PMMA, especially for frequencies between, say, 2 and 14 MHz. The theoretic and measured values for $\alpha(f)$ (and $c(f)$) appear more closely correlated inside this range than outside it.

Whereas figures 9.3 and 9.4 support the validity of this model for PMMA via the frequency domain, figure 9.2 suggests the validity of this model via the time domain. Figure 9.2 depicts measured and theoretic values for the distal pulse parsed from the EP calibration file. The 'theoretic' values for the EP distal pulse were computed by synthetically propagating the measured EP proximal pulse through a thickness $l =$ 2.121 mm slab of modelled $(m, c(f_o), f_o)$ material.

Figure 9.2 supports this model for PMMA – the time-domain modelled data fits the measured data like cellophane on a pickle. The author found that 'cross-propagation comparisons' (*ie*: comparing the measured EP output pulse with the result of synthetically propagating the ED input pulse through $l = 2.121$ mm of modelled material; and *vice versa*) yielded comparable success.

Because the sample was known to have electrons embedded within it, the only known method for obtaining a calibration file is the subtraction method discussed in section 4.8. Section 4.8 emphasizes the requirement that the experimental conditions ($H_e(t)$, $\alpha(f)$, $c(f)$, ϵ, l, *etc.*) remain roughly constant over the time between successive measurements (different mountings, different applied voltages, different number of averages, different temperature, pressure, *etc.*)

The EP calibration data was taken between 2:56 and 4:10 PM on June 29. The ED calibration data was taken between 11:31 AM and 12:44 PM on June 30. All ten (two calibration and eight bulk) of this experiment's data signals were obtained between June 28'th (4:35 PM) and June 30'th (3:14 PM).

The elapsed time between the measurement of the two calibration signals is on the order of (about one-half of) the elapsed time over which all the data (calibration and bulk signals) was obtained, and this 'total duration of data measurement' is only about one-twelfth of the elapsed time between the irradiation of the sample and the beginning of the duration of data measurement. The agreement between the measured calibration signals themselves, and also between the measured signals and the theoretic model, supports not only the model but also the validity of the assumption of constant experimental conditions.

So far, this experiment's investigations have focussed on calibration signals $V_c[t_n]$ to the exclusion of bulk signals $V_b[t_n]$. These investigations have also focussed on confirming the validity of the inverse medium solution $(m, c(f_o), f_o)$ to the exclusion of the inverse source solution.

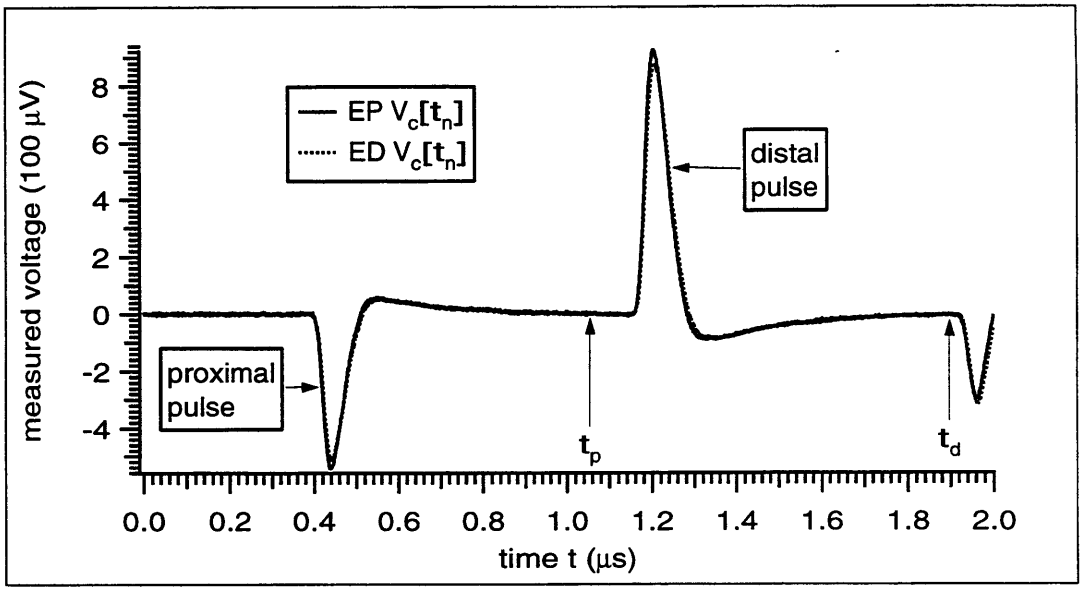

Figure 9.1: EP and ED calibration signals for the E-beam irradiation experiment.

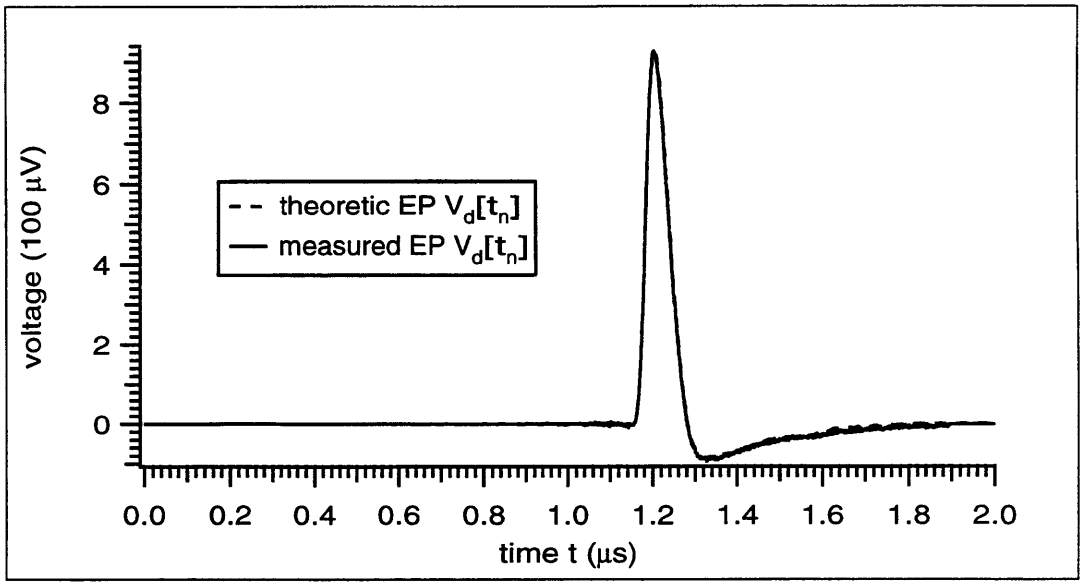

Figure 9.2: Measured (EP) and theoretic values of the distal pulse parsed from the calibration file corresponding to the 2.121 mm sample of PMMA investigated in the E-beam irradiation experiment.

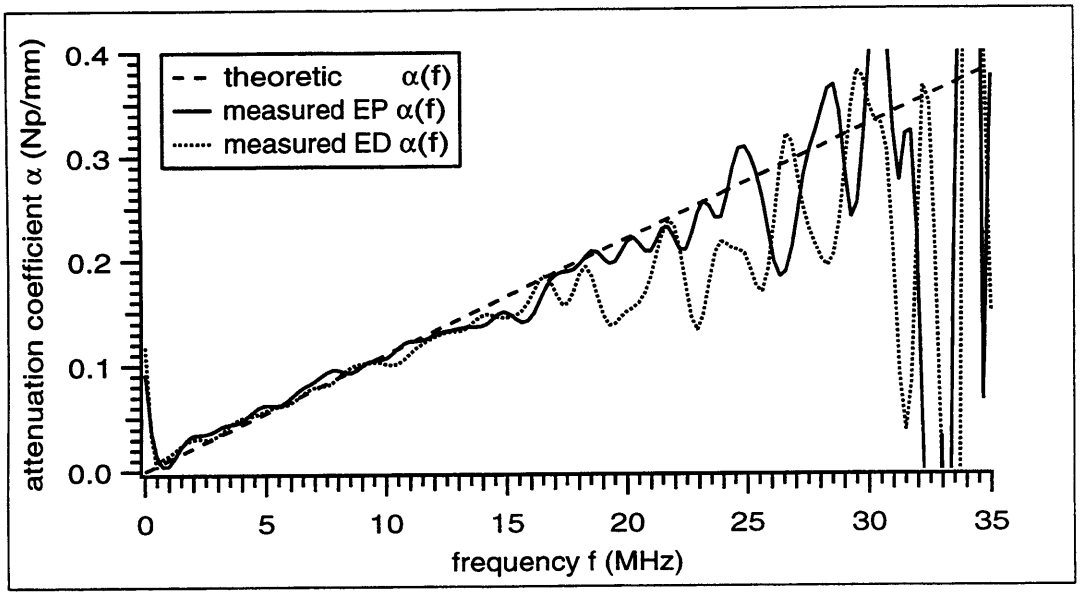

Figure 9.3: Measured (EP and ED) and theoretic values of the attenuation coefficient $\alpha[f_k]$ corresponding to the 2.121 mm sample of PMMA investigated in the E-beam irradiation experiment.

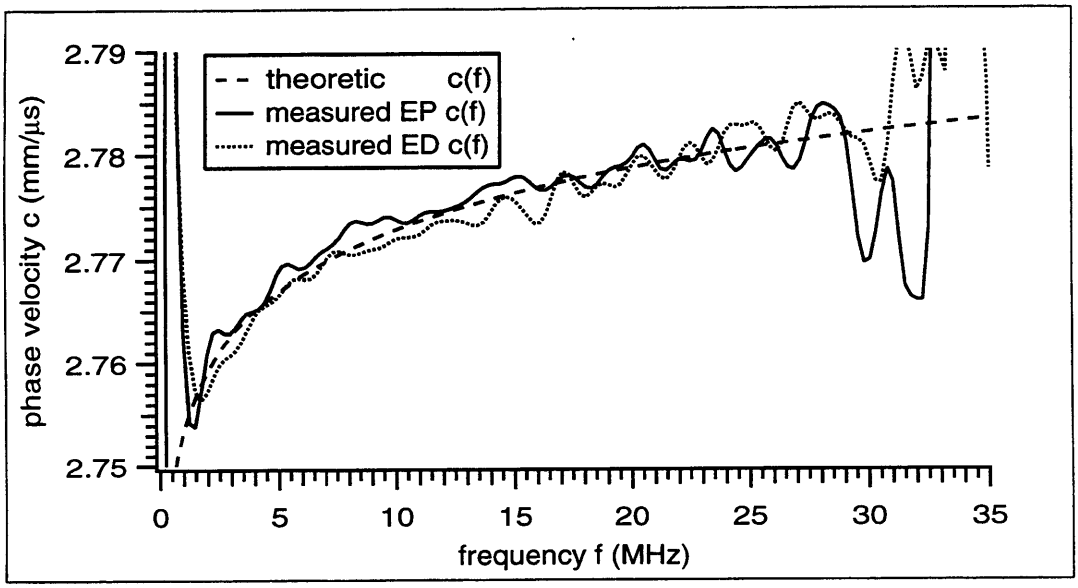

Figure 9.4: Measured (EP and ED) and theoretic values of the phase velocity $c[f_k]$ corresponding to the 2.121 mm sample of PMMA investigated in the E-beam irradiation experiment.

9.2.2 Inverse Source Solution - Calibration Waveforms

The transition to verification of the inverse source solution starts with the calibration files. The goal is to verify that the recovered charge distribution satisfies the known voltage boundary condition (9.8). Calibration signals, which correspond to the difference of V_o = +2 kV and V_o = -2 kV bulk signals, have an effective V_o of +4 kV. Analysis focusses arbitrarily upon the EP calibration signal – the author found that the ED calibration signal results were entirely comparable.

Figures 9.5 and 9.6 each depict two SIB source recoveries gleaned via page 82's equation (4.60), which is re-presented below:

$$R(z) \equiv \Delta f \sum_{k=0}^{k'} \text{two}[k]\ \Re_e \left\{ \frac{\underline{V}[f_k]\ B(f_c(z), f_k)}{\underline{H}_e[f_k]\ \underline{C}_g[f_k]}\ \exp(z\ \underline{K}(f_k)) \right\} \tag{9.9}$$

To be explicit, please recall that page 82's discussion points out that $k' = N_t/2$ (where N_t denotes the number of time samples, so that the number of frequency samples $N_f = 1 + k'$) and that two[0] = two[k'] = 1, whereas two[k] = 2 for $k \neq \{0, k'\}$.

The FFT of the EP calibration file was used as $\underline{V}[f_k]$ in (9.9); the negative of the FFT of the EP proximal pulse was used as $\underline{H}_e[f_k]$ (see figure 4.1 and equation (4.27); both state that $H_e(t)$ = - $V_p(t)$). The requisite $\Delta f = 1/(N_t \Delta t)$ sampled functions $\underline{K}[f_k]$ and $\underline{C}_g[f_k]$ were calculated by sampling the closed form functions

$$\underline{K}(f) = \alpha(f) + \text{j}\ 2\pi f/c(f) \tag{9.10}$$

and

$$\underline{C}_g(f) = \left[\frac{1}{c(f)} \left[1 - \frac{f}{c(f)}\ \frac{d\ c(f)}{df} \right] + \frac{1}{\text{j}2\pi}\ \frac{d\ \alpha(f)}{df} \right]^{-1} \tag{9.11}$$

where

$$\alpha(f) = m\ f \tag{9.12}$$

$$= [\frac{0.011\ \text{Np}}{\text{mm MHz}}]\ f \tag{9.13}$$

and

$$c(f) = c(f_o) + m\frac{c^2(f_o)}{\pi^2}\ln(\frac{f}{f_o}) \tag{9.14}$$

$$= [2.7534\frac{\text{mm}}{\mu\text{s}}] + [\frac{0.011\ \text{Np}}{\text{mm MHz}}]\ \frac{[2.7534\frac{\text{mm}}{\mu\text{s}}]^2}{\pi^2}\ln(\frac{f}{1\ \text{MHz}}) \tag{9.15}$$

The sampled complex group velocity $\underline{C}_g[f_k]$ was calculated by submitting

$$\frac{d\alpha(f)}{df} = m \qquad \text{and} \qquad \frac{dc(f)}{df} = \frac{m}{f}\ \frac{c^2(f_o)}{\pi^2} \tag{9.16}$$

into (9.11), then sampling. Note that the total number of time samples $N_t = 8192$, the sampling time-step $\Delta t = 0.5$ ns, so the frequency step $\Delta f = 1/(N_t\Delta t) = 0.2441$ MHz. The spatial sampling interval $\Delta z = 0.01$ mm.

Figure 9.5 compares $f_c = 50$ MHz and $f_c = 20$ MHz SIB recoveries. Note that the 50 MHz SIB recovery clearly exhibits significant non-physical oscillations with wavelength ~ 83 μm, whereas the 20 MHz SIB recovery does not. Further, it is clear that the f_c = 50 MHz plate charges (proximal and distal; near $z = 0$ and $z = l$, respectively) are more finely resolved than the $f_c = 20$ MHz plate charges – the resolution FWHM of the 50 MHz recoveries is ~ 185 μm whereas the resolution FWHM of the 20 MHz recoveries is about 100 μm less (~ 85 μm).

Figure 9.5 clearly demonstrates the need for the experimenter to make an arbitrary (application dependent) decision regarding the expected tradeoff between resolving power and suppression of noise. It is interesting to note that the $f_c = 50$ MHz recovery's noise appears as a wavelength ~ 83 μm oscillation which is on the order of that recoveries' resolution FWHM (~ 85 μm).

Figure 9.6 compares the $f_c = 20$ MHz SIB recovery described above with the f_c = 33 MHz SIB recovery. This value for f_c was chosen arbitrarily by modulating f_c until the characteristic noise oscillations were just barely discernible on a vertical scale including the plate charge recoveries. The resolution FWHM of the $f_c = 33$ MHz SIB recovery is 111 μm.

There is no need to invoke the SDB ($f_c(z) \neq$ constant) recovery – if the resolution were spatially dependent then, as the SIB f_c were decreased from $+\infty$ recovery-by-recovery, the proximal plate recovery would 'resolve itself up out of the noise' before the distal plate recovery (see, *eg*, figure 9.33). Figure 9.7, which compares the f_c = 90 MHz and the $f_c = 70$ MHz SIB recoveries, clearly depicts both plate recoveries simultaneously resolving themselves up from the noise. Interestingly, the noise in both these recoveries has the same characteristic wavelength (83 μm) as the 50 MHz SIB recovery.

The author proposes interpreting the seemingly ubiquitous 83 μm noise oscillation as follows: this experiment's measured signals inherently cannot be trusted to accurately resolve features smaller than 83 μm. The value $f_c = 33$ MHz is used for all of

this experiment's forthcoming recoveries; the spatially-independent 111 μm resolution FWHM of this recovery suggests that features larger than 83 μm yet smaller that 111 μm will not be resolvable either.

Figure 9.8 depicts the indefinite integral $\int_{-0.3\text{ mm}}^{z} \mathrm{R}[z_i]\Delta z_i$ of the $f_c = 33$ MHz recovery depicted in figure 9.6. This plot clearly demonstrates that the area of the raw recovered proximal pulse is approximately -1 whereas the area of the raw recovered distal pulse is nearly, but not quite, 2.

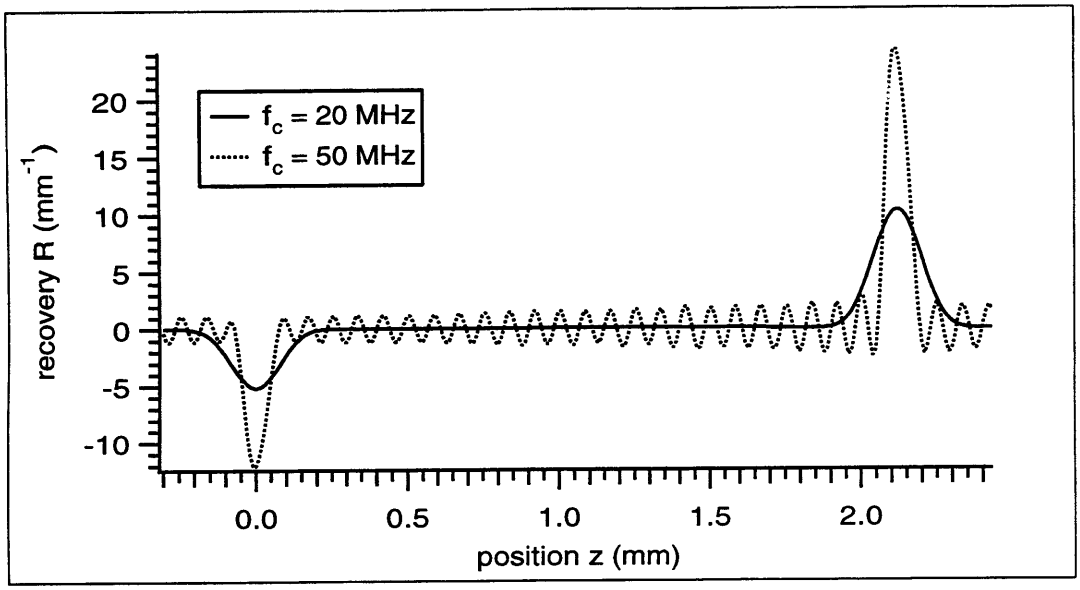

Figure 9.5: Comparison of the raw, $f_c = 50$ MHz and the rawm $f_c = 20$ MHz SIB recoveries gleaned by deconvolving the EP calibration signal with respect to the negative of its proximal pulse.

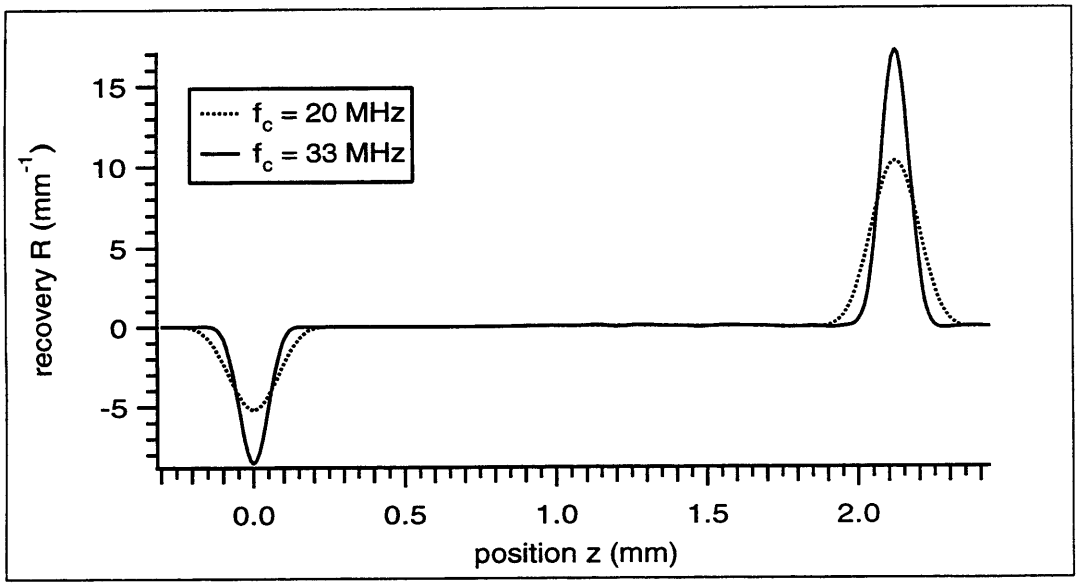

Figure 9.6: Comparison of the raw, $f_c = 33$ and the raw, $f_c = 20$ MHz SIB recoveries gleaned by deconvolving the EP calibration signal with respect to the negative of its proximal pulse.

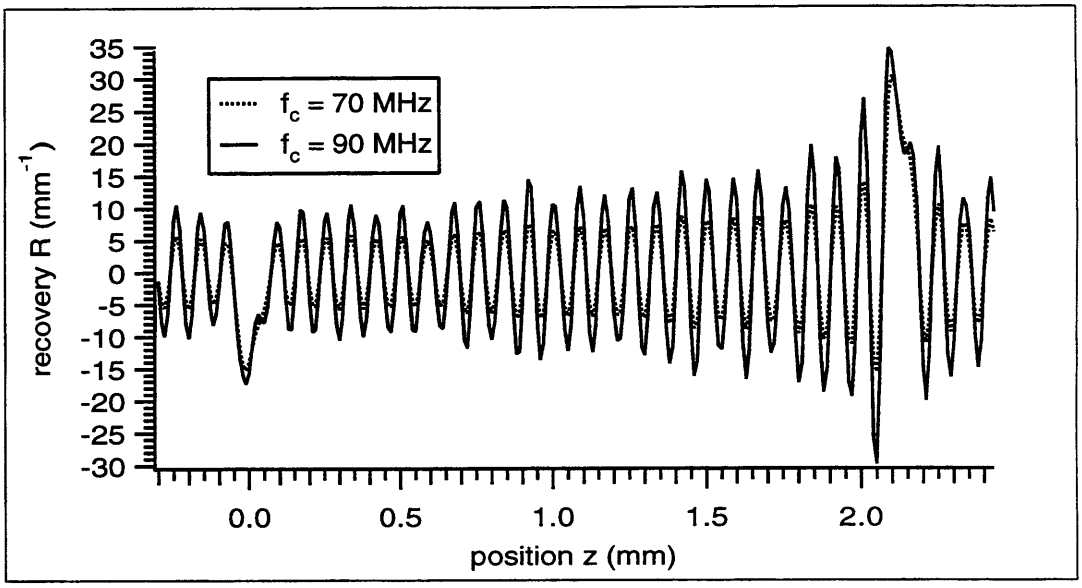

Figure 9.7: Comparison of the raw, $f_c = 70$ and the raw, $f_c = 90$ MHz SIB recoveries gleaned by deconvolving the EP calibration signal with respect to the negative of its proximal pulse.

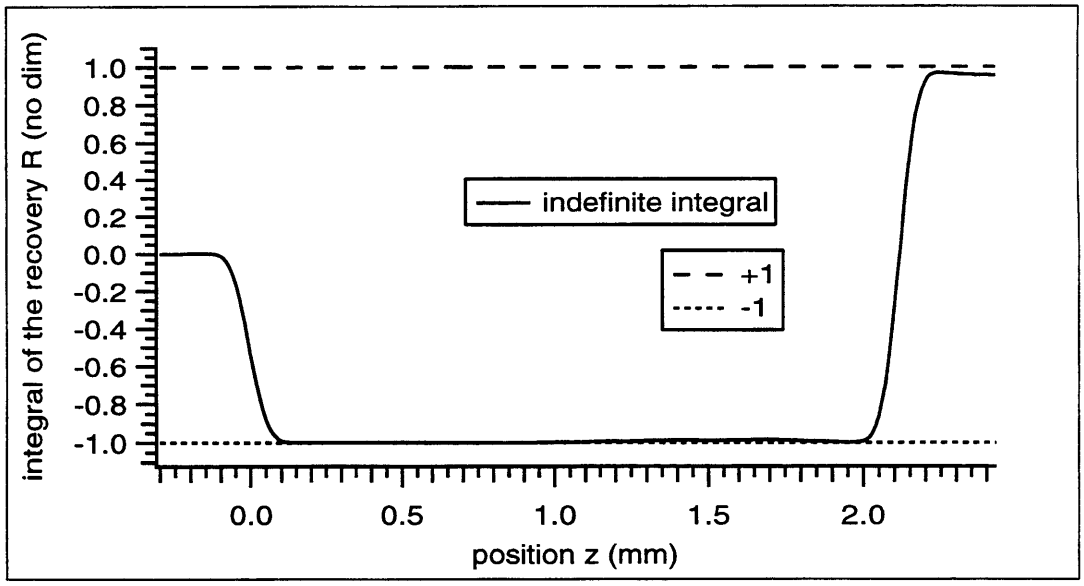

Figure 9.8: The indefinite integral (from -0.3 mm to z) of the raw, $f_c = 33$ MHz recovery depicted in figure 9.6.

9.2.3 Raw Lyons-Recovered Localized Area

Continuing the previous sections's discussion: that the ratio (distal/proximal) of some measure of the recovered localized area should be -2 is evident from the discussion (sections 4.2 through 4.8) culminating in equation (4.23), re-produced below:

$$\mathrm{V}_c(t) = \mathrm{H}_e(t) * [-\delta(t) + 2\ \mathrm{H}(l,t)] \tag{9.17}$$

In theory, the response signal corresponding to the distal plate charge is boosted by a factor of two arising from the given assumptions *re* acoustic impedence mismatches at the capacitor plates. The difference in sign arises from the fact that the the capacitor plates exert forces of equal magnitude but opposite sign.

There are an infinite number of ways that this ratio of recovered area could be -2; *eg*: the recovered proximal plate area could be 17 and the recovered distal plate area could be -34. The following argument proposes that, for calibration waveform recoveries, the raw recovered localized area of the proximal plate *should be* $\cong$ -1 whereas the raw recovered localized area of the distal plate *should be* $\cong$ 2.

Recall page 40's equation (2.19):

$$\int_{-\infty}^{\infty} \mathcal{P}(t)\ dt = \int_{-\infty}^{\infty} \mathcal{Q}(z)\ \exp(-z\ \alpha(0))dz \tag{9.18}$$

According to the polymeric $\alpha(f) = mf$ model, $\alpha(0) = 0$ so (9.18) can be simplified:

$$\int_{-\infty}^{\infty} \mathcal{P}(t)\ dt = \int_{-\infty}^{\infty} \mathcal{Q}(z)dz \tag{9.19}$$

Now note that the forward problem can be discretized (approximated) as a CLDP matrix equation. That is, when $\alpha(0) = 0$, the forward CLDP IE

$$\mathcal{P}(t) = \int_0^l \mathcal{Q}(z)\ \mathcal{F}^{-1}\{\exp(-z\ \underline{\mathcal{K}}(f))\}\ dz \tag{9.20}$$

can be approximated as

$$\overline{\mathcal{P}}[t_n] \cong \overline{\overline{\mathcal{K}}}[z_i, t_n] \bullet \overline{\mathcal{Q}}[z_i] \tag{9.21}$$

where

$$\overline{\mathcal{Q}}[z_i] = \int_{(i-1/2)\Delta z}^{(i+1/2)\Delta z} \mathcal{Q}(z)\, dz \tag{9.22}$$

$$\overline{\mathcal{P}}[t_n] = \int_{(n-1/2)\Delta t}^{(n+1/2)\Delta t} \mathcal{P}(t)\, dt \tag{9.23}$$

and

$$\overline{\overline{\mathcal{K}}}[z_i, t_n] = \mathrm{H}(z_i, t_n) \tag{9.24}$$

$$= \int_{-\infty}^{\infty} \overbrace{\exp(-z_i[\underbrace{\alpha(f) + \mathrm{j}\, 2\pi f/c(f)}_{\underline{\mathcal{K}}(f)}])}^{\underline{H}(z_i,f)} \exp(\mathrm{j}2\pi f t_n)\, df \tag{9.25}$$

Note that each column of the forward-propagation matrix $\overline{\overline{\mathcal{K}}}[z_i, t_n]$ corresponds to the sampled impulse response signal $\mathrm{H}[z_i, t_n]$ of a thickness z_i slab of material described by the propagation coefficient $\underline{\mathcal{K}}(f)$. By (9.19) and the definitions describing (9.21) it should be clear that

$$\sum_{z_i} \overline{\mathcal{Q}}[z_i] \cong \sum_{t_n} \overline{\mathcal{P}}[t_n] \tag{9.26}$$

That is, the modelled polymeric forward problem conserves area; the dimensionless, non-localized area of a source waveform embedded within an $\alpha(0) = 0$ material must give rise to a response signal with identical non-localized area.

Further, insofar as the various signals $\mathrm{H}(z = z', t)$ corresponding to various constants z' can be modelled as a well resolved center of area with an arrival time that increases smoothly with z, the matrix $\overline{\overline{\mathcal{K}}}[z_i, t_n]$ will tend toward diagonality.

In any real material, causality will ensure that (in some not-yet-precisely-defined sense) the temporal response pulses corresponding to deeper source pulses will 'arrive later' than the response pulses corresponding to shallower sources. Therefore, forward time-domain discretization matrices $\overline{\overline{\mathcal{K}}}[z_i, t_n]$ tend toward diagonality.

As an example, consider figure 2.2 (page 45). Figure 2.2 depicts the CLDP response signal corresponding to a set of equally-spaced, unit-amplitude impulses of source located at the positions $z_i = \{0.25 \text{ mm}, 0.75 \text{ mm}, \ldots, 4.25 \text{ mm}, 4.75 \text{ mm}\}$ within a modelled sample of standard polyethylene (see section 6.2.2). Unfortunately, figure 2.2 depicts the *sum* of the ten desired signals. However, it is still possible to observe that

the response to each successive source impulse arrives later than its predecessor. Standard polyethylene's forward-propagation matrix $\overline{\overline{\mathcal{K}}}_p[z_i, t_n]$ tends toward diagonality.

In the case of a diagonal matrix which preserves area it is reasonable to think of the forward transformation as conservatively mapping localized areas from the neighborhood of each z_i to an approximately localized distribution ('larger' neighborhood, *aka* region) of t_n's. It seems that the forward problem is linear and tends to preserve localized area in a smoothly varying manner.

If the approximate inverse CLDP matrix ($\overline{\overline{\mathcal{K}}}^{-1}[t_n, z_i]$, defined below) corresponding to the Lyons recovery shares these properties, then (it will be shown) it is a simple matter to see that the raw recovered localized area of the proximal plate charge should be -1 whereas the raw recovered localized area of the distal plate charge should be 2. Is it possible that the Lyons recovery has the property of conserved localized area?

Intuitively, the diagonal forward matrix interpretation (9.26) of (9.19) supports the proposal that the inverse CLDP matrix will also tend to preserve localized area. Or, simply interpret (9.19) from right to left (the inverse direction) rather than from left to right (the forward direction). This question could also be addressed mathematically via the results of section 2.5.2, which legitimizes the discretization matrix approach to the inverse source solution by formally casting the proposed inverse CLDP solution as a linear, first-kind Fredholm IE with inverse kernel $\mathrm{K}(t, z)$.

Intuition and mathematical theory aside, it is possible to numerically investigate whether a particular instance (the PMMA model given above) of the known-linear Lyons recovery investigated in this thesis results in a matrix that preserves localized area.

Figures 9.9 attempts to addresses this question. It depicts five columns of the 'inverse impulse response' matrix $\overline{\overline{\mathcal{K}}}^{-1}[t_n, z_i]$, where $\overline{\overline{\mathcal{K}}}^{-1}[t_n, z_i]$ is the recovery $\mathrm{R}[z_i]$ gleaned from a temporally impulsive response signal $\mathcal{P}[t'_n] = \delta[t'_n - t_n]$. That is,

$$\overline{\overline{\mathcal{K}}}[z_i, t_n] = \mathcal{K}\{\delta[z'_i - z_i]\}[t_n] \tag{9.27}$$

$$\overline{\overline{\mathcal{K}}}^{-1}[t_n, z_i] = \mathcal{K}^{-1}\{\delta[t'_n - t_n]\}[z_i] \tag{9.28}$$

where the inverse-CLDP mapping $\mathcal{K}^{-1}$ is approximated here via the Lyons recovery.

Figure 9.9 depicts the five columns (waveforms) of $\overline{\overline{\mathcal{K}}}^{-1}[t_n, z_i]$ which correspond to the five cases $t_n = \{0.0, 0.2, 0.4, 0.6, 0.8\}$ μs. Figure 9.10 depicts the indefinite integrals of these five 'inverse kernel waveforms.'

To be completely explicit, note that each of the five waveforms plotted in figure 9.9 is the $f_c = 33$ MHz SIB Lyons recovery (9.9) gleaned from a sampled signal

$$\mathcal{P}[t_n] \qquad \overset{\mathrm{FFT}}{\Longleftrightarrow} \qquad \frac{\underline{V}[f_k]}{\underline{H_e}[f_k]} \tag{9.29}$$

which is non-zero at exactly one time t_n, where the sole non-zero sample has value 2000 μs^{-1}.

The value 2000 μs^{-1} comes from the requirement that a continuous time Dirac delta function must have area unity; 2000 $\mu s^{-1} = 1/\Delta t$, where $\Delta t = 0.0005$ μs is the temporal sampling step. The model used to compute these waveforms is the PMMA model given above. Equation (9.9) was used to compute the waveforms shown. $H_e[t_n]$ was effectively set to $\delta[t_n]$ and $V[t_n]$ was zero for all samples except for the sole non-zero sample discussed above.

Figures 9.9 and 9.10 support the claim that the approximate inverse CLDP matrices determined by this thesis' implementation of the Lyons recovery tends to preserve localized area in a smoothly varying manner – as t_n increases, a localized, symmetric, approximately unit-area pulse clearly moves smoothly towards greater z's.

The observed increase (see figure 9.9) in undershoot of the columns (waveforms) of the inverse matrix $\overline{\overline{K}}^{-1}[t_n, z_i]$ with t_n suggests that hand-modification (regularization) of the columns of the inverse matrix matrix might well yield a more well-behaved recovery than the current implementation. The inverse matrix could be regularized to remove the observed undershoot of the columns corresponding to the larger t_n's. Intuition suggests that the inverse matrix, like the forward matrix, should have only positive entries. The regularization procedure should ensure that the recovered area for each t_n remains unity.

But the current goal is not to investigate some hand-regularized variant of the frequency-domain-based SDB/SIB recoveries that are this thesis' focus. Rather, the current goal is to understand the observed fact (see figures 9.6 and 9.8) that the raw Lyons-recovered area of the proximal plate is approximately -1 whereas the raw Lyons-recovered area of the distal plate is nearly 2.

To see why, start by considering the case where the $\underline{V}[f_k]$ submitted to (9.9) is given by $\underline{V}[f_k] = -\underline{H}_e[f_k] = \underline{V}_p[f_k]$. According to (9.9), the operant frequency domain signal $\underline{\mathcal{P}}[f_k] = \underline{V}[f_k]/\underline{H}_e[f_k]$ will be precisely -1. Inverse FFTing into the time domain, it follows that the operant time domain signal $\mathcal{P}[t_n]$ will be $-\delta[t_n]$.

The signal $-\delta[t_n]$ clearly has all its area (-1) localized at $t_n = 0$. Because the Lyons recovery preserves localized area, the recovery gleaned from this signal should have area -1 localized in some region. And in fact, by definition, the Lyons recovery of the signal $-\delta[t_n]$ will be the negative of the $t_n = 0.0$ μs waveform depicted in figure 9.9. Indeed, less than 0.16% of the total recovered area falls outside the region $z = \pm$ 0.3 mm.

In the more realistic case of a calibration signal with well resolved proximal and distal pulses, deconvolution with respect to the negative of the proximal pulse ($H_e[t_n]$ = - $V_p[t_n]$) will still leave net area $\cong$ -1 'near' $t_n = 0$, and will also leave net area $\cong$ 2 near the delay time of the distal pulse. The temporal regions distinct from these two special regions should have net zero area.

Therefore, by the conservation-of-localized-area property of the Lyons recovery, and by the expected distribution of localized area associated with a successfully deconvolved calibration signal, the localized area associated with the proximal plate recovery should

be -1 and the localized area associated with the distal plate recovery should be 2.

Figures 9.11 through 9.14 demonstrate the validity of these statements concerning the expected distribution of localized area in a successfully deconvolved calibration signal $V_c[t_n]$. Figure 9.11 depicts the raw deconvolved calibration signal

$$\mathcal{P}_c[t_n] = \mathrm{FFT}^{-1}\left\{\frac{\mathrm{FFT}\{V_c[t_n]\}}{\mathrm{FFT}\{-V_p[t_n]\}}\right\} \tag{9.30}$$

associated with the EP calibration signal. Note that the apparent noise is punctuated by the relatively large negative excursion at $t_n = 0$ which corresponds to the deconvolved proximal pulse. As expected, in figure 9.11 the $t_n = 0$ value is very nearly the -2000 μs^{-1} value which corresponds to area -1 at a single $\Delta t = 0.0005$ μs sample.

The observed deviation of the $t_n = 0$ sample from the value -2000 μs^{-1} can only be due to noise associated with the deconvolution of the distal pulse; deconcolving the proximal pulse with respect the the negative of the proximal pulse would result in the precise (to within numerical error) value -2000 μs^{-1} at $t_n = 0$, and zero at all other times.

Figure 9.12 depicts the $f_c = 33$ MHz BLG filtered version of $\mathcal{P}_c[t_n]$. Note the two regions of localized area. The first, located near $t_n = 0$ (and near $t_n = N_t\Delta t$; see 'wrap around' discussion below), corresponds to the localized area that maps to the proximal plate recovery. The second, which peaks near $t_n = 0.765$ μs, corresponds to the localized area that maps to the distal plate recovery. Further, note that the localized area associated with the proximal plate recovery 'wraps around' to large values of time.

This wrap-around effect is an artifact of the fact that the FFT effectively operates upon a periodic signal; *eg*: the largest value of time $t_n = (N_t - 1)\Delta t$ can be interpreted equally well as $t_n = -\Delta t$. Figure 9.13 depicts the same data as that depicted in figure 9.12. In figure 9.13, however, the data has been rotated 0.2 μs to the right and the formerly-rightmost points have been labelled as negative.

Figure 9.14 depicts the indefinite integral of the 33 MHz BLG-filtered $\mathcal{P}_c[t_n]$ depicted in figure 9.13. This plot clearly shows that the localized area associated with the portion of the signal corresponding to the proximal pulse is approximately -1 whereas the localized area associated with the portion of the signal corresponding to the distal pulse is not quite the expected value of 2. Given the localized-area-mapping behavior of the Lyons recovery, and given the fact that the localized temporal area of the measured signal corresponding to the distal pulse is not quite 2, it seems entirely reasonable that the Lyons recovery of the distal pulse should also have localized area that is not quite 2.

This seeming peculiarity of the measured signal could be explained by a frequency dependent reflection coefficient at the distal plate – if low frequency signals experienced a reflection coefficient with magnitude less than unity whereas higher frequency signals experienced a reflection coefficient with magnitude $\cong$ unity, the results would agree with these observations.

Regardless of the cause of the apparent decrease in localized area of the portion of the signal associated with the distal pulse, the result in terms of the measured

$\alpha[f_k]$ would be the sharp $f \rightarrow 0$ up-turn observed in the measured data depicted in figure 9.3. Similaraly, a difference in phase between low- and high-frequency values of the reflection coefficient could explain the observed low-frequency deviation from theory observed in the measured phase velocity (see figure 9.4).

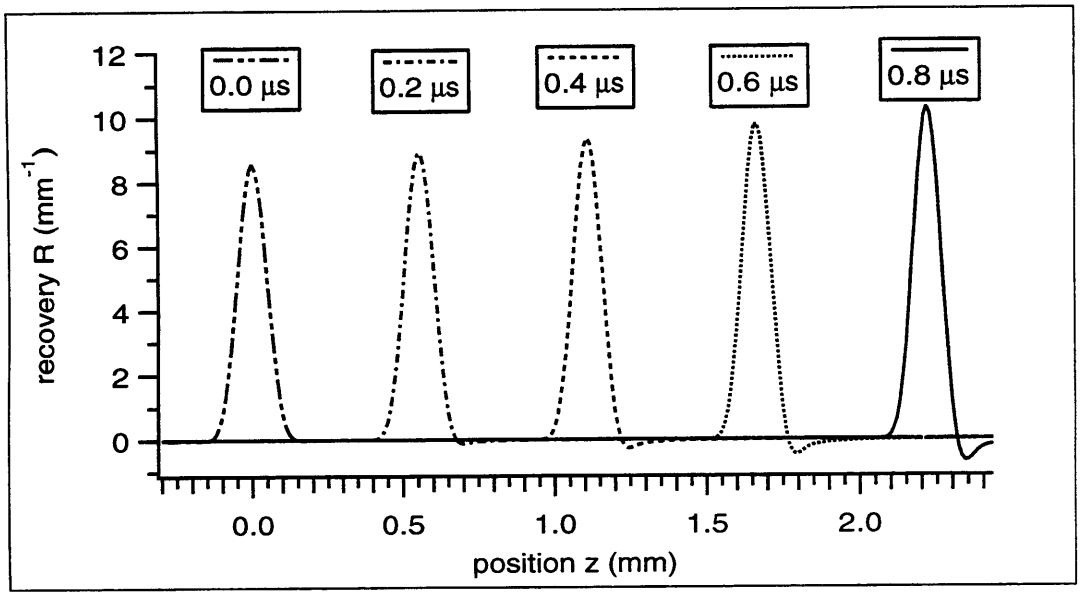

Figure 9.9: The five recoveries $\mathrm{R}[z_i]$ determined by submitting $\mathcal{P}[t_n] = \delta[t'_n - t_n]$ to the SIB Lyons recovery; $t_n = \{0.0, 0.2, 0.4, 0.6, \text{and } 0.8\ \mu s\}$. These five waveforms correspond to five distinct columns of the Lyons-recovered inverse CLDP matrix $\overline{\overline{\mathcal{K}}}^{-1}[t_n, z_i]$.

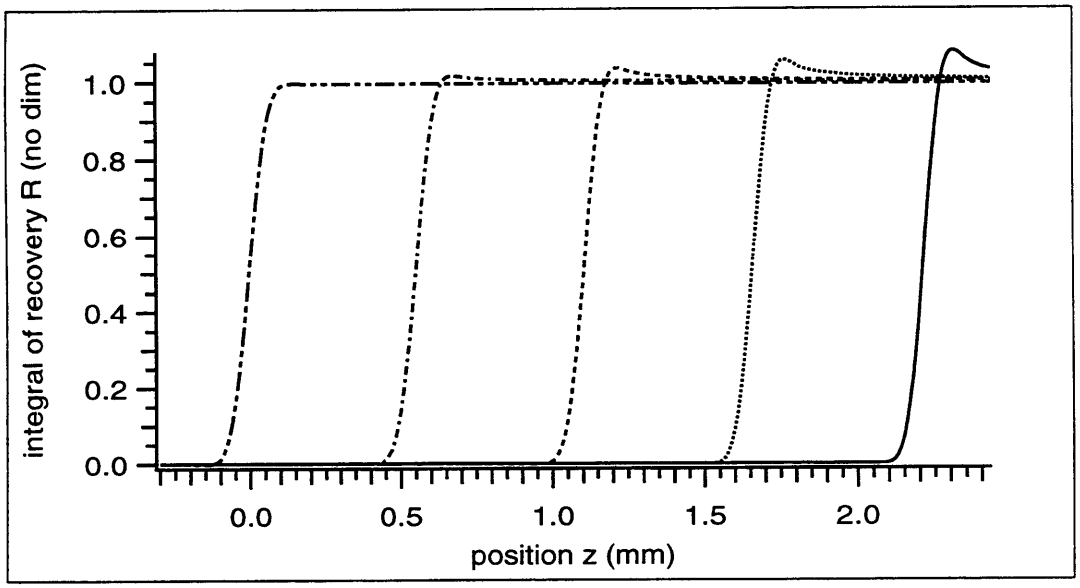

Figure 9.10: Indefinite integrals of the five waveforms depicted in figure 9.9.

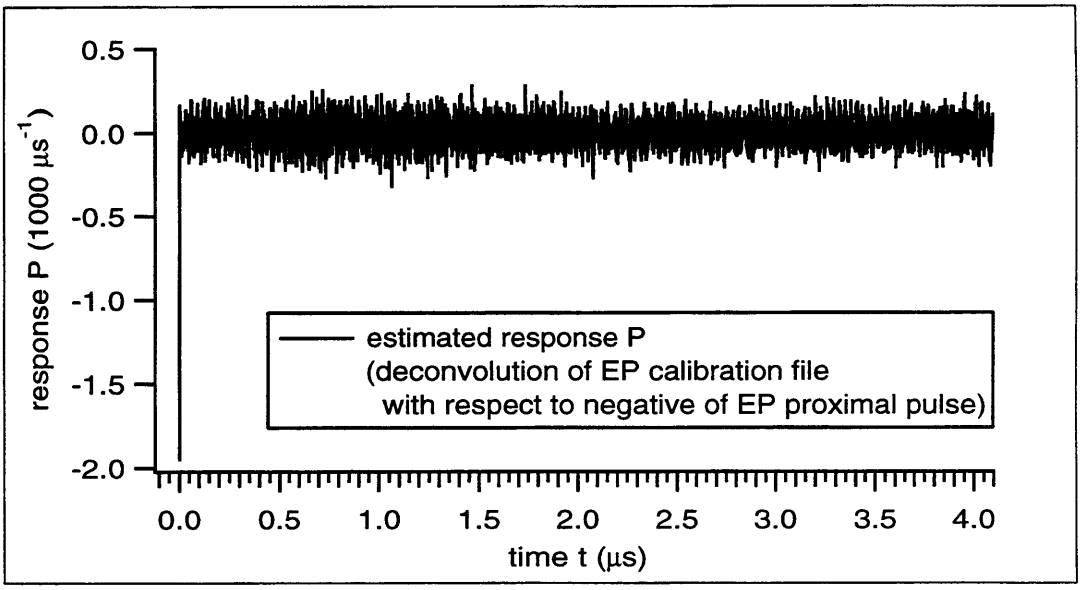

Figure 9.11: The raw deconvolved calibration signal $\mathcal{P}_c[t_n]$.

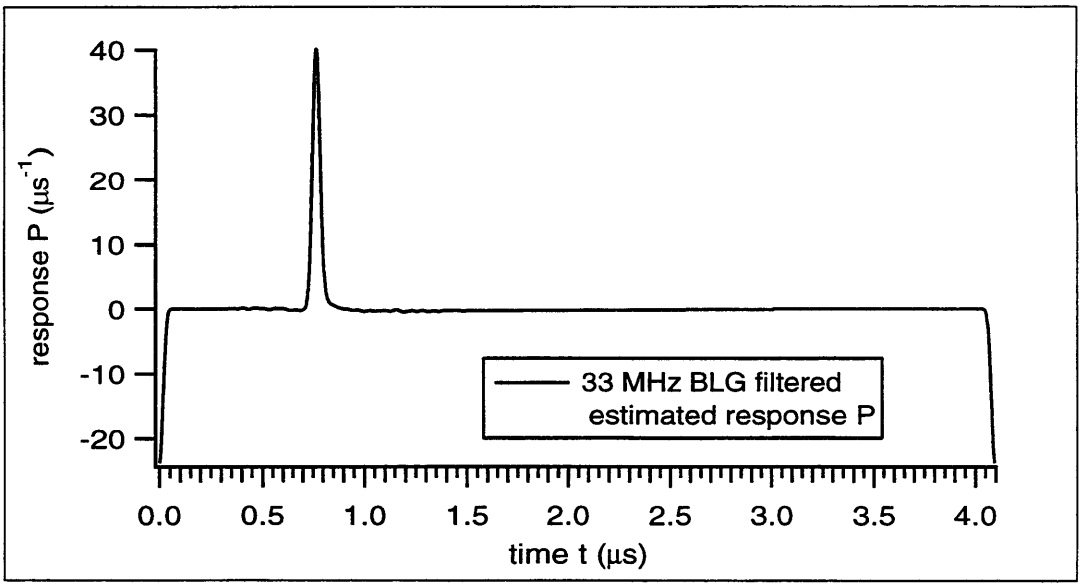

Figure 9.12: The raw deconvolved calibration signal $\mathcal{P}_c[t_n]$ after $f_c = 33$ MHz BLG filtering.

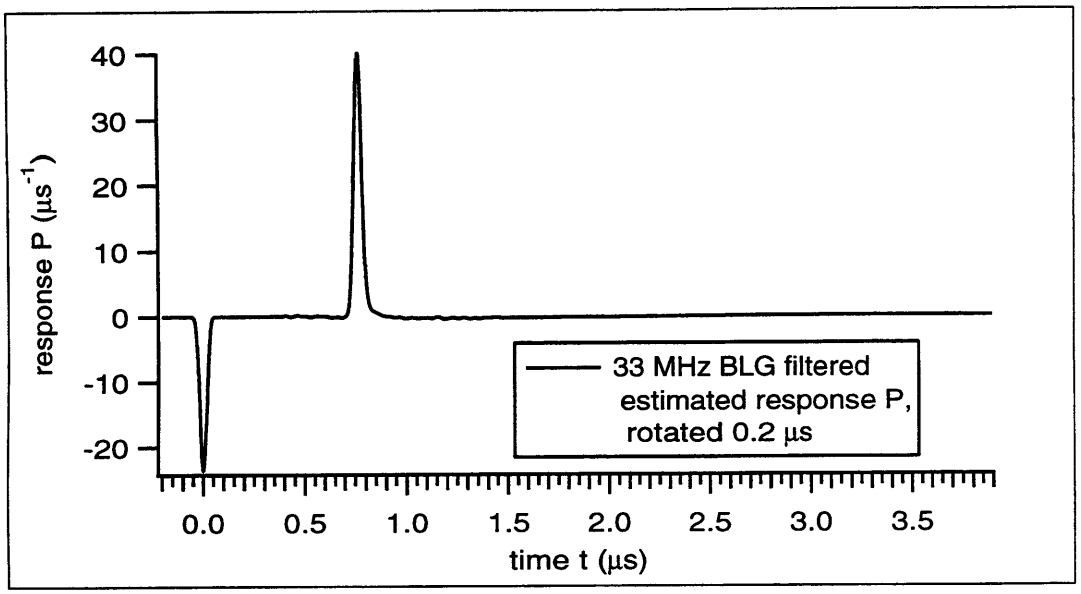

Figure 9.13: The raw deconvolved calibration signal $\mathcal{P}_c[t_n]$ after $f_c = 33$ MHz BLG filtering, and a 0.2 μs rotation to the right.

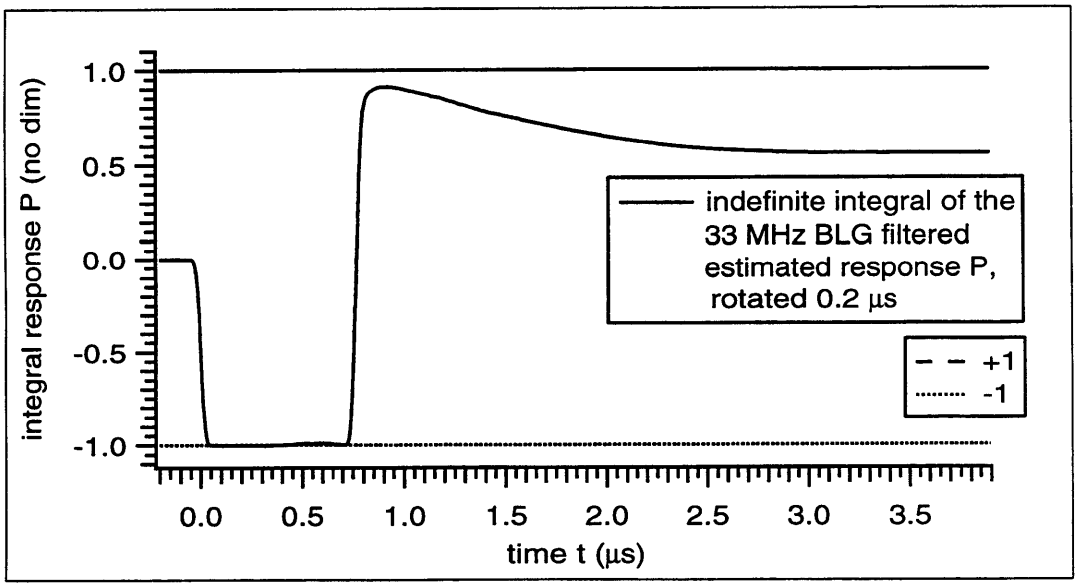

Figure 9.14: The indefinite integral of the signal depicted in figure 9.13.

9.2.4 Un-Normalization And The Voltage BC

According to the discussion in section 4.15.5, the $f_c = 33$ MHz waveform depicted in figure 9.6 need only be multiplied by some constant ν (which must have units of charge per area for the recovery to have the required units of charge per volume) to yield an actual estimated charge recovery $\tilde{Q}[z_i]$. According to the discussion in section 9.2.3, the area of the recovered proximal pulse should have area $\cong$ -1.

The recovered source waveform $R[z_i]$ has units of mm^{-1}, so multiplying by

$$\nu \cong q_p = \frac{\epsilon \, V_o}{l} \qquad \text{(equation (4.14))} \tag{9.31}$$

should yield a charge waveform with the correct units and magnitude.

If the ratio (distal/proximal) of the raw recovered localized areas corresponding to the two plate charges is not -2 then the experimenter is in an unfortunate situation: if ν is chosen such that the proximal plate recovery has area $-q_p$ then the distal plate recovery will not have the expected area $2q_p$. Conversely, if ν is chosen such that the distal plate recovery has area $2q_p$ then the distal plate recovery will not have the expected area $-q_p$.

The author has chosen to present recoveries with ν chosen such that the proximal pulse has area $-q_p$. The $f_c = 33$ MHz data depicted in figure 9.6 is known to have a ratio (distal/proximal) of raw recovered areas that is greater than -2: with localized area defined as the area between $\pm$ 0.14 mm, this ratio is -1.9634 = 1.9626/(-0.9996).

The permitivity ϵ of PMMA $\cong 3.4 \, \epsilon_o$, where ϵ_o is the permittivity of free space (see equation (2.2)). The sample thickness $l = 2.121$ mm. Because the EP calibration file discussed here is the difference of two bulk files acquired with $V_o = \pm$ 2 kV, the effective V_o of this calibration file is 4 kV. Therefore, the value of ν appropriate for this E-beam experiment is

$$\nu = \frac{3.4 \, [0.8854 \frac{\text{nC}}{\text{cm}^2} / \frac{\text{kV}}{\text{mm}}] \, 4 \text{ kV}}{(0.9996) \, 2.121 \text{ mm}} = 5.68 \, \frac{\text{nC}}{\text{cm}^2} \tag{9.32}$$

the fudge-factor (0.9996) included in the denominator is the magnitude of the recovered localized area associated with the proximal pulse recovery.

9.2.5 Verifying the Voltage BC for Calibration Waveforms

Figures 9.15 and 9.16 depict, respectively, the Lyons-recovered charge waveform associated with the EP calibration signal and its associated voltage waveform. The voltage waveform was calculated from the charge waveform via the right-hand side of page 167's equation (9.8).

The charge waveform was calculated from the $f_c = 33$ MHz source waveform depicted in figure 9.6 by multiplying it by the value of ν given in (9.32). This same value

of ν, and the same experimental impulse response signal $H_e(t)$, are used, respectively, to scale and deconvolve all the data associated with this E-beam experiment.

Figure 9.16 clearly shows that the charge waveform very nearly integrates to the correct effective applied voltage of +4 kV. The actual recovered voltage at $z = l$ is 3.828 kV, merely 4.4% less than the expected value. If the PESAW-recovered distal pulse was not doubled (due to an artifact of the PESAW experiment itself) then the voltage would level off for positions $z > l$. The EP calibration signal voltage BC appears to be satisfied.

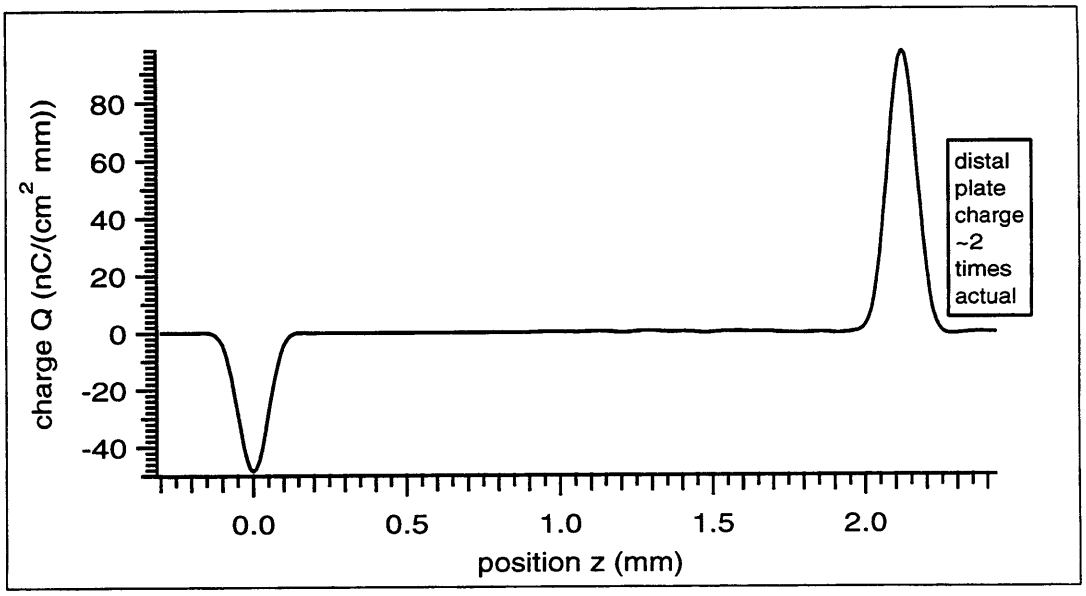

Figure 9.15: The recovered charge waveform associated with the EP calibration signal.

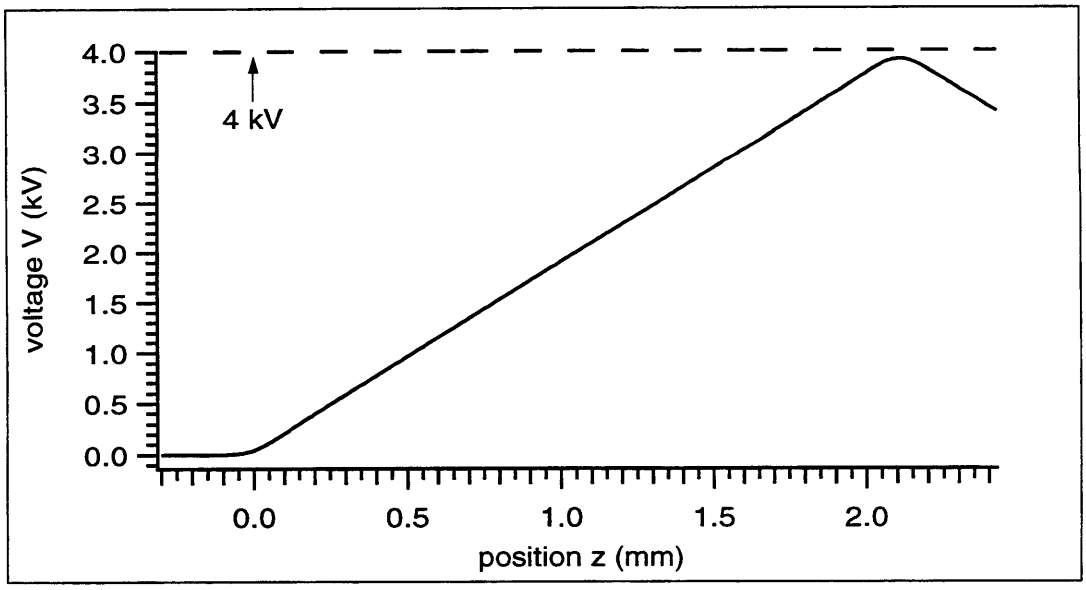

Figure 9.16: The recovered voltage waveform associated with the EP calibration signal.

9.2.6 Verifying the Voltage BC for Bulk Waveforms

Figure 9.17 depicts two raw measured PESAW bulk signals $V_b[t_n]$. Both signals were acquired from the same irradiated, $l = 2.121$ mm sample of PMMA analyzed previously. Both signals were acquired with the sample mounted in the EP configuration. However, the signal represented by the dashed line was acquired with the DC voltage bias V_o = -2 kV whereas the signal represented by the dotted line was acquired with V_o = +2 kV.

Figures 9.18 and 9.19 depict, respectively, the recovered charge waveforms and voltage waveforms associated with the signals depicted in figures 9.17. The same value $\nu = 5.68$ nC/cm^2 used to map the recovered source calibration waveform to its associated charge waveform was used for these recoveries as well.

The value of the $V_o = +2$ kV recovered voltage waveform at $z = l$ is 1.882 kV, just 5.9 % less than the expected value of 2 kV. The value of the V_o = -2 kV recovered voltage waveform at $z = l$ is -2.030 kV, a mere 1.5 % greater (in magnitude) than the expected value of $|-2$ kV$|$.

These errors (5.9% and 1.5%) seem small enough to justify the statement that the voltage boundary condition for these two recoveries has been verified. Besides the inexactness of the Lyons recovery itself, there are a number of possible sources for this error. Perhaps chief among them is the observed low frequency difference between the theoretic and modelled values for $\alpha(f)$ and $c(f)$ (see figures 9.3 and 9.4, especially the region below 2 MHz). But there is also a question concerning the DC offset of the measured PESAW signal itself.

The PESAW signals depicted in figure 9.17 (and the calibration signals depicted in figure 9.1) were 'zero adjusted' by adding a constant selected to force the temporal region before the 'start' of the signal (*ie*: between, say, 0 and 0.35 μs) to have zero average value. However, there is no reason to believe that the zero adjustment selected was correct. That is, there may well be a slight error in the DC value of the measured signal.

According to the Lyons recovery's observed property of preserved localized area, a DC error in the measured signal will map, at least approximately, to a DC error in the recovered charge waveform. Now note that the voltage waveforms depicted in figure 9.19 were calculated via two indefinite integrations of the charge waveforms depicted in figure 9.18.

Double integration of a constant waveform ($\sim$ unity) yields a quadratic waveform ($\sim z^2$), so even a 'small' (*ie*: invisible to the naked eye at the scale shown) DC error in the recovered charge waveform can lead to 'large' (*ie*: observable) error in the voltage waveform at $z = l$. Again, and even more emphatically, the observed errors (5.9% and 1.5%) seem small enough to justify the statement that the voltage boundary condition for these two recoveries has been verified.

It should prove possible to select a constant value to add to the measured PESAW signal to coerce the voltage waveform to have the correct value at $z = l$, but this procedure has been left for future researchers to investgate. Indubitably, it would be

possible select such a (presumably related, via conservation of area) constant value to add the charge waveform itself.

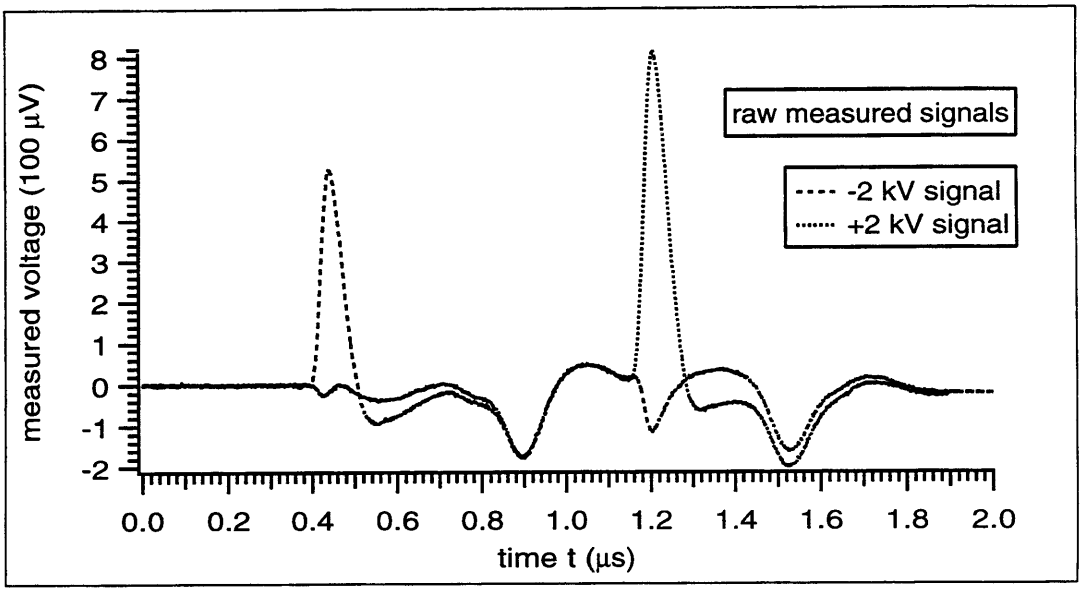

Figure 9.17: Two raw bulk PESAW signals gleaned from a l = 2.121 mm sample of E-beam irradiated PMMA. Dashed line depicts signal obtained with DC voltage V_o = -2 kV; dashed line depicts signal obtained with V_o = +2 kV.

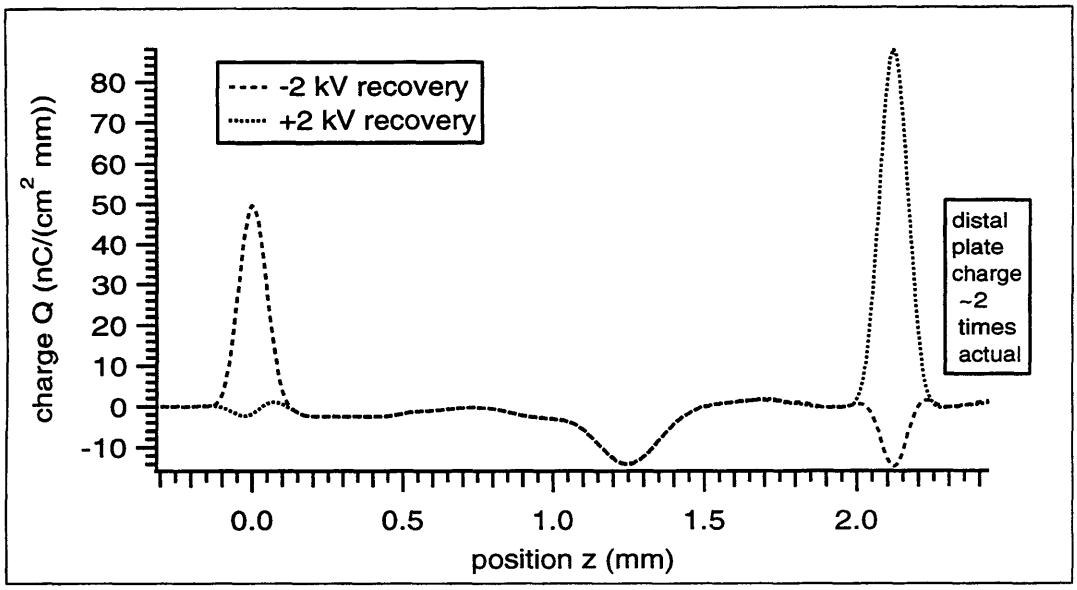

Figure 9.18: The two recovered charge waveforms gleaned from the two signals depicted in figure 9.17. *Ie*: the dashed line depicts the estimated (Lyons-recovered) charge waveform associated with the V_o = -2 kV E-beam experiment; the dotted line depicts the results of the +2 kV experiment.

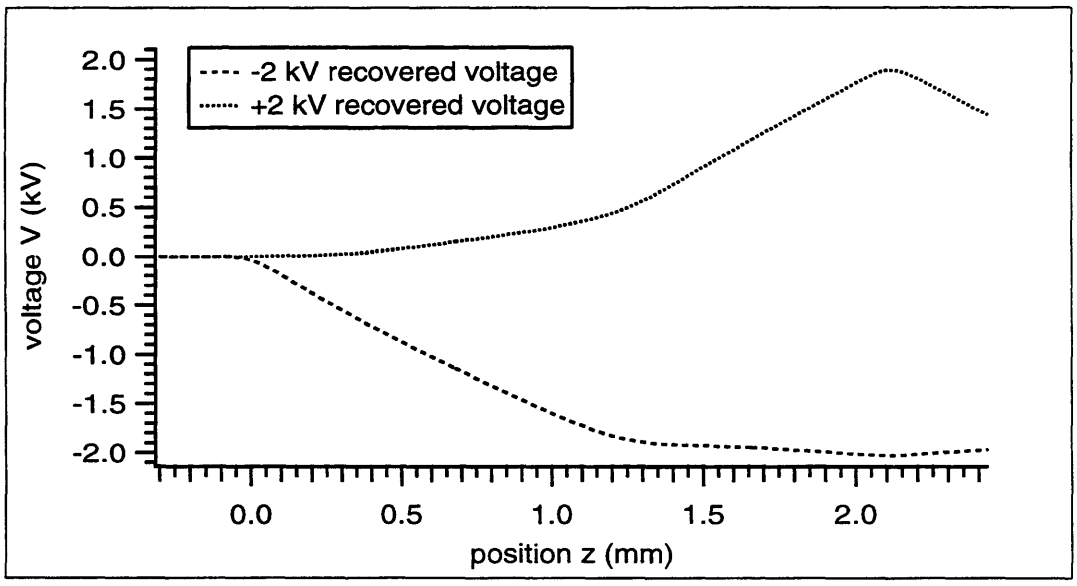

Figure 9.19: Voltage waveforms associated with the charge waveforms depicted in figure 9.18.

9.2.7 Closer Analysis Of The Bulk Signals

Figure 9.20 depicts the same two signals as those depicted in figure 9.17, except that:

I. the signals in figure 9.20 were deconvolved with respect to the negative of the EP proximal pulse depicted in figure 9.1 ($H_e(t) = -V_p(t)$)

II. these deconvolved signals were then filtered with a $f_c = 33$ MHz BLG filter

III. these deconvolved, filtered signals were then rotated 0.2 μs to the right to lessen the visual impact of the 'wrapping' associated with the periodic nature of FFT-based filtering (see, *eg*, figures 9.12 and 9.13)

Figure 9.20 is, therefore, an estimate to $\mathcal{P}[t_n]$, the actual (normalized) pressure signal arriving at the proximal plate. According to CLDP theory, such a normalized pressure signal is called a response signal.

In a relatively short, relatively low-loss sample such as the one under discussion the Lyons recovery reverts (approximately) to the dominant recovery. That is, in such a sample the deconvolved, filtered signal looks much like the Lyons-recovered waveform. The sample under discussion is an example of a short, low-loss sample – compare the signal depicted in figure 9.20 with the waveform depicted in figure 9.18. (The following experiment discusses a relatively thick, relatively high-loss sample.)

Focussing on the dashed (V_o = -2 kV) response signal depicted in figure 9.20, the first pulse (near $t_n = 0$) is large and has positive polarity. This pulse is associated with the relatively large, positive proximal plate charge generated by the negative voltage bias (note the convention *re* the polarity of the applied voltage $V_a(t)$ on page 10's figure 1.1). Comparing this first pulse with the first pulse appearing in the $V_o = +2$ kV response signal, it is clear that the change (+4 kV) in voltage bias has significantly reduced the quantity of proximal plate charge.

The +2 kV and -2 kV response signals are almost identical in the temporal region between, say, 0.2 and 0.6 μs. This temporal region contains information about the electrons deposited in the bulk of the dielectric. These signals diverge again in the temporal region near $t = 0.76$ μs. This latter temporal region contains information about the distal plate charges.

The negative polarity pulse appearing in the temporal region between, say, 0.95 and 1.4 μs also corresponds to the electrons deposited in the bulk of the dielectric. Please recall that charges in the bulk always emit two pressure waves in response to the PESAW excitation force. These two waves travel in opposite directions and are of opposite polarity.

The negative polarity pulse appearing between 0.95 and 1.4 μs is the 'image' (as in reflection) of the wave received between 0.2 and 0.6 μs. This image pulse reflected off the distal plate, which has a reflection coefficient $\Gamma \cong -1$. Reflection therefore reversed the image pulse's polarity and direction, sending it back towards the proximal plate with the same sign as its object (as in 'source of reflection'). Note the apparent

symmetry about $t_n \cong 0.76$ μs. In theory, this symmetry would be perfect in a lossless, dispersionless material – the image pulse must pass through more material than the object pulse.

Closer analysis of these twin pulses could help confirm or reject the frequency-dependent reflection coefficient hypothesis proposed near the end of section 9.2.3 (page 181). But this question will be left for future PESAW researchers.

Given some proximal and bulk charge distribution, the distal plate charge is completely determined by the physical necessity that the total charge in the sample vanish. That is, modifying equation (9.2)

$$q_d = -[\, q_p + \int_0^l Q_b(z)\, dz \,] \tag{9.33}$$

It is clear that changing the sign of the applied DC voltage bias V_o moves charges from the proximal to the distal plate, and leaves the bulk charge unmolested. This result will be still more evident in the plots of the actual recovered charge waveform. For now, please simply recall that the impact (upon the measured PESAW signal) of the distal plate charge q_d is doubled by an artifact of the PESAW experiment. The Lyons recovery itself cannot 'undo' the effects of this doubling; the recovered distal plate charges will appear twice as large as they actually are.

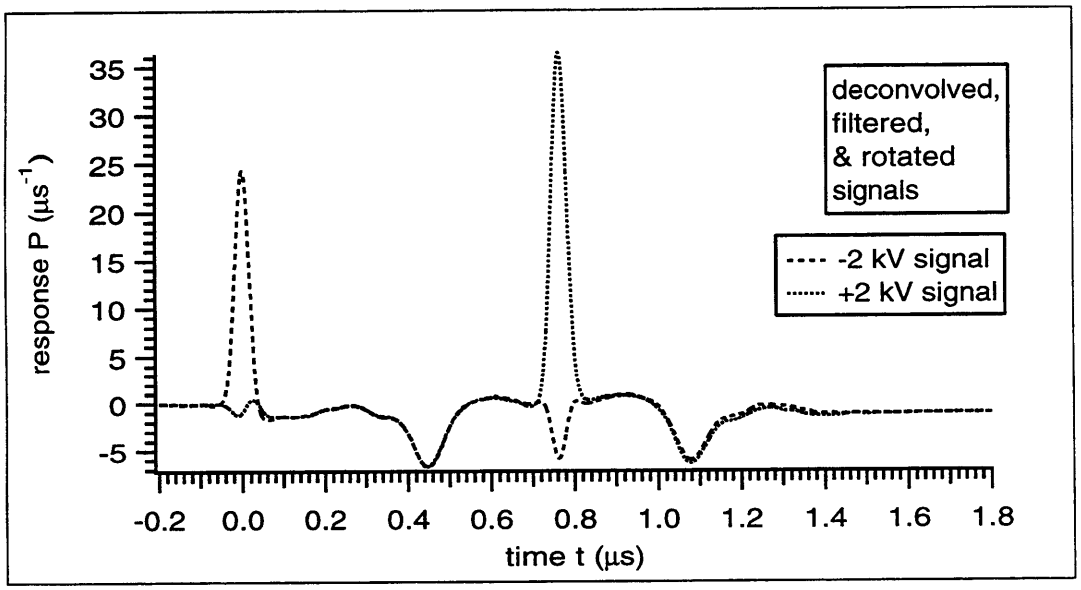

Figure 9.20: The same two signals as those depicted in figure 9.17 after deconvolving, $f_c = 33$ MHz BLG filtering, and a rotation of 0.2 μs. Deconvolution performed with respect to the negative of the EP proximal pulse depicted in figure 9.1.

9.2.8 Comparing Bulk Charge Recoveries

Returning to the V_o = +2 kV and V_o = -2 kV charge waveform recoveries depicted in figure 9.18, it seems clear that these waveforms agree in the bulk region (from, say, z = 0.15 to 1.95 mm) and disagree in the proximal and distal plate regions (from, say, z = -0.15 to 0.15 mm and z = 1.95 to 2.3 mm, respectively).

It should be evident from the discussion in the previous sections that the disagreement in the plate regions is due to the fact that the differing voltage bias conditions ($V_o = \pm 2$ kV) actually give rise to differing amounts of surface charge at the plates. The agreement of these waveforms in the bulk regions should come as no surprise – the discussion of figure 9.20 pointed out that the portion (between, say, 0.2 and 0.6 μs) of these signals which correspond to the bulk charges are almost identical.

But still, it is worth pointing out that the recovered qauntity of bulk charge seems not to depend upon the voltage bias conditions. Figures 9.21 and 9.22 depict the results of a more stringent test of the Lyons recovery method as applied to experimentally measured PESAW signals. These figures depict the recoveries gleaned from all eight of the PESAW signals gleaned from the double-sided E-beam experiment.

Figure 9.21 depicts the these recoveries for the range z = -0.3 to 2.43 mm. Figure 9.22 is a close-up of figure 9.21; figure 9.22 depicts the these recoveries for the range z = 0.15 to 1.95 mm. Figure 9.21 includes the plate charge recoveries; figure 9.21 does not. Preference was given to the EP configuration; the ED recoveries were 'reversed' (via $z = l - z'$; see page 165) so they could be compared directly with the EP recoveries.

There are two sources for the large deviations in the plate recoveries evident in figure 9.21. First, recoveries corresponding to various values of V_o were plotted together. Therefore, the actual amount of surface charge on each plate varies between recoveries corresponding to various values of V_o. Second, the distal plate (which has a relationship to the side of the sample through which the bombarding electrons entered which depends on whether the sample was mounted in the EP or the ED configuration) is always $\cong$ 2 times too large owing to the previously-discussed assumptions *re* acoustic impedence mismatches at the capacitor plates.

That is, the $z \cong l$ values for the solid lines (EP configuration) are known to be about twice as large as they should be, and the $z \cong 0$ values for the dotted lines (ED configuration) are known to be about twice as large as they should be. The agreement between waveforms plotted in figure 9.22 (which does not include the plate charge recoveries) amounts to a confirmation of the Lyons recovery as applied to measured PESAW signals – the recoveries for both configurations (EP and ED) and all three values of V_o (V_o = -2 kV, 0 kV, and +2 kV) agree as to the size and shape of the charge distribution within the bulk of the dielectric.

That is, all eight recoveries agree that bombarding a sample of PMMA with $\sim$ 0.35 MeV electrons, and then allowing the embedded electrons to 'settle' for $\sim$ 25 days, results in a charge distribution dominated by a negative pulse which has a peak value occuring at z = 1.23 mm (*ie*: 1.23 mm from the plane of entry of the bombarding electrons) and which has a width (FWHM) $\cong$ 0.26 mm.

The eight recoveries also agree on some of the finer details of the structure of the charge waveform embedded within this irradiated sample, *eg*: there is a region of positive charge between, say, 1.55 and 1.8 mm from the point of entry. Further, all eight recoveries roughly agree on the scale of the embedded charge waveform – the peak value of the charge waveform is $\cong$ -13.6 $\pm$ 0.6 nC/(cm^2 mm).

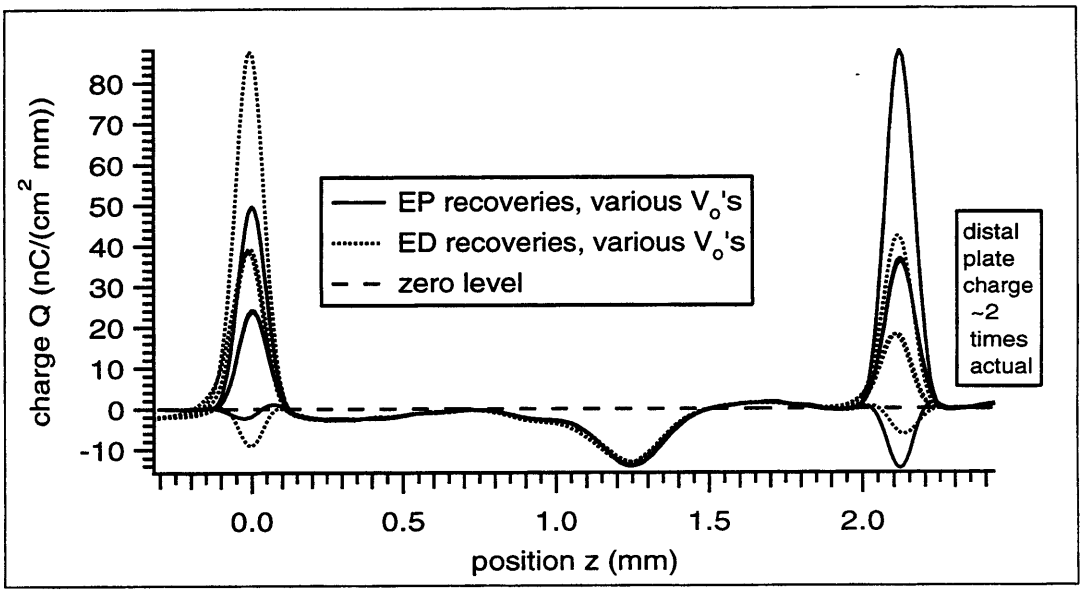

Figure 9.21: Recovered charge distributions corresponding to the eight PESAW bulk signals. Solid lines correspond to signals acquired with the sample mounted in the EP configuration; dotted lines correspond to signals acquired with the sample mounted in the ED configuration.

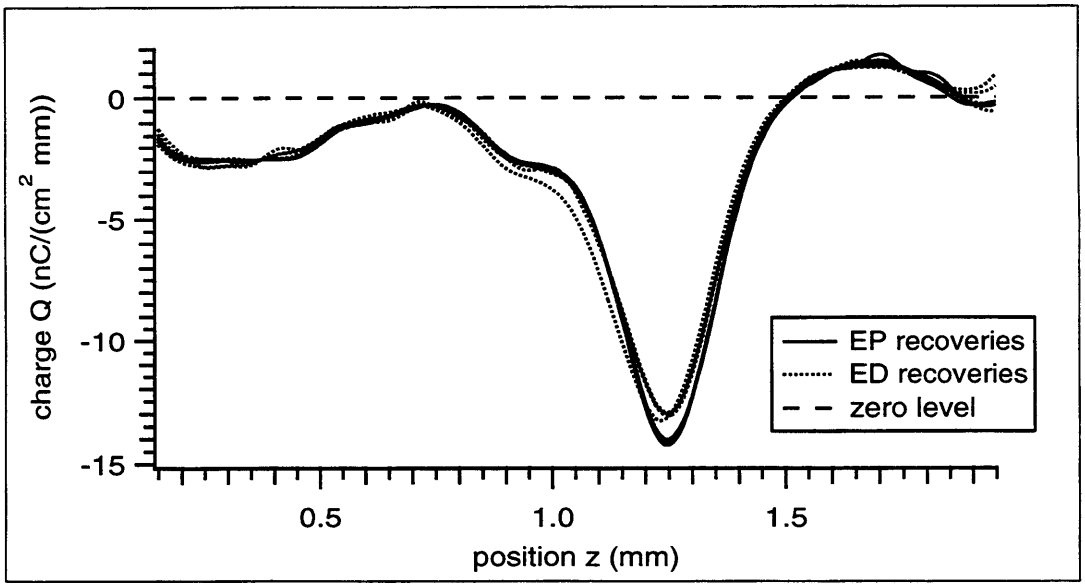

Figure 9.22: Closeup of of figure 9.21 corresponding to the bulk charge portion of these recoveries.

9.3 The Calibration Experiment

The Double-Sided E-beam Experiment focussed on a relatively thin (l = 2.121 mm), relatively low loss (m = 0.011 Np/(mm MHz)) sample of polymethylmethacrylate (PMMA). *The Calibration Experiment* focusses on a relatively thick (l = 6.27 mm), relatively high loss (m = 0.075 Np/(mm MHz), as will be shown) sample of polyethylene (PE).

The Double-Sided E-beam Experiment confirmed the efficacy of the Lyons recovery to the PESAW recovery of bulk charges situated relatively close to the receiving transducer by showing that recoveries gleaned with the transducer placed on each of the two opposing sides of the relatively thin sample agreed with each other.

It would be good if the double-sided E-beam experiment could be repeated for this thicker, lossier sample. Unfortunately, this was not possible. The data associated with the double-sided E-beam experiment takes significant time and care to acquire, and no such data is currently available. *The Calibration Experiment* therefore attempts to confirm the efficacy of the Lyons recovery to thicker, lossier samples by attempting a plate charge recovery of this sample of PE.

The argument is that, except for the apparent doubling of the distal plate charge caused by the acoustic impedence mismatch at the distal plate, plate charges behave like bulk charges (section 4.3 supports this argument mathematically, given certain assumptions *re* experimental conditions which are valid here).

Figure 9.23 depicts the raw measured (calibration) signal analyzed in this section. This data's sampling time step Δt = 2 ns. The proximal pulse $V_p(t)$ is defined by the values plotted between time $t = 0$ and time $t = t_p$. The end of the calibration signal is indicated by t_d. The BLG filter was used in the time domain to gracefully relax the non-zero value which terminates the proximal pulse down to zero over a duration of 2 μs.

The calibration signal was gracefully relaxed in the same manner. In each case, zeros were added to the end of the relaxed signal so that the total number of samples N_t = 8192. The distal pulse $V_d(t)$ was calculated via page 71's equation (4.23), which yields:

$$V_d(t) = \frac{1}{2} H_e(t) * H(l,t) = \frac{1}{2}[V_c(t) - V_p(t)] \tag{9.34}$$

where

$$H_e(t) = -V_p(t) \tag{9.35}$$

Comparing the calibration signal depicted in figure 9.23 with either of the calibration signals depicted in figure 9.1, it is clear that loss and dispersion had a greater effect upon the pressure waves which traversed the thicker sample.

In figure 9.1, the proximal and distal pulses have similar shapes and widths. In figure 9.23 the distal pulse is significantly thicker, and has significantly less structure (*eg*: fewer inflections), than the proximal pulse. More quantitatively, in figure 9.23 the ratio of the widths (FWHM, distal/proximal) is 4.36 whereas in figure 9.1 this ratio is less than 1.1. It should now be clear that this section's data poses a significantly greater challenge, in terms of the need to 'undo' the effects of attenuation and dispersion, than did the previous section's data.

9.3.1 Inverse Medium Solution

The parameters selected to describe this $l = 6.27$ mm slab of polyethylene (PE) are given in table 9.2. This model was chosen via analysis of the proximal and distal pulses in the manner described briefly in the previous section, and in more detail in chapter 4. Figures 9.24, 9.25, and 9.26 confirm this model by comparing measured and theoretic values of, respectively, the distal pulse $V_d[t_n]$, the attenuation coefficient $\alpha[f_k]$, and the phase velocity $c[f_k]$.

m	=	0.075	Np/(mm MHz)
$c(f_o)$	=	1.9528	mm/μs
f_o	=	1	MHz
b	=	0	Np/mm

Table 9.2: Polymeric model selected to describe the slab of polyethylene analyzed in *The Calibration Experiment.*

The measured and theoretic values for the attenuation coefficient agree well for frequencies between, say, 0 and 8 MHz. Measured and theoretic values of the phase velocity agree well between, say, 4 and 10 MHz. The measured and theoretic values for the distal pulse agree well overall, but there is some deviation evident between, say, 4.1 to 4.5 μs. In this range the theoretic values do follow the overall shape of the measured values, but fail to reach the same positive and negative extrema.

The agreement between theoretic and measured values is not as good as the agreement observed in *The Double-Sided E-beam Experiment.* However, experience suggests that the model selected is about as good as this thesis' hysteresis absorption/NLKK model for polymers allows: the author found that varying any of the four parameters from their given values gave worse results than those presented. This model will therefore be taken as the inverse medium solution for this slab of PE.

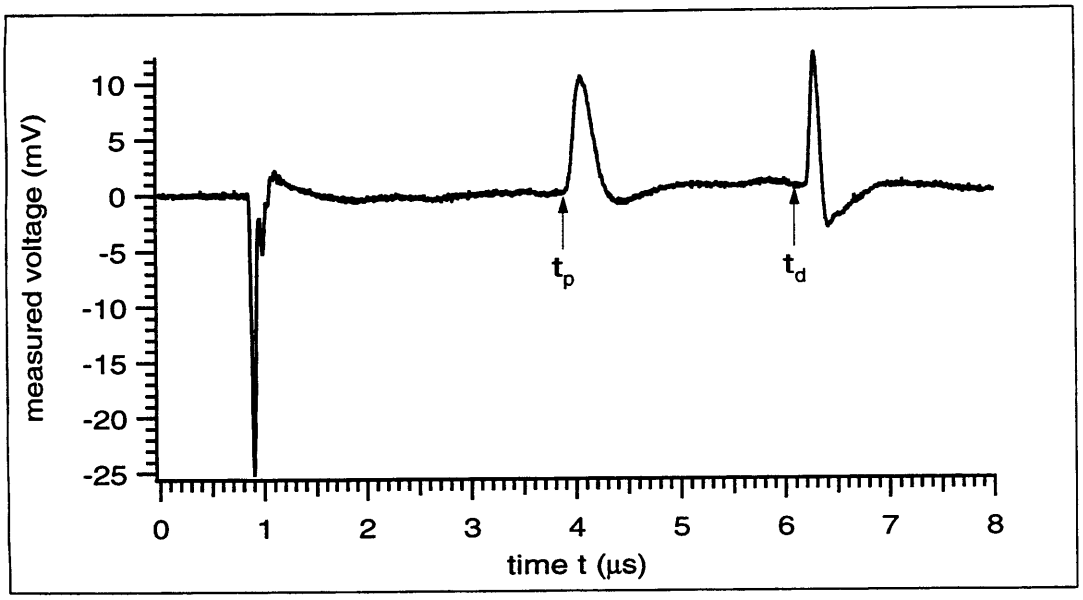

Figure 9.23: The raw measured PESAW calibration signal analyzed throughout *The Calibration Experiment.*

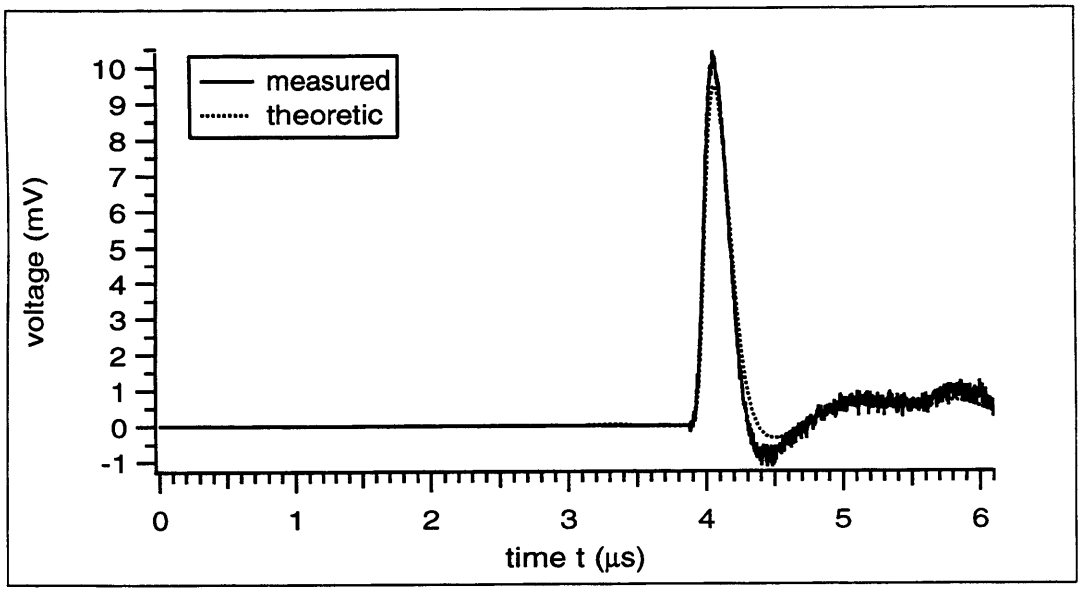

Figure 9.24: Comparison of measured and theoretic values of the distal pulse $V_d[t_n]$.

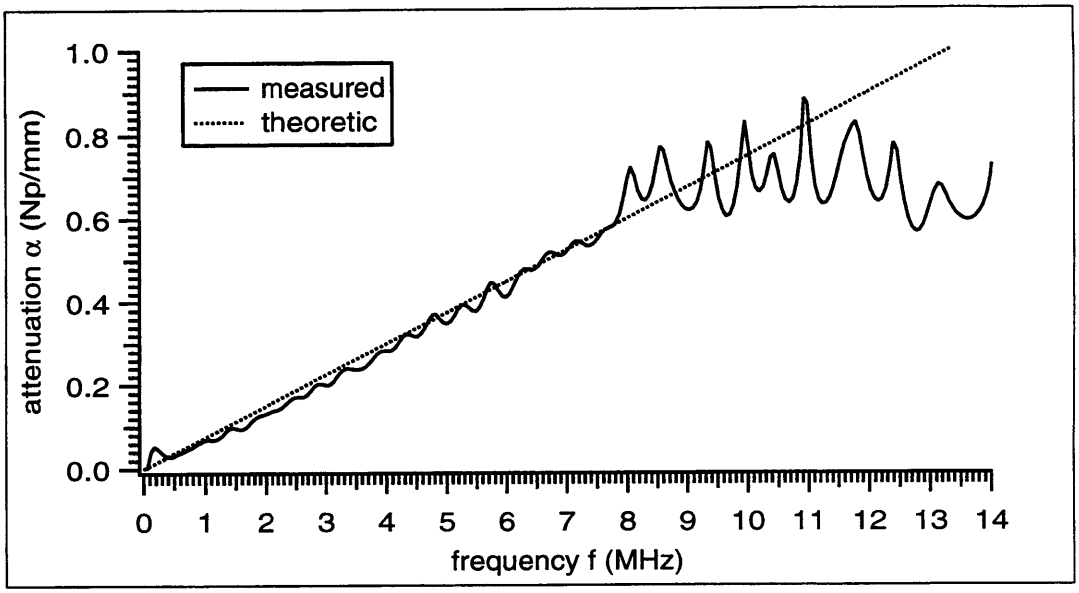

Figure 9.25: Comparison of measured and theoretic values of the attentuation coefficient $\alpha[f_k]$.

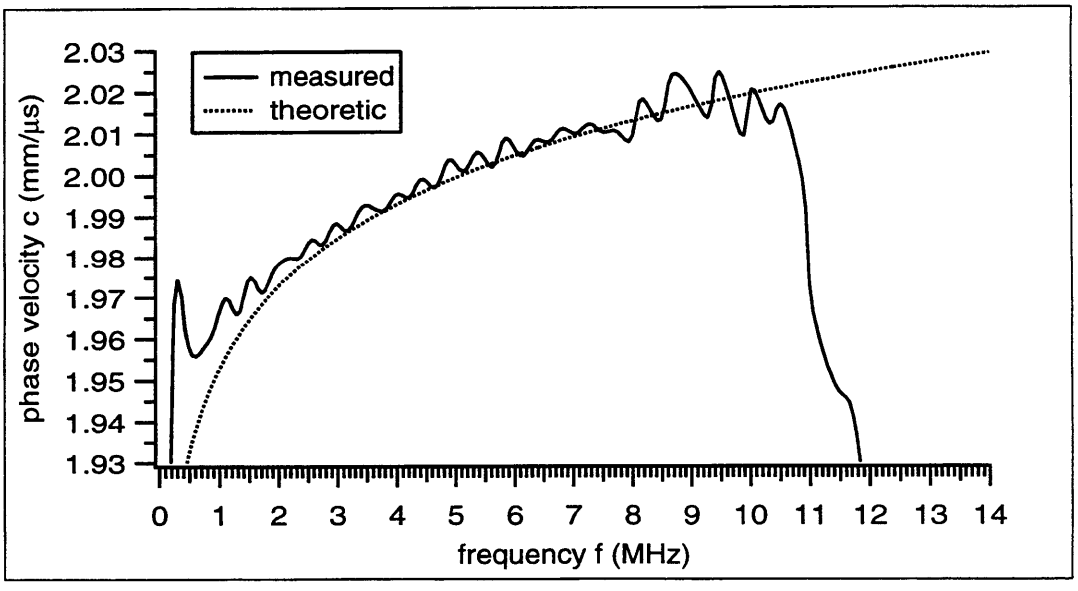

Figure 9.26: Comparison of measured and theoretic values of the phase velocity $c[f_k]$.

9.3.2 Inverse Source Solution

Pages 204 through 207 contain eight plots; two plots per page. At the top of each of these pages is a raw Lyons-recovered waveform corresponding to the raw PESAW signal depicted in figure 9.23. Each recovery corresponds to a different value of the SIB cutoff frequency f_c. In order of appearance, those values of f_c are: 10, 15, 20, and 25 MHz. At the bottom of each page is the indefinite integral of the recovery above it. The recovery was calculated at a set of z_i's ranging from z = -0.5 to 7 mm; the spatial sampling step $\Delta z = 2$ μm.

Excepting the distal pulse recovery depicted on the last ($f_c = 25$ MHz) page, all the recovered proximal and distal plate recoveries are well resolved pulses which can be assigned a meaningful width (FWHM) and position (location of extremum value, calculated to the nearest μm via a unique quadratic fit to the extremal point and the two points surrounding it).

The value of each plate recovery's width is shown on the plot depicting that recovery. The recovered proximal pulse positions are, in order of appearance (*ie*: in order of increasing f_c), z = 0.000, 0.001, 0.001, and 0.001 mm. The recovered distal pulse positions are, in the same order, z = 6.266, 6.271, 6.274, and ? mm (the '?' reflects the fact that the $f_c = 25$ MHz distal pulse was not resolvable). That is, the positions of all the resolvable recovered pulses were correct to within (usually well within) $\pm$ 4 μm.

In general, the position of the proximal pulses was more accurately recovered than the position of the distal pulses: the RMS deviation from the expected position (z = 0) of the four proximal plate recoveries was less than 1 μm. The RMS deviation from the expected position (z = 6.27 mm) of the three resolvable distal plate recoveries was 3.3 μm.

Of the three recoveries (f_c = 10, 15, and 20 MHz) which had resolvable proximal *and* distal plate recoveries, all but one (the $f_c = 10$ MHz recovery) resolved the proximal plate better than the distal plate (*ie*: the pulse corresponding to the proximal plate recovery had a smaller FWHM than did the pulse corresponding to the distal plate recovery). The $f_c = 10$ MHz recovery resolved the distal plate better than the proximal plate, but not by much: the ratio (proximal/distal) of FWHM's is $\cong$ 1.01.

The resolving power (*ie*: the 'smallness' of the recovered FWHM) clearly increased with f_c. Focussing first upon the proximal plate recoveries, the recovered FWHM's are (in order of appearance, which corresponds to increasing f_c): 0.267, 0.180, 0.135, and 0.109 mm. The corresponding sequence for the distal plate recoveries is: 0.264, 0.185, 0.161, and ? mm (where, as before, the '?' reflects the fact that the $f_c = 25$ MHz distal pulse was not resolvable). In each case (proximal and distal), the resolving power increased with f_c.

Figure 9.33 (which corresponds to $f_c = 25$ MHz SIB filtering) clearly illustrates the need for SDB filtering (rather than SIB filtering) in the case where maximum resolution of shallow charges is desired in a thick, lossy sample. At $f_c = 25$ MHz, the proximal pulse is well resolved whereas the relatively large value of f_c has included more of

the relatively noisier high frequency data than the Lyons recovery of the distal plate can 'manage' (the decrease in the signal-to-noise ratio with f is evidenced by figure 9.25, which shows the increasingly erratic behavior of the measured $\alpha(f)$ as f increases above, say, 8 MHz).

The Lyons recovery's inability to resolve the distal plate when $f_c > 20$ MHz is almost certainly due to the fact that the Lyons recovery of deeper charges utilizes a higher degree of amplification than does the Lyons recovery of shallower charges. To see this, note that the Lyons recovery (9.9) can be re-written by expanding $\underline{\mathcal{K}}(f)$ into its real and imaginary parts (see page 172's equation (9.10)):

$$\mathrm{R}(z) = \Delta f \sum_{f_k} |\underline{\mathcal{P}}[f_k]|\, \mathrm{B}(f_c(z), f_k)\, \overbrace{\exp(z\,\alpha(f_k))}^{\text{amplification}}$$

$$\cdot \frac{\mathrm{two}[f_k]}{|\underline{C}_g(f_k)|} \cos\left(z\, 2\pi f_k / c(f_k) + \langle \underline{\mathcal{P}}[f_k] \rangle - \langle \underline{C}_g(f_k) \rangle\right) \qquad (9.36)$$

where, *eg*, $\langle \underline{\mathcal{P}}[f_k] \rangle$ yields the phase of $\underline{\mathcal{P}}[f_k]$.

Inspecting equation (9.36), it is clear that the spatially-dependent degree of amplification (the $\exp(z\ \alpha(f_k))$ term) increases with z for some f_k if $\alpha(f_k) > 0$. Lossy materials generally have $\alpha(f) > 0$ independent of f, so the the degree of amplification used by the Lyons recovery in a lossy material will generally increase with z.

Further, materials (such as the one under discussion, for which $\alpha(f) = m\ f$) which have an attenuation coefficient that increases with frequency require the Lyons recovery to employ an increase in amplification with z that increases with f!

If the signal-to-noise ratio decreases with f (and if f_c is not small enough to prevent it) then the Lyons recovery of deeper sources will over-amplify the noise extant at these higher frequencies. This is almost certainly the reason that, when $f_c(z)$ is constant (*ie*: when SIB filtering is in effect), the Lyons recovery of the distal plate 'breaks up' before the proximal plate recovery breaks up.

Incidentally, this same effect is described in section 7.10. However, in that section, the increase in noise with frequency was (presumably) due mostly to the high-frequency inaccuracy (see page 80) of the FFT as an approximation to the Fourier transform. In the current situation, the increase in noise with frequency is presumably due mostly to weaknesses inherent to the data itself.

As mentioned previously, each of the four plots on the bottom of pages 204 through 207 depicts the indefinite integral of the raw waveform recovery above it. These plots were included to show that the Lyons recovery delivers raw source waveform recoveries with localized area that is only weakly dependent upon f_c: the first three indefinite integrals (corresponding to f_c = 10, 15, and 20 MHz) clearly show that, regardless of the f_c-dependent width of the recovered pulses, the recovered area of the proximal pulse is $\cong$ -1 whereas the recovered area of the distal pulse is $\cong$ 2.

Even more remarkably: figure 9.34 shows that, even in the case of an unresolved Lyons recovered pulse (*ie*: the unresolved distal pulse depicted in figure 9.33), the unresolved pulse is still possessed of an approximately correct area. Speaking colloquially, it seems that the Lyons recovery 'tries to do the right thing' (in terms of mapping localized areas from time to space) even in some of those cases where it appears to be dominated by noise.

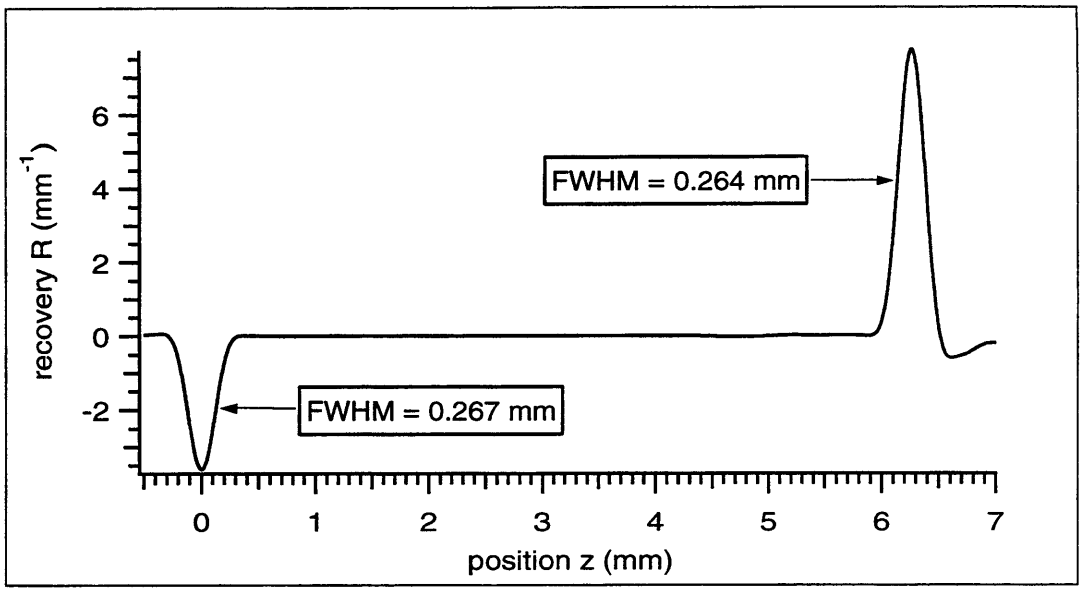

Figure 9.27: $f_c = 10$ MHz SIB recovery from *The Calibration Experiment.*

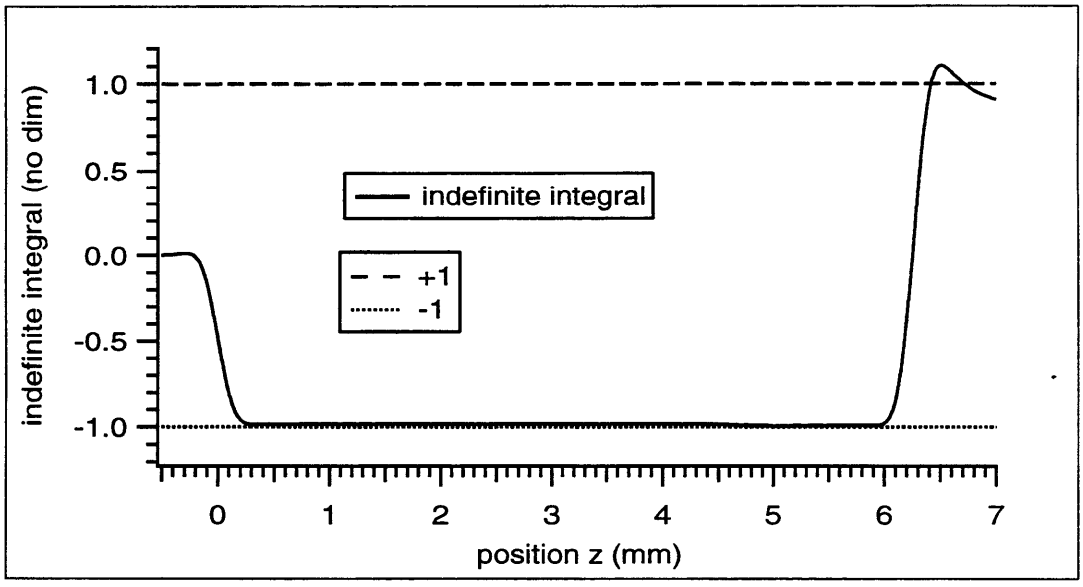

Figure 9.28: Indefinite integral of the $f_c = 10$ MHz SIB recovery from *The Calibration Experiment.*

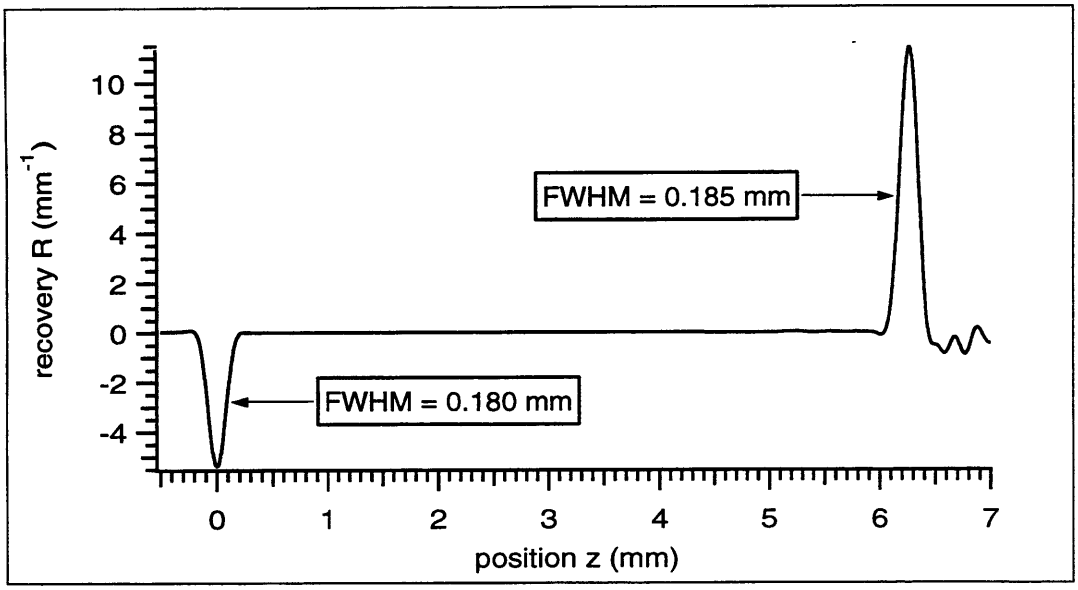

Figure 9.29: $f_c = 15$ MHz SIB recovery from *The Calibration Experiment.*

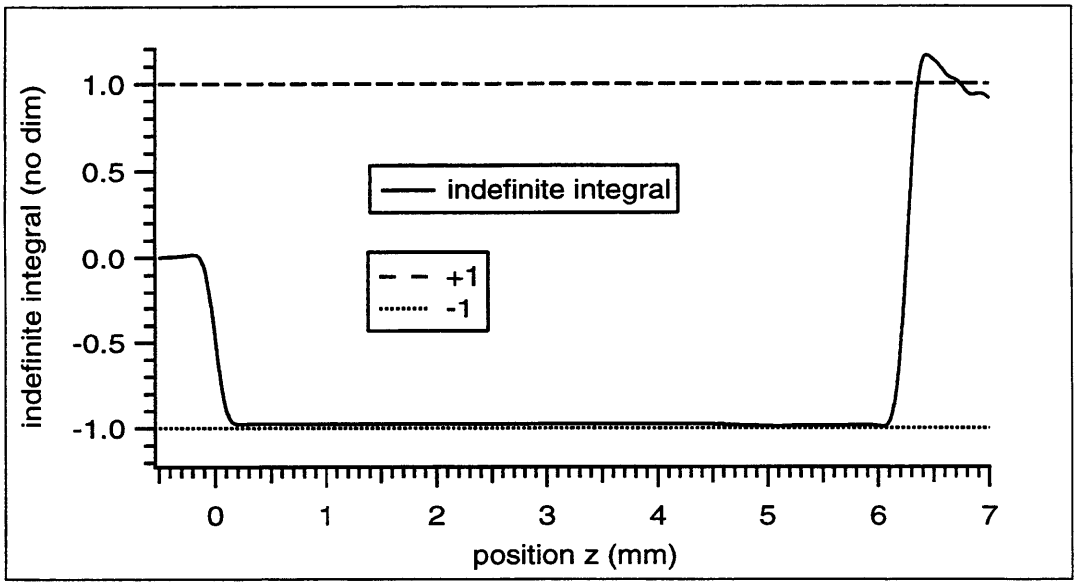

Figure 9.30: Indefinite integral of the $f_c = 15$ MHz SIB recovery from *The Calibration Experiment.*

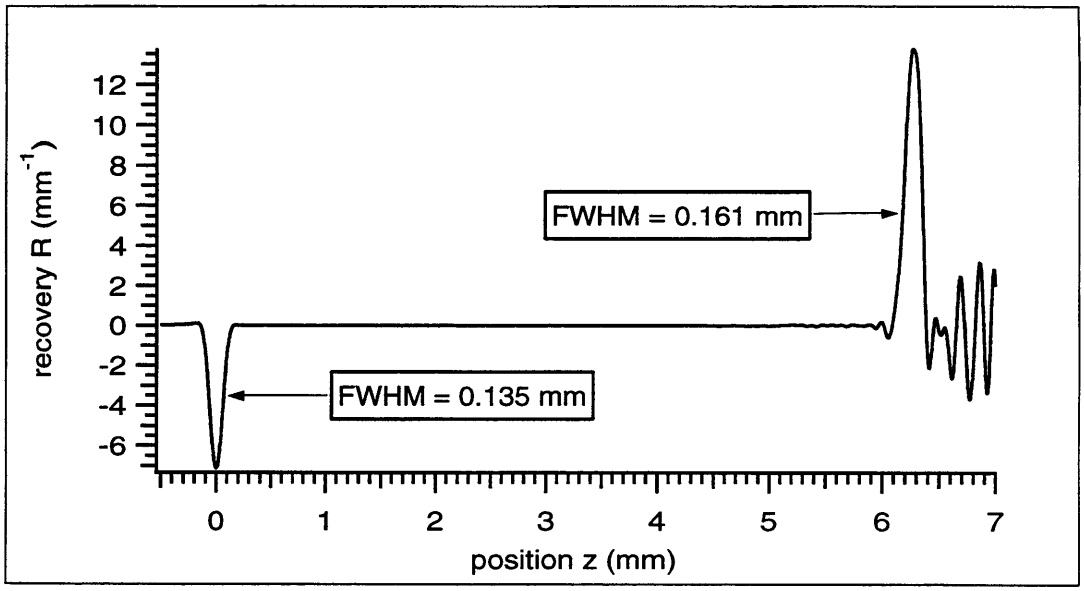

Figure 9.31: $f_c = 20$ MHz SIB recovery from *The Calibration Experiment.*

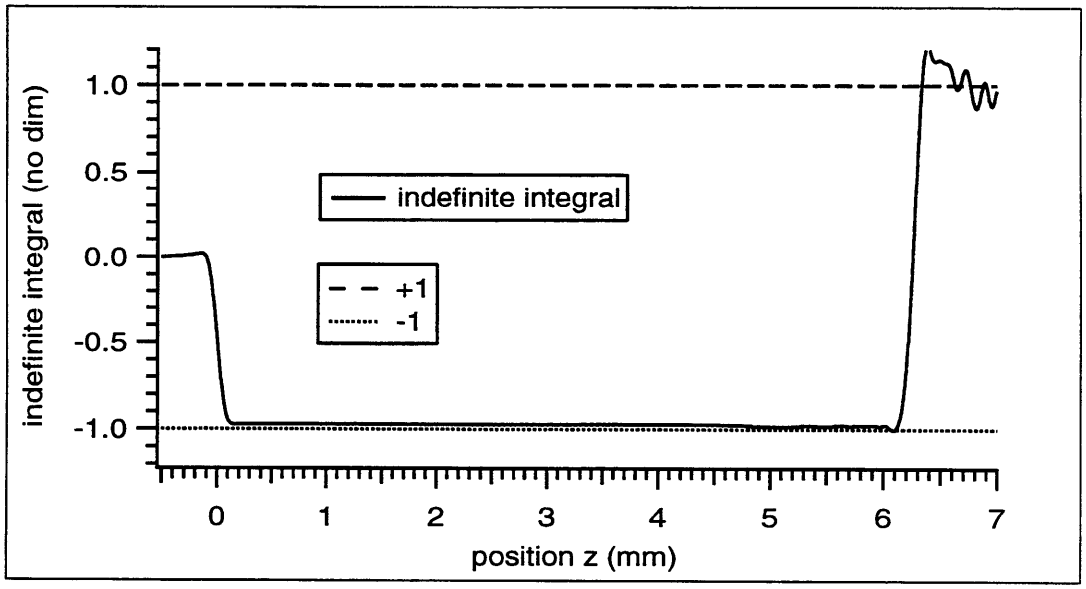

Figure 9.32: Indefinite integral of the $f_c = 20$ MHz SIB recovery from *The Calibration Experiment.*

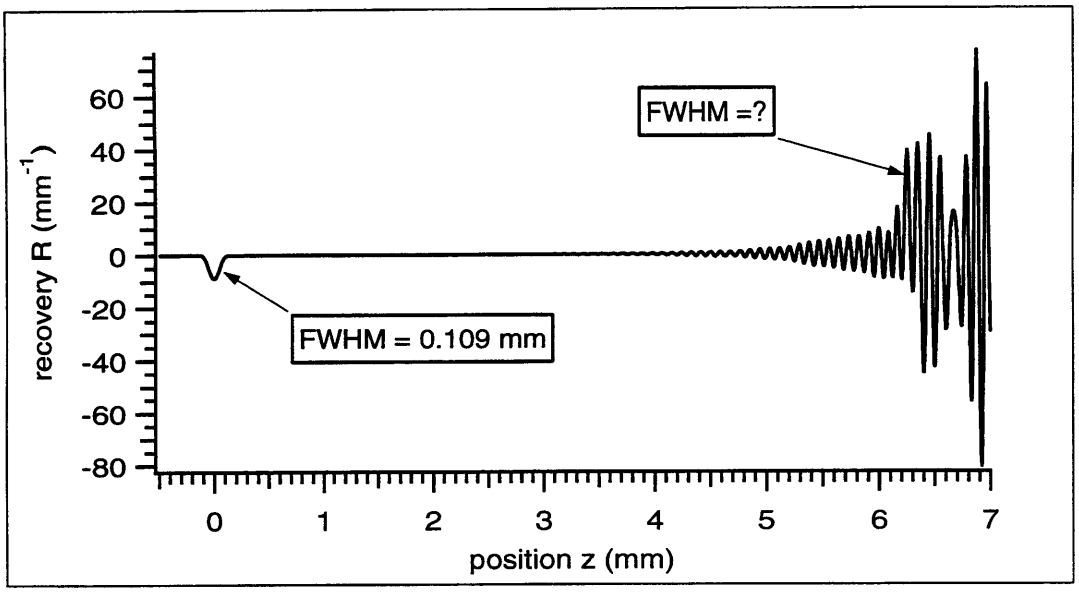

Figure 9.33: $f_c = 25$ MHz SIB recovery from *The Calibration Experiment.*

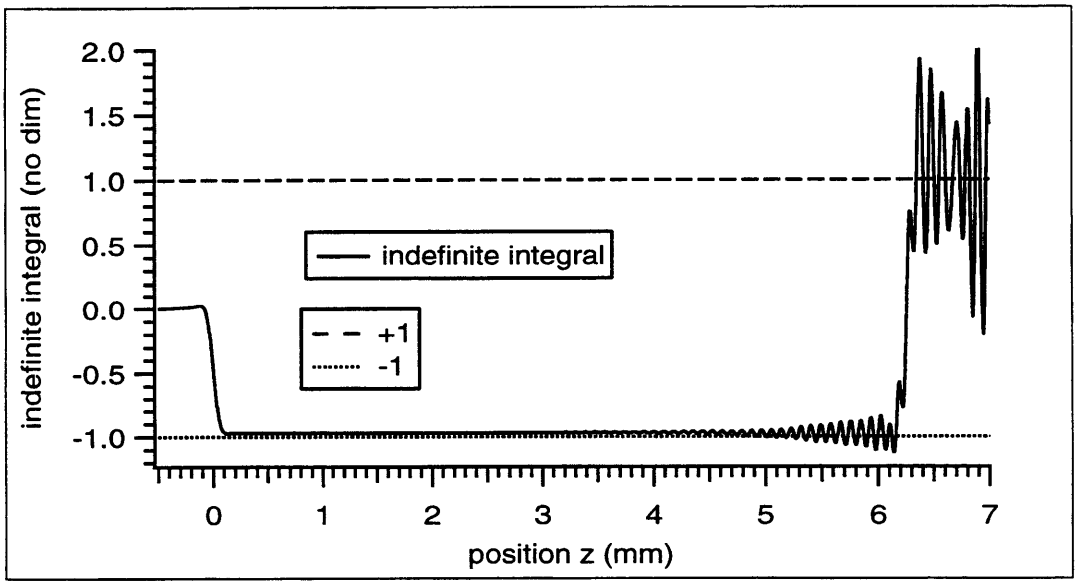

Figure 9.34: Indefinite integral of the $f_c = 25$ MHz SIB recovery from *The Calibration Experiment.*

9.3.3 Voltage Waveform Verification

Somewhat arbitrarily choosing the $f_c = 15$ MHz SIB raw source waveform recovery depicted in figure 9.29 as the best SIB recovery, only the un-normalization coefficient ν is required to determine the charge waveform recovery. To calculate the value of ν corresponding to that given by equation (9.32), it is necessary to know that

I. for PE, $\epsilon \cong 2.3\epsilon_o$

II. the calibration signal depicted in figure 9.23 was collected with the DC component V_o of the applied voltage $V_a(t)$ equal to 10 kV

III. the thickness l of this sample of PE is 6.27 mm

IV. the raw localized area (between $z = \pm$ 0.3 mm) associated with the $f_c = 15$ MHz proximal pulse recovery = -0.986

The result is:

$$\nu = \frac{2.3\ [0.8854 \frac{\text{nC}}{\text{cm}^2} / \frac{\text{kV}}{\text{mm}}]\ 10\ \text{kV}}{(0.986)\ 6.27\ \text{mm}} = 3.29\ \frac{\text{nC}}{\text{cm}^2} \tag{9.37}$$

Figures 9.35 and 9.36 compare, respectively, the recovered charge and voltage waveforms associated with the Lyons, and with the dominant, recoveries.

Please recall that the voltage waveform is determined from the charge waveform via the scaled double integration indicated by page 167's equation (9.8), and that the dominant recovery (see page 14's equation (1.2), page 51's equation (2.55), and page 52's equation (2.61)) is given by

$$\mathrm{R}_d(z) = \frac{1}{c_d} \mathcal{P}(\frac{z}{c_d}) \tag{9.38}$$

$$= \frac{1}{c_d} \int_{-\infty}^{\infty} \underline{\mathcal{P}}(f)\ \exp(\mathrm{j}\ 2\pi f z / c_d)\ df \tag{9.39}$$

where c_d is the assumed-frequency-independent phase velocity of pressure waves propagating through an assumed-lossless material.

With the inclusion of BLG filtering, the frequency-domain-based dominant recovery (9.39) becomes

$$\mathrm{R}_d(z) = \frac{1}{c_d} \int_{-\infty}^{\infty} \underline{\mathcal{P}}(f)\ \mathrm{B}(f_c, f) \exp(\mathrm{j}\ 2\pi f z / c_d)\ df \tag{9.40}$$

The value of c_d used was determined by $f_c = 15$ MHz BLG filtering the deconvolved signal derived from the signal depicted in figure 9.23, then dividing the length of the sample (6.27 mm) by the time separating the extremal values of the portions of the deconvolved, filtered signal associated with the proximal and distal pulses (3.150 μs). The result $c_d = 1.990$ mm/μs is designed to locate the peak of the recovered distal pulse at $z = l$.

The $f_c = 15$ MHz dominant recovery presented in figure 9.35 was calculated in the frequency domain (9.40) and, because the localized area of the this recovery's proximal plate pulse was -0.9995 (rather than the Lyons recovery's corresponding value -0.986), the value of ν used for the dominant recovery was 3.24 nC/cm^2 rather than the 3.29 nC/cm^2 value used for the Lyons recovery.

Figure 9.36 shows that the voltage boundary condition is very nearly satisfied by both the dominant and the Lyons recoveries. In terms of the recovered voltage at $z = l$, the dominant recovery betters the Lyons recovery: the value of the recovered voltage at the distal plate position $z = 6.27$ mm is 9.568 kV for the Lyons recovery (4.3% less than the expected value of 10 kV) whereas the corresponding voltage associated with the dominant recovery is 9.898 kV (only 1% less than the expected value).

Before concluding that the dominant recovery of the desired charge waveform is inherently superior to the Lyons recovery, please recall that a relatively small DC change in the measured PESAW signal (or in the recovered waveform itself) will result in a relatively large change in the recovered voltage at $z = l$. Similarly, by the linearity of the charge-to-voltage mapping, a mere 4.3% change in the value of ν used in the Lyons recovery (or a 1% change in the value of ν used in the dominant recovery) would yield the correct voltage at $z = l$. That is, the deviation of the $z = l$ value of the recovered voltage waveform from the expected value is not a robust measure of the accuracy of a recovery (it is included only to allow a 'ballpark' check of the validity of some recovery).

Figures such as those depicted on page 212 yield a more robust means to compare the efficacy of these two recoveries. On that page, figure 9.37 depicts the the raw Lyons recovered source waveform with the raw source waveform produced by the dominant recovery; figure 9.38 depicts the indefinite integrals of the waveforms depicted in figure 9.37

Perusing page 212, it is clear that the proximal plate recoveries are nearly identical and have area $\cong$ -1. On the other hand, it is clear from these figures that (1) the Lyons recovery has resolved the distal plate pulse much better than the dominant recovery has and (2) the localized area of the Lyons-recovered distal pulse is much closer to the expected value of 2 than is the dominant recovery.

More quantitatively, the width (FWHM) of the Lyons-recovered distal pulse is 0.185 mm whereas the width of the distal pulse recovered by the dominant method is 0.397 mm – more than twice the width of the Lyons-recovered distal pulse. With the area of the distal pulse defined as the definite integral over the region $z = l \pm 0.27$ mm, the dominant-recovered area is 1.34 (33% less than the expected value of 2) whereas the Lyons recovered area is 2.1 (5% greater than the expeced value of 2).

Perhaps most importantly, it is clear from figure 9.37 that the Lyons recovery of the distal pulse is much more symmetic than the dominant recovery of the distal pulse – the dominant recovery's distal pulse has a long tail extending toward positive z whereas the Lyons recovery's does not. It should be clear from all these analyses that, as expected from chapter 8's analyses of synthetic data, the Lyons recovery yields a better overall recovery of deep charges in lossy materials than does the dominant recovery.

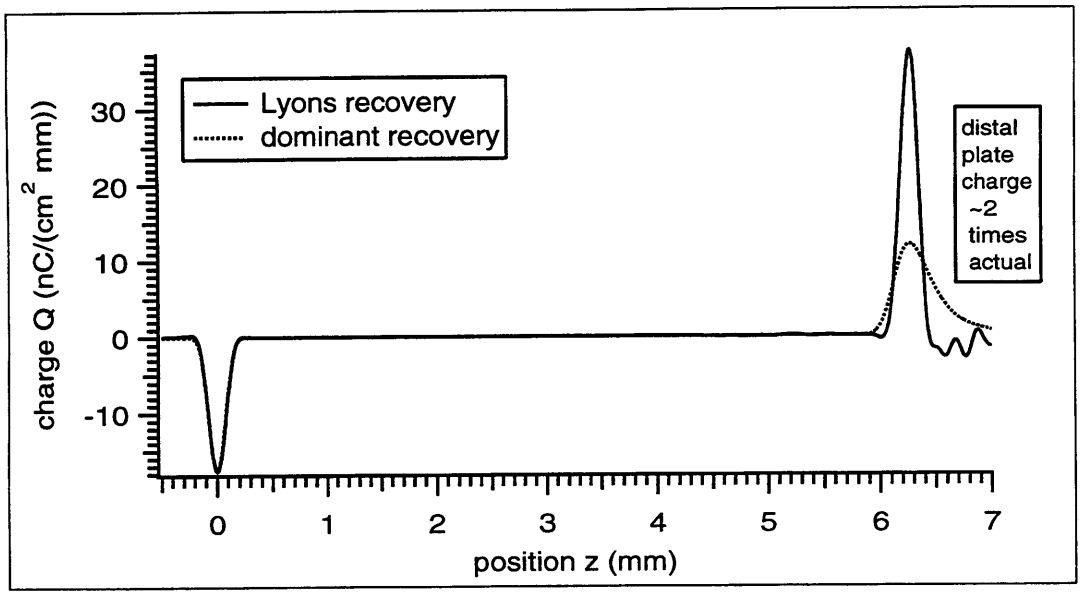

Figure 9.35: Recovered charge waveform associated with the $f_c = 15$ MHz SIB Lyons recovery.

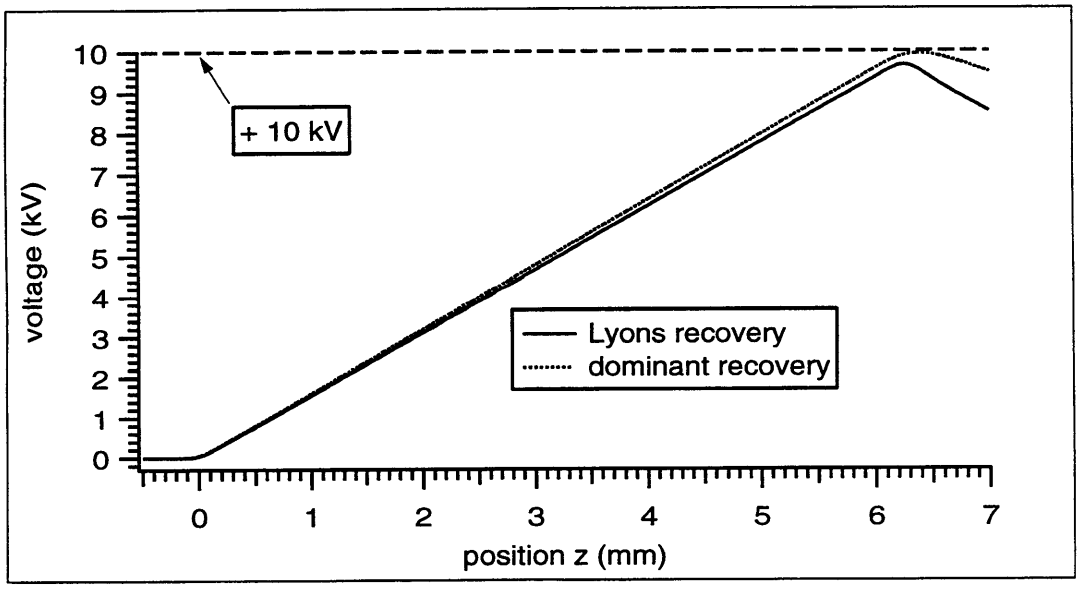

Figure 9.36: Recovered voltage waveform associated with the $f_c = 15$ MHz SIB Lyons recovery.

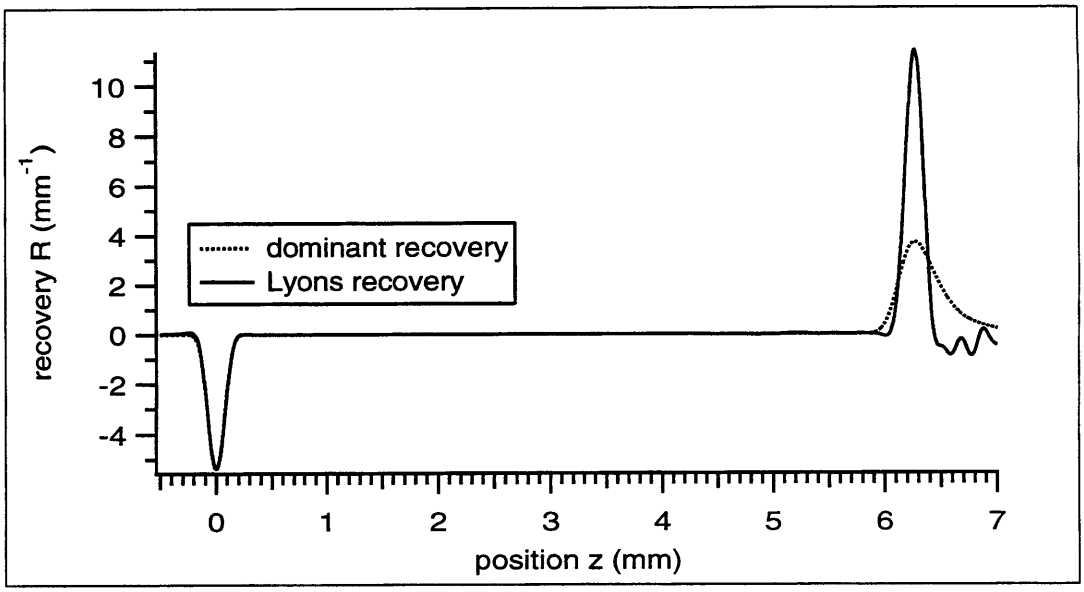

Figure 9.37: Comparison of the raw Lyons source recovery and the raw dominant source recovery.

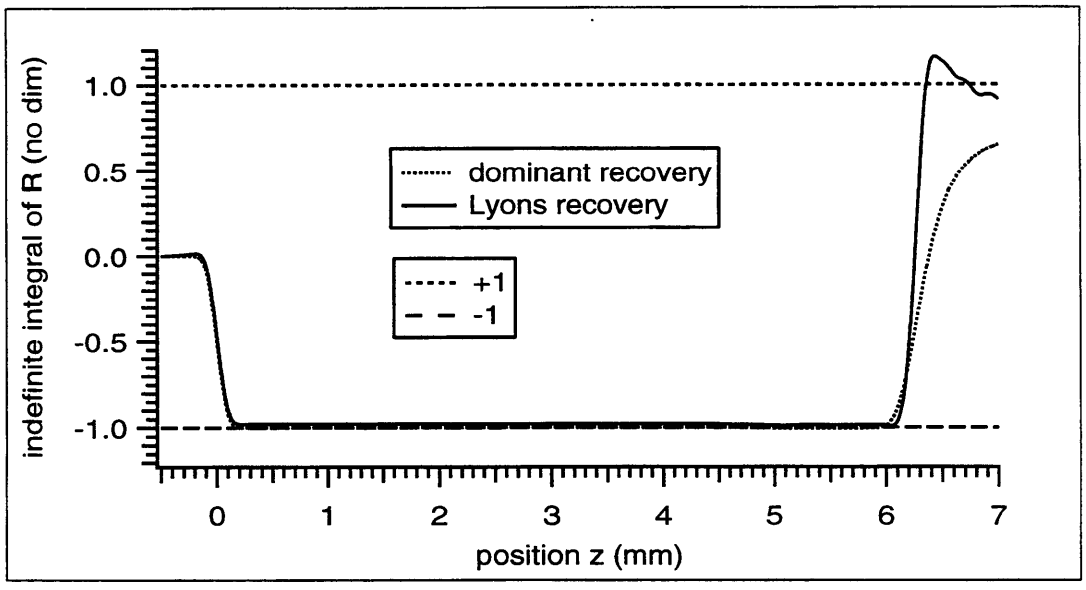

Figure 9.38: Comparison of the indefinite integrals of the raw Lyons source recovery and the raw dominant source recovery.

9.4 Overview Of The Remaining Two Experiments

At this point the general applicablity of the Lyons recovery to measured PESAW signals has been established via the analysis of the two preceeding experiments. Therefore, analyzing more experiments could arguably be dismissed as superfluous.

On the other hand, given that the motivation for this entire thesis is to establish the applicablity of the Lyons recovery to the PESAW experiment, analysis of more than two experiments seems entirely justified – the reader may not yet have gained confidence in the Lyons recovery. There are still important questions to be answered, *eg*: is the Lyons recovery applicable to PESAW signals obtained from samples containing –

- charges generated by long term exposure to DC electric fields?
- a charge dipole (closely spaced layers of charge with opposing polarity) located near the proximal plate?
- a charge dipole near the distal plate?

Seeking to reconcile these two opposing viewpoints, the author has chosen to present the results of applying the Lyons recovery to the remaining two experiments (*The DC Field Experiment* and *The Distal Dipole Experiment*) but forgo some of the exploratory analyses that can be found in the previous two sections.

The first of these latter two experiments (*The DC Field Experiment*) addresses the first two of the three questions posed above (it could be called *The DC Field and Proximal Dipole Experiment*). The second of these latter two experiments (*The Distal Dipole Experiment*) addresses the third question.

9.5 The DC Field Experiment

9.5.1 Inverse Medium Solution

The DC Field Experiment focusses on an $l = 0.983$ mm slab of polyethylene (PE) modelled via the parameters given in table 9.3. Figure 9.39 depicts the measured calibration signal from which this model was derived.

m	=	0.095	Np/(mm MHz)
$c(f_o)$	=	1.545	mm/μs
f_o	=	1	MHz
b	=	0	Np/mm

Table 9.3: Polymeric model selected to describe the slab of polyethylene analyzed in *The DC Field Experiment.*

The number of data points available in this measured calibration signal was relatively small and therefore failed to show the image (reflection) of the proximal pulse

signal which arrives after the distal pulse signal if the distal plate reflection coefficient is non-zero (this reflected signal is evident in the other experiments' measured calibration signals; see figures 9.1, 9.23, and 9.49).

It was therefore possible to show, on one graph, the measured signal *and* the 'Blackman tail' used to gracefully relax the last measured data point down to zero before zero-padding out to N_t, the power of 2 number of points chosen for the analysis.

The other experiments' calibration signals also had Blackman tails added (after t_p, when defining the operant proximal pulse; after t_d, when defining the operant calibration signal) but, for those signals, the author opted to display the raw measured signal and the two times (t_p and t_d) at which Blackman tails would be added rather than the two post-Blackman-tail-addition versions.

Figures 9.40, 9.41, and 9.42 depict, respectively, comparisons of measured and theoretic values for the distal pulse $V_d[t_n]$, the attenuation coefficient $\alpha[f_k]$, and the phase velocity $c[f_k]$. The agreement between theory and measurement evidenced by these plots is by no means perfect: the measured values for $\alpha[f_k]$ significantly exceed the theoretic values in the two frequency bands $f = \{0, 3\}$ and $\{27, 40\}$ MHz, and the measured values for $c[f_k]$ significantly exceed the theoretic values in the frequency band $f = \{0, 5\}$ MHz. Presumably relatedly, the theoretic values for the distal pulse failed to accurately track the measured values between, say, times $t = 0.92$ and 1.2 μs.

Although the agreement between theory and measurement evidenced by these three plots is by no means perfect, the author was unable to discover a more acceptable model and, so, opted to accept them as they are.

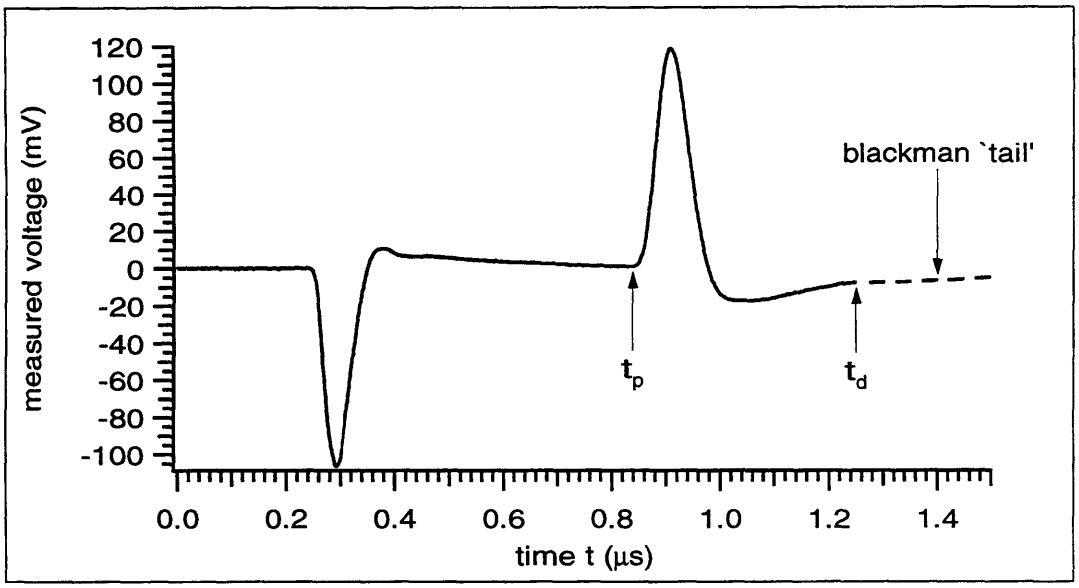

Figure 9.39: The calibration signal used in *The DC Field Experiment.*

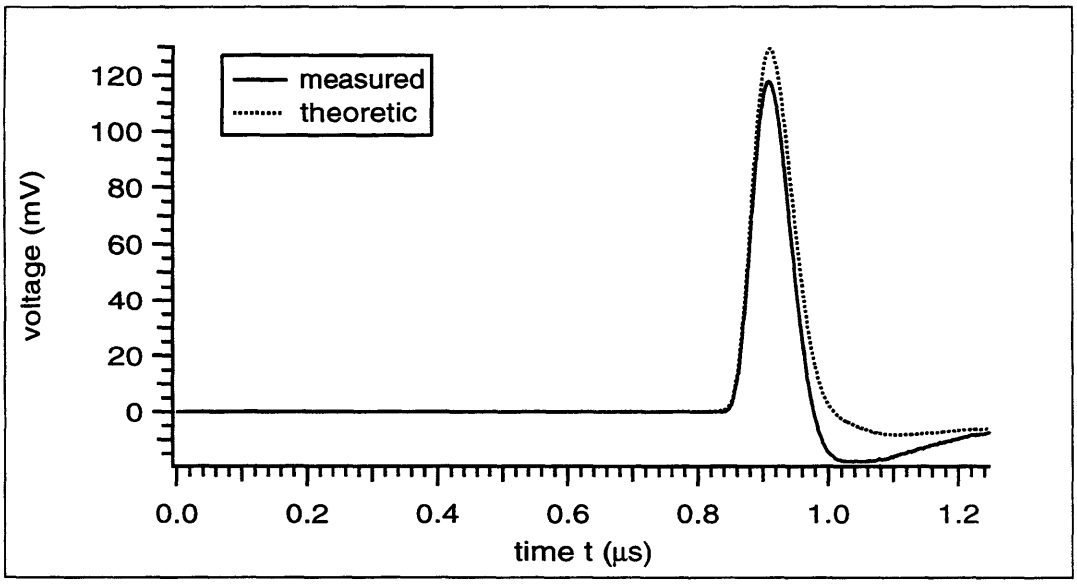

Figure 9.40: Comparison of *The DC Field Experiment*'s measured and theoretic distal pulses.

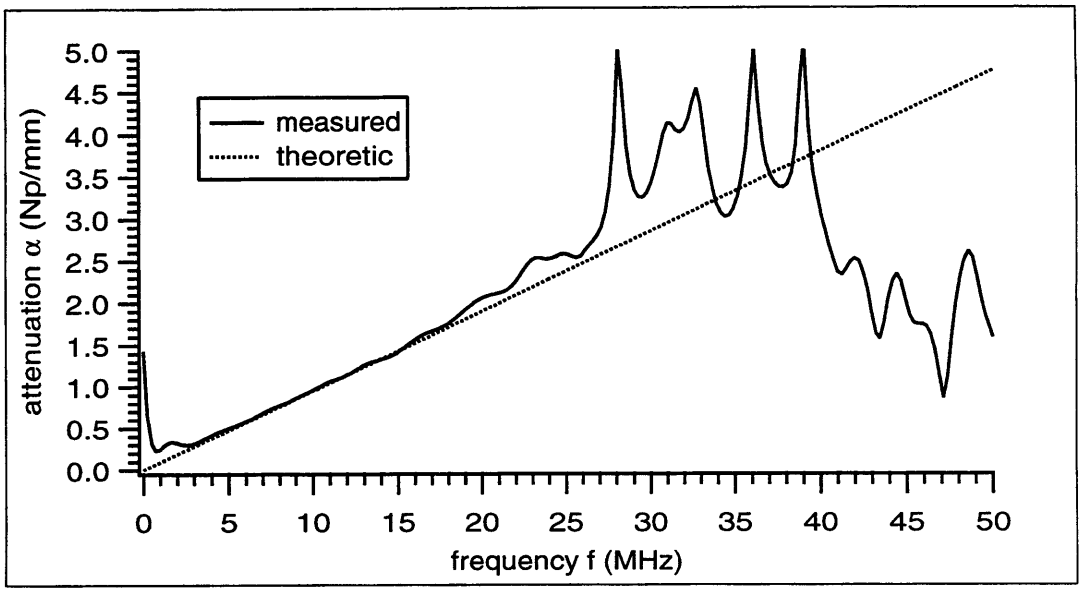

Figure 9.41: Comparison of *The DC Field Experiment*'s measured and theoretic values for the attenuation coefficient $\alpha[f_k]$.

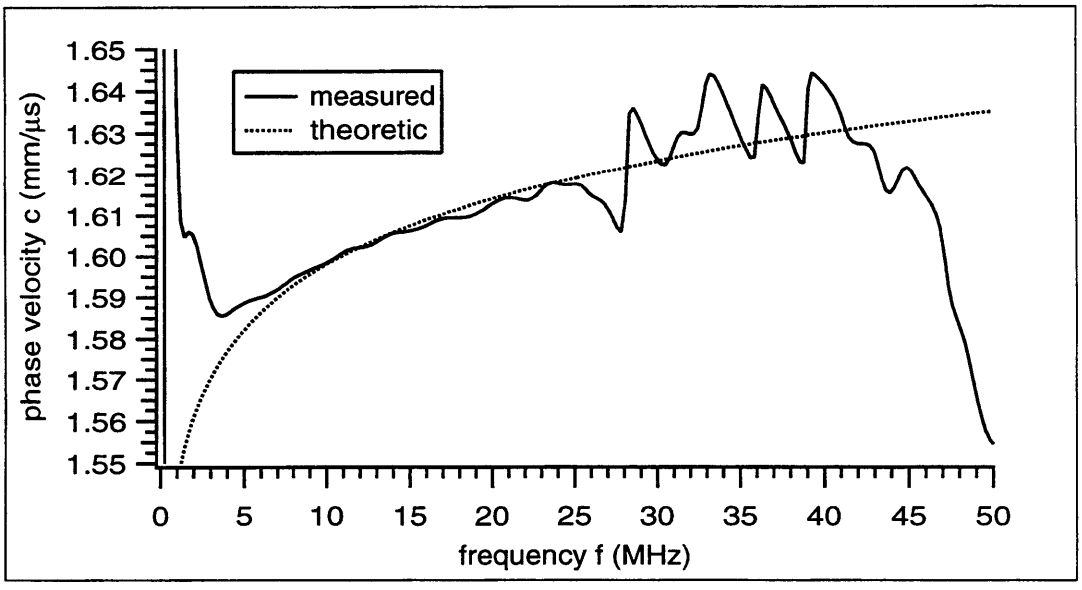

Figure 9.42: Comparison of *The DC Field Experiment*'s measured and theoretic values for the phase velocity $c[f_k]$.

9.5.2 Inverse Source Solution - Calibration Waveform

The calibration signal depicted in figure 9.39 was obtained with $V_o = 10$ kV. Applying the Lyons recovery to this calibration signal (deconvolved with respect to the negative of its proximal pulse) yields a waveform with a proximal pulse that has raw localized area of -0.994. The associated value of the un-normalization coefficient ν for this PE sample is, therefore:

$$\nu = \frac{2.3\ [0.8854 \frac{\text{nC}}{\text{cm}^2} / \frac{\text{kV}}{\text{mm}}]\ 10\ \text{kV}}{(0.994)\ 0.983\ \text{mm}} = 20.8\ \frac{\text{nC}}{\text{cm}^2} \tag{9.41}$$

Figures 9.43 and 9.44 depict, respectively, the recovered charge and voltage waveforms associated with *The DC Field Experiment*'s calibration signal. They were calculated via $f_c = 25$ MHz SIB filtering.

The width (FWHM) of the recovered charge pulse associated with the proximal plate is 86 μm. The width of the recovered distal pulse is 82 μm. Therefore the $f_c = 25$ MHz Lyons recovery of data associated with this experiment cannot be trusted to accurately resolve features of the actual embedded waveform which are significantly smaller than, say, 80 μm. Paraphrasing, the resolution limit of the $f_c = 25$ MHz Lyons recovery is 80 μm

The value of the recovered voltage waveform at $z = l$ is 9.42 kV , 5.8% lower than the expected value of 10 kV. Although this value for the recovered voltage waveform at $z = l$ is by no means exact it does ascertain that associated charge waveform has, at least approximately, the correct scale.

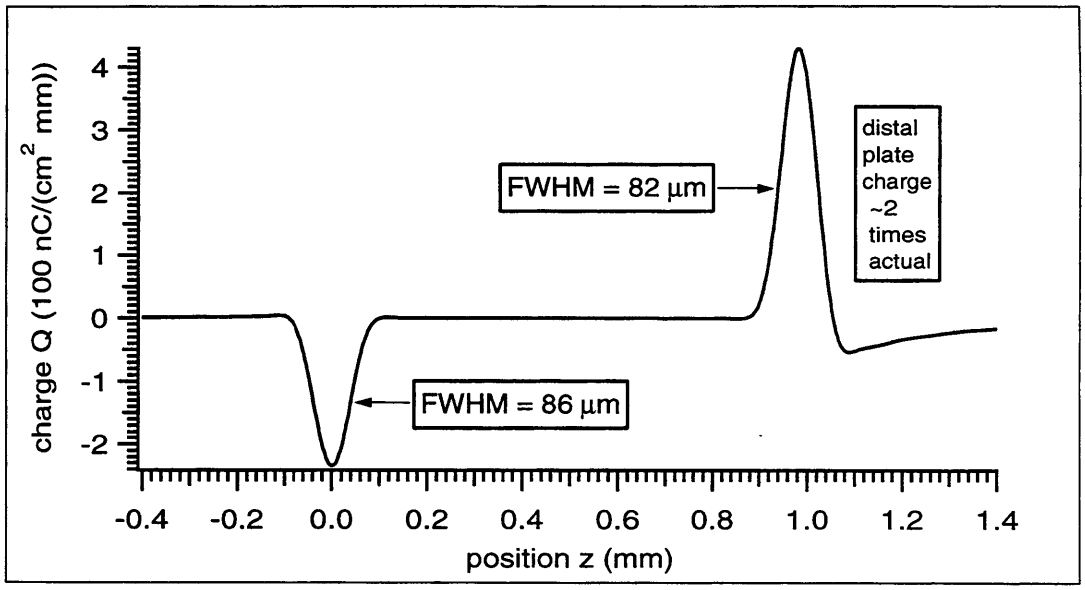

Figure 9.43: The $f_c = 25$ MHz Lyons-recovered charge waveform associated with *The DC Field Experiment*'s calibration signal.

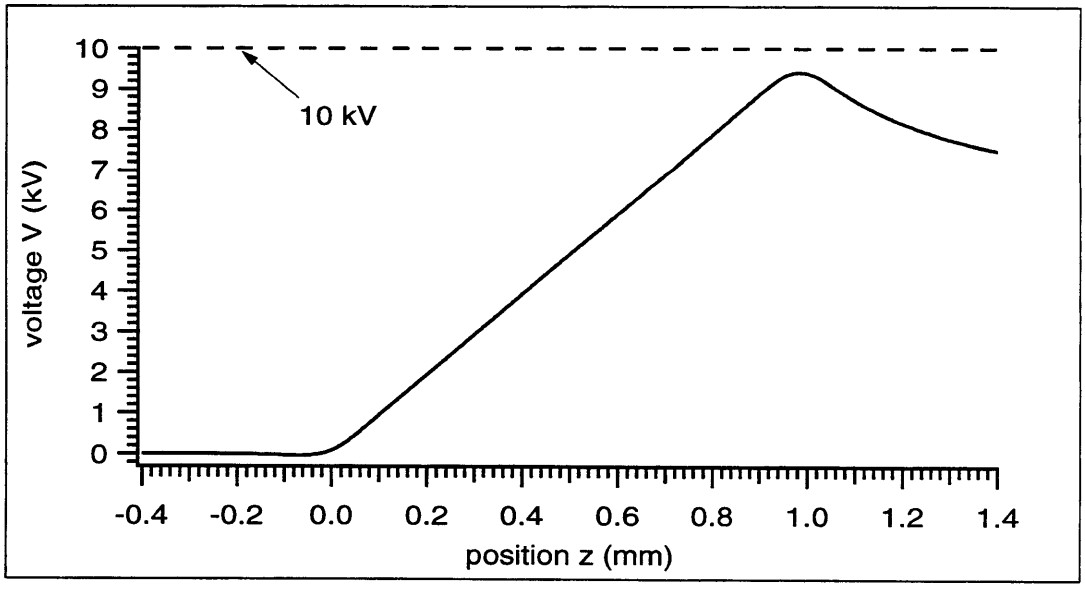

Figure 9.44: The $f_c = 25$ MHz Lyons-recovered voltage waveform associated with *The DC Field Experiment*'s calibration signal.

9.5.3 Inverse Source Solution - Bulk Waveform

This experiment's sample was subjected to a -10 kV DC voltage for 22 hours. At times t = 0.5, 2, 6, and 22 hours the sample was subjected to the PESAW experimental methodology. The applied DC voltage V_o at the time of measurement was 0 kV – for each measurement the applied voltage was increased from -10 kV to 0 kV, then the PESAW signal was obtained, and then the voltage was decreased back to -10 kV.

The duration of each PESAW measurement was small compared to the total time (22 hours) that the sample was under stress so the sample was 'almost always' under -10 kV stress. The resultant raw measured PESAW signals are depicted in figure 9.45.

Figure 9.46 depicts the f_c = 25 MHz Lyons-recovered charge waveforms associated with the four bulk signals depicted in figure 9.45. Figure 9.47 depicts the voltage waveforms derived from figure 9.46's charge waveforms.

At $z = l$ all of these voltage waveforms are within ± 0.05 kV of the expected value of 0 kV. The error associated with the $z = l$ value of the voltage waveform associated with with the calibration signal is 0.58 kV (10 kV - 9.42 kV; see page 217), so each of the bulk voltage waveforms has much less (a factor of $\sim$ 0.58/.05 less) error at $z = l$ than the 'calibration voltage waveform.'

Figure 9.46's waveforms clearly depict a broad (wider than the resolution limit of 80 μm) region of negative bulk charge growing in the region between, say, z = 0.2 and 0.84 mm. The central lobe of waveform associated with the signal acquired after 22 hours of applied field (the '22 hour charge waveform') has a width of 186 μm; this lobe is well resolved. It is safe to say that the applied voltage has caused negative bulk charges to form inside the dielectric.

The 22 hour charge waveform has a ± pair of charge pulses located near the proximal plate. The negative pulse component of this ± pulse pair peaks at z = -37 μm (outside the 'physical region' $0 < z < l$) and has width (FWHM) of 50 μm. The positive pulse peaks at z = 44 μm and has width of 69 μm.

The width of each of these pulses is less than the resolution limit of 80 μm. The distance (44 μm - (-37 μm)) between the pulse peaks is 81 μm, a value on the order of the resolution limit. These facts suggest that the charges near the proximal plate act like a dipole with respect to the f_c = 25 MHz Lyons recovery.

This 'dipole hypothesis' is confirmed by figure 9.48, which depicts the results of the f_c = 45 MHz Lyons recovery (which must have a smaller resolution FWHM than the f_c = 25 MHz Lyons recovery). In figure 9.48, the width of the negative pulse has shrunk to 32 μm and the width of the positive pulse has shrunk to 39 μm. Therefore the ± pulse pair which straddles the origin in figure 9.46 was indeed acting like a dipole with respect to the Lyons recovery – the width of a resolved object does not decrease when the resolving power of the observing instrument increases.

This section has shown that the Lyons recovery is applicable to PESAW signals obtained from samples containing bulk charges generated in response to an applied DC voltage, and that the Lyons recovery is applicable to PESAW signals obtained from samples containing dipole charges located near the proximal plate.

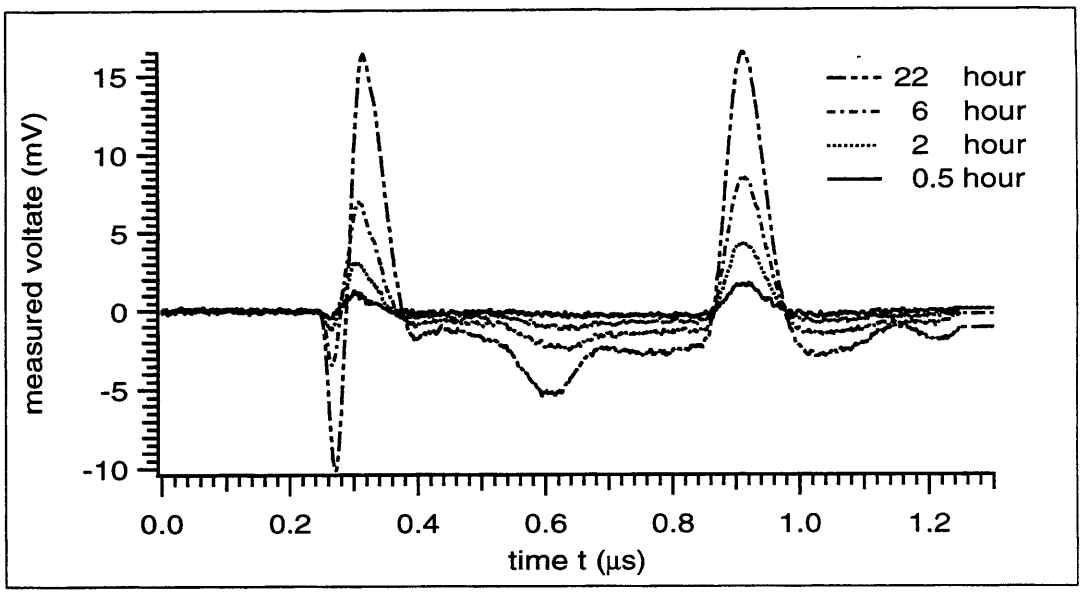

Figure 9.45: The four raw measured PESAW bulk signals associated with *The DC Field Experiment.*

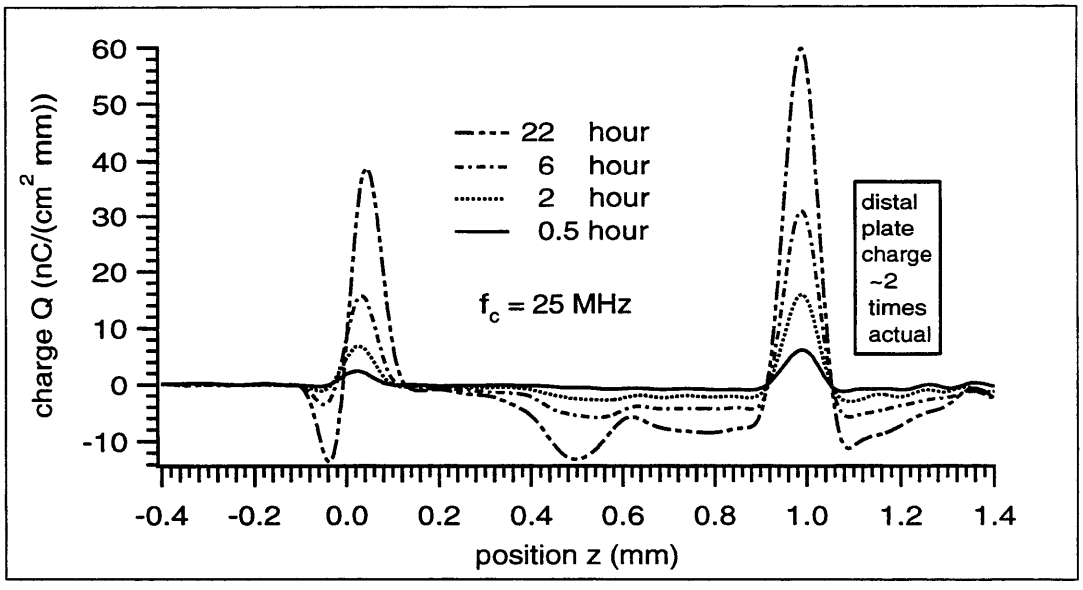

Figure 9.46: The four $f_c = 25$ MHz Lyons-recovered charge waveforms associated with *The DC Field Experiment*'s four measured PESAW bulk signals.

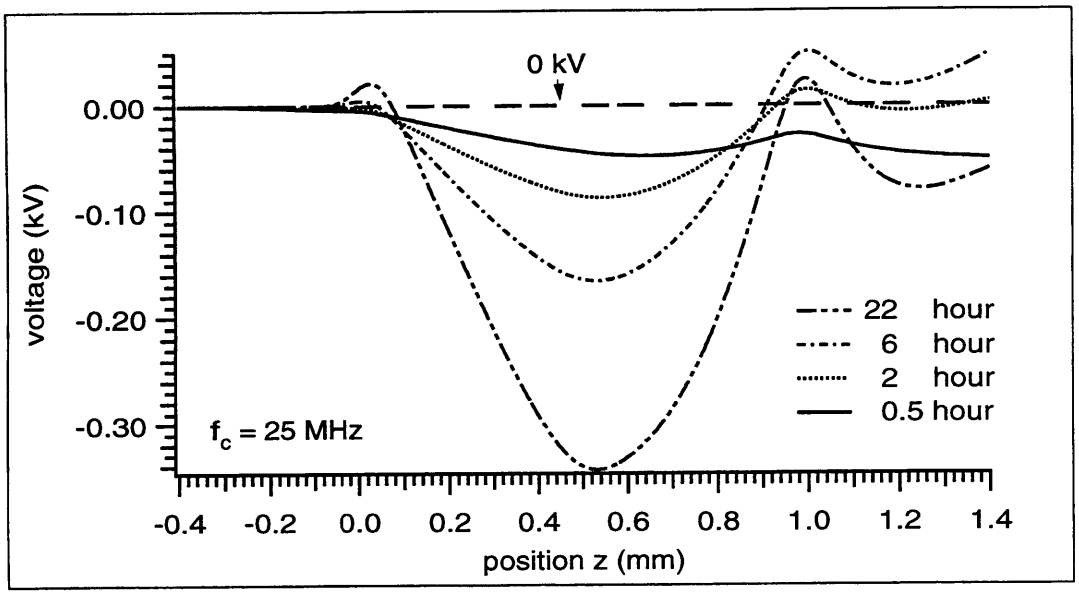

Figure 9.47: The four $f_c = 25$ MHz Lyons-recovered voltage waveforms associated with *The DC Field Experiment*'s four measured PESAW bulk signals.

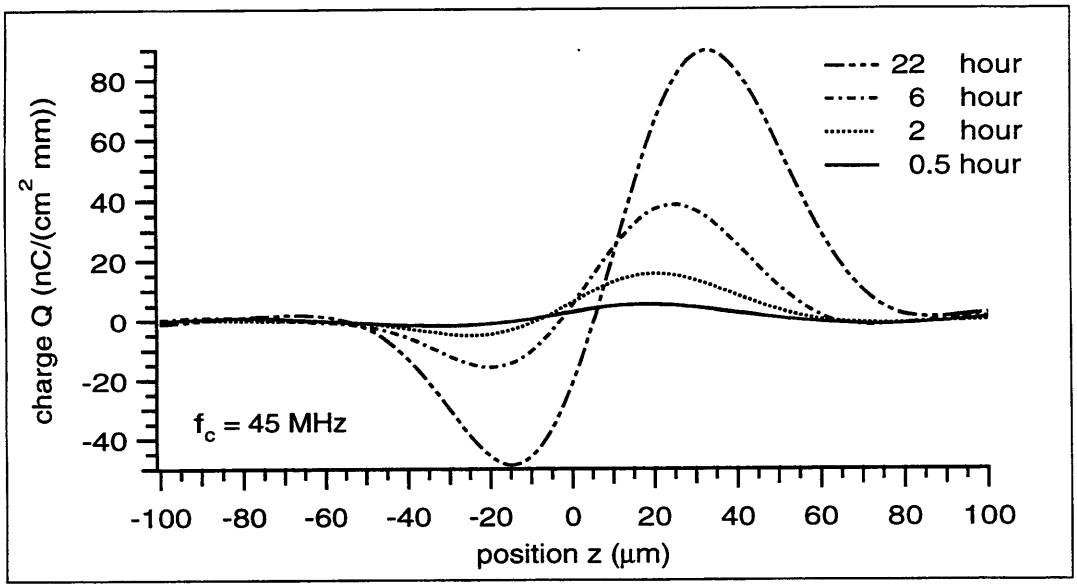

Figure 9.48: Proximal plate region of the four $f_c = 45$ MHz Lyons-recovered charge waveforms associated with *The DC Field Experiment*'s four measured PESAW bulk signals.

9.6 The Distal Dipole Experiment

9.6.1 Inverse Medium Solution

The Distal Dipole Experiment focusses on an $l = 4.445$ mm slab of polymethylmethacrylate (PMMA) modelled via the parameters given in table 9.4. Figure 9.49 depicts the calibration signal from which this model was derived.

m	=	0.011	Np/(mm MHz)
$c(f_o)$	=	2.7050	mm/μs
f_o	=	1	MHz
b	=	0	Np/mm

Table 9.4: Polymeric model selected to describe the slab of polymethylmethacrylate analyzed in *The Distal Dipole Experiment.*

Figures 9.50, 9.51, and 9.52 depict, respectively, comparisons of measured and theoretic values for the distal pulse $V_d[t_n]$, the attenuation coefficient $\alpha[f_k]$, and the phase velocity $c[f_k]$.

The time domain agreement between theory and measurement exhibited in figure 9.50 is quite good; except for times near $t = 2.128$ μs (the time of the positive extremum of the measured distal pulse) the theoretic model fits the measured data like a hand in a glove. Near time $t = 2.128$ μs, the theoretic values for the distal pulse exceed the measured values by about 8%.

The theoretic values for the phase velocity fit the measured values well for all frequecies up to 20 MHz, except for the frequency range $f = 0.3$ to 2 MHz. In this range the measured data exceeds the theoretic data. The maximum deviation between theoretic and measured data in this range is 0.017 mm/μs.

The theoretic values for the attenuation coefficient track the measured values well up to 20 MHz, except that they are an average of about 0.015 Np/mm too small. It would have been possible to use $b = 0.015$ Np/mm (recall that the hysteresis absorption model is given by $\alpha(f) = m\ f + b$) to make the theoretic values of $\alpha(f)$ track the measured values more successfully.

But except for the 'DC offset' (*ie*: the apparent non-vanishing value of b) between the measured and theoretic values for the attenuation coefficient, the given theoretic model fits the measured data well. The given model was chosen also because no other set of parameters fit the data as well; a non-vanishing value of b was found to yield a less successful fit between measured and theoretic values of both the distal pulse and the phase velocity.

Besides, the question of finding a polymeric mechanism to explain the physical origin of a non-vanishing value of b was thought to be too great to justify its inclusion at this point. An apparent non-vanishing value of b can just as easily be explained by hypothesizing that the distal-plate reflection coefficient $\Gamma_d \neq -1$, or that the proximal plate reflection coefficient $\Gamma_p \neq 0$.

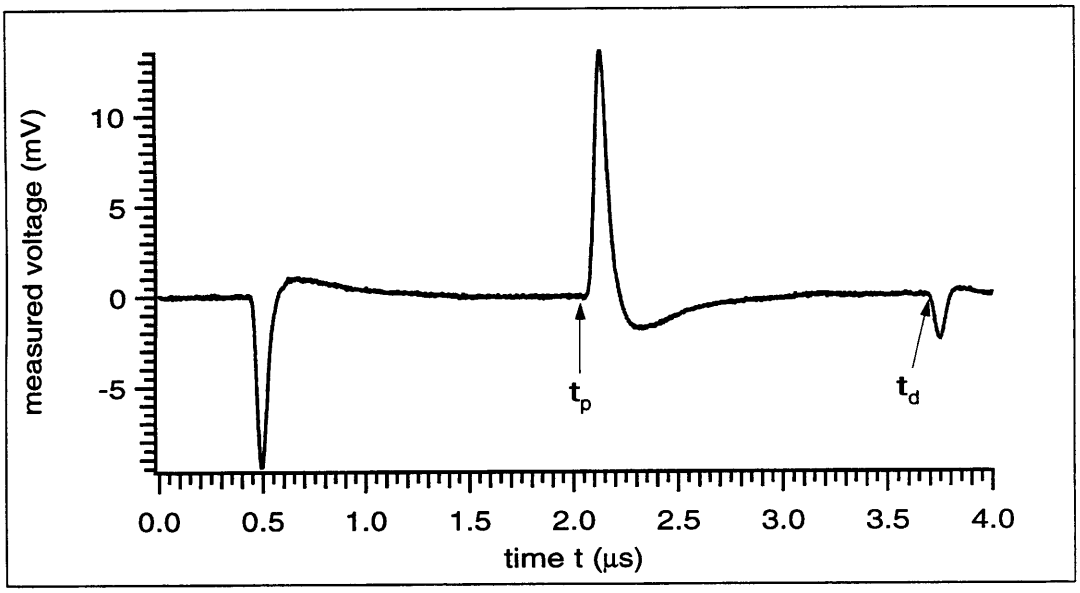

Figure 9.49: The calibration signal used in *The Distal Dipole Experiment.*

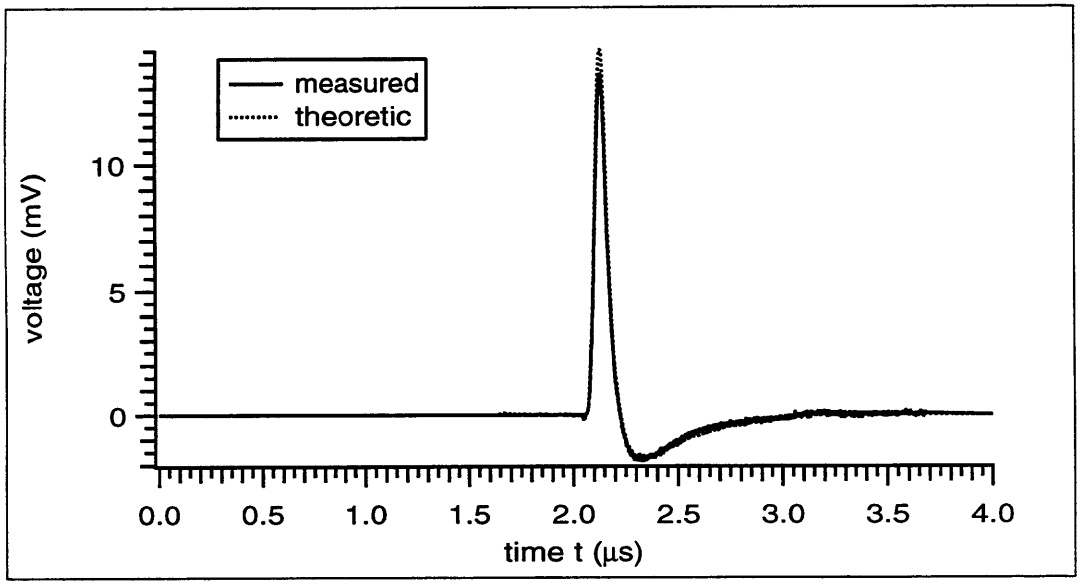

Figure 9.50: Comparison of *The Distal Dipole Experiment*'s measured and theoretic distal pulses.

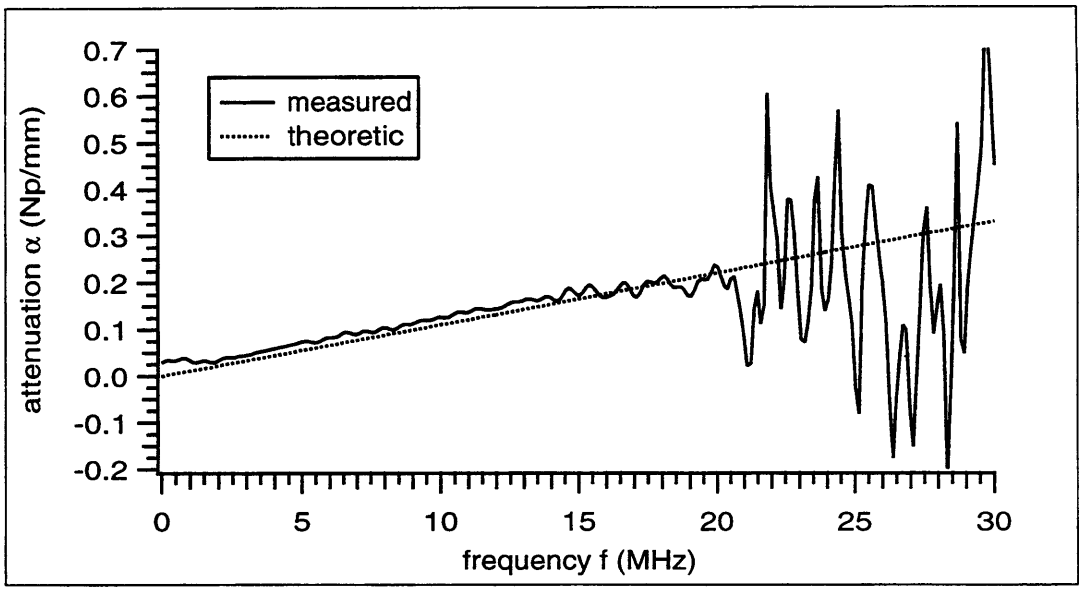

Figure 9.51: Comparison of *The Distal Dipole Experiment*'s measured and theoretic values for the attenuation coefficient $\alpha[f_k]$.

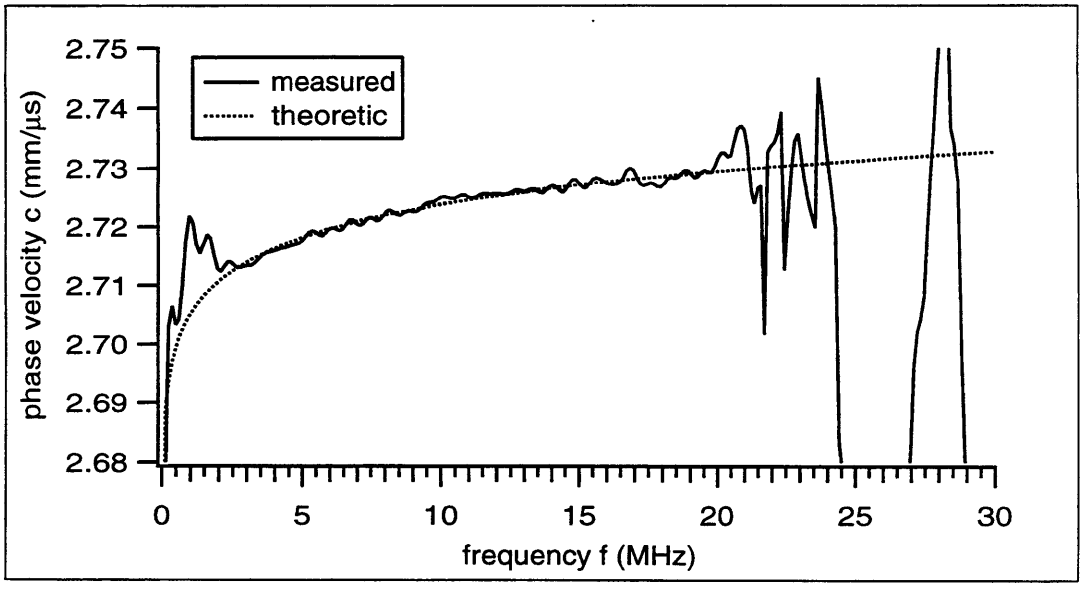

Figure 9.52: Comparison of *The Distal Dipole Experiment*'s measured and theoretic values for the phase velocity $c[f_k]$.

9.6.2 Inverse Source Solution - Calibration Waveform

The calibration signal depicted in figure 9.49 was obtained with $V_o = 10$ kV. Applying the Lyons recovery to this calibration signal (deconvolved with respect to the negative of its proximal pulse) yields a waveform with a proximal pulse that has raw localized area of -0.998. The associated value of the un-normalization coefficient ν for this PMMA sample is, therefore:

$$\nu = \frac{3.4\ [0.8854 \frac{\text{nC}}{\text{cm}^2} / \frac{\text{kV}}{\text{mm}}]\ 10\ \text{kV}}{(0.998)\ 4.445\ \text{mm}} = 6.79\ \frac{\text{nC}}{\text{cm}^2} \tag{9.42}$$

Figures 9.53 and 9.54 depict, respectively, the recovered charge and voltage waveforms associated with *The DC Field Experiment*'s calibration signal. They were calculated via $f_c = 30$ MHz SIB filtering.

The width (FWHM) of the recovered charge pulse associated with the proximal plate is 121 μm. The width of the recovered distal pulse is 120 μm. Therefore the resolution limit of the $f_c = 30$ MHz Lyons recovery is 120 μm The value of the recovered voltage waveform at $z = l$ is 9.918 kV, only 0.82% lower than the expected value of 10 kV. This rather small (0.082 kV) error suggests that the charge waveform depicted in figure 9.53 does indeed have the correct scale.

With the localized area at position z defined as the area between $z \pm$ 0.2 mm, the ratio (proximal/distal) of the recovered plate charge is -1.85 (7.5% less, in magnitude, than the expected value of -2). Rather remarkably, the recovered position (location of extremum value, as determined via a quadratic to the extremum data point and its two nearest neighbors) of the proximal and distal pulses is correct to the nearest μm.

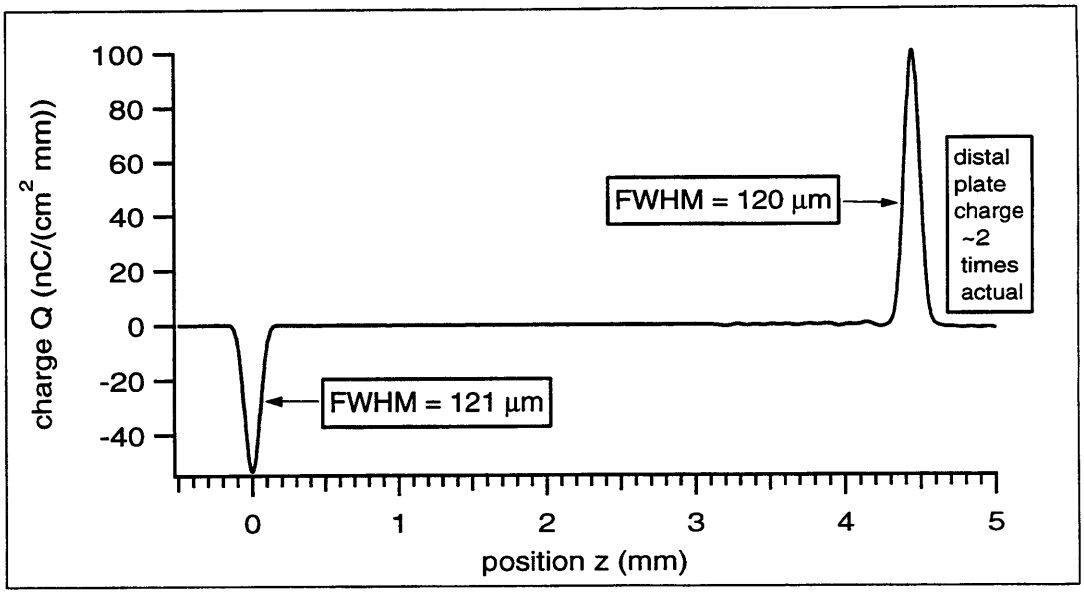

Figure 9.53: The $f_c = 30$ MHz Lyons-recovered charge waveform associated with *The Distal Dipole Experiment*'s calibration signal.

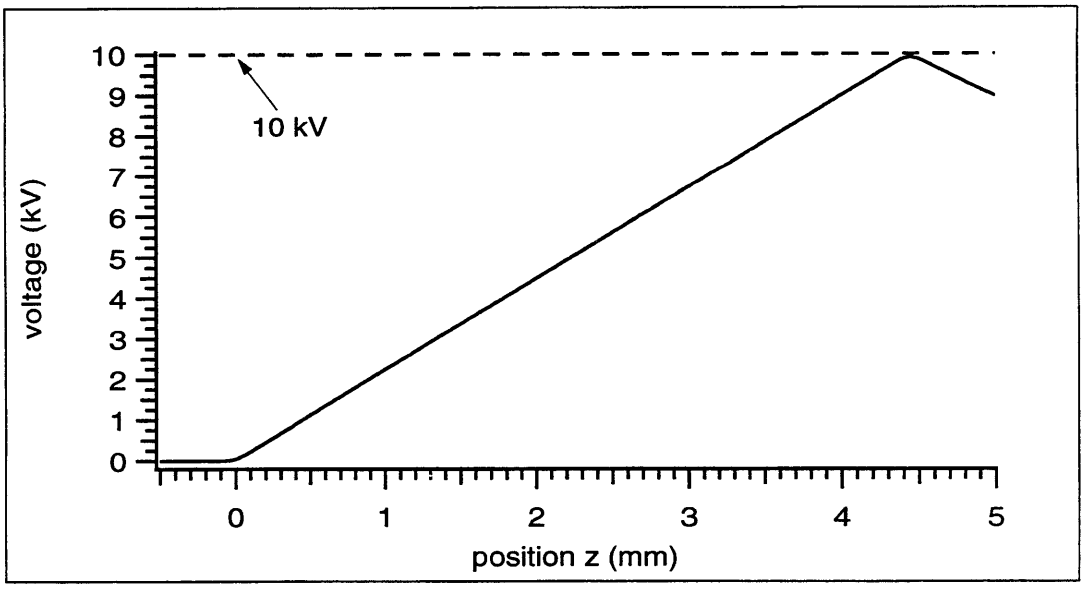

Figure 9.54: The $f_c = 30$ MHz Lyons-recovered voltage waveform associated with *The Distal Dipole Experiment*'s calibration signal.

9.6.3 Inverse Source Solution - Bulk Waveform

This experiment's sample was irradiated with a dose of 0.85 MeV electrons designed to deliver 400 nC/cm^2 of charge. The sample was then left alone for 25 hours at 25^o C with no voltage applied. Bulk PESAW signals were acquired from the sample 2 minutes after irradiation, 37 minutes after irradiation, and 25 hours after irradiation. The value of the DC component V_o of the applied PESAW excitation voltage $V_a(t)$ was 0 kV. These three raw measured PESAW bulk signals are depicted in figure 9.55.

Figure 9.56 depicts the f_c = 30 MHz Lyons-recovered charge waveforms associated with the three signals depicted in figure 9.55. Figure 9.57 depicts the voltage waveforms derived from figure 9.56's charge waveforms.

At $z = l$ all three of these voltage waveforms have negative values whereas, according to $V_o = 0$, these three values should all be zero. The $z = l$ value of the '2 minute voltage waveform' (*ie*: the waveform depicted with a solid line in figure 9.57) is -0.44 kV. The $z = l$ value of the 37 minute voltage waveform is -1.94 kV. The $z = l$ value of the 25 hour voltage waveform is -1.05 kV. The error (10 kV - 9.918 kV) in the calibration voltage waveform (figure 9.54) is only 0.082 kV; the errors in the $z = l$ values of these bulk voltage waveform is between 5 and 13 times as great as the corresponding error in the calibration voltage waveform.

But, according to the previous discussion *re* the uncertainty in the DC value of the measured PESAW signal and the relatively large impact of this uncertainty upon the uncertainty in the recovered value of the voltage waveform at $z = l$, the recovered value of the voltage waveform at $z = l$ is not a robust measure of a charge recovery's success.

Further, the recovered value of the voltage waveform at $z = l$ is also effected by the fact that the impact of the distal plate charge is (in theory, assuming a distal plate reflection coefficient Γ_d = -1 and a proximal plate reflection coefficient $\Gamma_p = 0$) multiplied by a factor of 2. The analysis of the calibration charge waveform uncovered the fact that, for this experiment, this expected value of 2 was closer to 1.85.

There is another measure of the likely validity of a charge recovery but, unfortunately, it too is complicated by both the fact that the 'distal plate multiplication factor' is not unity, and by the fact that the recovery has finite resolution. This other measure is the physical requirement that the total recovered charge (proximal plate, distal plate, and bulk; see page 166's equation (9.1)) vanish.

The problem lies both in the inability to accurately determine the value of the distal plate charge (the distal plate charge is, approximately, the integration over some region about $z = l$ – but which region? And, what if some bulk charge is included in this region?) and in the uncertainty in the distal plate multiplication factor, which must be used to reduce the impact of the distal plate charge so that the requirement that the total charge vanish can be verified.

Focussing on the '2 minute charge waveform,' the charge on the proximal plate (between $z = \pm$ 0.2 mm) is 81 nC/cm^2. The charge on the distal plate (between z = 4.445 mm $\pm$ 0.2 mm) is 205 nC/cm^2. The charge in the bulk region (between z = 0.2 mm and z = 4.245 mm) is -203 nC/cm^2. If the distal plate multiplication factor

were known to be 2 then it would be required that the raw recovered distal plate charge be -2 times the sum of the proximal plate and bulk charges.

But, because the distal plate multiplication factor was found to be 1.85 (rather than 2), in the current situation 'the total charge vanishes' if the distal plate charge is -1.85 times the sum of the proximal and distal plate charges. That is, according to this analysis the distal plate charge should be

$$(81 \text{ nC/cm}^2 - 203 \text{ nC/cm}^2) \cdot (-1.85) = 226 \text{ nC/cm}^2 \tag{9.43}$$

The actual distal plate charge is 205 nC/cm^2, 9% smaller than expected. A similar analysis of the 37 minute charge waveform yields an actual distal plate charge that is 4.5% smaller than expected; the 25 hour charge waveform's distal plate charge is 10% smaller than expected.

Figure 9.58 depicts a close-up of the distal plate region of the bulk charge recoveries depicted in figure 9.56. The positions $z = l \pm 0.2$ mm (4.245 and 4.645 mm) are clearly indicated. As discussed previously, the various (2 min, 37 min, 25 hour) estimated distal plate charges were calculated by integrating these various charge waveforms between 4.245 and 4.645 mm.

On this scale it becomes clear that the estimated plate charges were smaller than expected, at least in part, because the integration region included negative bulk charges. The 25 hour waveform illustrates especially well the fact that the integration region has also included a contribution from the image of (*ie*: the reflection off the distal plate of) the negative charges extant just inside (*ie*: just to the left of) the distal plate. The inclusion of this negative image charge has exacerbated the unwanted effect of the negative charge in the physical region just inside the distal plate.

It might well have been wiser to choose more narrow integration limits when attempting to verify that the Lyons recovery yields results that are consistent with the physical requirement that the total charge within and upon the sample must vanish.

Regardless, at this point it seems reasonable to say that the observed errors in the values of the recovered voltage waveforms at $z = l$, and the deviations between the expected and the 'measured' (quotes because the measurement is manifestly inexact) values of the distal plate charge, seem to be small enough (in light of their known dependency upon quantities which have, quite likely, non-neglibible errors associated with them) to justify the statement that the Lyons recovery of charges embedded within (and upon) this slab of PMMA seem to have been reasonably well recovered.

Figure 9.58's dashed line (which represents the 25 hour charge waveform) depicts a negative pulse of bulk charge near the positively-charged distal plate. This $\pm$ pulse pair is the 'distal dipole' after which this experiment was named. The negative pulse has its extremem value at 4.232 mm, 213 μm from the position (l= 4.445 mm) of the distal plate. The FWHM of this negative pulse is 123 μm, so that it is just resolved. The Lyons recovery has successfully recovered this distal dipole.

Figure 9.59 depicts a bulk charge closeup of the three $f_c = 30$ MHz Lyons-recovered charge waveforms. The abscissae plotted include both plate regions but the ordinates

plotted were selected such that the plate charges themselves would not dominate the figure (figure 9.57 plots this same data with the same abscissae, but the ordinates plotted in figure 9.57 are such that the plate charges dominate).

At the scale plotted, the dominant feature of each of the three waveforms depicted in figure 9.59 is a single well-resolved negative pulse. The 25 hour waveform also includes a striking spike of negative charge near the proximal plate; this is the negative portion of the previously mentioned distal dipole. The image of this striking negative spike is also clearly apparent in the non-physical region just outside (*ie*: just to the right of) the distal plate.

Noting the various post-irradiation acquisition times of the various PESAW signals to which these waveforms correspond, it seems that as time progressed –

- the center of area of the dominant bulk pulse moved toward the proximal plate
- a thin region (a 'spike') of negative charge accumulated just inside the distal plate

These observations are confirmed in figure 9.60, which differs from figure 9.59 only in that its recovered waveforms were calculated using $f_c = 25$ MHz rather than $f_c = 30$ MHz. In figure 9.60, the readily observable short wavelength (where 'short' means 'significantly shorter than the width of the dominant pulse') fluctuations seemingly superposed onto the broad shape of each dominant pulse are exposed as noise: decreasing f_c by 5 MHz removed these fluctuations but did not disturb the overall shape of the dominant pulse.

Note that whereas decreasing f_c significantly reduced the noise fluctuations, decreasing f_c did not have a significant impact upon the negative spike: although the magnitude of its maximum excursion decreased 15% (from 13.7 nC/(cm^2 mm) to 11.7 nC/(cm^2 mm)) its width increased only 3.3% (from 123 μm to 127 μm). That is to say, whereas decreasing f_c significantly decreased the visible impact of the noise, this decrease in f_c did not significantly decrease the visible impact of the negative spike.

Figure 9.63 is to figure 9.58 as figure 9.60 is to figure 9.59: the only difference between figure 9.63 and figure 9.58 is that the waveforms depicted in figure 9.63 were calculated using $f_c = 25$ MHz whereas the waveforms depicted in figure 9.58 were calculated using $f_c = 30$ MHz.

Figure 9.63 confirms the existence of the negative 'spike' (quotes because the spike appears more like a lobe at this scale) just inside the distal plate. Further, figure 9.63 makes it clear that the short wavelength fluctuations evident in figure 9.58 were an artifact of the recovery process (in particular, the relatively high value of f_c) and not a feature of the desired charge waveform itself.

Figure 9.64 confirms these conclusions even more strongly. It compares the $f_c = 30$ MHz recovery of the 25 hour charge waveform with its $f_c = 25$ MHz counterpart. In the bulk region, where the dominant pulse is much wider than the ~ 130 μm fluctuations, $f_c = 25$ MHz waveform appears to act like a curve-fit to the relatively noisy $f_c = 30$ MHz recovery. In the region near the voltage spike the $f_c = 30$ MHz recovery does not appear to act like a curve fit to noisy data. As discussed previously, the $f_c = 30$ MHz

recovery of this spike is wider and has an extremum that is smaller in magnitude than the $f_c = 25$ MHz recovery.

The author proposes that –

- the 'curve-fit like' behavior effected by the decrease in f_c upon the recovery of the dominant pulse is a generic feature of the Lyons recovery as applied to a signal which contains enough information to enable the resolution of its source waveform.
- the 'sagging' behavior effected by the decrease in f_c upon the recovery of the negative spike is a generic feature of the Lyons recovery as applied to a signal which does not contain enough information to enable the resolution of its source waveform.

Further, the author proposes that the wavelength of the noise fluctuations (if they can be determined) give at least as good an estimate of the resolution limit of the charge recovery as the FWHM of the calibration signal recovery.

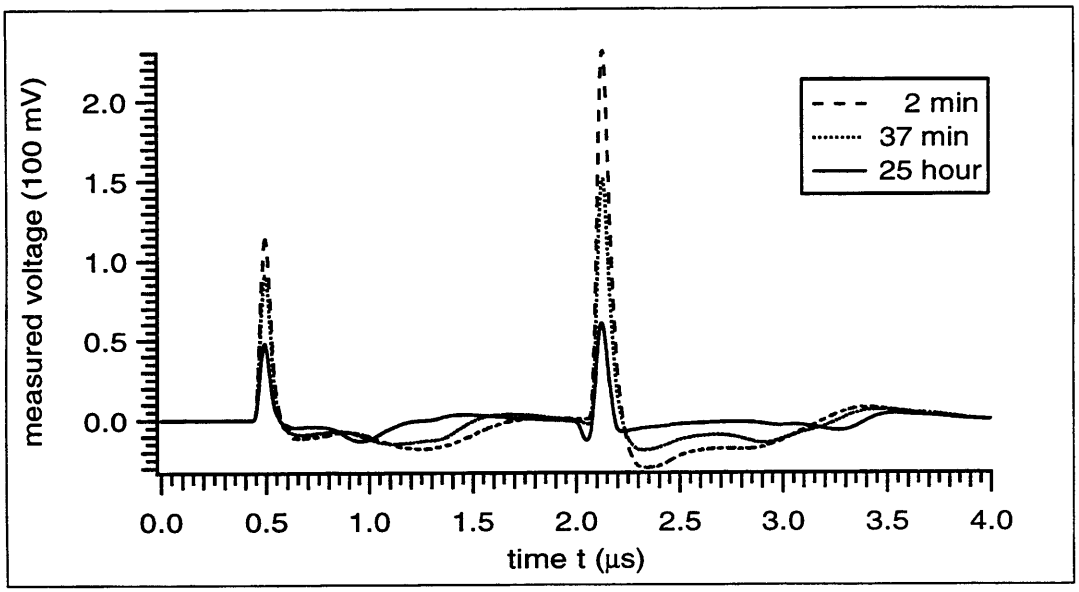

Figure 9.55: The three raw measured PESAW bulk signals associated with *The Distal Dipole Experiment.*

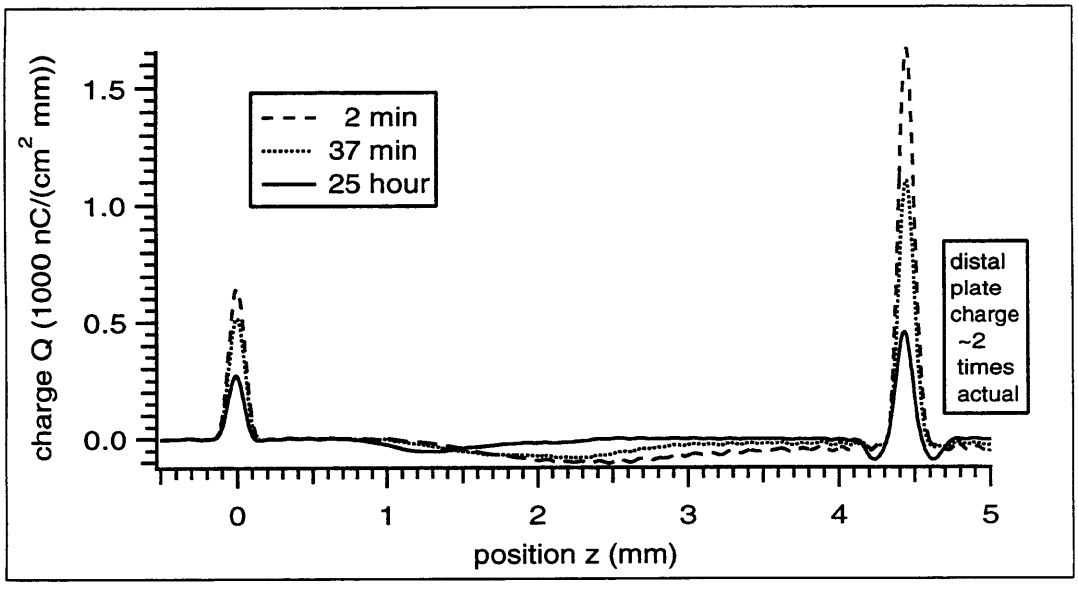

Figure 9.56: The three $f_c = 30$ MHz Lyons-recovered charge waveforms associated with *The Distal Dipole Experiment*'s three measured PESAW bulk signals.

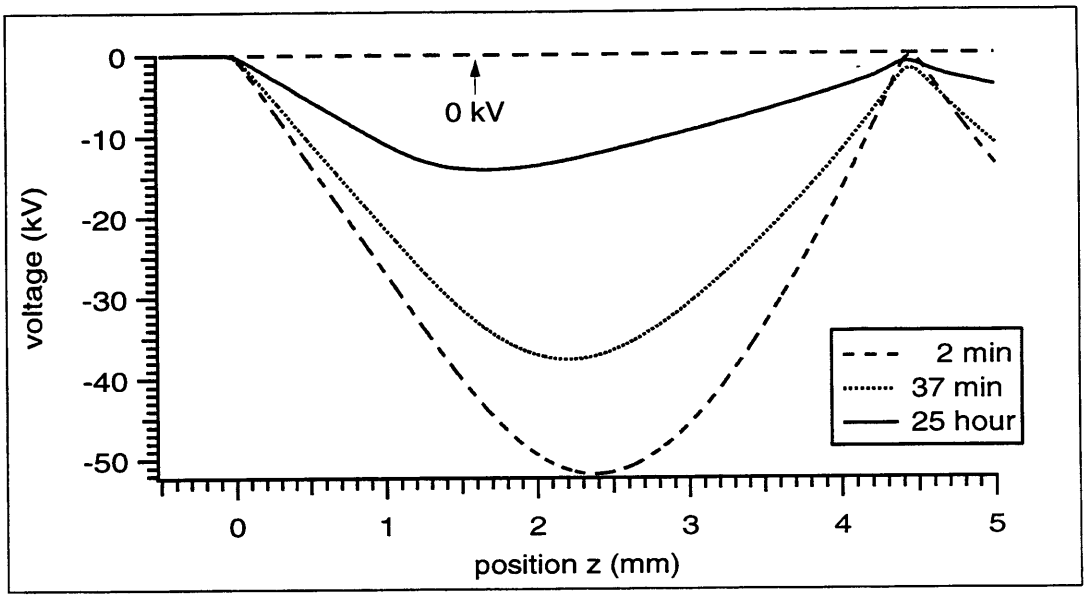

Figure 9.57: The three $f_c = 30$ MHz Lyons-recovered voltage waveforms associated with *The Distal Dipole Experiment*'s three measured PESAW bulk signals.

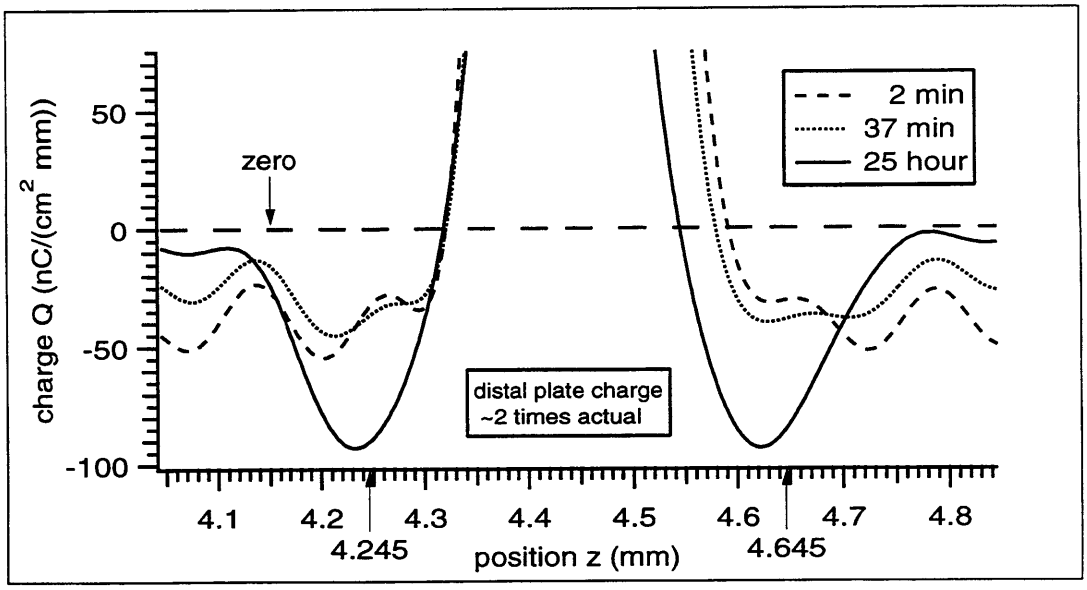

Figure 9.58: Distal plate closeup of the three $f_c = 30$ MHz Lyons-recovered charge waveforms associated with *The Distal Dipole Experiment*'s three measured PESAW bulk signals.

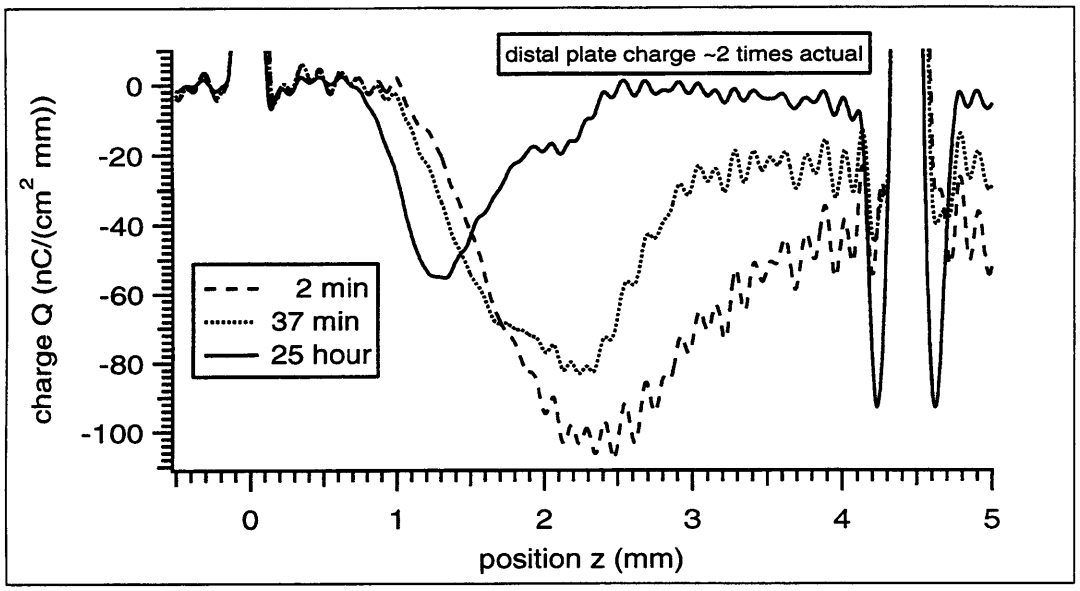

Figure 9.59: Bulk charge closeup of the three $f_c = 30$ MHz Lyons-recovered charge waveforms associated with *The Distal Dipole Experiment*'s three measured PESAW bulk signals.

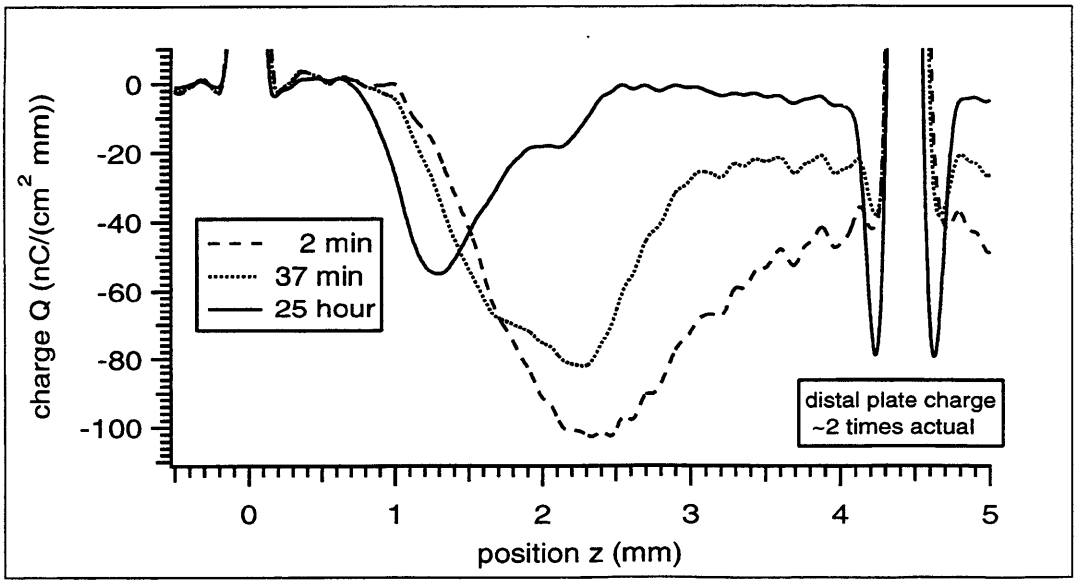

Figure 9.60: Bulk charge closeup of the three $f_c = 25$ MHz Lyons-recovered charge waveforms associated with *The Distal Dipole Experiment*'s three measured PESAW bulk signals.

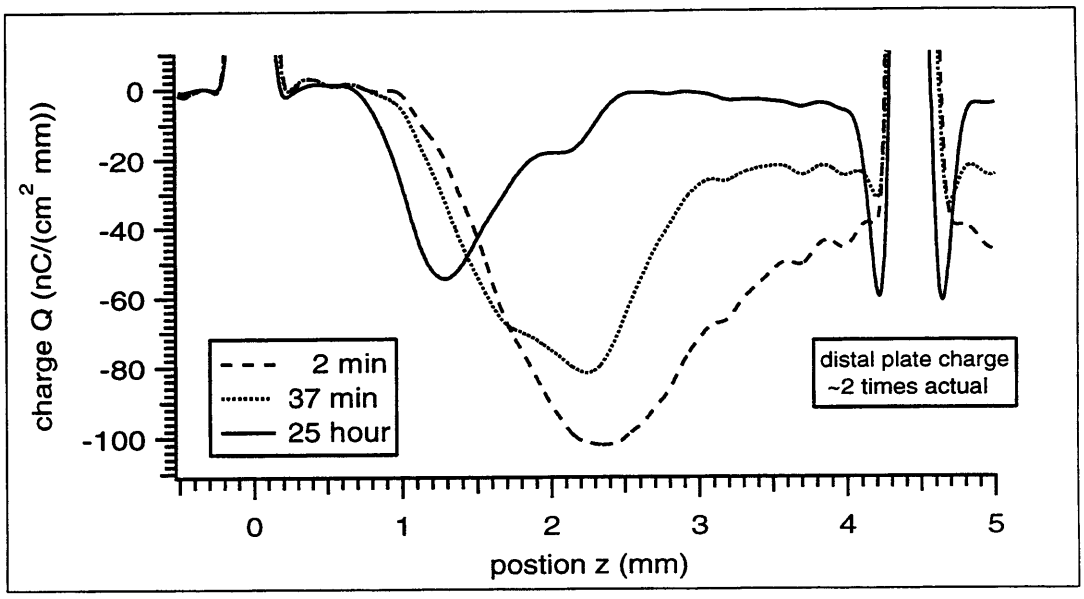

Figure 9.61: Bulk charge closeup of the three $f_c = 20$ MHz Lyons-recovered charge waveforms associated with *The Distal Dipole Experiment*'s three measured PESAW bulk signals.

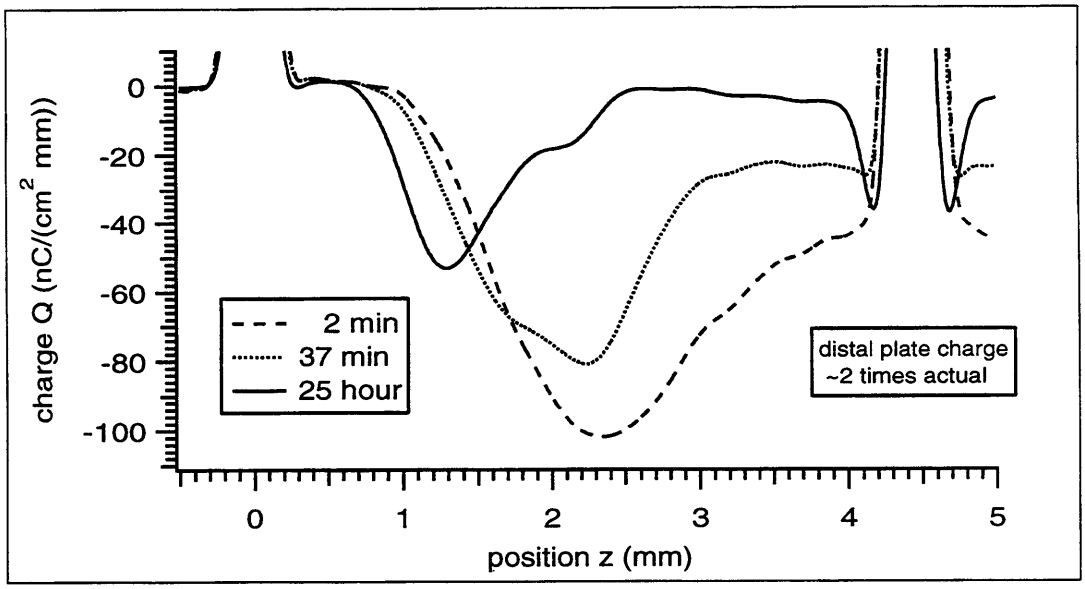

Figure 9.62: Bulk charge closeup of the three $f_c = 15$ MHz Lyons-recovered charge waveforms associated with *The Distal Dipole Experiment*'s three measured PESAW bulk signals.

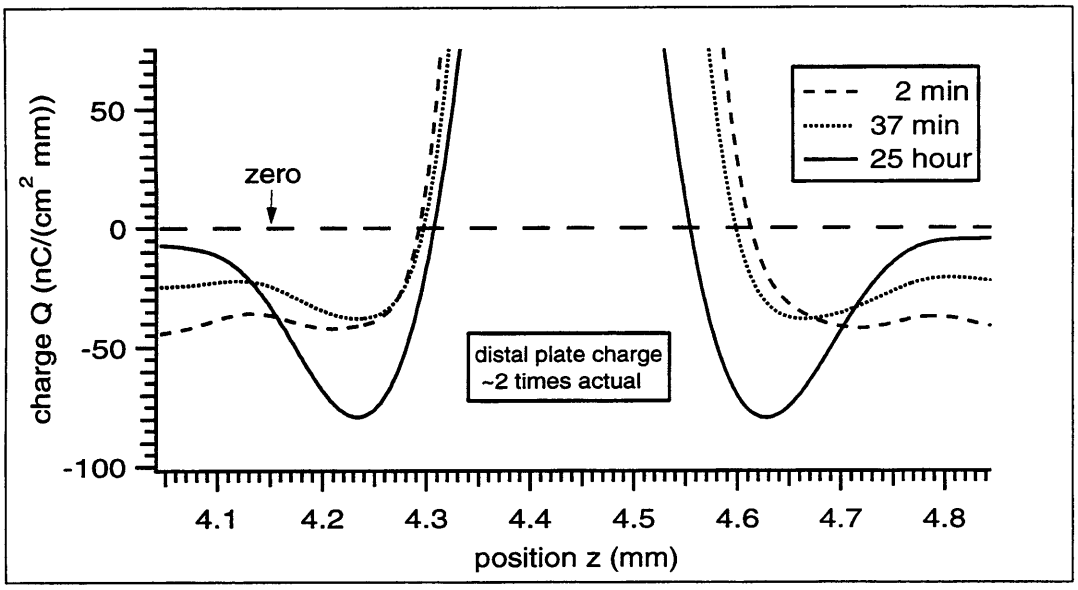

Figure 9.63: Distal plate closeup of the three $f_c = 25$ MHz Lyons-recovered charge waveforms associated with *The Distal Dipole Experiment*'s three measured PESAW bulk signals.

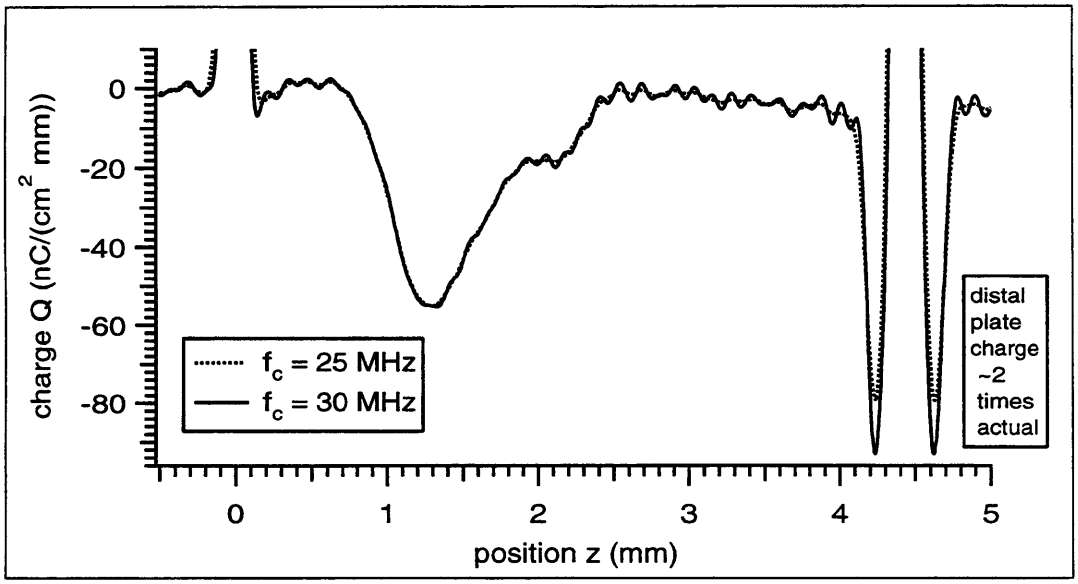

Figure 9.64: Comparison of the $f_c = 30$ MHz recovery of the 25 hour charge waveform with the $f_c = 25$ MHz recovery.

Chapter 10

Conclusions And Surmises

10.1 Conclusions

This thesis' goal has been

- to present novel inverse source mathematics for the solution (inversion) of a subclass of linear, first-kind Fredholm IEs (CLDP IEs) which map waveforms (functions of space alone) to signals (functions of time alone)
- to present the novel PESAW inverse medium solution for determining a pressure wave propagation model $\alpha(f)$ and $c(f)$ from a measured PESAW calibration signal
- to employ these 'inverse procedures' in the service of the PESAW charge waveform recovery method

10.1.1 CLDP IEs

Chapter 7, which forms the mathematical core of the thesis, points out that the (temporal) Fourier transform of a CLDP IE's response signal can be interpreted as the values of the (spatial) Laplace transform of the source waveform along a Laplace plane path determined by the material's complex wavenumber $\underline{k}(f)$.

That is, with

$$\mathrm{H}(z,t) \quad \stackrel{\mathcal{F}}{\Longleftrightarrow} \quad \exp(-z\,\underline{\mathcal{K}}(f)) \tag{10.1}$$

where

$$\underline{\mathcal{K}}(f) = \alpha(f) + \mathrm{j}\,\underbrace{2\pi f/c(f)}_{\beta(f)} \equiv \mathrm{j}\,\underline{k}(f) \tag{10.2}$$

and

$$\mathcal{P}(t) = \int_0^\infty \mathcal{Q}(z)\, \mathrm{H}(z,t)\, dz \qquad \stackrel{\mathcal{F}}{\Longleftrightarrow} \qquad \underline{\mathcal{P}}(f) = \int_0^\infty \mathcal{Q}(z)\, \exp(-z\, \underline{\mathcal{K}}(f))\, dz \quad (10.3)$$

the Fourier transform $\underline{\mathcal{P}}(f)$ of $\mathcal{P}(t)$ is given by

$$\underline{\mathcal{P}}(f) = \underline{\tilde{\mathcal{Q}}}(\underline{\mathcal{K}}(f)) \quad (10.4)$$

where $\underline{\tilde{\mathcal{Q}}}(\underline{\mathcal{K}})$ is the spatial Laplace transform of $\mathcal{Q}(z)$:

$$\underline{\tilde{\mathcal{Q}}}(\underline{\mathcal{K}}) = \mathcal{L}\{\mathcal{Q}(z)\} \equiv \int_0^\infty \mathcal{Q}(z)\, \exp(-z\, \underline{\mathcal{K}})\, dz \quad (10.5)$$

Equation (10.3) is called a CLDP IE if $\underline{\mathcal{K}}(f)$ is chosen such that $\mathrm{H}(z,t)$ is causal (*ie*: satisfies $\mathrm{H}(z,t) = \mathrm{H}(z,t)\, \mathrm{U}(t)$) for any positive z, in which case $\mathrm{H}(z,t)$ is causal for all positive z). Equation (10.3) demonstrates the fact that the CLDP IE may be expressed equally well in either time or frequency.

Expressed in the frequency domain, the causality of $\mathrm{H}(z,t)$ requires that $\exp(-z\, \underline{\mathcal{K}}(f))$ satisfy the Kramers-Kronig relations (which state that the real and imaginary parts of a 'causal' $\exp(-z\, \underline{\mathcal{K}}(f))$ form a Hilbert transform pair); $\exp(-z\, \underline{\mathcal{K}}(f))$ will satisfy the Kramers-Kronig relations if $\underline{\mathcal{K}}(f)$ is analytic.

A material is called stable if $\alpha(f) = \Re_e\{\underline{\mathcal{K}}(f)\} \geq 0$ for all f. All passive materials are stable. If a material is stable, it follows that the frequency-f-parameterized Laplace plane CLDP path $\underline{\mathcal{K}}(f)$ will not leave the right hand plane (RHP, defined as including the j-axis).

This thesis only considers the inversion of CLDP IEs corresponding to stable materials. The waveforms $\mathcal{Q}(z)$ considered are real, causal (meaning they vanish for negative z's) and Fourier transformable (meaning that there exists a complex function $\underline{\mathcal{Q}}(\flat)$ which yields $\mathcal{Q}(z)$ when subjected to the inverse Fourier transformation operation defined in section F.1).

10.1.2 Inverting CLDP IEs

The proposed method for inverting CLDP IEs is itself expressed an IE: the inverse CLDP IE. The inverse CLDP IE may be derived by extending the Bromwich inversion integral [42, 75, 44]. In the CLDP context, the Bromwich inversion integral may be expressed as

$$\mathcal{Q}(z) = \int_{-\infty}^{\infty} \underline{\mathcal{P}}_b(f)\, \frac{1}{\mathrm{j}2\pi} \frac{d\, \underline{\mathcal{K}}_b(f)}{df} \exp(z\, \underline{\mathcal{K}}_b(f))\, df \quad (10.6)$$

where

$$\underline{\mathcal{P}}_b(f) = \underline{\tilde{\mathcal{Q}}}(\underline{\mathcal{K}}_b(f)) \tag{10.7}$$

and

$$\underline{\mathcal{K}}_b(f) = \alpha_b + \mathrm{j}\, 2\pi f/c_b \qquad ; \quad \alpha_b \geq 0 \text{ and } c_b > 0 \tag{10.8}$$

The inverse CLDP IE is simply obtained by replacing $\underline{\mathcal{P}}_b(f) \rightarrow \underline{\mathcal{P}}(f)$ (where $\underline{\mathcal{P}}(f)$ is given by (10.3)) and replacing $\underline{\mathcal{K}}_b(f) \rightarrow \underline{\mathcal{K}}(f)$ (where $\underline{\mathcal{K}}(f)$ corresponds to a stable CLDP material).

The result

$$\mathcal{Q}(z) = \int_{-\infty}^{\infty} \underline{\mathcal{P}}(f)\, \frac{1}{\mathrm{j}2\pi} \frac{d\, \underline{\mathcal{K}}(f)}{df} \exp(z\, \underline{\mathcal{K}}(f))\, df \tag{10.9}$$

is one form of the so-called inverse CLDP IE.

When considering the range of applicability of (10.9) (*ie*: for which $\{\underline{\mathcal{K}}(f), \mathcal{Q}(z)\}$ pairs does (10.9) yield a valid recovery from the $\underline{\mathcal{P}}(f)$ produced by (10.3)?), note that the Paley-Wiener criteria (sections 6.3 and 6.4) ensure that the generic CLDP $\underline{\mathcal{K}}(f)$ (as well as the particular case $\underline{\mathcal{K}}(f) = \underline{\mathcal{K}}_b(f)$) will satisfy

$$\lim_{f \rightarrow \infty} \{|\underline{\mathcal{K}}(f)|\} = \infty \tag{10.10}$$

and

$$\lim_{f \rightarrow \infty} \{\langle \underline{\mathcal{K}}(f) \rangle\} = \frac{\pi}{2} \tag{10.11}$$

where $|\underline{Z}|$ and $\langle \underline{Z} \rangle$ denote, respectively, the magnitude and principal value of the phase of the complex number$\underline{Z}$: $\underline{Z} = |\underline{Z}| \exp(\mathrm{j}\, \langle \underline{\mathcal{K}}(f) \rangle)$.

The argument for the validity of the inverse CLDP IE as applied to stable CLDP materials satisfying

$$\alpha_\infty \equiv \lim_{f \rightarrow \infty} \{\alpha(f)\} < \infty \tag{10.12}$$

proceeds apace: because the integrand is analytic in the RHP (and because the CLDP path does not leave the RHP) the value of the integral is independent of path; it depends only upon the endpoints. By equations (10.10) and (10.11) these endpoints coincide with those of the $\alpha_b = \alpha_\infty$ Bromwich materials (see sections 6.1.1 and 7.3).

Therefore the Bromwich inversion integral result applies directly to stable CLDP materials satisfying (10.12).

For stable CLDP materials failing (10.12), however, the correspondence to the Bromwich inversion integral result is less clear. Section 7.8 derives the so-called CLDP constraint (10.13) which must hold for the proposed inverse CLDP IE to yield the desired $\mathcal{Q}(z)$. This result holds whether or not α_∞ is finite. Using the given assumptions, the CLDP constraint follows directly from complex variable and Laplace transform theory. It amounts to an implicit constraint on the $\mathcal{Q}(z)$'s which are CLDP transformable under a particular $\underline{\mathcal{K}}(f)$.

Besides the requirements that the CLDP material $\underline{\mathcal{K}}(f) = \alpha(f) + \mathrm{j}\ 2\pi f/c(f)$ be stable and the waveform $\mathcal{Q}(z)$ be real, causal, and Fourier transformable, for the inverse CLDP IE to yield $\mathcal{Q}(z)$ from the given $\underline{\mathcal{P}}(f)$ the Laplace transform $\underline{\tilde{\mathcal{Q}}}(\underline{\mathcal{K}})$ of $\mathcal{Q}(z)$ must also satisfy

$$\lim_{f\to\infty}\left\{\int_0^{\alpha(f)} \Im_m\{\underline{\tilde{\mathcal{Q}}}([\alpha' + \mathrm{j}\ 2\pi f/c(f)])\ \exp(z\ [\alpha' + \mathrm{j}\ 2\pi f/c(f)])\}\ d\ \alpha'\right\} = 0 \quad (10.13)$$

Section 7.9 attempts to determine the $\underline{\mathcal{K}}(f)$-dependent constraints on CLDP transformable $\mathcal{Q}(z)$'s from a Darrell-oriented perspective. The result, which was derived without reference to the Laplace plane, states that $\mathcal{Q}(z)$ must satisfy

$$\lim_{z\to\infty}\left\{\mathcal{Q}(z)\ \frac{\exp(z\alpha_\infty)}{z\alpha_\infty}\right\} = 0 \quad (10.14)$$

Equation (10.14) must be consistent with (10.13), but (10.14) is not as definitive as (10.13), partly because it does not constrain the high frequency behaviour of $\mathcal{Q}(z)$. Equation (10.13) relies directly upon Laplace transform theory, whereas (10.14) was derived in a 'hand-waving' manner. Therefore (10.13), although opaque in comparison with (10.14), is proferred as the CLDP criterion.

When (10.13) holds, the waveform $\mathcal{Q}(z)$ and the signal $\underline{\mathcal{P}}(f)$ are said to be CLDP transforms of each other:

$$\mathcal{Q}(z) \quad \overset{\mathcal{K}}{\Longleftrightarrow} \quad \underline{\mathcal{P}}(f) \quad (10.15)$$

10.1.3 Group Velocity

Because

$$\frac{1}{\mathrm{j}2\pi}\frac{d\,\underline{\mathcal{K}}(f)}{df} = \frac{1}{2\pi}\frac{d\,\underline{k}(f)}{df} = \frac{1}{\underline{C}_g(f)} \quad (10.16)$$

where $\underline{C}_g(f)$ is the material's group velocity, the inverse CLDP IE (10.9) may be re-expressed as

$$\mathcal{Q}(z) = \int_{-\infty}^{\infty} \frac{\underline{\mathcal{P}}(f)}{\underline{C}_g(f)} \exp(z\, \underline{\mathcal{K}}(f))\, df \tag{10.17}$$

10.1.4 CLDP Theory And The PESAW Charge Recovery

Under certain seemingly reasonable assumptions (see chapters 2 and 4) the PESAW forward problem can be modelled *via* a CLDP IE. According to this model, the measured PESAW voltage signal $\mathrm{V}(t)$ is related to the desired charge waveform $\mathrm{Q}(z)$ via the experimental impulse response $\mathrm{H}_e(t)$ and the CLDP dielectric's acoustic propagation coefficient $\underline{\mathcal{K}}(f)$ (which is related to $\mathrm{H}(z,t)$ via (10.1)):

$$\mathrm{V}(t) = \mathrm{H}_e(t) * \left[\mathcal{P}(t) = \int_0^l \mathcal{Q}(z)\, \mathrm{H}(z,t)\, dz \right] \tag{10.18}$$

where the $*$ denotes temporal convolution, $\mathrm{H}_e(t)$ is determinable from some measured PESAW calibration signal $\mathrm{V}_c(t)$ (see chapter 4), and

$$\mathcal{Q}(z) = \frac{\mathcal{V}}{l}\, \mathrm{Q}(z) \tag{10.19}$$

where l is the sample thickness (which is also the parallel plate capacitor's plate separation distance) and $\mathcal{V}$ is the strength of the impulsive component of the applied PESAW voltage signal $\mathrm{V}_a(t) = \mathrm{V}_o + \mathcal{V}\delta(t)$.

Fourier transforming both sides of (10.18) and re-arranging yields

$$\underline{\mathcal{P}}(f) = \int_0^l \mathcal{Q}(z)\, \exp(-z\, \underline{\mathcal{K}}(f))\, dz = \frac{\underline{V}(f)}{\underline{H}_e(f)} \tag{10.20}$$

Chapter 4 discusses how to determine a model for $\underline{\mathcal{K}}(f)$ from the aforementioned $\mathrm{V}_c(t)$, so it seems that one need only replace the $\underline{\mathcal{P}}(f)$ extant in the inverse CLDP IE (10.17) with $\underline{V}(f)/\underline{H}_e(f)$ to determine the desired charge waveform $\mathrm{Q}(z)$. That is, it seems that

$$\mathrm{Q}(z) = \frac{l}{\mathcal{V}} \int_{-\infty}^{\infty} \frac{\underline{V}(f)}{\underline{H}_e(f)\, \underline{C}_g(f)} \exp(z\, \underline{\mathcal{K}}(f))\, df \tag{10.21}$$

would yield the desired PESAW charge recovery.

10.1.5 The Darrell

Unfortunately it is known that, even in the absence of noise in the measured signal $\underline{\mathcal{P}}(f) = \underline{V}(f)/\underline{H}_e(f)$, the unregularized recovery given by (10.21) will be unsatisfactory because the measured (time-sampled) signals $\mathrm{V}[t_n]$ and $\mathrm{H}_e[t_n]$ are inherently bandlimited due to the finite value of the sampling rate Δt operant in $t_n = n\ \Delta t$. The signals $\mathrm{V}[t_n]$ and $\mathrm{H}_e[t_n]$ contain no information about the desired signals $\mathrm{V}(t)$ and $\mathrm{H}_e(t)$ for frequencies f greater than $f_M \equiv 1/(2\Delta t)$ (see sections 4.9 and 4.14.3).

That is, with f_m some generic bandlimiting frequency, it is known that if

$$\underline{\mathcal{P}}_m(f) \equiv \mathrm{W}(f_m, f)\left[\underline{\mathcal{P}}(f) = \int_0^\infty \mathcal{Q}(z)\ \exp(-z\ \underline{\mathcal{K}}(f))\ dz\right] \tag{10.22}$$

where

$$\mathrm{W}(f_m, f) \equiv \mathrm{U}(f + f_m) - \mathrm{U}(f - f_m) \tag{10.23}$$

then

$$\begin{aligned}\mathcal{Q}_m(z) &\equiv \int_{-\infty}^{\infty} \frac{\underline{\mathcal{P}}_m(f)}{\underline{C}_g(f)}\ \exp(z\ \underline{\mathcal{K}}(f))\ df \\ &= \int_{-f_m}^{f_m} \frac{\underline{\mathcal{P}}(f)}{\underline{C}_g(f)}\ \exp(z\ \underline{\mathcal{K}}(f))\ df \\ &= \mathcal{Q}(z) * \mathrm{D}(f_m, z)\end{aligned} \tag{10.24}$$

where

$$\mathrm{D}(f_m, z) = \exp(z\ \alpha(f_m))\ \frac{\sin(2\pi z f_m / c(f_m))}{\pi z} \tag{10.25}$$

is called 'the Darrell' and (10.24) is called 'the Darrell property.' Section 7.10 numerically investigated and validated both the Darrell property and the shape of the Darrell.

Clearly, if the quantity $[z\ \alpha(f_M)]$ operant in an experimantal (bandlimited via finite Δt) implementation of (10.21) is non-neglibible then that recovery will be unacceptable due to the impact of the Darrell.

With $f_k \equiv k\ \Delta f$ and $\Delta f \equiv 1/(N_t \Delta t)$ (where N_t is the number of time samples comprising both $\mathrm{V}[t_n]$ and $\mathrm{H}_e[t_n]$), this thesis investigates regularization of the numeric implementation of (10.21) by lowpass filtering $\mathcal{P}[f_k]$ via the filter $\mathrm{B}(f_c, f)$ known

as Blackman's Lucky Guess (see appendix B). This thesis' resultant Lyons recovery (regularized numeric implementation of (10.17)) is:

$$\mathrm{R}(z) \equiv \tilde{\mathcal{Q}}(z)$$

$$= \Delta f \sum_{f_k=-f_M}^{f_M} \mathrm{B}(f_c(z), f)\, \frac{\underline{\mathcal{P}}[f_k]}{\underline{C}_g(f_k)}\, \exp(z\, \underline{\mathcal{K}}(f_k)) \tag{10.26}$$

from which it follows (in accordance with (10.21)) that

$$\tilde{\mathrm{Q}}(z) = \frac{l}{\mathcal{V}}\, \mathrm{R}(z) \tag{10.27}$$

when $\underline{\mathcal{P}}[f_k]$ is replaced with $\underline{V}[f_k]/\underline{H}_e[f_k]$ where $\underline{V}[f_k]$ and $\underline{H}_e[f_k]$ are, respectvely, the FFT's of $\mathrm{V}[t_n]$ and $\mathrm{H}_e[t_n]$.

If the BLG cutoff frequency $f_c(z)$ is a function of z the resultant recovery is termed an SDB recovery (spatially dependent Blackman); if $f_c(z)$ is a constant the resultant recovery is termed an SIB recovery (spatially independent Blackman).

10.1.6 Synthetic Validation Of The Lyons Recovery

Chapter 8 investigated both SIB and SDB recoveries of source waveforms $\mathcal{Q}(z)$ embedded in standard polyethylene $\underline{\mathcal{K}}_p(f)$. Both recoveries were found to be satisfactory, but it was found that the SDB recovery was superior (when $f_c(z)$ was selected appropriately) in the case where the effects of attenuation and dispersion upon the deep charges was non-negligible *and* maximum resolution of shallow charges was desired.

The SIB and SDB recoveries were also *relaxed*, *ie*: modulated between the $\underline{\mathcal{K}}_p(f)$ used in the forward problem and an appropriately chosen delay-only $\underline{\mathcal{K}}_d(f) = \mathrm{j}\ 2\pi f/c_d$. The relaxation model $\underline{\mathcal{K}}_r(f)$ used in the Lyons recovery (10.26) was modulated via the relaxation parameter X:

$$\underline{\mathcal{K}}_r(f) = \mathrm{X}\, \underline{\mathcal{K}}_p(f) + (1 - \mathrm{X})\, \underline{\mathcal{K}}_d(f) \tag{10.28}$$

When X = 0 the delay-only model results; when X = 1 the standard model for polyethylene results. The relaxed recovery was investigated for values of X between zero and unity in 0.25 increments. It was found that, independent of source-placement depth, the recovered width and the recovered localized areas of the embedded source pulses each moved monotonically towards their correct values as X increased. The error in the location of peak position was not a monotonic function of X for each source location and for each range of X, but the peak-location error did decrease for each source location as X was increased from 0.75 to 1.

These results were confirmed for two functional forms for $f_c(z)$: $f_c(z) = \grave{f}_c(z)$ (the standard SDB function; see appendix B) and $f_c(z) = 0.65\grave{f}_c(z) \equiv f'_c(z)$. For the case X = 1, the position-independent 35% decrease in the operant $f_c(z)$ (from $\grave{f}_c(z)$ to $f'_c(z)$) resulted in a position-independent 53% increase in the recovered pulses' FWHM. This suggests that the SDB-regularized Lyons recovery exhibits a kind of generalized bound duration•bandwidth (here, spatial width•bandwidth) product relationship analogous to that exhibited by the Fourier transform [58].

Because using $\underline{\mathcal{K}}_r(f)$ with X = 0 in (10.26) results in the dominant recovery whereas using X = 1 results in the Lyons recovery, the fact that the X $\rightarrow$ 1 recovery of embedded source pulse width, localized area, and peak location bettered the X $\rightarrow$ 0 recovery suggests that the Lyons recovery should give a better overall recovery than the dominant recovery in the experimental setting.

10.1.7 Experimental Validation Of The Lyons Recovery

It is difficult to experimentally validate non-destructive charge recovery methods because the desired charge waveform embedded within the dielectric is not known in advance; the current situation is markedly different from the previous section's. Chapter 9's endeavor to address this difficulty proceeded by attempting to confirm that the recoveries gleaned from one single sample, mounted in each of the two possible mounting orientations, agree with each other. The idea is that if the recoveries gleaned from these two mounting orientations 'agree with each other' (however that might be defined) then that common charge recovery will be, in effect, independently confirmed and therefore validated.

It is, of course, possible that the Lyons recoveries gleaned from the signals acquired from each of these two mounting orientations may agree with each other and yet substantively disagree with the true charge waveform because some unknown effect is at work to make the recoveries appear so.

However, the successes observed in the previous section suggest that the 'unknown effect' hypothesis may reasonably be rejected by appealing to Occam's Razor. The likelihood of the 'unknown effect' hypothesis being valid may be reduced even further by (A) investigating whether the recovered charge waveform 'satisfies' (however that might be defined) the known applied voltage boundary condition and (B) investigating whether the physical requirement that the total charge in and on the sample vanish is 'satisfied.'

If the charge waveforms gleaned from the signals acquired with the sample mounted in the two orientations agree with each other, and if that common charge waveform also satisfies the two known physical requirements of the embedded charge waveform, then the simplest (and therefore the most likely, according to Occam) explanation is that the recovered charge waveform is actually 'correct.'

Section 9.2 (*The Double Sided E-Beam Experiment*) executes this 'recovery from two sides.' In this experiment, as in the three others, comparisons of measured and theoretic values corresponding to the inverse medium problem (determining $\underline{\mathcal{K}}(f)$)

suggest that a useful model has been obtained. This thesis' proposed inverse medium solution appears to be valid.

Visual inspection of the charge waveform recoveries (see page 196's figure 9.22) shows that the recoveries gleaned from the two mounting orientations agree quite well with each other insofar as the gross features of the embedded charge waveform are concerned. The voltage boundary condition was also reasonable well confirmed. It seems that the Lyons recovery is indeed applicable to the required PESAW time to space mapping.

However, the sample analyzed in *The Double Sided E-Beam Experiment* was not thick, lossy, and dispersive enough to pose a real challenge for the Lyons recovery; the dominant recovery might have succeeded almost as well. The next experiment (*The Calibration Experiment*) focussed on a thicker, lossier, and more dispersive sample. Unfortunately the signal analyzed in *The Calibration Experiment* corresponds only to plate charges, not bulk charges – but according to PESAW theory the validity of the recovery can be verified by analyzing such a calibration signal. *The Calibration Experiment*'s charge recovery seems to be as successful as *The Double Sided E-Beam Experiment*'s. Taken together, the results of these two experiments suggest that the Lyons recovery is applicable to the PESAW time to space mapping even in the case of deep-seated bulk charges.

The remaining two experiments (*The DC Field Experiment* and *The Distal Dipole Experiment*) start from this standpoint and proceed to validate that the Lyons recovery is applicable to the PESAW time to space mapping of signals acquired from samples containing (A) charges generated by long term exposure to DC fields and (B) charge dipoles, even if they are located near the capacitor plates.

Although it is difficult to quantify – qualitatively, the novel PESAW inverse medium procedure for determining a pressure wave propagation model $\{\alpha(f), c(f)\}$ from a measured PESAW calibration signal appears quite successful. For example, see figures 9.3 and 9.4. These figures show that the raw (pre-parameter estimation) recovered models for $\alpha(f)$ and $c(f)$ gleaned from calibration signals acquired with the sample mounted in each of its two possible configurations agree admirably.

10.1.8 Overall

This thesis has presented and employed a novel theory for the inversion of a class of IEs (the CLDP IEs) arising from the analysis of the PESAW experiment. Although the focus has been placed upon polymeric materials, the mathematical theory (and the preliminary numeric results concerning the Darrell property and the shape of the Darrell) suggest that these methods should also work for non-polymeric dielectrics.

These mathematics may well prove useful beyond the PESAW context – they are independent of the PESAW experiment. The results concerning the Darrell and the CLDP criterion may prove important to the theory of the inversion of the Laplace transform.

10.2 Surmises

10.2.1 Recovery From Inhomogeneous Materials

Consider a slab of material with an inhomogeneous (spatially dependent) propagation coefficient $\underline{\mathcal{K}}'(z,f)$, where the diacritical mark $'$ denotes a correspondence to the inhomogeneous case. The relationship between a homogeneous material's $\underline{\mathcal{K}}(f)$ and its transfer function $\underline{H}(z,f)$ has already been established: $\underline{H}(z,f) = \exp(-z\,\underline{\mathcal{K}}(f))$. But what is the generalization $\underline{H}'(z,f)$ corresponding to $\underline{\mathcal{K}}'(z,f)$? And how might the recovery (10.17) be generalized for this inhomogeneous case?

This analysis starts by attempting to calculate $\underline{H}'(\xi,f)$, where ξ is some specific value of z. By mentally subdividing the material between $z = 0$ and $z = \xi$ into a series of N_z thin ($\Delta z = \xi/N_z$) slabs of material, $\underline{H}'(\xi,f)$ must (by Fourier theory's convolution theorem) be the $N_z \to \infty$ limit of the product of the N_z slabs between $z = 0$ and $z = \xi$:

$$\underline{H}'(\xi,f) = \lim_{N_z\to\infty}\left\{\prod_{i=1}^{N_z}\exp\Big(-\frac{\xi}{N_z}\,\underline{\mathcal{K}}'\big([i-\tfrac{1}{2}]\,\frac{\xi}{N_z},\ f\big)\Big)\right\} \tag{10.29}$$

This process can clearly be repeated for arbitrary ξ. The result is that $\underline{H}'(z,f)$ has effectively been obtained. Now note that replacing $\exp(z\,\underline{\mathcal{K}}(f)) = 1/\underline{H}(z,f)$ in (10.17) yields

$$\mathcal{Q}(z) = \int_{-\infty}^{\infty}\frac{\dot{\underline{\mathcal{P}}}(f)\,df}{\underline{C}_g(f)\,\underline{H}(z,f)} \tag{10.30}$$

It seems that if an (inhomogeneous) analogue $\underline{C}'_g(z,f)$ to the (homogeneous) $\underline{C}_g(f)$ in (10.30) could be found, then

$$\mathcal{Q}'(z) = \int_{-\infty}^{\infty}\frac{\underline{\mathcal{P}}'(f)\,df}{\underline{C}'_g(z,f)\,\underline{H}'(z,f)} \tag{10.31}$$

might well yield an at least approximate recovery from the $\underline{\mathcal{P}}'(f)$ given by

$$\underline{\mathcal{P}}'(f) = \int_{0}^{\infty}\mathcal{Q}'(z)\,\underline{H}'(z,f)\,dz \tag{10.32}$$

The author proposes generalizing the usual definition of the group velocity

$$\frac{1}{\underline{C}_g(f)} = \frac{1}{\mathrm{j}2\pi}\left[\frac{d\,\underline{\mathcal{K}}(f)}{df}\right]^{-1} \tag{10.33}$$

to

$$\frac{1}{\underline{C}'_g(z,f)} = \frac{1}{\mathrm{j}2\pi}\left[\frac{\partial\,\underline{\mathcal{K}}'(z,f)}{\partial f}\right]^{-1} \tag{10.34}$$

and simply notes that, in this case, the proposed recovery for inhomogeneous materials (10.31) reduces to the inverse CLDP IE in the case of a homogeneous material.

Unfortunately, given the proposed definitions of $\underline{H}'(z,f)$ and $\underline{C}'_g(z,f)$, neither (10.31) nor (10.32) take into account the spatially distributed wave reflections that will occur in the bulk as a result of the spatially dependent acoustic impedence corresponding to the spatially dependent $\underline{\mathcal{K}}'(z,f)$.

10.2.2 Supplanting The BLG Filter

Defining

$$\gamma(f_c; z, f) \equiv z\,\alpha(f) + \ln\Big(\mathrm{B}(f_c, f)\Big) \tag{10.35}$$

allows this thesis' BLG-regularized Lyons recovery

$$\mathrm{R}(z) = \int_{-\infty}^{\infty} \frac{\underline{\mathcal{P}}(f)\;\mathrm{B}(f_c,f)}{\underline{C}_g(f)}\;\exp(z\;[\alpha(f) + \mathrm{j}\;2\pi f/c(f)])\;df \tag{10.36}$$

to be expressed as

$$\mathrm{R}(z) = \int_{-\infty}^{\infty}\left[\;|\underline{\mathcal{P}}(f)|\;\exp(\gamma(f_c; z, f))\;\right]\;\frac{\exp(\langle\underline{\mathcal{P}}(f)\rangle - \langle\underline{C}_g(f)\rangle + \mathrm{j}\;z\;2\pi f/c(f))}{|\underline{C}_g(f)|}\;df \tag{10.37}$$

where, *eg*,

$$\underline{\mathcal{P}}(f) = |\underline{\mathcal{P}}(f)|\;\exp(\mathrm{j}\;\langle\underline{\mathcal{P}}(f)\rangle) \tag{10.38}$$

The term $\exp(\gamma(f_c; z, f))$ corresponds to the frequency-dependent amplification used in the BLG-regularized Lyons recovery of a source at z; the term $\gamma(f_c; z, f)$ is the natural logarithm of that amplification.

Figure 10.1 depicts the frequency dependent logarithm of the amplification used in the BLG-regularized Lyons recovery of a $z = 5$ mm source (solid lines) and a $z = 1$ mm source (dashed lines) embedded in standard polyethylene $\underline{\mathcal{K}}_p(f)$. For each source depth z, figure 10.1 depicts the frequency dependent logarithm of both the unfiltered

($f_c = \infty$; circled lines) amplification and the filtered ($f_c = 25$ MHz; un-circled lines) amplification. Note that $\mathrm{B}(f_c = \infty, f) = 1$.

In each case ($z = 1$ mm and $z = 5$ mm) the amplification used by the filtered recovery decreases significantly with frequency. It seems that if the data in $\underline{\mathcal{P}}(f)$ were valid up to, say, 25 MHz then the BLG-regularized Lyons would, in effect, be 'throwing out the baby with the bathwater' by not fully including the information in the lower ($f < 25$ MHz) frequencies.

The author surmises that, in this case, it might be wiser to implement a non-BLG $\gamma(z, f)$ that (for any particular z) falls between the filtered and the unfiltered versions of $\gamma(f_c; z, f)$.

In the extreme case, $\gamma(z, f)$ would be given by $z\alpha(f)$ for $f < 25$ MHz and would equal negative infinity for $f \geq 25$ MHz. This would amount to $\underline{\mathcal{P}}(f)$ being sharply bandlimited at 25 MHz and so the recovery (not including the influence of noise at these lower frequencies) would then be, according to the Darrell property, the true charge convolved with the Darrell determined by $\alpha(f_m), c(f_m)$, and f_m. This un-regularized recovery could then be regularized post-recovery (*ie*: in the space domain) via some technique optimized to remove both the Darrell's oscillations and the influence of noise.

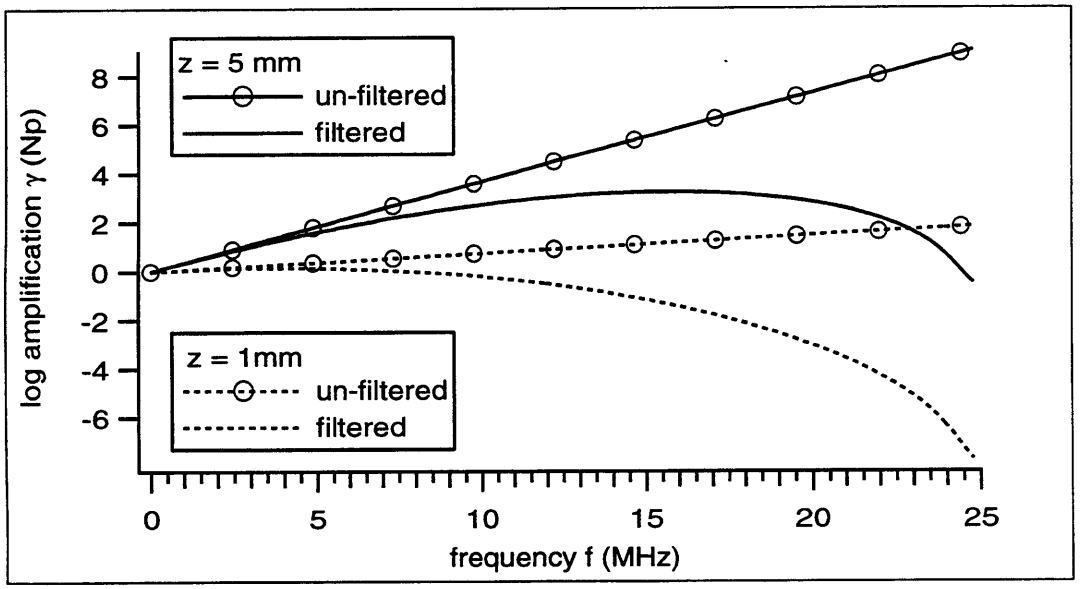

Figure 10.1: Logarithm of the frequency dependent amplification used in the BLG-regularized Lyons recovery of a $z = 5$ mm source (solid lines) and a $z = 1$ mm source (dashed lines) embedded in standard polyethylene. Circled lines correspond to un-filtered ($f_c = \infty$) recoveries; un-circled lines correspond to $f_c = 25$ MHz recoveries.

Appendix A

Wave Equation Transfer Function

This appendix provides a self-contained, shorthand derivation of chapter 3's result that the transfer function $\mathrm{H}(l, f)$ for a thickness l slab of CLDP material is given by

$$\mathrm{H}(l, f) = \exp(-l\, \underline{\mathcal{K}}(f)) \tag{A.1}$$

where the complex propagation coefficient $\underline{\mathcal{K}}(f)$ is given by

$$\underline{\mathcal{K}}(f) = \alpha(f) + \mathrm{j}\, 2\pi f/c(f) \tag{A.2}$$

This appendix is meant to augment, not replace, chapter 3's discussion by emphasizing the importance of the frequency domain to analysis of the wave equation. This appendix's starting point is the familiar linear, one dimensional linear wave equation

$$\frac{\partial^2}{\partial z^2}\mathrm{g}(z,t) - \frac{1}{c^2}\frac{\partial^2}{\partial t^2}\mathrm{g}(z,t) = 0 \tag{A.3}$$

for which c is assumed positive and real. Note that in the time domain it is unclear how to include the possibility of a frequency dependent $c \rightarrow c(f)$, and even less clear how to include the possibility of frequency dependent attenuation $\alpha(f)$.

In shorthand form, Fourier analysis advocates replacing

$$\frac{\partial}{\partial t} \rightarrow \mathrm{j}\, 2\pi f \tag{A.4}$$

and

$$\mathrm{g}(z,t) \rightarrow \underline{g}(z,f) \tag{A.5}$$

where $\underline{g}(z,f)$ is the Fourier transform of $\mathrm{g}(z,t)$ (see appendix F for this thesis' definition of the Fourier transform). Performing these transformations upon (A.3) results in

$$\frac{d^2}{dz^2}\underline{g}(z,f) + \mathrm{k(f)}^2\ \underline{g}(z,f) = 0 \tag{A.6}$$

where

$$\mathrm{k(f)} = \frac{2\pi f}{c} \tag{A.7}$$

is the familiar propagation wavenumber [21].

According to the definitions outlined by Churchill and Brown [78], Fourier transforming (A.3) changes it from a hyperbolic to a parabolic differential equation. It also changes it from a real, partial differential equation to a complex, total differential equation. Churchill and Brown state that the generic second order linear partial differential equation

$$\mathrm{A}\ u_{zz} + \mathrm{B}\ u_{zy} + \mathrm{C}\ u_{yy} + \mathrm{D}\ u_z + \mathrm{E}\ u_y + \mathrm{F}\ u = \mathrm{G} \tag{A.8}$$

in $u(z,y)$ where A, B, ... , G are constants or functions of z and y only, is of hyperbolic, elliptic, or parabolic type in a region of the zy plane if the quantity $\Gamma \equiv \mathrm{B}^2 - 4\mathrm{AC}$ is positive, negative, or zero, respectively, throughout that region.

In the time domain, $y \rightarrow t$ whereas in the frequency domain $y \rightarrow f$. Reviewing the time domain expression of the wave equation (A.3) and the frequency domain expression of the wave equation (A.6) it is clear that, in either domain, A = 1, B = D = E = G = 0, and the relevant region is the entire zy plane. In either domain, Γ reduces to - 4 C.

In the time domain $\mathrm{C} = -1/c^2$ and F = 0 so $\Gamma = 4/c^2 > 0$. The time domain wave equation is hyperbolic. After Fourier transforming, C = 0 and $\mathrm{F} = \mathrm{k}^2(f)$. The frequency domain expression of the temporal wave equation is parabolic. Fourier transforming the wave equation fundamentally changes its nature so that it becomes directly integrable. The solutions to (A.6) are

$$\underline{g}(z,f) = \exp(\pm\ \mathrm{j}\ z\ \mathrm{k}(f))\ \underline{g}(0,f) \tag{A.9}$$

Although the $\mathrm{k}(f)$ given by (A.7) is certainly real because all of its terms are real, the solution (A.9) to (A.6) would still be valid if k(f) were complex:

$$\underline{k}(f) = \mathrm{k}_r(f) + \mathrm{j}\ \mathrm{k}_i(f) \tag{A.10}$$

where both $\mathrm{k}_r(f)$ and $\mathrm{k}_i(f)$ are real. Inserting this complex $\underline{k}(f)$ in place of the real $\mathrm{k}(f)$ in (A.9) yields

$$\underline{g}(z,f) = \exp(\mp\, z\ \mathrm{k}_i(f))\ \exp(\pm\ \mathrm{j}\ z\ \mathrm{k}_r(f))\ \underline{g}(0,f) \tag{A.11}$$

Inverse Fourier transforming (A.11) via the convolution theorem yields

$$\mathrm{g}(z,t) = \left[\mathcal{F}^{-1}\{\ \exp(\mp\ z\ \mathrm{k}_i(f))\}(t)\right] * \mathrm{g}(0, t \pm z/c(f)) \tag{A.12}$$

where the phase velocity $c(f)$ is given by

$$c(f) = \frac{2\pi f}{\mathrm{k}_r(f)} \tag{A.13}$$

Assuming $c(f) > 0$ and requiring $+z$ propagating solutions (because the goal is to find the $z = l$ transfer function) excludes one of the two solutions for $\mathrm{g}(z,t)$ given in (A.12), so that

$$\mathrm{g}(z,t) = \left[\mathcal{F}^{-1}\{\ \exp(z\ \mathrm{k}_i(f))\}(t)\right] * \mathrm{g}(0, t - z/c(f)) \tag{A.14}$$

Fourier transforming (A.14) yields

$$\underline{g}(z,f) = \exp(z\ \mathrm{k}_i(f))\ \exp(-\mathrm{j}\ 2\pi f z/c(f))\ \underline{g}(0,f) \tag{A.15}$$

or, substituting l for z and rearranging,

$$\frac{\underline{g}(l,f)}{\underline{g}(0,f)} \equiv \underline{H}(l,f) = \exp(l\ \mathrm{k}_i(f))\ \exp(-\mathrm{j}\ 2\pi f l/c(f)) \tag{A.16}$$

Defining the attenuation coefficient $\alpha(f)$ via [62]

$$\alpha(f) \equiv \frac{-\ln|\underline{H}(l,f)|}{l} \tag{A.17}$$

implies

$$\alpha(f) = -\mathrm{k}_i(f) \tag{A.18}$$

so that

$$\underline{H}(l,f) = \exp(-l\ [\alpha(f) + \mathrm{j}\ 2\pi f/c(f)]) \tag{A.19}$$

This result is completely in agreement with (A.1) and (A.2). Finally, note that expressing (A.2) in terms of $\mathrm{k}_r(f)$ and $\mathrm{k}_i(f)$ via equations (A.13) and (A.18) yields

$$\begin{aligned}
\underline{\mathcal{K}}(f) &= \alpha(f) + \mathrm{j}\,\frac{2\pi f}{c(f)} \\
&= [-\mathrm{k}_i(f)] + \mathrm{j}\,\frac{2\pi f}{[2\pi f/\mathrm{k}_r(f)]} \\
&= \mathrm{j}\,[\mathrm{k}_r(f) + \mathrm{j}\,\mathrm{k}_i(f)] \\
&= \mathrm{j}\,\underline{\mathrm{k}}(f) \qquad \text{(A.20)}
\end{aligned}$$

Appendix B

The BLG Filter $\mathrm{B}(f_c, f)$ And The Standard SDB Function $\grave{f}_C(z)$

B.1 The Filter $\mathrm{B}(f_c, f)$ (Blackman's Lucky Guess)

In this thesis, the lowpass filter known as Blackman's Lucky Guess (BLG) is used exclusively because it has an historic connection to the PESAW experiment that arose from its almost total lack of the time domain ripple generally effected by lowpass filtering.

The BLG filter $\mathrm{B}(f_c, f)$ is not defined for $f < 0$. For $f \geq f_c$, $\mathrm{B}(f_c, f)$ yields zero. For $0 \leq f < f_c$,

$$\begin{aligned} \mathrm{B}(f_c, f) = \; & 0.35875 \\ & +0.48829 \cos(\pi f/f_c) \\ & +0.14128 \cos(2\pi f/f_c) \\ & +0.01168 \cos(3\pi f/f_c) \end{aligned} \tag{B.1}$$

Figure B.1 depicts the BLG filter. Note that $\mathrm{B}(f_c, 0.24445 f_c) \cong 1/\sqrt{2}$, so that the 3 dB point f_3 of the BLG filter is given approximately by

$$f_3(f_c) \cong \kappa_3 f_c \tag{B.2}$$

where

$$\kappa_3 = 0.24445 \tag{B.3}$$

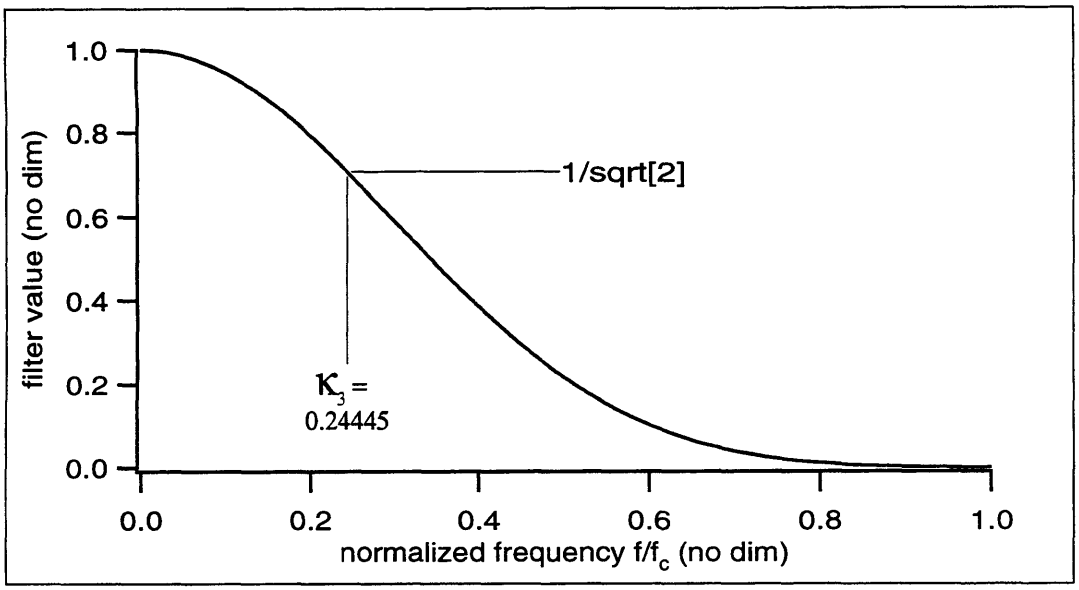

Figure B.1: The BLG filter.

B.2 The Standard SDB Function $\grave{f}_c(z)$

The BLG filter $B(f_c, f)$ (figure B.1) and the standard SDB function $\grave{f}_c(z)$ (figure B.2) are used together to in part define this thesis' SDB-regularized Lyons recovery (4.60).

As discussed on page 89, the standard SDB function was hand-modified to determine a shape that would yield "acceptable suppression" of the λ oscillations *and* yield as small a resolution FWHM as possible *and* preserve an apparently intrinsic tendency towards linear FWHM *vs* z behavior.

The exponential fit $f_c^{\mathrm{e}}(z)$ shown is defined through equations (4.82) and (4.83) using $f_c^{\mathrm{hi}} = 80$ MHz, $f_c^{\mathrm{lo}} = 23.3$ MHz, and $l = 6$ mm so $z' \cong 4.864$ mm. Equation (4.82) and equation (4.83) are re-produced below:

$$f_c^{\mathrm{e}}(z) = f_c^{\mathrm{hi}} \exp(-z/z^{\mathrm{e}}) \tag{B.4}$$

where

$$z^{\mathrm{e}} = \frac{l}{\ln(f_c^{\mathrm{hi}}/f_c^{\mathrm{lo}})} \tag{B.5}$$

Figure B.3 depicts $B(\grave{f}_c(z), f)$ for two values of z: $z = 0.25$ mm and $z = 4.75$ mm.

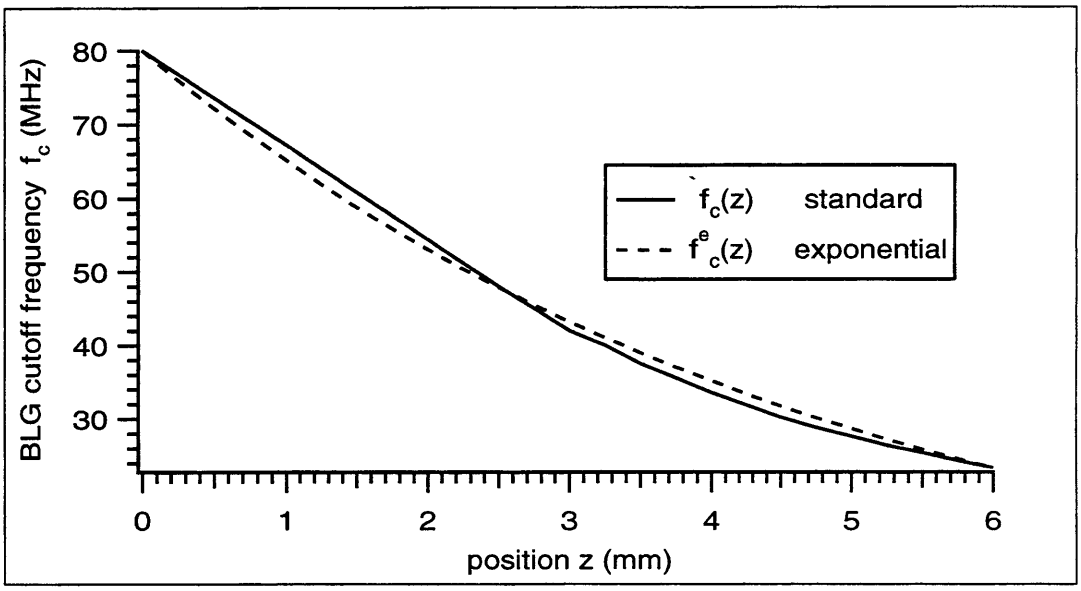

Figure B.2: Comparison of the standard SDB function $\hat{f}_c(z)$ with the exponential SDB function $f_c^e(z)$ that agrees with $\hat{f}_c(z)$ at $z = 0$ and $z = l = 6$ mm.

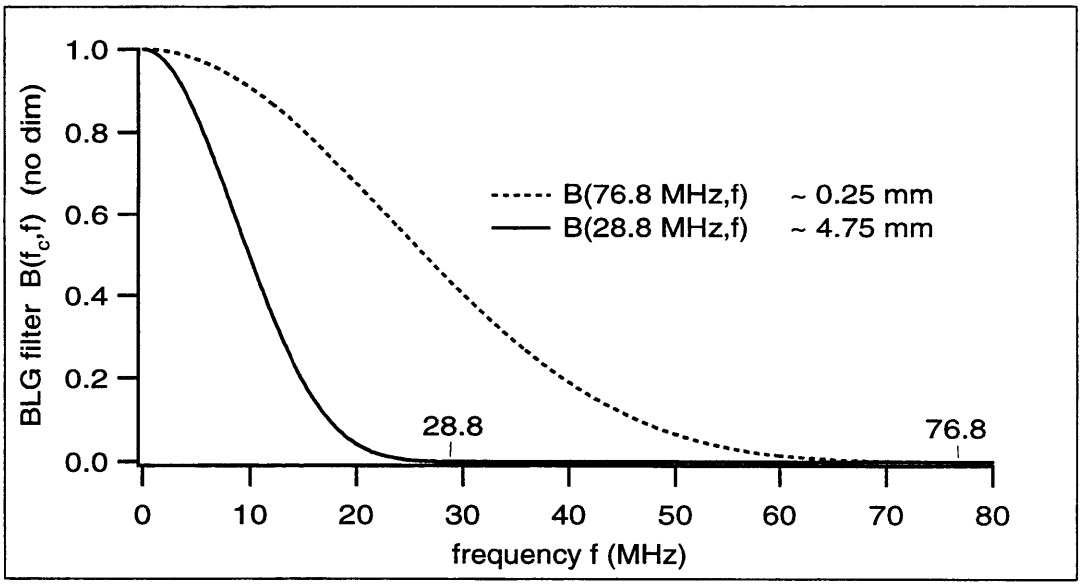

Figure B.3: Comparison of $B(\hat{f}_c(0.25 \text{ mm}), f)$ with $B(\hat{f}_c(4.75 \text{ mm}), f)$. Note that $\hat{f}_c(0.25 \text{ mm}) = 76.8$ MHz whereas $\hat{f}_c(4.75 \text{ mm}) = 28.8$ MHz.

Appendix C

Data Describing The Three Standard Materials

Section 6.2.2 introduces the model $\{\alpha_p(f), c_p(f)\}$ for standard polyethylene . Section 6.5.1 introduces the model $\{\alpha_s(f), c_s(f)\}$ for the standard skin-effect material. Section 6.1.1 introduces the Bromwich materials $\{\alpha_b(f), c_b(f)\} = \{\alpha_b, c_b\}$.

The standard skin-effect and Bromwich materials were chosen so that all three $\alpha(f)$'s have the same 25 MHz value, and all three $c(f)$'s have the same 25 MHz value. That is,

$$\alpha_b = \alpha_p(25 \text{ MHz}) = \alpha_s(25 \text{ MHz}) = 1.825 \text{ Np/mm} \tag{C.1}$$

$$c_b = c_p(25 \text{ MHz}) = c_s(25 \text{ MHz}) = 2.07553 \text{ mm/us} \tag{C.2}$$

Figure C.1 on page 256 depicts each material's 1 mm impulse response function. That is, figure C.1 depicts $\{\mathrm{H}_p(1 \text{ mm}, t), \mathrm{H}_s(1 \text{ mm}, t), \mathrm{H}_b(1 \text{ mm}, t)\}$.

The fast Fourier transform (FFT) was used to produce these plots. The number of time samples $N_t = 4096$; the temporal sampling rate $\Delta t = 2$ ns. This implies

$$\Delta f = (N_t \, \Delta t)^{-1} = (8.192 \, \mu\text{s})^{-1} \cong 1.2207 \text{ MHz} \tag{C.3}$$

and

$$f_M = (2\Delta t)^{-1} = (0.004 \, \mu\text{s})^{-1} = 250\text{MHz} \tag{C.4}$$

Figure C.2 on page 257 depicts each material's $\alpha(f)$ over the full 250 MHz range. Figure C.3 on page 257 depicts each material's $\alpha(f)$ over the $\{0, 25\}$ MHz range.

Figure C.4 on page 258 depicts each material's $c(f)$ over the full 250 MHz range. Figure C.5 on page 258 depicts each material's $c(f)$ over the $\{0, 25\}$ MHz range.

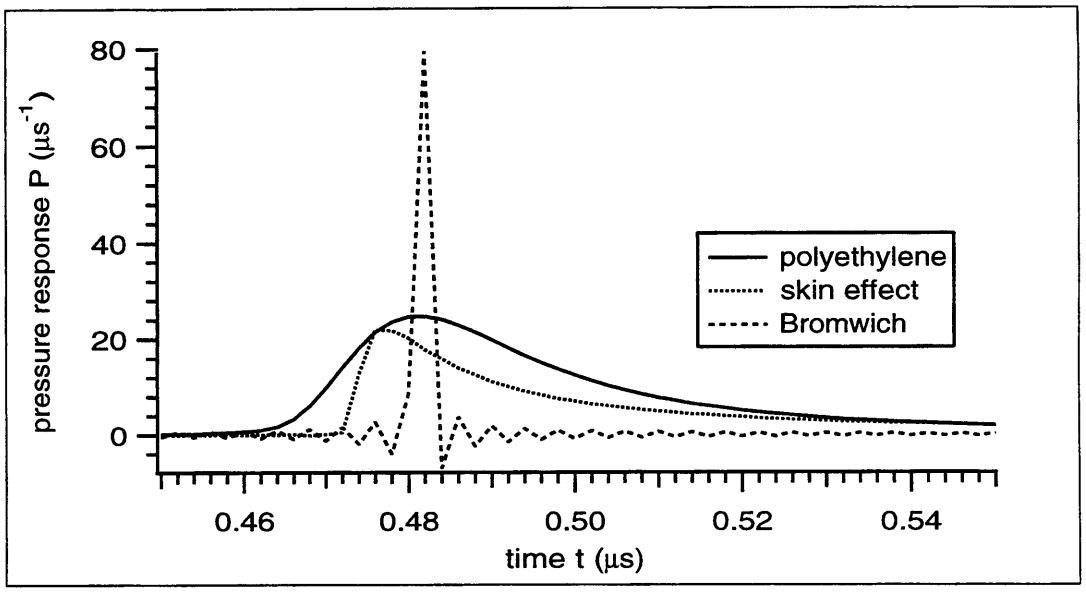

Figure C.1: The 1 mm impulse response for standard polyethylene, skin-effect, and Bromwich materials. That is, the plotted functions are $\hat{\mathrm{H}}_p[1\text{ mm}, t_n]$, $\hat{\mathrm{H}}_s[1\text{ mm}, t_n]$, and $\hat{\mathrm{H}}_b[1\text{ mm}, t_n]$. Only the most interesting 0.1 μs of a total of 8.192 μs are plotted.

		250 MHz	25 MHz	
$\alpha(f)$	polyethylene	18.25	1.825	Np/mm
	skin effect	5.45392	1.825	
	Bromwich	1.825	1.825	
$c(f)$	polyethylene	2.14243	2.07553	mm/μs
	skin effect	2.10756	2.07553	
	Bromwich	2.07553	2.07553	

Table C.1: Values of the attenuation coefficient and phase velocity of this thesis' three standard materials at the two special frequencies $f_M = 250$ MHz and $\grave{f}_m = 25$ MHz.

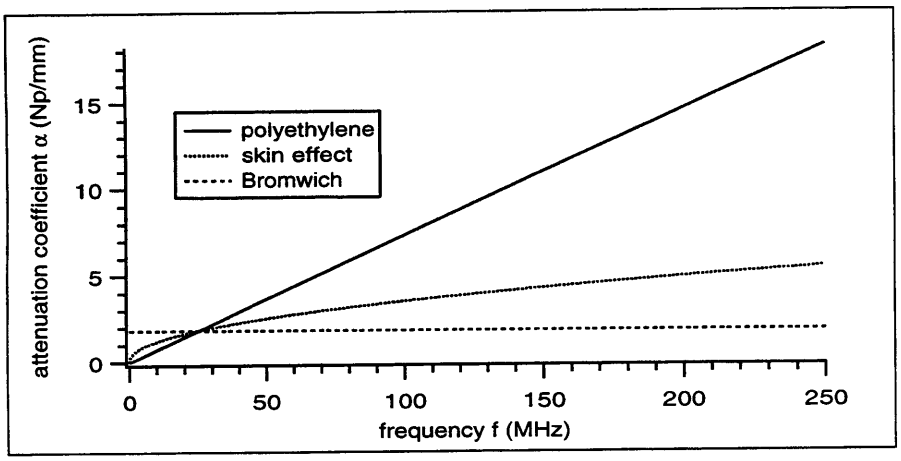

Figure C.2: Full frequency range plots of the attenuation coefficient $\alpha(f)$ for standard polyethylene, skin effect, and Bromwich materials. That is, $\alpha_p(f)$, $\alpha_s(f)$, and $\alpha_b(f)$ are plotted.

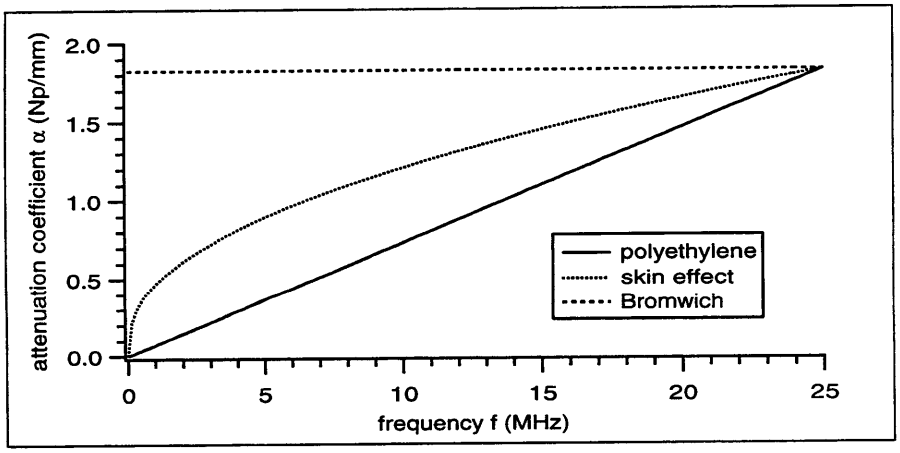

Figure C.3: Low frequency range plots of the attenuation coefficient $\alpha(f)$ for standard polyethylene, skin effect, and Bromwich materials. That is, $\alpha_p(f)$, $\alpha_s(f)$, and $\alpha_b(f)$ are plotted.

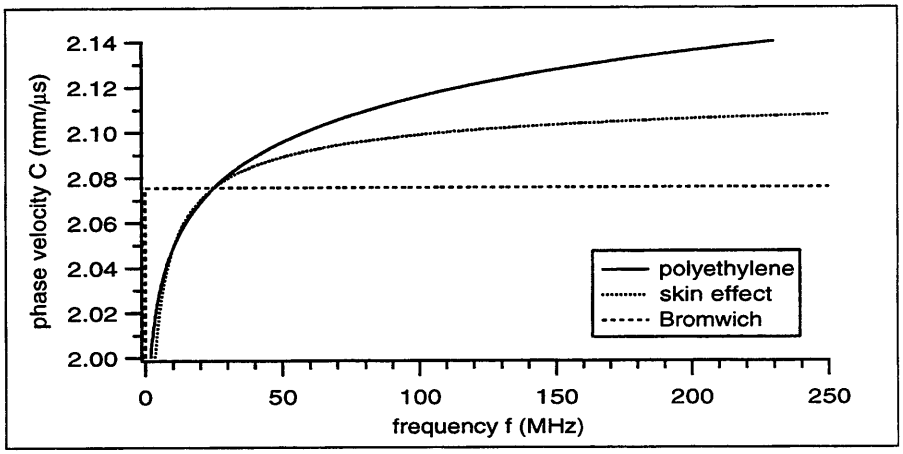

Figure C.4: Full frequency range plots of the phase velocity $c(f)$ for standard polyethylene, skin effect, and Bromwich materials. That is, $c_p(f)$, $c_s(f)$, and $c_b(f)$ are plotted.

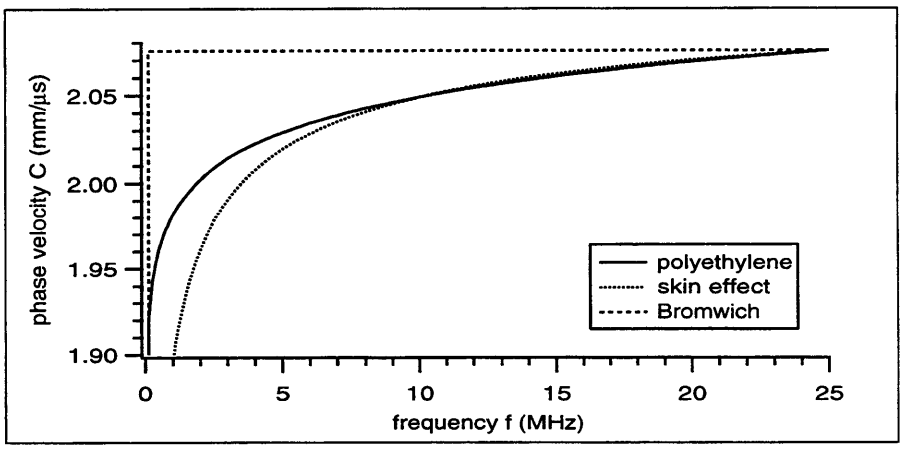

Figure C.5: Low frequency range plots of the phase velocity $c(f)$ for standard polyethylene, skin effect, and Bromwich materials. That is, $c_p(f)$, $c_s(f)$, and $c_b(f)$ are plotted.

Note that $c(f = 0)$ is set to $-\infty$ for each material. This ensures that the angle of the transfer function at the zero frequency will vanish; $\langle \underline{H}(l, f = 0) \rangle = 0$. The true constraint is that $\lim\{f \to 0\}[f/c(f)] = 0$; enforcing $c(0) = -\infty$ ensures that this constraint is met.

Appendix D

Graphical Depiction Of The Principal Insight

The principal insight of CLDP theory (see section 7.1) is stated mathematically as

$$\underline{\mathcal{P}}(f) = \tilde{\underline{\mathcal{Q}}}(\underline{\mathcal{K}}(f)) \tag{D.1}$$

That is, the temporal Fourier transform $\underline{\mathcal{P}}(f)$ of a CLDP IE's response signal $\mathcal{P}(t)$ can be interpreted as the values of the spatial Laplace transform $\tilde{\underline{\mathcal{Q}}}(\underline{\mathcal{K}})$ of that IE's source waveform $\mathcal{Q}(z)$ along a Laplace plane path determined by the material's propagation coefficient

$$\underline{\mathcal{K}}(f) = \alpha(f) + \mathrm{j}\ \underbrace{2\pi f/c(f)}_{\beta(f)} \tag{D.2}$$

For this reason, the propagation coefficient $\underline{\mathcal{K}}(f)$ is sometimes called a CLDP path. Now note that, by Laplace transform theory,

$$\underline{\mathcal{P}}(f) = \tilde{\underline{\mathcal{P}}}(\underline{s} = \sigma + \mathrm{j}\omega)|_{\underline{s}=\mathrm{j}2\pi f} \tag{D.3}$$

That is, the Fourier transform (if it exists) of a causal $\mathcal{P}(t)$ is given by the values of $\mathcal{P}(t)$'s Laplace transform along the j axis. The principal insight therefore relates, point-by-point, a particular path in $\mathcal{P}(t)$'s Laplace plane to a particular path in $\mathcal{Q}(z)$'s Laplace plane. Most explicitly,

$$\tilde{\underline{\mathcal{P}}}(\ 0 + \mathrm{j}\ 2\pi f\ ) = \tilde{\underline{\mathcal{Q}}}(\ \alpha(f) + \mathrm{j}\ 2\pi f/c(f)\ ) \tag{D.4}$$

so that any one particular frequency f (say, $f = 30$ MHz) relates a specific point in the $\underline{s}$ plane to a particular point in the $\underline{\mathcal{K}}$ plane. Figure D.1 (the temporal Laplace plane) and D.2 (the spatial Laplace plane) demonstrate this correspondence graphically for the case of standard polyethylene $\underline{\mathcal{K}}_p(f)$ (see section 6.2.2).

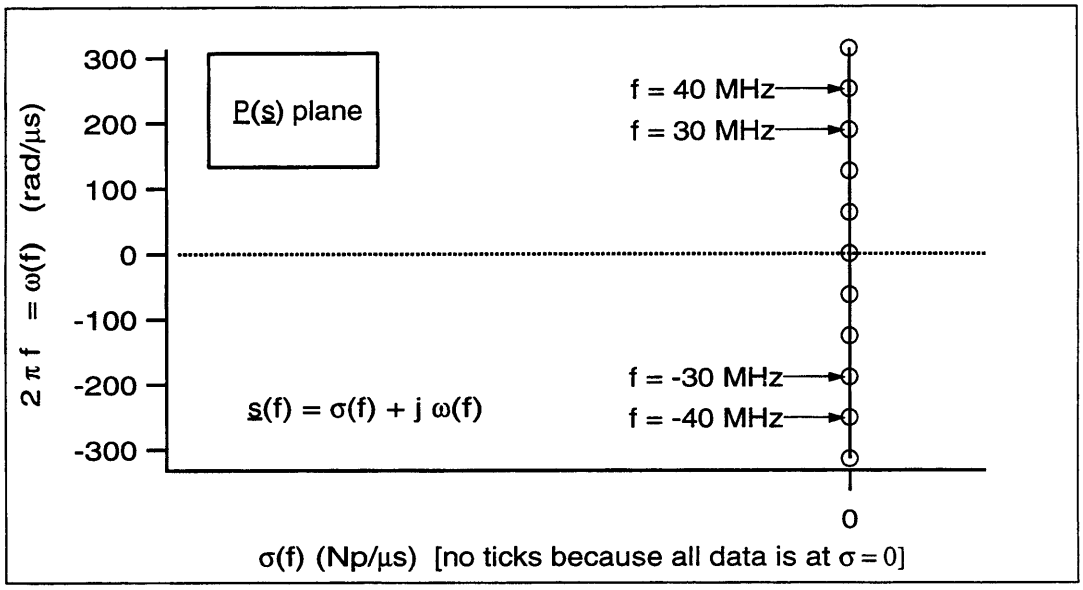

Figure D.1: The temporal Laplace plane.

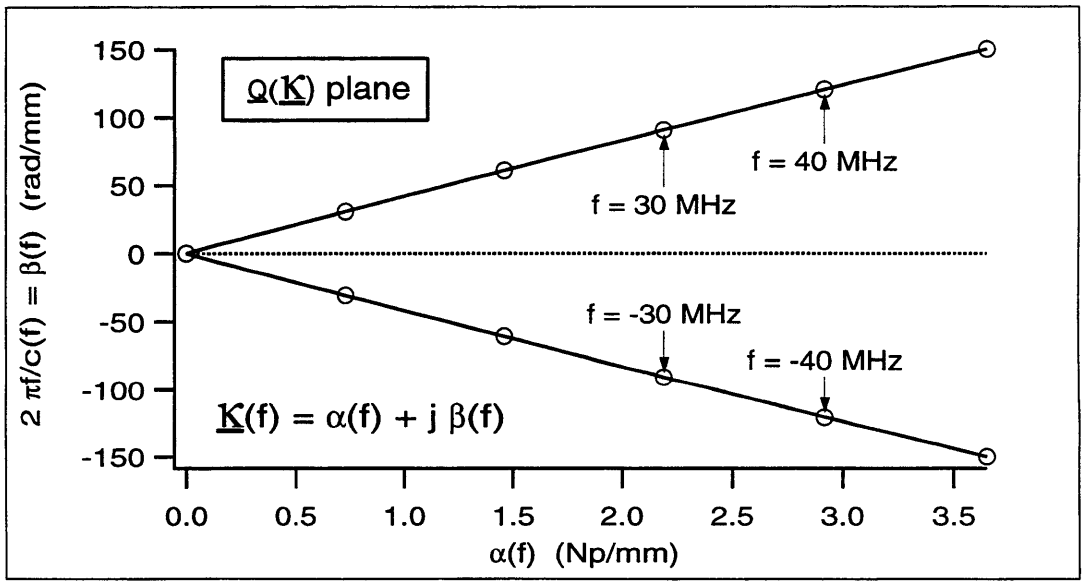

Figure D.2: The spatial Laplace plane.

Figure D.3 is the same as figure D.2 except that standard skin effect and Bromwich CLDP paths are shown as well.

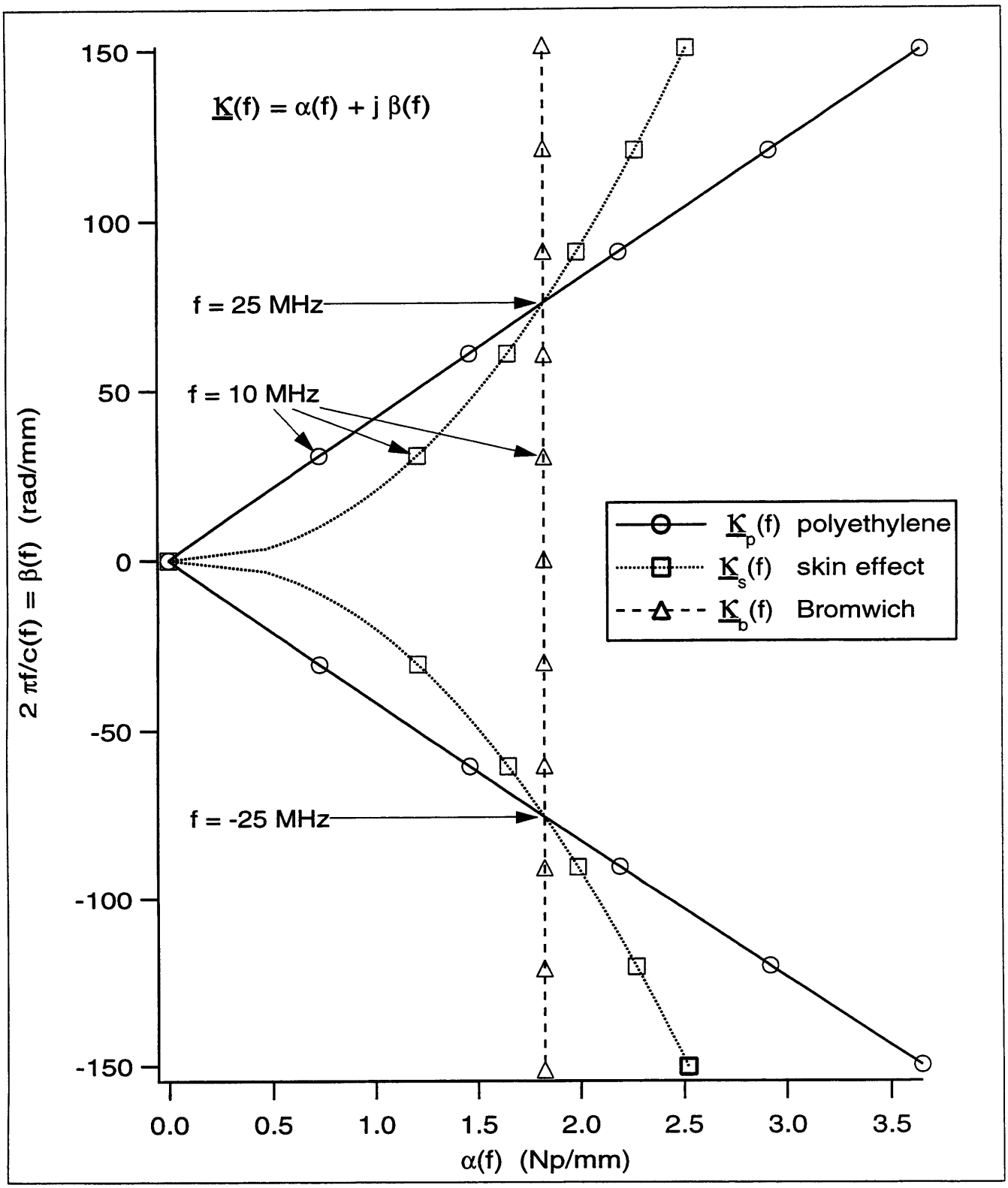

Figure D.3: The spatial Laplace plane.

Appendix E

Key Concepts & Notation

E.1 Bars, Tildes, Hats, Checks

Quantities which may be complex are denoted with an underbar. The temporal Fourier transform $\underline{\mathcal{P}}(f)$ of $\mathcal{P}(t)$ is an example, as is the temporal Laplace transform variable

$$\underline{s} = \sigma + \mathrm{j}\omega = \sigma + \mathrm{j}2\pi f \qquad \text{(E.1)}$$

and as is the temporal Laplace transform $\underline{\tilde{\mathcal{P}}}(\underline{s})$ of $\mathcal{P}(t)$. The $\mathcal{P}$ denoting the Laplace transform $\underline{\tilde{\mathcal{P}}}(\underline{s})$ has a tilde as well as an underbar, to distinguish it from the Fourier transform.

Quantities with tildes but no underbars represent approximate quantities. Functions with square brackets are discrete-valued (meaning: the abscissa's are equally spaced).

For example, $\tilde{\alpha}[f_k]$ represents a series of approximate values of the continuously-valued attenuation coefficient $\alpha(f)$. The f_k's are given by $f_k = k\Delta f$, $0 \leq k < N_f$. In this same vein, $\mathcal{P}[t_n]$ denotes a set of equally spaced temporal samples of $\mathcal{P}(t)$ and $\tilde{\mathcal{Q}}[z_i]$ denotes a set of equally spaced, approximate spatial samples of $\mathcal{Q}(z)$. In this thesis $\mathrm{R}[z_i]$ is used in place of $\tilde{\mathcal{Q}}[z_i]$ to emphasize 'recovery,' and also to avoid producing calligraphic effects in the plotting package.

The spatial Fourier transform of $\mathcal{Q}(z)$ is denoted $\underline{\mathcal{Q}}(\flat)$. The spatial Laplace transform of $\mathcal{Q}(z)$ is denoted $\underline{\tilde{\mathcal{Q}}}(\underline{\mathcal{K}})$ where the spatial Laplace transform variable

$$\underline{\mathcal{K}} = \alpha + \mathrm{j}\beta = \alpha + \mathrm{j}2\pi\flat \qquad \text{(E.2)}$$

There are exceptions to these conventions for the use of underbars and tildes. For example, equation (1.3) uses the notation $\underline{\tilde{\mathcal{P}}}(z, f)$ to denote a filtered approximation to $\underline{\mathcal{P}}(f)$. So bear in mind that, in all cases, if the argument of a function bearing both an underbar and a tilde is complex then that function is a Laplace transform. If the argument of such a function is not complex then that function is not a Laplace transform; rather, it is an approximate complex quantity.

The Fourier and Laplace transforms of temporal (*eg*: $\mathcal{P}(t)$), spatial (*eg*: $\mathcal{Q}(z)$), and generic (*eg*: $\mathrm{G}(x)$) functions are introduced in appendix F. The Hilbert transform and this thesis' proposed CLDP transforms are introduced as well.

An $\mathcal{F}$ denotes the Fourier transformation. For example, $\mathcal{P}(t) \overset{\mathcal{F}}{\Longleftrightarrow} \underline{\mathcal{P}}(f)$ states that $\mathcal{P}(t)$ and $\underline{\mathcal{P}}(f)$ are a Fourier transform pair, implying both that $\mathcal{P}(t) = \mathcal{F}^{-1}\{\underline{\mathcal{P}}(f)\}$ and $\underline{\mathcal{P}}(f) = \mathcal{F}\{\mathcal{P}(t)\}$. In the same vein: an $\mathcal{L}$ denotes the Laplace transformation, an $\mathcal{H}$ denotes the Hilbert transformation, and a $\mathcal{K}$ denotes one of the proposed CLDP transformations.

Hats denote modelled quantities. *Eg*: $\hat{\mathrm{V}}[\overline{\varsigma}, t_n]$ represents a modelled set of samples of $\mathrm{V}(t)$ parameterized by the vector $\overline{\varsigma}$ of m parameters $\{\varsigma_1, \varsigma_2, \varsigma_3 \cdots, \varsigma_m\}$.

Checks denote the causal convolution inverse $\check{\mathrm{G}}(x)$ (if it exists) of a given causal $\mathrm{G}(x)$. A function $\mathrm{G}(x)$ is causal if $\mathrm{G}(x) = \mathrm{G}(x)\ \mathrm{U}(x)$ where $\mathrm{U}(x)$ is the Heaviside unit step function (integral of the Dirac delta function $\delta(x)$). By definition, a function $\mathrm{G}(x)$ and its convolution inverse $\check{\mathrm{G}}(x)$ satisfy $\mathrm{G}(x) * \check{\mathrm{G}}(x) = \delta(x)$ where the $*$ denotes convolution. $|\underline{Z}|$ denotes the magnitude of the complex number $\underline{Z}$; $\langle \underline{Z} \rangle$ represents the principal value of its phase, so that $\underline{Z} = |\underline{Z}| \exp(\mathrm{j}\langle \underline{Z} \rangle)$.

E.2 Acronyms

BC	Boundary Condition
ED	E-beam Entering Distal plate
EP	E-beam Entering Proximal plate
IE	Integral Equation
KK	Kramers-Kronig
PE	Polyethylene
SD	Spatially Dependent
TL	Transmission Line
BLG	Blackman's Lucky Guess
FFT	Fast Fourier Transform
PEA	Pulsed Electro-Acoustic
QSA	Quasi-Static Approximation
RHP	Right Half Plane
RMS	Root Mean Square
SDB	Spatially Dependent BLG filtering
SIB	Spatially Independent BLG filtering
CLDP	Causal, Lossy, Dispersive, Plane-wave
FWHM	Full Width at Half Maximum
FWZC	Full Width at first Zero Crossing
NLKK	Nearly Local Kramers-Kronig
PESAW	Pulsed Electrically Stimulated Acoustic Wave
PMMA	Polymethylmethacrylate
PW	Paley-Wiener
PWG	Paley-Wiener-Guillemin

E.3 Signals, Waveforms, Standards

Signal = function of time (or inverse time) alone.
Eg: $\mathcal{P}(t)$, $\underline{\mathcal{P}}(f)$, and $\tilde{\underline{\mathcal{P}}}(\underline{s})$.

Waveform = function of space (or inverse space) alone.
Eg: $\mathcal{Q}(z)$, $\underline{\mathcal{Q}}(\flat)$, and $\tilde{\underline{\mathcal{Q}}}(\underline{\mathcal{K}})$.

Standard = standard with respect to this thesis only.
Eg: No manufacturer intentionally produces 'standard polyethylene' (section 6.2.2) nor has any other researcher discussed it.

E.4 Functions Describing Experiment & Recovery

- $V_a(t)$ The pulsive applied excitation voltage.
  Volts; $V_a(t) = V_o + v_p(t)$
- $Q(z)$ The desired distributed source charge waveform.
  $(nC/cm^2)/mm$
- $\mathcal{P}(t)$ The pressure signal entering the transducer (CLDP response signal).
  Pa = 0.1 (nC/cm^2) (kV/mm); normalized: μs^{-1}
- $H_T(t)$ The pressure-to-voltage transducer.
  V/(Pa μs)
- $V(t)$ The measured voltage signal.
  Volts
- $\mathcal{Q}(z)$ The distributed source pressure waveform (CLDP input waveform).
  $R(z)$ Pa/(mm/μs); normalized: mm^{-1}. $R(z)$ is the recovered estimate to $\mathcal{Q}(z)$.
- $H_e(t)$ The experimental impulse response
  Volts; $H_e(t) = (q_p/l)\, v_p(t) * H_T(t)$
- $E_z(z)$ The spatial component of the separable electric field $E(z,t) = E_z(z)E_t(t)$
  Volt μs/mm. $\mathcal{Q}(z) = Q(z)E_z(z) = Q(z)\ \mathcal{V}/l$.
- $B(f_c, f)$ The filter known as Blackman's Lucky Guess (BLG). $B(\infty, f) = 1$
  no dimension. $B(f_c, f)$ describes a lowpass filter that vanishes for $f > f_c$.
- $f_c(z)$ The spatially dependent BLG cutoff frequency.
  MHz. Used as $B(f_c(z), f)$ to implement SDB filtering.

Appendix G is a one page diagram depicting the relations between the six most important of these functions. The top bar of the Π shaped diagram represents the proposed CLDP transform relations between $\mathcal{Q}(z)$ and $\mathcal{P}(t)$. The left leg shows the relationship between $\mathcal{Q}(z)$ and $Q(z)$, the right leg shows the relationship between $\mathcal{P}(t)$ and $V(t)$.

E.5 The Meanings Of $\mathcal{K}$

With $\alpha(f)$ denoting the attenuation coefficient (Np/mm) and $c(f)$ denoting the phase velocity (mm/μs) of some material, the quantity

$$\underline{\mathcal{K}}(f) = \alpha(f) + \mathrm{j}\ \underbrace{2\pi f/c(f)}_{\beta(f)} \tag{E.3}$$

is defined as the propagation coefficient (see appendix A, or section 3.1). This thesis' principal insight (section 7.1) is that

$$\underline{\mathcal{P}}(f) = \underline{\tilde{\mathcal{Q}}}(\underline{\mathcal{K}}(f)) \tag{E.4}$$

so that whereas $\underline{\mathcal{K}}$ by itself denotes a generic spatial Laplace plane point $\alpha + \mathrm{j}\,\beta$, $\underline{\mathcal{K}}(f)$ denotes both a propagation coefficient and a frequency-parameterized path $\alpha(f) + \mathrm{j}\,\beta(f)$ in the spatial Laplace transform plane $\underline{\mathcal{K}}$.

E.6 The Derivative Of $\mathcal{K}(f)$

Note that $\underline{\mathcal{K}}(f) = \mathrm{j}\,\underline{k}(f)$ (where $\underline{k}(f)$ is the familiar propagation wavenumber from travelling wave theory; see appendix A) so travelling wave theory's $\underline{C}_g(\omega) = d\omega/d\underline{k}(\omega)$ (where $\omega = 2\pi f$ and $\underline{C}_g(\omega)$ is the material's group velocity; see section 2.5.1) becomes

$$\frac{d\,\underline{\mathcal{K}}(f)}{df} = \frac{\mathrm{j}2\pi}{\underline{C}_g(f)} \tag{E.5}$$

The group signal $\mathrm{g}(t)$ (see section 2.5.4) is defined as the inverse Fourier transform of $1/\underline{C}_g(f)$:

$$\mathrm{g}(t) \quad \overset{\mathcal{F}}{\Longleftrightarrow} \quad \underline{g}(f) \equiv \frac{1}{\underline{C}_g(f)} = \frac{1}{\mathrm{j}\,2\pi}\,\frac{d}{df}\left[\alpha(f) + \mathrm{j}2\pi f/c(f)\right] \tag{E.6}$$

E.7 Lyons Recovery *vs* Inverse CLDP IE

A Lyons recovery is the process, or the result, of computing a recovery $\mathrm{R}[z_i]$ via a numeric implementation of the proposed inverse CLDP IE (F.9). Defined this way, the efficacy of the Lyons recovery to PESAW (or other) problems can be evaluated independently of the CLDP transform theorem.

The inverse CLDP IE describes a specific path for inverting the Laplace transform (see sections 7.2 through 7.5). Whether integrating along that path truly inverts the Laplace transform in the appropriate limit is a separate question from whether some specific, truncated, regularized numeric implementation of the proposed inverse CLDP IE yields a worthwhile recovery.

Equation (4.60) specifies this thesis' version of the Lyons recovery.

E.8 CLDP Transfer Function

The transfer function for a thickness l slab of CLDP material is $\underline{H}(l, f) = \exp(-l\,\underline{\mathcal{K}}(f))$ (see appendix A, or section 3.1). That is, if an impulse (Dirac delta function) of pressure is input at position $z = 0$, the output at $z = l$ will be $\mathrm{H}(l, t) = \mathcal{F}^{-1}\{\underline{H}(l, f)\}$. The quantity $\mathrm{H}(l, t)$ is called the thickness l material impulse response function.

The quantity $\underline{\mathcal{K}}(\underline{s}/(\mathrm{j}2\pi))$ is the analytic continuation of $\underline{\mathcal{K}}(f)$:

$$\underline{\mathcal{K}}(\underline{s}/(\mathrm{j}2\pi))\big|_{\underline{s}=\mathrm{j}2\pi f} \quad = \quad \underline{\mathcal{K}}(f) \tag{E.7}$$

so that

$$\mathcal{L}\{\mathrm{H}(l,t)\} = \underline{\tilde{H}}(l,\underline{s}) = \exp(-l\ \underline{\mathcal{K}}(\underline{s}/(\mathrm{j}2\pi))) = \exp(\underline{\gamma}(\underline{s})) \tag{E.8}$$

where $\underline{\gamma}(\underline{s})$ is Guillemin's 'propagation function' (see section 6.5).

E.9 The Darrell

The Darrell $\mathrm{D}(f_m, z)$ is the sharply bandlimited (at $f = f_m$) inverse CLDP transform (F.9) of unity (see section 7.7). The Darrell depends implicitly upon the real and imaginary parts of $\underline{\mathcal{K}}(f_m) = \alpha(f_m) + \mathrm{j}\ 2\pi f_m/c(f_m)$:

$$\mathrm{D}(f_m, z) = \mathcal{K}^{-1}\{\overbrace{\mathrm{U}(f+f_m) - \mathrm{U}(f-f_m)}^{\mathrm{W}(f_m,f)}\} \tag{E.9}$$

$$= \exp(z\ \alpha(f_m))\frac{\sin(2\pi z f_m/c(f_m))}{\pi z} \tag{E.10}$$

$$= \exp(z/\Lambda(f_m))\frac{\sin(2\pi z/\lambda(f_m))}{\pi z} \tag{E.11}$$

The Darrell bears this name because, when $\alpha(f) = \alpha_b$ and $c(f) = c_b$ ($\alpha_b \geq 0, c_b > 0$), the $f_m \to \infty$ limit of the Darrell is the Dirac delta function $\delta(z)$. The Dirac delta function is thin and symmetric whereas the finite f_m lossy ($\alpha(f_m) \neq 0$) Darrell $\mathrm{D}(f_m, z)$ is asymmetric and has finite width. The name 'Darrell' starts with a capital D meant to connote finite width and asymmetry *and* a relationship to $\delta(z)$.

The Darrell's importance lies in the fact that (see section 7.6), if

$$\underline{\mathcal{P}}(f) = \mathcal{K}\{\mathcal{Q}(z)\} \tag{E.12}$$

then

$$\mathrm{R}(f_m, z) \quad \equiv \quad \mathcal{K}^{-1}\{\ \underline{\mathcal{P}}(f)\ \mathrm{W}(f_m, f)\ \} \tag{E.13}$$

$$= \quad \mathrm{D}(f_m, z) * \mathcal{Q}(z) \tag{E.14}$$

That is, if a CLDP output signal $\mathcal{P}(f)$ is sharply bandlimited at f_m then the recovery effected by the proposed inverse CLDP transform will be completely characterized by $\mathrm{D}(f_m, z)$. This is called the Darrell property of the inverse CLDP transform.

$$\Gamma(f_m) \equiv \frac{\Lambda(f_m)}{\lambda(f_m)} = \frac{f_m}{\alpha(f_m)c(f_m)} = \frac{\beta(f_m)}{2\pi\ \alpha(f_m)} \tag{E.15}$$

is a figure of merit for the Darrell specifying how many wavelengths λ fit within the e-fold length Λ.

E.9.1 f_m *vs* f_M

Equation (4.52) and the surrounding discussion point out that if some signal $\mathcal{P}(t)$ is sampled with a time step Δt then the maximum frequency available in the FFT $\underline{\mathcal{P}}[f_k]$ of $\mathcal{P}[t_n] = \mathcal{P}(n\Delta t)$ is $f_M = (2\Delta t)^{-1}$.

That is, sampling with a finite time step Δt implicitly imposes abrupt bandlimiting at $f = f_M$. However, given some $\underline{\mathcal{P}}[f_k]$ implicitly bandlimited at f_M, it is possible to impose abrupt bandlimiting at $f = f_m$ (where $f_m < f_M$) by multiplying $\underline{\mathcal{P}}[f_k]$ by the ideal, square window lowpass filter

$$\mathrm{W}[f_m, f_k] = \mathrm{U}[f_k + f_m] - \mathrm{U}[f_k - f_m] \tag{E.16}$$

In short, f_m is the generic frequency at which $\underline{\mathcal{P}}(f)$ is abruptly bandlimited (as in (E.13)) whereas f_M is the value of f_m implicitly imposed upon sampled functions of time. Unbandlimited Fourier transforms $\underline{\mathcal{P}}(f)$ have $f_m = \infty$. If a function has been non-abruptly filtered (*ie*: smoothly filtered via the BLG filter $\mathrm{B}(f_c, f)$ rather than abruptly filtered via $\mathrm{W}(f_m, f)$) then there is no associated value of f_m.

The appearance of the variable f_m in some expression implies that some function of frequency has been abruptly bandlimited at f_m; the appearance of the variable f_M in some expression implies that the abrupt bandlimiting at $f_m = f_M$ has been implicitly imposed by the finite sampling time step Δt.

E.10 Subscripts: Usual Meaning, Example

- a applied $\mathrm{V}_a(t)$
- b Bromwich $\underline{\mathcal{K}}_b(f)$; or bulk $\mathrm{V}_b(t)$
- c calibration $\mathrm{V}_c(t)$; or cutoff $f_c(z)$
- d delay-only $\underline{\mathcal{K}}_d(f)$; or dominant $\mathrm{R}_d(z)$; or distal $\mathrm{V}_d(t)$
- e experimental $\mathrm{H}_e(t)$
- em electromagnetic $\mathcal{T}_{em}$
- g group $\underline{\mathcal{C}}_g(f)$; or Gaussian $\mathcal{Q}_g(z)$
- i particular value of z: z_i; or impulsive $\mathcal{Q}_i(z)$
- k particular value of f: f_k
- κ kappa $\underline{\mathcal{K}}_\kappa(f)$
- m maximum f_m
- n particular value of t: t_n
- o Ohmic $\underline{\mathcal{K}}_o(f)$; or specific value f_o
- p polyethylene $\underline{\mathcal{K}}_p(f)$; or proximal $\mathrm{V}_p(t)$; or pulsive $v_p(t)$; or plate $\mathrm{F}_p(t)$
- pp peak-to-peak $\mathcal{T}_{pp}$
- r relaxation $\underline{\mathcal{K}}_r$
- rc resistor-capacitor $\mathcal{T}_{rc}$
- s skin-effect $\underline{\mathcal{K}}_s(f)$; or spreading $\mathcal{T}_s$
- T transducer $\mathrm{H}_T(t)$
- z z-dependent portion of a separable function of space and time.
  Eg: the $\mathrm{E}_z(z)$ in $\mathrm{E}(z,t) = \mathrm{E}_z(t)\ \mathrm{E}_t(t)$

Appendix F

Transform Definitions

To ensure that any transform-related results will be readily extensible to either the space or time domain, the transform relations presented here are expressed in terms of a generic real, causal function $\mathrm{G}(x)$ where x can be thought of as either space or time. The Fourier and Laplace transform relations presented here agree with those defined by Siebert [63]. Although the definitions agree, the notation does not.

In this thesis, the Laplace transform $\mathcal{L}$ of $\mathrm{G}(x)$ is denoted $\underline{\tilde{G}}(\underline{\chi})$, where the complex Laplace transform variable $\underline{\chi}$ has real part χ_r and imaginary part χ_i. The Fourier transform $\mathcal{F}$ of $\mathrm{G}(x)$ is denoted $\underline{G}(\aleph)$, where the Fourier transform variable $\aleph = \chi_i/(2\pi)$.

The following table outlines how to relate the generic results for $\mathrm{G}(x)$ to signals and waveforms:

	$\mathcal{L}$ variable	$\mathcal{L}$	$\mathcal{F}$ variable	$\mathcal{F}$
signal $\mathrm{P}(t)$	$\underline{s} = \sigma + \mathrm{j}\,\omega$	$\underline{\tilde{P}}(\underline{s})$	$f = \omega/(2\pi)$	$\underline{P}(f)$
waveform $\mathcal{Q}(z)$	$\underline{\mathcal{K}} = \alpha + \mathrm{j}\,\beta$	$\underline{\tilde{\mathcal{Q}}}(\underline{\mathcal{K}})$	$\mathfrak{b} = \beta/(2\pi)$	$\underline{\mathcal{Q}}(\mathfrak{b})$
generic $\mathrm{G}(x)$	$\underline{\chi} = \chi_r + \mathrm{j}\,\chi_i$	$\underline{\tilde{G}}(\underline{\chi})$	$\aleph = \chi_i/(2\pi)$	$\underline{G}(\aleph)$

Table F.1: Relationship between temporal, spatial, and generic versions of the Fourier and Laplace transforms.

F.1 The Fourier Transform

Following Siebert, the Fourier transform relation is defined by

$$\underbrace{\mathrm{G}(x) = \int_{-\infty}^{\infty} \underline{G}(\aleph) \exp(\mathrm{j}2\pi x\aleph)\, d\aleph}_{\text{Fourier synthesis integral}} \quad \overset{\mathcal{F}}{\Longleftrightarrow} \quad \underbrace{\underline{G}(\aleph) = \int_{-\infty}^{\infty} \mathrm{G}(x) \exp(-\mathrm{j}2\pi\aleph x)\, dx}_{\text{Fourier analysis integral}} \tag{F.1}$$

A 2π factor has been explicitly included in the exponent of both the Fourier analysis and synthesis integrals. This choice obviates the need for the product of the integral prefactors of the synthesis and analysis equations to equal $(2\pi)^{-1}$ (*cf* Oppenheim [64]). Inclusion of the 2π factor in both exponents requires that the prefactor product equal unity. This requirement is simply and symmetrically met by letting both prefactors equal unity.

F.2 The Laplace Transform

Following Siebert again, the Laplace transform relation is defined without the 2π factor in the exponent:

$$\underbrace{\mathrm{G}(x) = \frac{1}{\mathrm{j}2\pi} \int_{\mathcal{C}} \underline{\tilde{G}}(\underline{\chi}) \exp(x\, \underline{\chi})\, d\underline{\chi}}_{\text{Laplace synthesis integral}} \quad \overset{\mathcal{L}}{\Longleftrightarrow} \quad \underbrace{\underline{\tilde{G}}(\underline{\chi}) = \int_{0}^{\infty} \mathrm{G}(x) \exp(-x\, \underline{\chi})\, dx}_{\text{Laplace analysis integral}} \tag{F.2}$$

The subscript $\mathcal{C}$ on the Laplace synthesis integral denotes a line integral along an appropriate path (contour) in the Laplace plane [74].

Section 7.5 has much to say about what these 'appropriate paths' might be, but this is not the place for such a discussion. However, it is worth pointing out that if the $\chi_r = 0$ path is chosen then the inverse Laplace transform reduces to the inverse Fourier transform in the sense that, for causal $\mathrm{G}(x)$,

$$\underline{\tilde{G}}(\underline{\chi})\Big|_{\underline{\chi}=\mathrm{j}2\pi\aleph} = \underline{G}(\aleph) \tag{F.3}$$

It follows that if the region of convergence of $\underline{\tilde{G}}(\underline{\chi})$ does not include the $\mathrm{j}\chi_i$ axis then the Fourier transform does not exist.

Conversely, because the Laplace transform is analytic wherever it is convergent [57], if a causal $\mathrm{G}(x)$'s Fourier transform $\underline{G}(\aleph)$ exists (*ie*: converges for all χ_i) then $\underline{\tilde{G}}(\underline{\chi})$ must be an analytic function of $\underline{\chi}$ in the entire right half plane (RHP, inclusive of j χ_i axis).

F.3 The Fast Fourier Transform

Chapter 4's definitions of the fast Fourier transform (FFT, equation (4.54)) and inverse fast Fourier transform (FFT^{-1}, equation (4.56)) are repeated below for convenience:

$$\overbrace{\underline{G}[\aleph_h] = \text{FFT}\{\text{G}[x_m]\} \equiv \Delta x \sum_{m=0}^{N_x-1} \text{G}[x_m]\ \exp(-\text{j}\ 2\pi\ h\ m/N_x)}^{\text{FFT analysis equation}} \tag{F.4}$$

$$\underbrace{\text{G}[x_m] = \text{FFT}^{-1}\{\underline{G}[\aleph_h]\} \equiv \Delta\aleph \sum_{h=0}^{N_x-1} \underline{G}[\aleph_h]\ \exp(\text{j}\ 2\pi\ m\ h/N_x)}_{\text{FFT synthesis equation}} \tag{F.5}$$

where N_x is an integer power of 2 and $\Delta\aleph = 1/(N_x\Delta x)$. Note that $\Delta x\Delta\aleph = 1/N_x$ so these definitions satisfy the usual FFT prefactor-product constraint.

F.4 The Hilbert Transform

The Hilbert transform relations are introduced in terms of the Kramers-Kronig relations in section 6.1. The Hilbert transform $\text{G}_h(x)$ of some generic $\text{G}(x)$ is given by

$$\underbrace{\text{G}(x) = \text{G}_h(x) * \frac{1}{\pi x}}_{\text{Hilbert synthesis equation}} \quad \overset{\mathcal{H}}{\Longleftrightarrow} \quad \underbrace{\text{G}_h(x) = \text{G}(x) * \frac{-1}{\pi x}}_{\text{Hilbert analysis equation}} \tag{F.6}$$

where the $*$ denotes convolution and the principal value of the convolution integral is to be taken in the case of a singular integrand. Note that the argument of the Hilbert transform of some given function is the same as the argument of the given function.

Hahn [47] and Guillemin [45] both offer extensive discussions of both the Hilbert transform and its relationship to causal and analytic functions. They both ultimately express the Hilbert transform in terms of Laplace plane contour integrals.

F.5 The CLDP Transforms

If some analytic $\underline{\mathcal{K}}(f)$ yields a stable (and necessarily causal; see below) $\mathrm{H}(z,t)$ via

$$\mathrm{H}(z,t) \quad \overset{\mathcal{F}}{\Longleftrightarrow} \quad \underline{H}(z,f) \equiv \exp(-z\,\underline{\mathcal{K}}(f)) \tag{F.7}$$

then

$$\underline{\mathcal{P}}(f) = \int_0^\infty \mathcal{Q}(z)\,\underline{H}(z,f)\,dz \tag{F.8}$$

and

$$\mathcal{Q}(z) = \int_{-\infty}^{\infty} \frac{1}{\mathrm{j}\,2\pi} \frac{d\,\underline{\mathcal{K}}(f)}{df} \frac{\underline{\mathcal{P}}(f)}{\underline{H}(z,f)}\,df \tag{F.9}$$

form a valid CLDP transform relation ($\mathcal{Q}(z) \overset{\mathcal{K}}{\Longleftrightarrow} \underline{\mathcal{P}}(f)$) under that $\underline{\mathcal{K}}(f)$ provided $\mathcal{Q}(z)$ is real, causal (vanishes for negative values of z), has a convergent Fourier transform $\underline{\mathcal{Q}}(\flat)$, and also satisfies the CLDP criterion:

$$\lim_{f\to\infty} \left\{ \int_0^{\alpha(f)} \Im_m\{\underline{\tilde{\mathcal{Q}}}([\alpha' + \mathrm{j}\,2\pi f/c(f)])\,\exp(z\,[\alpha' + \mathrm{j}\,2\pi f/c(f)])\}\,d\,\alpha' \right\} = 0 \tag{F.10}$$

where

$$\underline{\mathcal{K}}(f) = \alpha(f) + \mathrm{j}\overbrace{2\pi f/c(f)}^{\beta(f)} \tag{F.11}$$

satisfies $\alpha(f) \geq 0$ for all f, in which case the material (and $\mathrm{H}(z,t)$) is called stable. An impulse response function $\mathrm{H}(z,t)$ is called causal if it vanishes for all $t < 0$ if $z > 0$. The assumed analyticity of $\underline{\mathcal{K}}(f)$ implies the causality of $\mathrm{H}(z,t)$ because analytic $\underline{\mathcal{K}}(f)$'s yield $\underline{H}(z,f)$'s which satisfy the Kramers-Kronig relations; see chapter 6 for more details. Note that (F.10) provides a material dependent constraint on the waveforms $\mathcal{Q}(z)$ which are 'CLDP transformable.'

The plural (transforms) used in this section's title reflects the fact that each acceptable $\underline{\mathcal{K}}(f)$ defines one integral transform relation; the CLDP transforms determine as many unique transform relations as there are unique (and acceptable) $\underline{\mathcal{K}}(f)$'s.

Choosing the shortest path in (F.10)'s Laplace plane integral allows the following re-expression of this constraint:

$$\lim_{f\to\infty} \left\{ \int_0^{\alpha(f)} \underline{\tilde{\mathcal{Q}}}(\alpha' + \mathrm{j}\,2\pi f/c(f))\,d\,\alpha' \right\} = 0 \tag{F.12}$$

Appendix G

PESAW-CLDP Overview

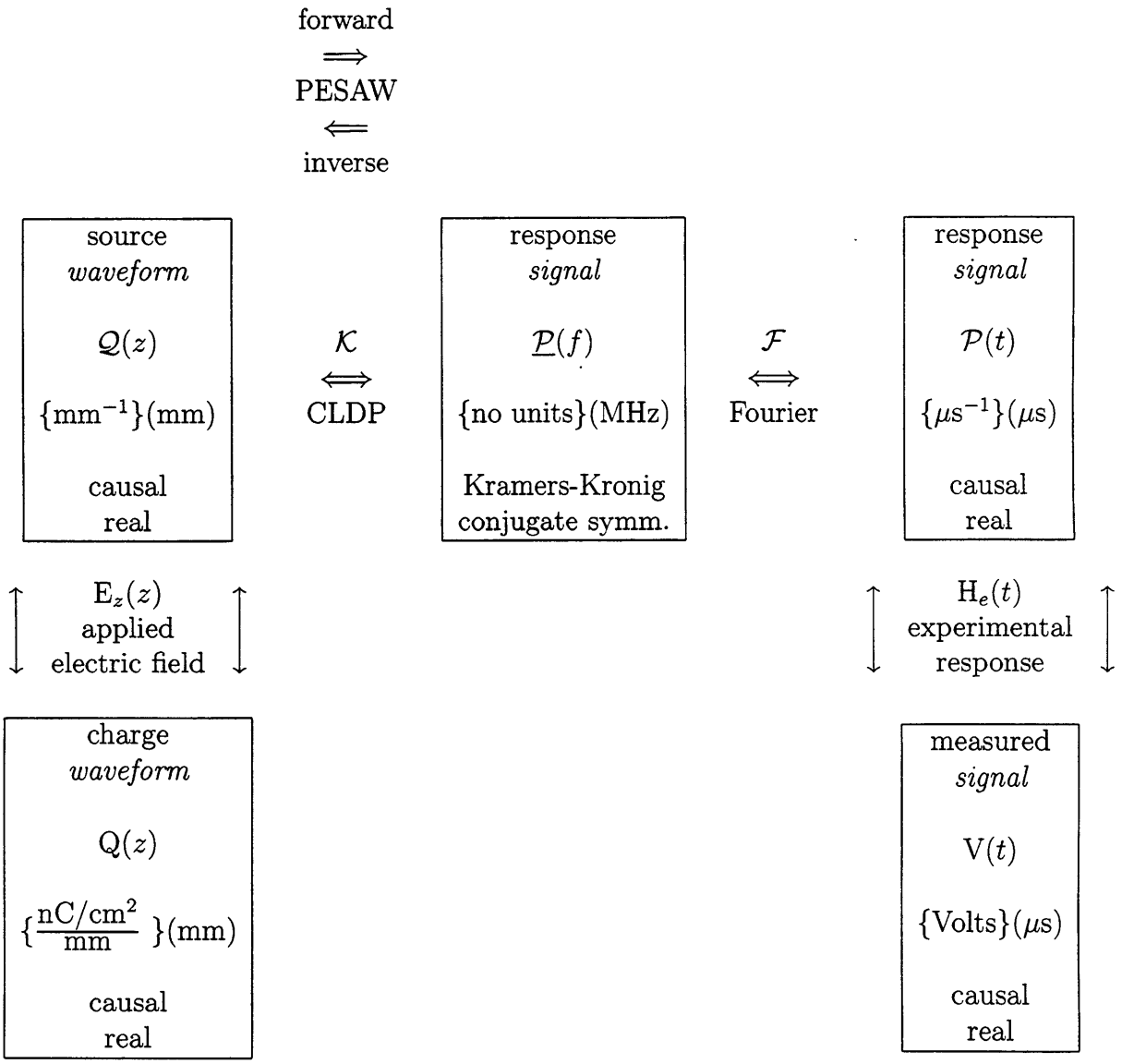

List of Figures

List of Tables

Bibliography

[1] T. Maeno, T. Futami, H. Kushibe, T. Takada and C. M. Cooke, "Measurement of spatial charge distribution in thick dielectrics using the pulsed electroacoustic method", IEEE Trans. Electr. Insul., Vol. 23, No. 3, pp. 433-439, 1988

[2] M. Hikita, M. Zahn, K. A. Wright, C. M. Cooke and J. Brennan, "Kerr Electro-optic field mapping measurements in electron-beam irradiated polymethylmethacrylate", IEEE Trans. Electr. Insul., Vol. 23, No. 5, pp. 861-880, 1988

[3] T. Mizutani, "Space charge measurement techniques and space charge in polyethylene", IEEE Trans. Dielectrics and Electr. Insul., Vol. 1, No. 5, pp. 923-933, 1994

[4] S. Mahdavi, C. Alquie and J. Lewiner, "Measurement of charge distributions in coaxial structures. Application to high voltage cables", IEEE Proc. CEIDP, Leeburg, Virginia, pp. 296-302, 1989

[5] Y. Zhang, J. Lewiner and C. Alquié, "Evidence of strong correlation between space-charge buildup and breakdown in cable insulation", IEEE Trans. Dielectrics and Electr. Insul., Vol. 3, No. 6, pp. 778-783, 1996

[6] K. Fukunaga and T. Maeno, "Measurement of the internal space charge distribution of an anti-electrostatic discharge polymer", IEEE Trans. Dielectrics and Electr. Insul., Vol. 2, No. 1, pp. 36-39, 1995

[7] X. Wang, D. Tu, Y. Tanaka, T. Muronaka, T. Takada, C. Shinoda and T. Hashizumi, "Space charge in XLPE power cable under dc electrical stress and heat treatment", IEEE Trans. Dielectrics and Electr. Insul., Vol. 2, No. 3, pp. 467-474, 1995

[8] S. H. Lee, J. Park, J. H. Han and K. S. Suh, "Space charge and electrical conduction in maleic anhydride-grafted polyethylene", IEEE Trans. Dielectrics and Electr. Insul., Vol. 2, No. 6, pp. 1132-1139, 1995

[9] R. Shimizu, M. Matsuoka, K. Kato, N. Hayakawa, M. Hikita and H. Okubo, "Development of kerr electro-optic 3-d electric field measuring technique and its experimental verification", IEEE Trans. Dielectrics and Electr. Insul., Vol. 3, No. 2, pp. 191-196, 1996

[10] K. S. Suh, D. Damon and J. Tanaka, "Space charge in polyethylene/ionomer blends", IEEE Trans. Dielectrics and Electr. Insul., Vol. 2, No. 1, pp. 1-11, 1995

[11] K. S. Suh, J. Tanaka and D. Damon, "What is TSC?", IEEE Electr. Insul. Mag., Vol. 8, No. 6, pp. 13-20, 1992

[12] J. Lewiner, "Evolution of experimental techniques for the study of the electrical properties of insulating materials", IEEE Trans. Electr. Insul., Vol. EI-21, No. 3, pp. 351-360, 1986

[13] G. M. Sessler and R. Gerhard-Multhaupt, "A review of methods for charge- or field-distribution studies on radiation-charged dielectric films", Radiat. Phys. Chem., Vol. 23, No. 3, pp. 363-370, 1984

[14] A. S. De Reggi, M. G. Broadhurst, G. T. Davis and F. I. Mopsik, "Measurement of space charge fields in polymers", Ann. Rept. CEIDP, pp. 307-312, 1987

[15] J. A. Giacometti, G. Minami, A. S. De Reggi, B. Dickens and D. L. Chinaglia, "Thermal pulse measurements on electron-beam irradiated fluoroethylene-propylene copolymer", Proc. 8th Intl. Symp. Electrets, pp. 212-217, 1994

[16] B. Sanden, *XLPE cable insulation subjected to HVDC stress*, Ph.d-thesis, Norwegian University of Science and Technology, 1996

[17] K. S. Suh, J. Y. Kim, C. R. Lee and T. Takada, "Charge distribution in polyethylene/ethylene vinylacetate laminates and blends", IEEE Trans. Dielectrics and Electr. Insul., Vol. 3, No. 2, pp. 201-206, 1996

[18] T. Maeno and K. Fukunaga, "High-resolution PEA charge distribution measurement system", IEEE Trans. Dielectrics and Electr. Insul., Vol. 3, No. 6, pp. 754-757, 1996

[19] Y. Li, M. Yasuda and T. Takada, "Pulsed electroacoustic method for measurement of charge accumulation in solid dielectrics", IEEE Trans. Dielectrics and Electr. Insul., Vol. 1, No. 2, pp. 188-195, 1994

[20] Y. Li, M. Aihara, K. Murata, Y. Tanaka and T. Takada, "Space charge measurement in thick dielectric materials by pulsed electroacoustic method", Rev. Sci. Instrum., Vol. 66, No. 7, pp. 3909-3916, 1995

[21] D. H. Staelin, A. W. Morgenthaler and J. A. Kong, *Electromagnetic Waves*, Prentice Hall, pp. 6-10, 1994

[22] S. Ramo, J. R. Whinnery and T. V. Duzer, *Fields And Waves In Communication Electronics*, John Wiley & Sons, pp. 127-136, 1965

[23] J. M. Park and H. C. Kim, "The effects of attenuation and dispersion on the waveform analysis of acoustic emission", J. Phys. D, Vol 22, No. 5, pp. 617-622, 1989

[24] M. N. Bassim and M. Houssny-Emam, "Time and frequency analysis of acoustic emission signals", pp. 139-163 of *Acoustic Emission*, edited by J. R. Matthews, Gordon and Breach Science Publishers, New York, 1983

[25] J. R. Andrews, "Pulse measurements in the picosecond domain", application note AN-3a, Picosecond Pulse Labs, Boulder, CO, Oct. 1988 (unpublished)

[26] N. S. Naham, "Transient analysis of coaxial cables using the skin effect approximation $A + B\sqrt{s}$", IEEE Trans. Circuit Theory, Vol. 19, No. 5, pp. 443-451, 1972

[27] S. M. Riad, "The deconvolution problem: an overview", Proc. IEEE, Vol. 74, pp. 82-85, 1986

[28] L. R. Rabiner, *Theory And Application Of Digital Signal Processing*, Prentice-Hall, Englewood Cliffs, NJ, 1975

[29] J. B. Bernstein, *Electrical characterization of polymeric insulation by ESAW measurements*, Ph.d-thesis, Massachussetts Inst. of Tech., 1990

[30] W. H. Press, S. A. Teukolsky, W. T. Vetterling and B. P. Flannery, *Numerical Recipes In C*, Cambridge University Press, pp. 788-826, 1994

[31] R. P. Kanwal, *Linear Integral Equations: Theory And Technique*, Birkhauser Boston, Cambridge, MA, pp. 2-4, 1997

[32] P. C. Hansen, "Numerical tools for analysis and solution of fredholm integral equations of the first kind", Inverse Problems, Vol. 8, pp. 849-872, 1992

[33] A. Tarantola, *Inverse Problem Theory*, Elsevier, New York, 1987

[34] J. C. Goswami, A. K. Chan, C. K. Chui, "On solving first-kind integral equations using wavelets on a bounded interval", IEEE Trans. Anten. Prop., Vol. 43, No. 6, pp. 614-622, 1995

[35] M. O'Donnell, E. T. Jaynes and J. G. Miller, "Kramers-Kronig relationship between ultrasonic attenuation and phase velocity", J. Acoust. Soc. Am. , Vol. 69, No. 3, pp. 696-701, 1981

[36] B. Davies and B. Martin, "Numerical inversion of the Laplace transform: a survey and comparison of methods", J. Comp. Phys. , Vol. 33, pp. 1-32, 1979

[37] L. E. Franks, *Signal Theory*, Dowden & Culver, Inc., Stroudsburg, PA, 1981

[38] L. E. Franks, *Signal Theory*, Dowden & Culver, Inc., Stroudsburg, PA, pp. 66-79, 1981

[39] F. Stenger, *Numerical Methods Based On Sinc And Analytic Functions*, Springer-Verlag, New York, New York, pp. 326-329 & pp. 422-424, 1993

[40] A. N. Tikhonov and V. Y. Arsenin, *Solution Of Ill-Posed Problems*, Winston, Washington, DC, 1977

[41] W. H. Press, S. A. Teukolsky, W. T. Vetterling and B. P. Flannery, *Numerical Recipes In C*, Cambridge University Press, pp. 538-549, 1994

[42] F. Stenger, *Numerical Methods Based On Sinc And Analytic Functions*, Springer-Verlag, New York, New York, p. 55, 1993

[43] F. Stenger, *Numerical Methods Based On Sinc And Analytic Functions*, Springer-Verlag, New York, New York, p. 261, 1993

[44] W. R. LePage, *Complex Variables And The Laplace Transform For Engineers*, Dover Publications, New York, New York, p. 318-322, 1961

[45] E. A. Guillemin, *Theory Of Linear Physical Systems*, John Wiley and Sons, New York, New York, pp. 536-559, 1963

[46] E. A. Guillemin, *Theory Of Linear Physical Systems*, John Wiley and Sons, New York, New York, p. viii, 1963

[47] S. L. Hahn, "Hilbert Transforms," pp. 463-629 of *The Transforms And Applications Handbook*, edited by A. D. Poularikas, CRC Press, Boca Raton, Florida 1996

[48] A. D. Poularikas, "Appendix 1: Functions Of A Complex Variable," pp. 990-999 of *The Transforms And Applications Handbook*, edited by A. D. Poularikas, CRC Press, Boca Raton, Florida 1996

[49] D. H. Staelin, A. W. Morgenthaler, J. A. Kong, *Electromagnetic Waves*, Prentice Hall, Englewood Cliffs, New Jersey, pp. 207-216, 1994

[50] S. Ramo, J. R. Whinnery and T. V. Duzer, *Fields And Waves In Communication Electronics*, John Wiley & Sons, pp. 178-183, 1965

[51] R. L. Wigington and N. S. Nahman "Transient analysis of coaxial cables considering skin effect", Proc. IRE, Vol. 45, No. 2, pp. 166-174, 1957

[52] M. Abramowitz and I. Stegun, *Handbook Of Mathematical Functions*, Dover Publications, New York, New York, p. 228, 1970

[53] W. Siebert, *Circuits, Signals, And Systems*, MIT Press, p. 481, 1989

[54] D. H. Staelin, A. W. Morgenthaler, J. A. Kong, *Electromagnetic Waves*, Prentice Hall, Englewood Cliffs, New Jersey, p. 98, 1994

[55] J. J. Tuma, *Engineering Mathematics Handbook*, McGraw-Hill Book Company, New York, New York, p. 148, 1987

[56] W. R. LePage, *Complex Variables And The Laplace Transform For Engineers*, Dover Publications, New York, New York, pp. 297-299, 1961

[57] M. Abramowitz and I. Stegun, *Handbook Of Mathematical Functions*, Dover Publications, New York, New York, p. 1020, 1970

[58] W. Siebert, *Circuits, Signals, And Systems*, MIT Press, pp. 488-502, 1989

[59] F. Stenger, *Numerical Methods Based On Sinc And Analytic Functions*, Springer-Verlag, New York, New York, pp. 311-440, 1993

[60] W. Siebert, *Circuits, Signals, And Systems*, MIT Press, pp. 318-323 & pp. 400-409 & pp. 481-483, 1989

[61] W. H. Press, S. A. Teukolsky, W. T. Vetterling and B. P. Flannery, *Numerical Recipes In C*, Cambridge University Press, p. 827, 1994

[62] S. Ramo, J. R. Whinnery and T. V. Duzer, *Fields And Waves In Communication Electronics*, John Wiley & Sons, pp. 241-242, 1965

[63] W. Siebert, *Circuits, Signals, And Systems*, MIT Press, pp. 62-63 & pp. 415-416 & pp. 481-483, 1989

[64] A. V. Oppenheim and A. S. Willsky, *Signals And Systems*, Prentice-Hall, p. 189, 1983

[65] W. Siebert, *Circuits, Signals, And Systems*, MIT Press, p. 479, 1989

[66] M. S. Hughes, S. M. Handley, and J. G. Miller, "Nearly local Kramers-Kronig relations applied to porous epoxy", Proc. IEEE Ultrasonics Symposium, pp. 1041-1045, 1987

[67] M. O'Donnell, E. T. Jaynes, and J. G. Miller, "General relationships between ultrasonic attenuation and dispersion", Journal Of The Acoustical Society Of America, Vol. 63, No. 6, pp. 1935-1937, 1978

[68] C. C. Lee, M. Lahham, and B. G. Martin, "Experimental verification of the Kramers-Kronig relationship for acoustic waves", IEEE Trans. Ultrasonics, Ferroelectrics, and Frequency Control, Vol. 37, No. 4, pp. 286-294, 1990

[69] C. M. Cooke and R. J. Lyons, "Determining the attenuation coefficient and phase velocity of plane longitudinal waves in bulk polymer dielectrics with the Pulsed Electrically Stimulated Acoustic Wave method," in press.

[70] B. Hartmann and J. Jarzynski, "Ultrasonic hysteresis absorption in polymers", Journal Of Applied Physics, Vol. 43, No. 11, pp. 4304-4312, 1972

[71] B. Hung and A. Goldstein, "Acoustic parameters of commercial plastics", IEEE. Trans. On Sonics and Ultrasonics, Vol. SU-30, No. 4, pp. 249-254, 1983

[72] W. Siebert, *Circuits, Signals, And Systems*, MIT Press, p. 476, 1989

[73] M. Zahn, *Electromagnetic Field Theory*, John Wiley & Sons, p. 509, 1979

[74] W. Siebert, *Circuits, Signals, And Systems*, MIT Press, p. 49, 1989

[75] S. Seely, "Laplace Transforms," pp. 331-386 of *The Transforms And Applications Handbook*, edited by A. D. Poularikas, CRC Press, Boca Raton, Florida 1996

[76] R. V. Churchill and J. W. Brown, *Complex Variables And Applications*, 5'th ed., McGraw Hill, p. 93, 1990

[77] R. V. Churchill and J. W. Brown, *Fourier Series And Boundary Value Problems*, 4'th ed., McGraw Hill, p. 183, 1987

[78] R. V. Churchill and J. W. Brown, *Fourier Series And Boundary Value Problems*, 4'th ed., McGraw Hill, p. 23, 1987

[79] R. V. Churchill and J. W. Brown, *Complex Variables And Applications*, 5'th ed., McGraw Hill, p. 108, 1990

[80] H. A. Haus and J. R. Melcher, *Electromagnetic Fields And Energy*, Prentice-Hall, p. 19, 1989

[81] H. A. Haus and J. R. Melcher, *Electromagnetic Fields And Energy*, Prentice-Hall, p. 486-495, 1989

[82] R. P. Feynman, R. B. Leighton, and M. Sands, *The Feynman Lectures On Physics*, Addison-Wesley, pp. II-8-2 to II-8-4.

[83] R. A. Serway, *Physics For Scientists And Engineers*, 3rd Ed., Saunders College Publishing, Philadelphia, PA, p.158

[84] D. K. Cheng, *Field And Wave Electromagnetics*, 2nd Ed., Addison-Wesley, New York, NY, p. 123

[85] W. H. Hayt and J. E. Kemmerly, *Engineering Circuit Analysis*, 4th Ed., McGraw-Hill, New York, NY, p. 157

[86] H. A. Haus and J. R. Melcher, *Electromagnetic Fields And Energy*, Prentice-Hall, p. 77, 1989

[87] R. V. Churchill and J. W. Brown, *Complex Variables And Applications*, 5'th ed., McGraw Hill, p. 13, 1990

[88] W. H. Press, S. A. Teukolsky, W. T. Vetterling and B. P. Flannery, *Numerical Recipes In C*, Cambridge University Press, pp. 412-420, 1994

[89] W. Siebert, *Circuits, Signals, And Systems*, MIT Press, p. 295, 1989

[90] W. H. Press, S. A. Teukolsky, W. T. Vetterling and B. P. Flannery, *Numerical Recipes In C*, Cambridge University Press, pp. 584-591, 1994

[91] W. H. Press, S. A. Teukolsky, W. T. Vetterling and B. P. Flannery, *Numerical Recipes In C*, Cambridge University Press, pp. 504-510, 1994

[92] W. Siebert, *Circuits, Signals, And Systems*, MIT Press, pp. 578-579, 1989

[93] W. Siebert, *Circuits, Signals, And Systems*, MIT Press, pp. 435-439, 1989

[94] F. Stenger, *Numerical Methods Based On Sinc And Analytic Functions*, Springer-Verlag, New York, New York, p. vi, 1993

[95] W. Siebert, *Circuits, Signals, And Systems*, MIT Press, p. 426, 1989

[96] R. V. Churchill and J. W. Brown, *Complex Variables And Applications*, 5'th ed., McGraw Hill pp. 55-57, 1990

[97] G. James and R. C. James, *Mathematics Dictionary*, Van Nostrand Reinhold, NYC, NY, p. 155, 1976

[98] T. Fritz in T. McNeil's, "Stormy weather in space", Bostonia, Winter 1997-98, No. 4, pp. 14-19

[99] W. Siebert, *Circuits, Signals, And Systems*, MIT Press, pp. 274-283, 1989

[100] W. H. Press, S. A. Teukolsky, W. T. Vetterling and B. P. Flannery, *Numerical Recipes In C*, Cambridge University Press, pp. 129-130 & pp. 140-141, 1994

[101] H. Stark and J. W. Woods, *Probability, Random Processes, And Estimation Theory For Engineers*, Prentice-Hall, pp. 44-45, 1986

[102] H. A. Haus and J. R. Melcher, *Electromagnetic Fields And Energy*, Prentice-Hall, pp. 95-96, 1989

[103] G. S. Kino, *Acoustic Waves: Devices, Imaging, and Analog Signal Processing*, Prentice-Hall, pp. 1-15, 1987

[104] H. W. Bode, "Relations between attenuation and phase in feedback amplifier design", Bell System Technical Journal, Vol. 19, pp. 421-454, 1940

[105] P. M. Morse and K. U. Ingard, *Theoretical Acoustics*, M^{c}Graw-Hill, New York pp. 356-358, 1968

[106] W. Siebert, *Circuits, Signals, And Systems*, MIT Press, pp. 394-395 & 402-404, 1989

[107] W. Siebert, *Circuits, Signals, And Systems*, MIT Press, p. 397, 1989

[108] R. V. Churchill and J. W. Brown, *Complex Variables And Applications*, 5'th ed., McGraw Hill p. 63, 1990

[109] M. D. Greenberg, *Foundations Of Applied Mathematics*, Prentice-Hall, pp. 80-81 & 103-105 & 283-285, 1978

[110] M. Abramowitz and I. Stegun, *Handbook Of Mathematical Functions*, Dover Publications, New York, New York, pp. 231-232, 1970

[111] V. Krylov and N. Skoblya, *(Handbook Of) Numerical Inversion of Laplace Transforms*, Isreal Program for Scientific Translations, Jerusalem, 1969